Copy

remove

DOE/ER-0045/3

ALLOY DEVELOPMENT FOR IRRADIATION PERFORMANCE QUARTERLY PROGRESS REPORT FOR PERIOD ENDING JUNE 30,1980

Compiled and Edited by B. G. Ashdown, ORNL.
from Contributions of Participating Laboratories

ARGONNE NATIONAL LABORATORY

GENERAL ATOMIC COMPANY

HANFORD ENGINEERING DEVELOPMENT LABORATORY

McDONNELL DOUGLAS ASTRONAUTICS COMPANY

MASSACHUSETTS INSTITUTE OF TECHNOLOGY

NAVAL RESEARCH LABORATORY

OAK RIDGE NATIONAL LABORATORY

SANDIA NATIONAL LABORATORIES

WESTINGHOUSE FUSION POWER SYSTEMS

Prepared by
OAK RIDGE NATIONAL LABORATORY
Oak Ridge, Tennessee 37830
operated by
UNION CARBIDE CORPORATION
for the
DEPARTMENT OF ENERGY
Under Contract No. W-7405-eng-26

Printed in the United States of America Available from
National Technical Information Service
U S Department of Commerce
5285 Port Royal Road, Springfield. Virginia 22161
NTIS price codes — PrintedCopy A16 Microfiche A01

DOE/ER-0045/3
Distribution
Category
UC-20, 20c

ALLOY DEVELOPMENT FOR IRRADIATION PERFORMANCE QUARTERLY PROGRESS REPORT FOR PERIOD ENDING JUNE 30. 1980

Compiled and Edited by B. G. Ashdown. ORNL.
from Contributions of Participating Laboratories

ARGONNE NATIONAL LABORATORY

GENERAL ATOMIC COMPANY

HANFORD ENGINEERING DEVELOPMENT LABORATORY

McDONNELL DOUGLAS ASTRONAUTICS COMPANY

MASSACHUSETTS INSTITUTE OF TECHNOLOGY

NAVAL RESEARCH LABORATORY

OAK RIDGE NATIONAL LABORATORY

SANDIA NATIONAL LABORATORIES

WESTINGHOUSE FUSION POWER SYSTEMS

Date **Published:** October **1980**

Prepared by
OAK RIDGE NATIONAL LABORATORY
Oak Ridge, Tennessee 37830
operated by
UNION CARBIDE CORPORATION
for the
DEPARTMENT OF ENERGY
Under Contract No. W-7405-eng-26

FOKEWOKD

This report is the tenth in a series of Quarterly Technical Progress Reports on *"Alloy Development for Irradiation Performance"* (ADIP), which is one element of the Fusion Reactor Materials Program, conducted in support of the Magnetic Fusion Energy Program of the U.S. Department of Energy. Other elements of the Materials Program are

- *Damage Analysis and Fundamental Studies (DAFS)*
- *Plasma-Materials Interaction (PMI)*
- *Special-Purpose Materials (SPM)*

The first seven reports in this series are numbered DOE/ET-0058/1 through 7. This report is the third in a new numbering sequence that begins with DOE/ER-0045/1.

The ADIP program element is a national effort composed of contributions from a number of National Laboratories and other government laboratories, universities, and industrial laboratories. It was organized by the Materials and Radiation Effects Branch, Office of Fusion Energy, DOE, and a Task Group on *Alloy Development for Irradiation Performance,* which operates under the auspices of that Branch. The purpose of this series of reports is to provide a working technical record of that effort for the use of the program participants, for the fusion energy program in general, and for the Department of Energy.

This report is organized along topical lines in parallel to a Program Plan of the same title so that activities and accomplishments may be followed readily relative to that Program Plan. Thus, the work of a given laboratory may appear throughout the report. Chapters 1, 2, 8, and 9 review activities on analysis and evaluation, test methods development, status of irradiation experiments, and corrosion testing and hydrogen permeation studies, respectively. These activities relate to each of the alloy development paths. Chapters 3, 4, 5, 6, and 7 present the ongoing work on each alloy development path. The Table of Contents is annotated for the convenience of the reader.

This report has been compiled and edited under the guidance of the Chairman of the Task Group on *Alloy Development for Irradiation Performance.* E. E. Bloom, Oak Ridge National Laboratory, and his efforts and those of the supporting staff of ORNL and the many persons who made technical contributions are gratefully acknowledged. T. C. Reuther, Materials and Radiation Effects Branch, is the Department of Energy Counterpart to the Task Group Chairman and has responsibility for the ADIP Program within DOE.

Klaus M. Zwilsky, Chief
Materials and Radiation Effects Branch
Office of Fusion Energy

CONTENTS

1. ANALYSIS AND EVALUATION STUDIES

1.1 MATERIALS HANDBOOK FOR FUSION ENERGY SYSTEMS - J. W. Davis (McDonnell Douglas Company-St. Louis) and T. K. Bierlein (Hanford Engineering Development Laboratory)

1.1.1 ADIP Task

Task Number 1.A.1 - Define material property requirements and make structural life predictions

1.1.2 Objective

To provide an authoritative and consistent source of material property data for use by the fusion energy community in concept evaluation design, safety analysis, and performance/verification.

1.1.3 Summary

The handbook activity is progressing slower than desired with inputs. The primary delay seems to center around conflicting priorities between preparing for reactor experiments and preparing data sheets. A portion of the data sheets, those relating to fatigue crack growth and irradiation creep have been received and are being reviewed. To speed up the turn around time for these data sheets an alternate approach is being tried which involves placing more emphasis on the people working on projects since they have to be responsive to project needs in a timely manner.

1.1.4 Progress and Status

The Materials Handbook for Fusion Energy Systems has now been formally released. Initial input to the handbook involves informational pages relating to format, contents, and overall objective. Comments from people who have received the book have been favorable and several people have requested that they be added to the distribution list. Our target date for the next release of data for inclusion in the handbook is mid-September This data packet will essentially contain data on 316 stainless steel which is needed to support the ETF project. Preparation of these data sheets is under the auspices of the austenitic stainless steel working group.

In February this group was requested to be responsible for the preparation of data sheets on 316 stainless steel and to identify a time schedule for having data ready. Based on this request the working group in March assigned HEDL the responsibility of preparing data sheets on crack growth and creep, NRL the responsibility of data sheets relating to fatigue and ORNL the responsibility of preparing data sheets on tensile properties and swelling. The targeted schedule of completion for these data sheets was 15 July. At the same time the DFAS task group was asked to develop a standardized approach for the treatment or correlation of dpa, He, and $MW \cdot Yr/m^2$ also to be ready by July 15.

At the present time the preparation of the austenitic stainless steel data sheets are behind schedule. The only contributions received within the July 15 time frame were those from HEDL. The HEDL contributions are currently being reviewed and should be released for inclusion in the handbook on the original schedule. The primary reason given for the delay appears to be conflicting priorities between preparing for experiments and preparing data sheets, with the data sheets coming in last. There does not appear to be any simple resolution to this problem because of the interactions of many groups in preparing for long term experiments and a delay in schedule could result in a significant delay in reactor loading. As a result an alternate approach for the preparation of the data sheets seems to be necessary if the handbook is to be responsive to the project needs. The approach that will be tried is to get greater involvement of project personnel who, in many cases, are developing design curves in support of the projects. These people have agreed that when they prepare the data sheets in support of the projects, they will put the data in a format that is compatible with the handbook and submit these data sheets along with supporting documentation to the handbook chairman for inclusion in the handbook. These data sheets would then be routed to the various task groups or working groups for review and comments. This approach is currently being implemented on a trial basis to see if it improves the turn-around time for the data sheets.

2. TEST MATRICES AND TEST METHODS DEVELOPMENT

2.1 TEM SPECIMEN MATRIX FOK EBR-II EXPERIMENT AD-2 — D. T. Peterson (Hanford Engineering Development Laboratory)

2.1.1 ADIP Task

2.1.2 Objective

2.1.3 Summary

No report for this period.

2.L NEUTRONIC CALCULATIONS IN SUPPORT OF THE ORR-MFE-4 SPECTKAL TAILORING EXPERIMENT — T. A. Gabriel, K. A. Lillie, B. L. Bishop, and K. L. Childs (OKNL)

2.2.1 ADIP Task

ADIP Task I.A.2, Define Test Matrices and Test Procedures.

2.2.2 Objective

The objective of this work is to provide the neutronic design for materials irradiation experiments in the Oak Ridge Research Reactor (ORR). Spectral tailoring to control the fast and thermal neutron fluxes is required to provide the desired displacement and helium production rates in alloys containing nickel.

2.2.3 Summary

Three-dimensional neutronic calculations are under way to follow the irradiation environment of the MFE-4A experiment, which has recently been loaded into the ORR, and are in progress to determine the response of the ORR to multiple tungsten core pieces that will be used during later irradiations to reduce the thermal flux levels seen by the nickel-containing alloys. Preliminary results indicate that two core pieces of 50%W or four core pieces of 25%W can be used simultaneously in the reactor. However, since additional fuel is required to maintain criticality, the core fuel loading exceeded the standard 6 kg ^{235}U by about 15%. In addition, one-dimensional neutronic calculations are being planned to determine the heating rates within these tungsten core pieces and within the experimental capsules.

2.2.4 Progress and Status

The first spectral tailoring experiment (MFE-4A) has been loaded into the ORR reactor, and three-dimensional neutronic calculations using the VENTURE[1] code are under way to monitor the environment. We presently anticipate that the core piece (63% H_2O, 37% Al) currently being used will remain in the reactor for about three to four months. At that time the

core piece will he removed and replaced by a solid aluminum core piece. At approximately the same time a nickel wire will he removed from the center of the experimental capsule, and the helium content will he measured. This will check the rate at which helium is being generated in the experiment. In addition, these data will allow, if needed, modification to the helium production equation, which was obtained from High Flux Isotope Reactor (HFIK) data and which is currently being used to relate the thermal neutron fluence to the helium production for ^{58}Ni in the alloys under irradiation.

Since the possibility exists that several spectral-tailored experiments will be in the ORR at the same time, three-dimensional neutronic calculations using the VENTURE code are in progress to determine the response of the ORR to multiple tungsten core pieces. These core pieces will be used during later irradiations to reduce the thermal flux levels seen by the nickel-containing alloys. Preliminary results indicate that two core pieces of 50% W or four core pieces of 25% W can be used simultaneously in the reactor. However, since additional fuel is required to maintain criticality, the core fuel loading used exceeded the standard 6 kg ^{235}U by about 15%.

2.2.5 Future Work

Since strict control is being maintained over the temperature of the irradiated samples, one-dimensional neutronic calculations using ANISN[2] are being planned to determine the heating rates within these tungsten core pieces and within the experimental capsules. The one-dimensional cylindrical model of the experimental capsule and core element, which will be surrounded by a fuel rod,* has been devised so that these calculations can be performed (Fig. 2.2.1). The neutron source, which will be distributed around the fuel rod, will be obtained from a VENTURE calculation for an ORR core loading that contains tungsten. The incident gamma flux, which cannot be obtained directly from the VENTURE code, will be approximated by reflecting the leak of gammas from the source surface.

---

* This fuel rod represents eight ORR fuel elements.

2.3 ORR-MFE-4: A SPECTRAL TAILORING EXPERIMENT TO SIMULATE THE He/dpa RATIO OF A FUSION REACTOR IN AUSTENITIC STAINLESS STEL —

M. L. Grossbeck and K. R. Thoms (ORNL)

2.3.1 ADIP Task

ADIP Task I.A.2, Define Test Matrices and Test Procedures.

2.3.2 Objective

Through neutron spectrum tailoring, this experiment will irradiate austenitic stainless steels to achieve the same He/dpa ratio as predicted for fusion reactor first-wall service. The experiment will include type 316 stainless steel and Path A Prime Candidate Alloy (PCA).

2.3.3 Summary

This experiment consists of two capsules, each with two isothermal chambers. The first, ORR-MFE-4A, operates at 300 and 400°C; the second, ORR-MFE-4B, will operate at 500 and 600°C. The ORR-MFE-4A experiment is now in the reactor, operating successfully. It contains a total of 1326 specimens almost entirely of type 316 stainless steel and Path A PCA.

2.3.4 Progress and Status

2.3.4.1 Introduction

This experiment will provide the first high-fluence data on specimens irradiated under conditions providing the He/dpa ratio expected in an austenitic stainless steel fusion reactor first wall.

The details of the neutronics, temperature control, and experiment construction have been described in previous reports.[1,2] The experiment dosimetry package has been planned and supplied by the Fusion Reactor Materials Dosimetry activity at Argonne National Laboratory. The dosimetry will not be discussed here. This report will primarily address the specimen loading. All specimens are submerged in NaK and arranged in racks. The tensile and fatigue specimens are bundled together in packages of three or four. Specimen discharge will occur at 10, 20, 30, and *50* dpa.

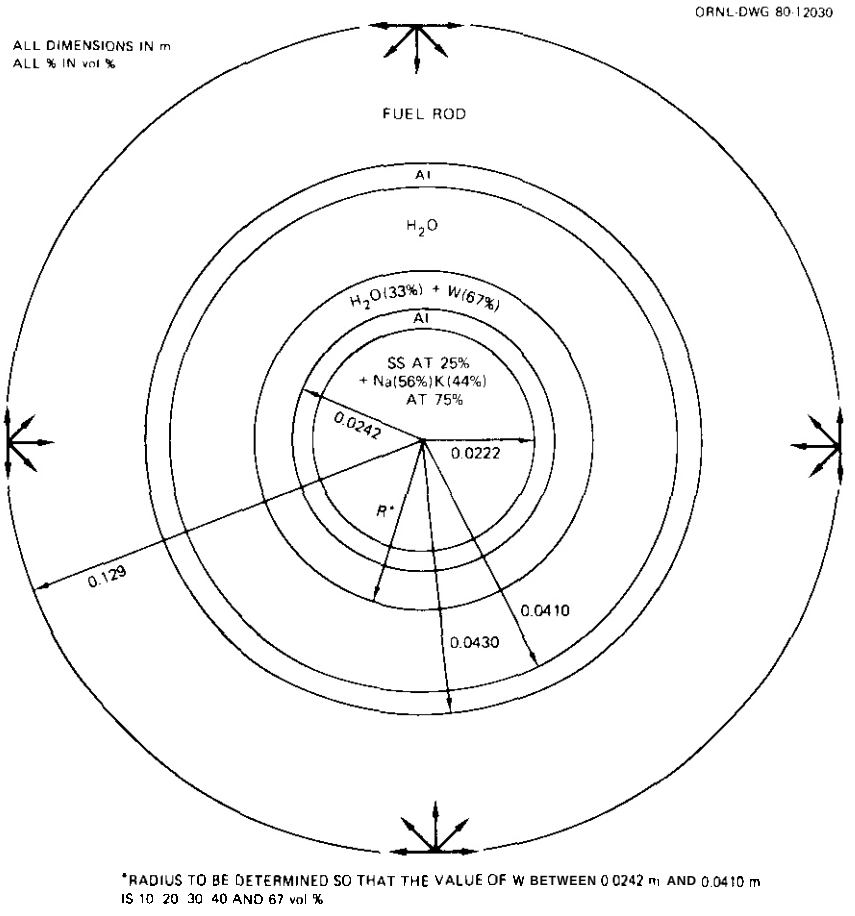

Fig. 2.2.1. One-Dimensional Model of the MFE-4A Experiment and Surrounding Oak Ridge Reactor Core Region.

The coupled neutron and gamma ray transport cross-section data sets, which were created for the TRIO-01 in-reactor solid breeder experiment, will be expanded to include W, K, and Na. Preliminary results are expected within one to two months.

2.2.6 References

1. D. R. Vondy, T. B. Fowler, and G. W. Cunningham, *VENTURE, A Code Block for Solving Multigroup Neutron Problems Applying Fine-Diffusion-Theory Approximations to Neutron Transport,* ORNL-5062 (October 1975).
2. W. W. Engle, Jr., *A User's Manual for ANISN, A One-Dimensional Discrete Ordinates Code with Anisotropic Scattering,* K-1693, Oak Ridge Gaseous Diffusion Plant (1967).

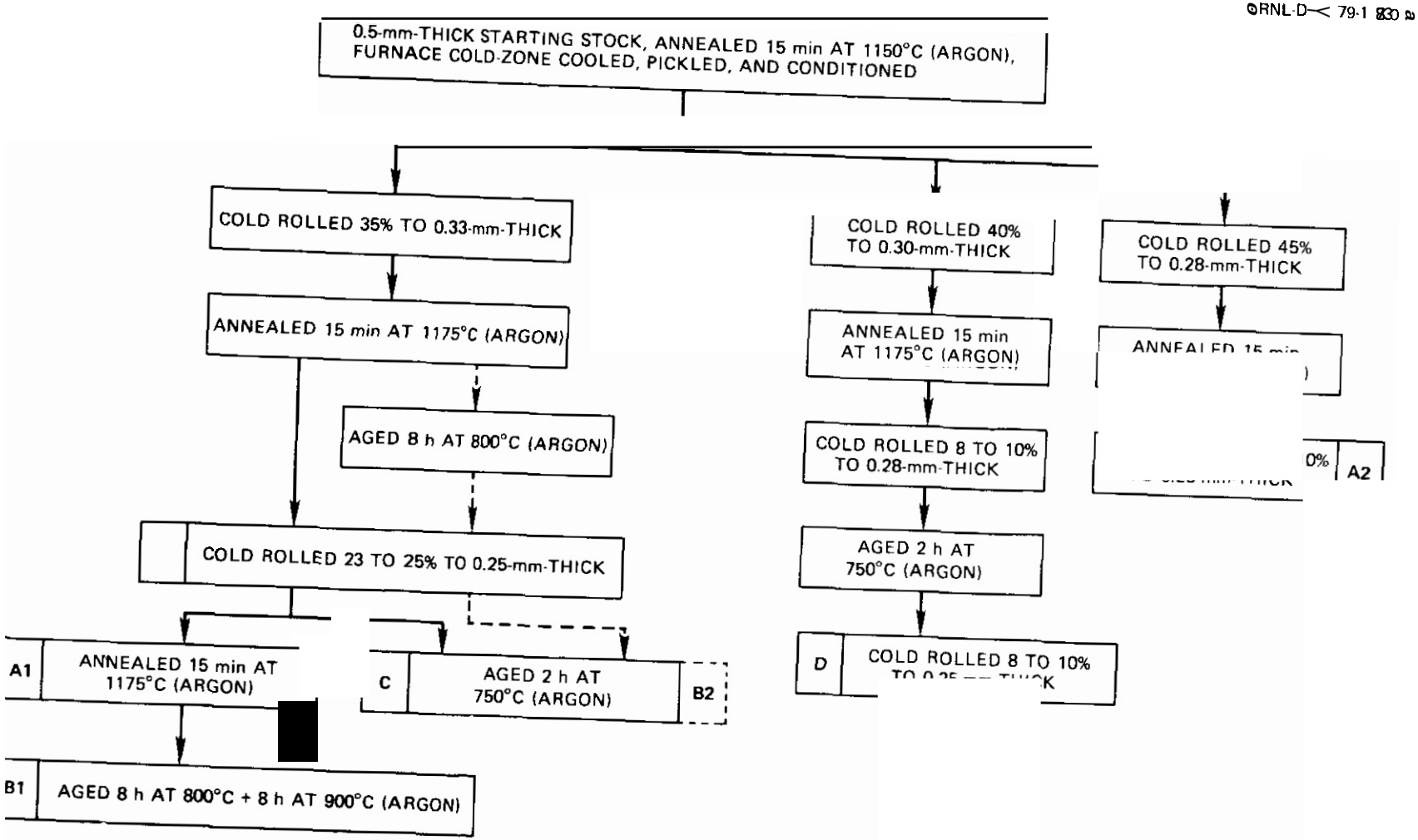

Fig. 2.3.2. Final Processing Steps to Produce Designed Microstructures of the Path A Prime Candidate Alloy (PCA). Number and letter codes are explained in Section 2.3.3.

Specimen loading information for ORNL TEM disks is described in Table *2.3.3;* the processing steps for the ORNL Path A PCA specimens used are described in Fig. *2.3.2.* The material conditions and loading information for Hanford Engineering Development Laboratory (HEDL) specimens are contained in Tables *2.3.4* and *2.3.5,* respectively. Table *2.3.6* describes the TEM disk specimens from Massachusetts Institute of Technology (MIT).

Postirradiation testing will consist of microscopic examination as well as ductility measurements using a tensile machine fitted with a special punch and die apparatus.[3]

Table *2.3.3.* Oak Ridge National Laboratory Transmission Electron Microscope Disks to be Loaded at Each of Four Temperatures

Alloy[a]	Condition[b]	Number of Specimens to be Loaded for dpa Levels at Scheduled Removal				
		10 dpa	*20* dpa	*30* dpa	*50* dpa	TBD[c]
316 SS	Argon Anneal + *20%* cold worked	*2*	*2*	*2*	*2*	4
316 SS	H_2 Anneal + *20%* cold worked	*2*	*2*	*2*	*2*	*4*
—> Path A PCA	A1	4	4	4	4	3
Path A PCA	A2	3	3	3	3	4
—> Path A PCA	A3	4	4	4	4	3
Path A PCA	B1	4	4	4	4	3
Path A PCA	B2	4	4	4	4	3
Path A PCA	C	4	4	4	4	4

[a] PCA = Prime Candidate Alloy.

[b] The designations used here for material conditions are defined in Fig. *2.3.2.*

[c] Level to be decided.

Table 2.3.4. Material Conditions for Specimens Prepared by Hanford Engineering Development Laboratory

Designation	Thermal–Mechanical Treatment[a]
A	1030°C/0.5 h/AC + 30% CW + 950°C/15 min/AC
B	1030°C/0.5 h/AC + 30% CW
C	1050°C/2 min/AC + 20% CW
D	30% CW + 1025°C/5 min/AC + 750°C/8 h/AC
E	30% CW + 1025°C/5 min/AC + 800°C/8 h/AC
F	30% CW + 1025°C/5 min/AC + 850°C/3 h/AC + 720°C/8 h/FC to 620°C/10 additional h/AC
G	1025°C/5 min/AC + 30% CW
H	1025°C/5 min/AC + 30% CW + 750°C/8 h/AC
I	1025°C/5 min/AC + 40% CW
J	1025°C/5 min/AC + 30% CW + 800°C/8 h/AC
K	1025°C/5 min/AC + 40% CW + 800°C/8 h/AC
L	1030°C/0.5 h/AC + 40% CW + 950°C/15 min/AC

[a]AC = air cooled; CW = cold worked; FC = furnace cooled.

Table 2.3.5. Transmission Electron Nicroscope Disks Prepared by Hanford Engineering Development Laboratory[a]

Alloy[b]	Material Conditions[c] for Holders to be Discharged at Various dpa Levels		
	10, 20, and 30 dpa	50 dpa	TBD[d]
E19	A	A	
E20	A, B	A, B	
E21	A	A	
E22	A, B	A, B	
E23	A	A	
E37	A	A	
E38	A	A	
316 SS	C	C	
81	D	D, G	G, H
B2	E	E, G	G, J
B3	D	D, H	G, H
B4	F	F, G	G, H
B6		I	I, K

[a]Loading is mixed between ADIP and Damage Analysis and Fundamental Studies (DAFS) program alloys. Each entry indicates two disks for each holder, for each irradiation temperature.

[b]Alloy designation defined in Table 2.3.1.

[c]Material conditions are explained in Table 2.3.4.

[d]Level to be decided.

Table 2.3.6. Transmission Electron Microscope Disks Prepared by Massachusetts Institute of Technology

Alloy[a]	Condition[b]	Irradiation Temperature[c] (°C)	Number of Specimens to be Loaded for dpa Levels at Scheduled Discharge		
			10 dpa	20 dpa	30 dpa
Path A PCA	3	All	10	10	10
Path A PCA	20% cold worked	All	10	10	10
Path A PCA	1	All	10	10	10
Path A PCA	2	All	10	10	10
PA–2	4	All	10	10	10
Path A PCA	2	400	4		
Path A PCA	2	500	4	4	
Path A PCA	2	600	4		
Path A PCA	1	400	4		
Path A PCA	1	500	4		
PA–2	2	400	4		
PA–2	2	500	4	4	
PA–2	2	600	4		
PA–2	1	400	4		
PA–2	1	500	4	4	
PA–2	1	600	4		

[a] PCA = Prime Candidate Alloy.

[b] 1 — splatted, annealed; 2 — splatted, 20% cold worked; 3 — ingot annealed; 4 — rapidly quenched and extruded.

[c] All = four irradiation temperatures: 300, 400, 500, and 600°C.

2.3.4.3 Tensile and Fatigue Specimens

The SS-1 type tensile specimens (Fig. 2.3.3) were loaded in bundles of three to facilitate removal and reinsertion at the 10, 20, and 30 dpa intervals. Since the SS–1 type specimens have the same external dimensions as Grodzinski fatigue specimens, the two may be interchanged at future loadings. The SS-1 loading is shown in Table 2.3.7.

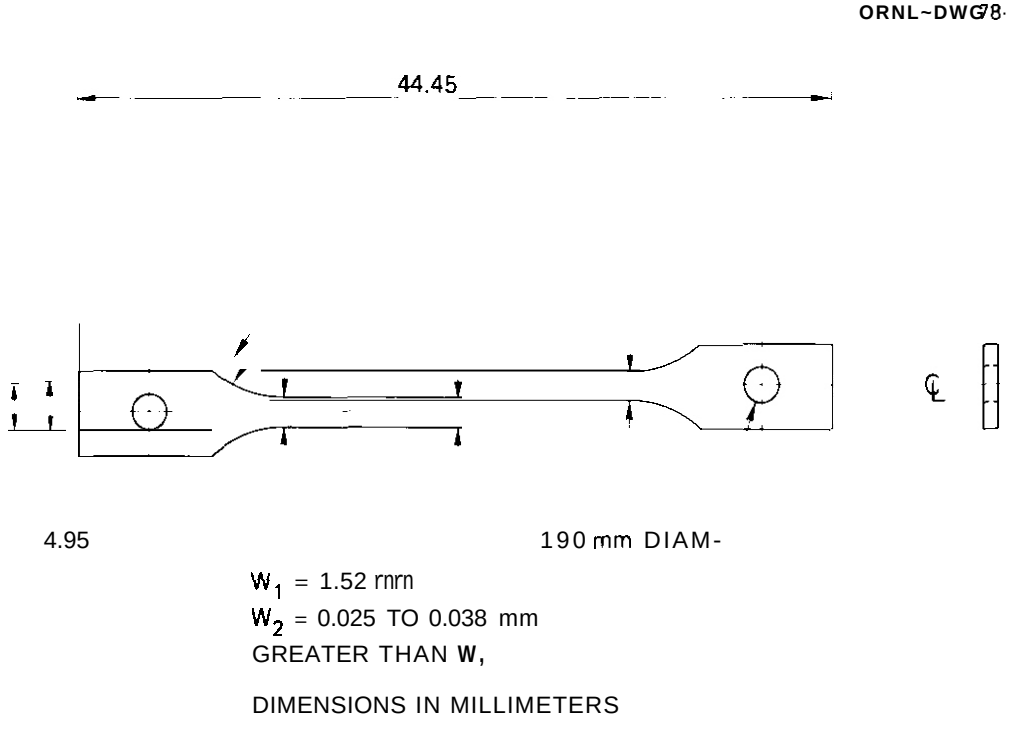

Fig. 2.3.3. The SS-1 Sheet Tensile Specimen.

Table 2.3.7. The SS-1 Tensile Specimen Loading at Each Irradiation Temperature

Alloy[a]	Condition	Number of Specimens to be Loaded for dpa Levels at Scheduled Discharge			
		10 dpa	20 dpa	30 dpa	50 dpa
316 SS	20% cold worked	8	8	8	9
Path A PCA	25% cold worked	8	8	8	9

[a]For alloy composition see Table 2.3.1. PCA = Prime Candidate Alloy.

The SS-2 type specimens (Fig. 2.3.4) were loaded in bundles of four. The matrix for these specimens is given in Tables 2.3.8 and 2.3.9.

The Crodzinski fatigue specimens (Fig. 2.3.5) were loaded in bundles of three. The loading matrix appears in Table 2.3.10.

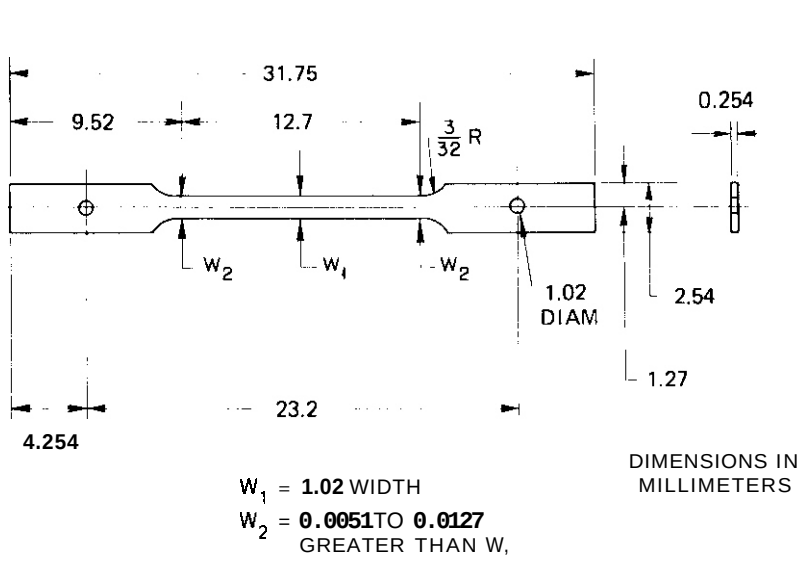

Fig. 2.3.4. The SS-2 Sheet Tensile Sample.

Table 2.3.8. The SS-2 Tensile Specimen[a] Loading at Each Irradiation Temperature

Alloy[b]	Condition[c]	Number of Specimens to be Loaded for dpa Levels at Scheduled Discharge			
		10 dpa	20 dpa	30 dpa	50 dpa
316 SS	20% cold worked	8	8	8	4
Path A PCA	A1	4	4	4	4
Path A PCA	B1	4	4	4	4
Path A PCA	B2	4	4	4	4
Path A PCA	C	4	4	4	4
E20	L	3			3
E22	L	3			3
E23	L	2			2
E38	L	2			4

[a] Specimens prepared by both Oak Ridge National laboratory and Hanford Engineering Development Laboratory.

[b] For alloy composition see Table 2.3.1.

[c] For conditions A1, B1, and B2, see Fig. 2.3.2. For condition L, see Table 2.3.5.

Table 2.3.9. Loading for SS-2 Tensile Specimens Prepared by Massachusetts Institute of Technology

Alloy[a]	Condition[b]	Irradiation Temperature (°C)	Number of Specimens Loaded for dpa Level at Scheduled Discharge	
			10 dpa	20 dpa
Path A PCA	2	300	1	
		400	4	
		500	4	3
		600	4	
Path A PCA	1	400	4	
		500	4	2
		600	4	
PA-2	2	300	1	
		400	4	
		500	4	3
		600	4	3
PA-2	1	400	4	
		500	4	2
		600	4	

[a] PCA = Prime Candidate Alloy.

[b] 1 — splatted, annealed; 2 — splatted, 20% cold worked.

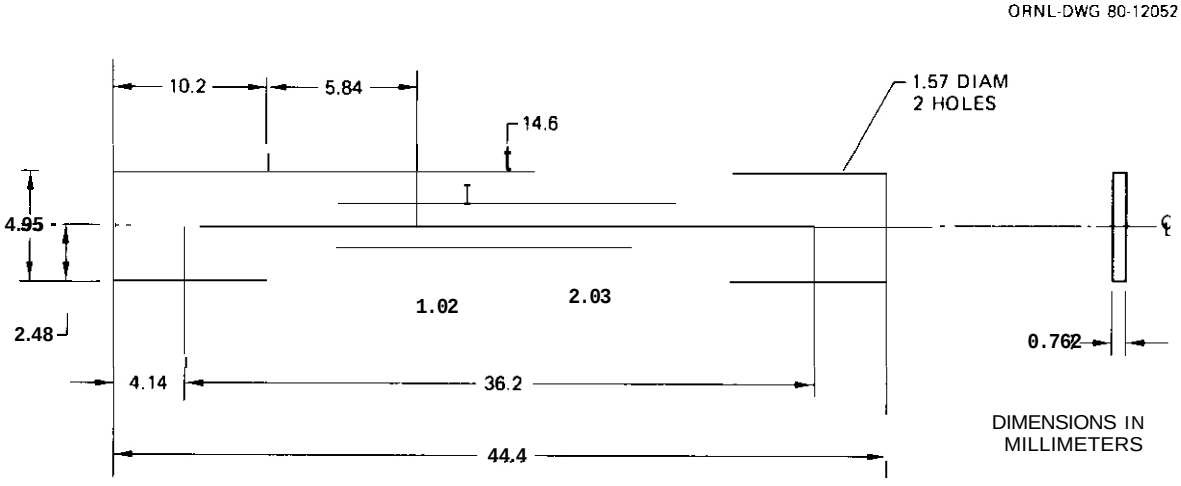

Fig. 2.3.5. Grodzinski Fatigue Specimen.

Table 2.3.10. Grodzinski Fatigue Specimen Loading at Each Irradiation Temperature, 300 to 600°C

Alloy[a]	Condition	Number of Specimens Loaded for dpa Levels at Scheduled Discharge			
		10 dpa	20 dpa	30 dpa	50 dpa
316 SS	20% cold worked	4	4	4	4
Path A PCA	25% cold worked	4	4	4	4

[a]PCA = Prime Candidate Alloy.

2.3.4.4 Pressurized Tubes

Since no irradiation creep data exist on alloys containing fusion reactor concentrations of helium, pressurized tubes of type 316 stainless steel and Path A PCA were included in this experiment. Tubes with 4.57-mm (0.180-in.) diameters, 0.25-mm (0.010-in.) wall thicknesses, and 25.4-mm (1.0-in.) lengths were used. To measure zero stress swelling, four rings — two of each alloy — were used at each temperature. Details of the irradiation creep experiment specimen loading are given in Table 2.3.11. The tubes will be removed from the experiment, their diameters will be measured, and then they will be reloaded for continued irradiation at each experiment change-out, scheduled at 10, 20, 30, and 50 dpa.

2.3.4.5 Crack Growth Specimens

Five crack growth specimens (Fig. 2.3.6) were included at each temperature. At the time of the first specimen discharge, a decision will be made as to which specimens will be tested. The test results will be used to determine the dpa level to which the remaining specimens will be irradiated. The irradiation matrix appears in Table 2.3.12.

Table 2.3.11. Irradiation Matrix for Pressurized Tubes in Irradiation Creep Experiment

Hoop stress (MPa)	Pressurized Tube Loadings[a] at Various Irradiation Temperatures			
	300°C	400°C	500°C	600°C
20				S, P
35				S, P
50				S, P
65				S, P
80			S, P	S, P
90				S, P
100	S, P	S, P	S, P	S, P
136		S		
140			S, P	
144	S			
150		S, P		
170			S, P	
200	S, P	S, P	S, P	
240			S, P	
250	S, P	S, P		
270			S, P	
300	S, P	S, P		
350	P	P		
400	S, P	S, P		
450	S, P			

[a] S = type 316 stainless steel, 20% cold worked; P = Path A Prime Candidate Alloy, 20% cold worked.

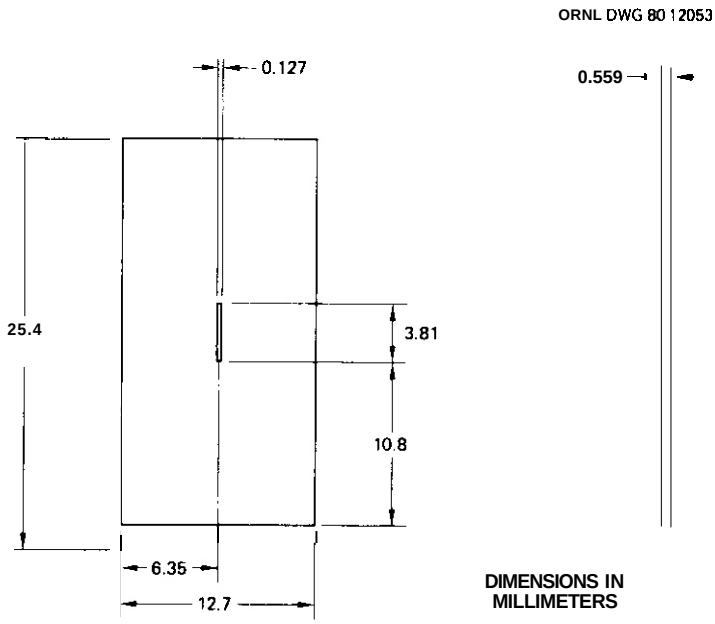

Fig. 2.3.6. Crack Growth Specimen. Tabs are welded along the 25.4-mm edge following irradiation.

determine the tritium production rates within the breeder region and the neutron and gamma ray heating rates within the core and capsule elements.

The material compositions used in the six zone calculations are presented in Table *2.4.1.*

Table 2.4.1. Composition of the Six Zones of the Calculation Model[a]

Zone	Outer Radius of Zone (mm)	Material	Density (atoms/m3)	Comments
1	1.58	^{4}He	2.69 x 10^{25}	^{4}He at 0.1 MPa (1 atm)
2	2.82	Fe	5.86 x 10^{28}	Stainless steel at 7.87 Mg/m^3
		Ni	9.69 x 10^{27}	
		Cr	1.73 x 10^{28}	
3[b]	17.8	7Li	5.25 x 10^{28}	Li_2O at 1.41 Mg/m^3, 70% of fully dense Li_2O
		^{6}Li	4.26 x 10^{27}	
		He	8.07 x 10^{24}	^{4}He at 30 kPa (0.3 atm)
		O	2.84 x 10^{28}	
4	19.1	Same as zone 2		
5	43.0	Al	6.02 x 10^{28}	2.7 Mg/m^3
6[c]	129.0	^{235}U	1.64 x 10^{26}	
		^{238}U	1.15 x 10^{25}	[d]
		Al	2.35 x 10^{28}	
		O	2.03 x 10^{28}	
		H	4.06 x 10^{28}	

[a]The one-dimensional zone model of the reactor core region is described in detail in T. A. Gabriel, R. A. Lillie, and B. L. Bishop, "Neutronic Calculations for the Conceptual Design of an 'In-Pile' Solid Breeder Experiment IPSB-01," *ADIP Quart. Prog. Rep. Mar. 31, 1980,* DOE/ER-0045/2, pp. 16-18.

[b]Naturally occurring lithium. For some calculations the lithium was assumed to be 0.5% ^{6}Li and 99.5% ^{7}Li.

[c]Represents standard fuel rods that surround the experiment. For some calculations this value was reduced by 14/24, representing 140 g fuel per rod rather than 240 g.

[d]See T. P. Hamrick and J. H. Swanks, *The Oak Ridge Research Reactor — A Functional Description,* OWL-4169 (September 1968).

The source neutron distribution was taken from the VENTURE[3] run VITAOO.INP (C-3).

When these preliminary calculations were carried out, the coupled neutron and gamma ray transport cross-section data sets were not totally complete. The delayed fission gamma ray cross sections needed to account for the gamma rays produced from fission products were not available. To obtain an estimate of the influence of these gamma rays, the thermal neutron group gamma transfer coefficient was increased by a factor of about 2. This, of course, forces the shape of the energy spectra of the delayed gammas to be equal to the prompt gammas. Results are presented that indicate the effect of these gammas. In addition, only the incident neutron spectrum and not' the gamma spectrum was known. Since these source gammas were deemed important, all gammas that leaked from the system were reflected back into the system so that an approximate gamma source could be obtained.

The tritium production rates for two lithium compositions and two fuel rod loadings are presented in Table 2.4.2 as a function of radial position in the capsule. These values can be compared with those obtained for the EPR fusion reactor,[4] which yielded tritium production levels ranging from 1.2×10^{18} to 6.2×10^{18} atoms/s m^3 at 1 MW/m^2 wall loading. For natural lithium, a rather large production gradient exists that is far less important for 0.5% ^6Li. In addition, for a lower fuel loading in fuel elements surrounding the breeder region, the tritium production from ^6Li increases while that from ^7Li decreases. The reduced fuel offers a smaller capture cross section for the incident thermal neutrons, thereby allowing for more capture in the breeder region. Also the reduced number of fissions in the fuel assembly reduces the number of fast neutrons and thereby reduces the number of $n + {}^7Li \rightarrow n' + {}^4He + {}^3H$ reactions, where n represents neutrons. Because of the large tritium production levels, we have tentatively decided to use about 0.5% 6Li to reduce the amount of tritium inventory and to maintain a relatively flat energy deposition profile.

The heating rates in the breeder region and in the core piece are presented in Table 2.4.3. The effect of gamma ray reflection and the approximate treatment of the delayed fission gammas is apparent.

Table 2.4.2. Tritium Production Rates in the Capsule

Radial Position (mm)	Tritium Production Rate,[a] atoms/s m3					
	7.5% ^{6}Li		0.5% ^{6}Li			
	240 g Fuel		240 g Fuel		140 g Fuel	
	^{6}Li	^{7}Li	^{6}Li	7Li	^{6}Li	^{7}Li
	x 10^{19}	x 10^{19}	x 10^{19}	x 10^{19}	x 10^{19}	x 10^{19}
2.82–5.82	2.08	0.0184	2.36	0.0210	2.95	0.0168
5.82–8.81	2.49	0.0185	2.39	0.0211	2.98	0.0169
8.81–11.8	3.24	0.0186	2.44	0.0212	3.05	0.0170
11.8–14.8	5.16	0.0188	2.51	0.0214	3.15	0.0172
14.8–17.8	13.1	0.0190	2.62	0.0217	3.29	0.0174

[a]Grams of fuel indicate nominal content of each element surrounding the experiment.

Table 2.4.3. Heating Rates in the Breeder Region (0.5% ^{6}Li) and in the Aluminum Core Piece for a 240-g Fuel Loading

Zone[a]	Zone[a] Content	Heating Rates,[b] (MW/m^3)			
		Neutron	Gamma Ray		
			No Reflection	Reflection	Reflection + Modified Thermal Neutron to Gamma Transfer
2	SS	0.53 (0.42)	29.4	59.0	121 (98.3)
3	Breeder	15.7 (18.6)	4.31	8.64	17.8 (14.2)
4	SS	0.54 (0.43)	30.1	59.4	122 (99.2)
5	Al	0.83 (0.77)	9.68	18.8	38.8 (31.0)

[a]The one-dimensional zone model of the reactor core region is described in detail in T. A. Gabriel, R. A. Lillie, and B. L. Bishop, "Neutronic Calculations for the Conceptual Design of an 'In-Pile' Solid Breeder Experiment IPSB-01," *ADIP Quart. Prog. Rep. Mar. 31, 1980,* DOE/ER-0045/2, pp. 15-18.

[b]Numbers in parentheses are for a core loading with 140 g fuel per fuel element.

The heating rates have been zone averaged but are reasonably flat throughout the zone. The total heating (neutron plus gamma) in the breeder region is about 33 MW/m^3 and is somewhat insensitive to the fuel loading.

So far we have not attempted to account for the effect of axial position on the source flux gradient in the ORR. The source neutron distribution for these calculations has been assumed to be constant and at a maximum level over the surface of the system. As far as can be determined, the numbers presented in the text for both the breeding and the heating rates should be reduced by about 25% to account for this change in the incident flux. The numbers so obtained would then represent the maximum values and should, to a reasonable approximation, fall below this maximum, according to the change in the total flux. Since the breeder region height is only about 0.10 m, variations in axial profile will be reasonably small.

2.4.5 Conclusions and Future Work

The expected tritium production and energy deposition rates within the breeder region for 0.5% ^6Li and fuel elements with 140 g fuel loading are presently determined to be 2.30 $\times 10^{19}$ atoms/s m^3 and 24.6 MW/m^3, respectively. As soon as the cross sections for the delayed fission gammas have been processed, more definitive heating rates will be detemined.

2.4.6 References

1. T. A. Gabriel, R. A. Lillie, and B. L. Bishop, "Neutronic Calculations for the Conceptual Design of an 'In-Pile' Solid Breeder Experiment IPSB-01," *ADIP Quart. Prog. Rep. Mar. 31, 1980*, DOE/ER-0045/2, pp. 16-18.
2. W. W. Engle, Jr., *A User's Manual for ANISN, A One-Dimensional Discrete Ordinates Code with Anisotropic Scattering*, K-1693, Oak Ridge Gaseous Diffusion Plant (1967).

3. D. R. Vondy, T. B. Fowler, and G. W. Cunningham, ***VENTURE, A Code Block for Solving Multigroup Neutron Problems Applying Fine-Diffusion-Theory Approximations to Neutron Transport,*** **OKNL-5062** (October *1975*).

4. R. T. Santoro, V. C. Baker, and J. M. Barnes, "Neutronics and Photonics Calculations for the Tokamak Experimental Power Reactor," *Nucl.* ***Technol.*** 37: *274 (1978)*.

2.5 AN IRRADIATION EXPERIMENT TO SCOPE THE TENSILE PKOPEKTIES OF FEKKITIC ALLOYS — HFIK–CTK–33 — M. L. Grossbeck and J. W. Woods (ORNL)

2.5.1 ADIP Task

ADIP Task I.A.2, Define Test Matrices and Test Procedures.

2.5.2 Objective

This experiment is designed primarily to evaluate the tensile properties of ferritic steels following irradiation in a mixed–spectrum fusion reactor at 50°C. Nickel has been added to HT9 and 9 Cr-1 Mo to provide transmutation helium at levels relevant to fusion reactor first-wall service.

2.5.3 Summary

An irradiation capsule was constructed containing sheet tensile specimens for irradiation in the High Flux Isotope Reactor (HFIK). The specimens were sealed in an aluminum rod to isolate them from the reactor coolant yet still maintain good thermal contact with the coolant water. The alloys were unmodified and nickel–doped HT9 and 9 Cr-1 Mo steels' as well as reference type 316 stainless steel and the USSK austenitic stainless steel from the U.S.-USSR Fusion Reactor Materials Agreement.

2.5.4 Progress and Status

The experiment primarily supports the Engineering Test Facility (ETF) design project, in which the first wall will operate in the *50* to 300°C range. It is also the first mixed–spectrum reactor irradiation of Path E alloys and, therefore, will produce the first specimens of such alloys containing both displacement damage and helium.

2.5.4.1 Capsule Description

The irradiation capsule consists of an aluminum rod. *520* mm long and 12.7 mm in diameter, split longitudinally with a channel milled along the axis to accommodate sheet specimens of the type shown in Fig. *2.5.1.* When loaded with specimens, the rod was welded along the longitudinal seams.

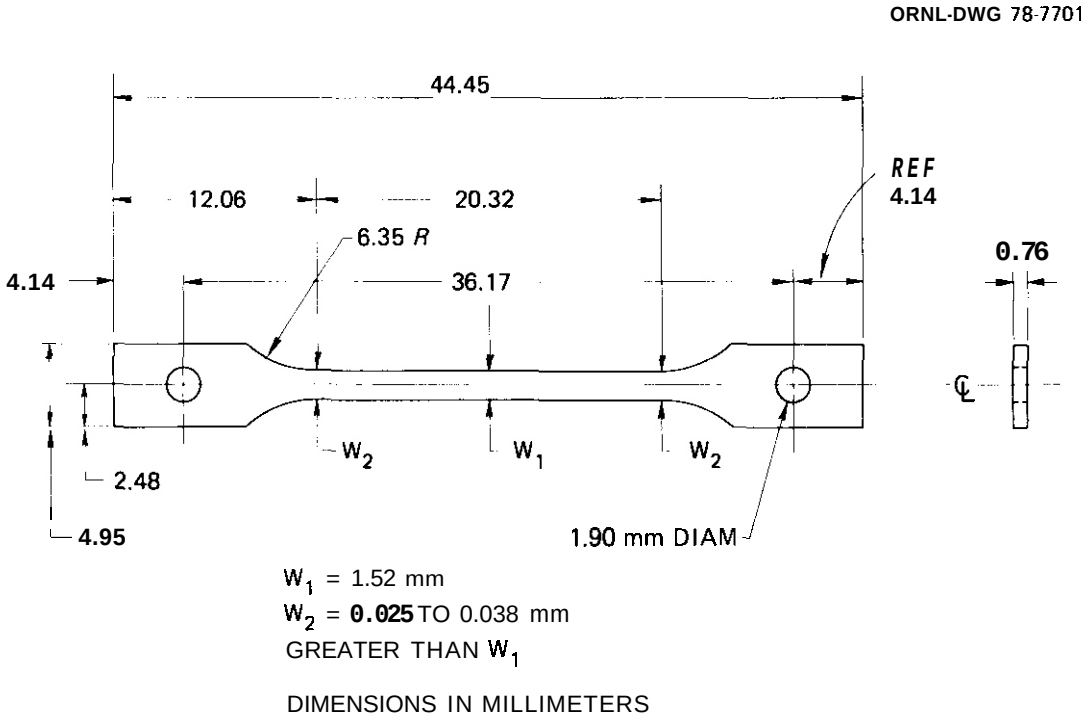

Fig. 2.5.1. The SS-1 Type Tensile Specimen.

Large weld beads were used to also serve as centering fins. Top and bottom end fittings as used in previous HFIR experiments were welded in place and a shroud tube was fastened over the entire capsule to provide high-velocity coolant flow around the capsule.

2.5.4.2 Specimen Loading

The specimens were sheet tensile of the SS-1 design (Fig. 2.5.1). This is a standard specimen used previously in Experimental Breeder Reactor (EBR)-II and Oak Ridge Research Reactor (ORR) irradiation experiments.

A total of 44 specimens was included in 4 strings parallel to the rod axis. Table 2.5.1 shows the specimen loading. The compositions of specimen materials are shown in Table 2.5.2, and detailed analyses of the nickel-doped alloys are in a previous report.' The heat treatments are described in Table 2.5.3.

All ferritic allays were heat-treated in flowing helium. The furnace chamber was evacuated to a pressure of 10^{-3} Pa, then backfilled with helium. Specimens were cooled in the cold zone of the furnace.

Table 2 5 1. Distribution of and Predicted Displacement and Helium Production Levels[a] for Alloys in the HFIR-CTR-33

Position[b]	Displacement Level (dpa)	String 1		String 2			String 3			String 4		
		Alloy	He (at. ppm)	Alloy	Heat	He (at. ppm)	Alloy	Heat	He (at. ppm)	Alloy	Heat	He (at. ppm)
1	5	EP 838	170	HT9	91354	7	HT9	XAA 3587	7	9 Cr-1 Mo + 2 Ni Adjusted	XA 3593	31
2	7	316	250	HT9 + 1 Ni	XAA 3588	25	9 Cr-1 Mo + 2 Ni	XA 3591	50	2 1/4 Cr-1 Mo	72768 (HT1)	0
3	9	316	360	HT9	91354	14	HT9	XAA 3587	14	9 Cr-1 Mo + 2 Ni Adjusted	XA 3593	63
4	9	316	425	HT9 + 1 Ni	XAA 3588	38	9 Cr-1 Mo + 2 Ni	XA 3591	75	2 1/4 Cr-1 Mo	72768 (HT2)	0
5	10	316	480	9 Cr-1 Mo	XA 3590	4	9 Cr-1 Mo + 2 Ni Adjusted	XA 3593	85	9 Cr-1 Mo + 2 Ni	XA 3591	85
6	10	316	510	HT9	91354	21	HT9	91354	21	HT9	XAA 3587	21
7	10	316	480	HT9 + 2 Ni Adjusted	XAA 3592	89	HT9 + 1 Ni	XAA 3588	43	2 1/4 Cr-1 Mo	72768 (HT1)	0
8	9	316	425	2 1/4 Cr-1 Mo	72768 (HT1)	0	2 1/4 Cr-1 Mo	72768 (HT2)	0	HT9 + 2 Ni	XAA 3589	79
9	9	316	360	HT9	91354	14	9 Cr-1 Mo	XA 3590	3	HT9 + 2 Ni Adjusted	XAA 3592	66
10	7	316	280	HT9 + 2 Ni	XAA 3589	52	HT9 + 2 Ni	XAA 3589	52	2 1/4 Cr-1 Mo	72768 (HT2)	0
11	5	316	170	EP 838		70	9 Cr-1 Mo	XA 3590	1.4	HT9 + 2 Ni Adjusted	XAA 3592	32

[a]Calculated level of helium from ^{58}Ni.

[b]Position 1 is top of the experiment.

Table 2.5.2. Compositions[a] of Alloys Included in HFIK–CTK–33

Alloy	Content, wt %							
	Cr	Ni	Mo	W	V	Si	Mn	Al
HT9	11.5	0.5	1.0	0.5	0.3	0.25	0.5	
HT9 + 1 Ni	11.9	1.1	1.1	0.5	0.3	0.14	0.5	
HT9 + 2 Ni	11.7	2.3	1.0	0.5	0.3	0.14	0.5	
HT9 + 2 Ni Adjusted	13.5	2.3	1.6	0.7	0.3	0.14	0.5	
9 Cr-1 Mo	8.6	0.1	1.0		0.2		0.4	
9 Cr-1 Mo + 2 Ni	8.5	2.2	1.0		0.2		0.4	
9 Cr-1 Mo + 2 Ni Adjusted	12.2	2.2	1.7		0.3		0.4	
2 1/4 Cr-1 Mo	2.27		1.0			0.33	0.5	
316	17.3	12.4	2.1			0.7	1.7	
EP 838	12	4.6	0.45			0.6	13	1.0

[a]Balance Fe.

Table 2.5.3. Heat Treatments Used for Alloys in Irradiation Experiment HFIK–CTK–33

Alloy	Heat	Specimens	Austenitizing		Tempering	
			Temperature (°C)	Time (h)	Temperature (°C)	Time (h)
HT9	91354	5	1050	0.5	780	2.5
HT9	XAA3587	3	1050	0.5	780	2.5
HT9 + 1 Ni	XAA3588	3	1050	0.5	780	2.5
HT9 + 2 Ni	XAA3589	3	1050	0.5	700	5
HT9 + 2 Ni Adjusted	XAA3592	3	1050	0.5	700	8
9 Cr-1 Mo	XA3590	3	1040	0.5	760	1
9 Cr-1 Mo + 2 Ni	XA3591	3	1040	0.5	700	5
9 Cr-1 Mo + 2 Adjusted	XA3593	3	1050	0.5	700	8
2 1/4 Cr–1 Ma (HT1)	72768	3	900	0.5	700	1
2 1/4 Cr-1 Ma (HT2)	72768	3	900	0.5[a]	700	2
316 (20% cold worked)	X15893	10	1050	1		
EP 838		2	1160	0.08 (5 min)[b]		

[a]Furnace cool to 700°C.

[b]Water quench.

2.5.4.3 Irradiation Conditions

Irradiation began on June 6, 1980, with HFIK cycle 194 and is planned to continue through November 1980, cycle 198. The experiment is being conducted in a peripheral target position, thus maximizing fast fluence. A calculated damage level of up to 10 dpa will be achieved, and helium levels up to 90 at. ppm are expected in the ferritic steels.

Flux monitors provided by L. R. Greenwood of Argonne National Laboratory have been included to measure fluence, spectrum, and helium production.

2.5.5 Conclusions

The first HFLR ferritic alloy experiment has been initiated. This will provide the first tensile data for low-temperature irradiations (~50°C).

2.5.6 Reference

1. M. L. Grossbeck, V. K. Sikka, T. K. Roche, and R. L. Klueh, "Preparation of Nickel-Doped Ferritic Alloys for HFIR Irradiation to Produce Helium," *ADIP Quart. Prog. Rep. Dec. 31,* 1979, DOE/ER-0045/1, pp. 100-04.

2.6 SPECIMEN MATRIX FOR HFIR IRRADIATION OF PATH B ALLOY — D. T. Peterson (Hanford Engineering Development Laboratory)

2.6.1 ADIP Task

2.6.2 Objective

2.6.3 Summary

No report for this period.

3. PATH A ALLOY DEVELOPMENT — AUSTENITIC STAINLESS STEELS

3.1 THE EXCHANGE OF AUSTENITIC STAINLESS STEELS UNUEK THE U.S.-USSR FUSION REACTOR MATERIALS AGREEMENT — T. K. Roche (ORNL)

3.1.1 ADIP Task

ADIP Task I.D.l, Materials Stockpile for MFE Programs.

3.1.2 Objective

The United States and the USSR have agreed to develop common physical points of reference (in materials and tests) to which other irradiation effects research and development studies may be related. The first step of this agreement was to exchange a stock of austenitic stainless steels.

3.1.3 Summary

Sheet and rod stock of austenitic stainless steels have been exchanged between the U.S. and USSK fusion reactor materials irradiation effects programs. The United States supplied type 316 stainless steel, while the USSR submitted a low-nickel, high-manganese austenitic stainless steel.

3.1.4 Description of Material Exchanged

The United States supplied 41 pieces (8.8 kg total) of 7.9-mm-diam (0.313-in.) rod with total length of 23 m (904 in.) and 50 pieces (10.7 kg total) of 279- by 51- by l.9-mm (11 x 2 x 0.075-in.) sheet processed from the U.S.-MFE reference heat type 316 stainless steel X-15893 in the 50%-cold-worked condition. A photograph of this material is shown in Fig. 3.1.1. Although our reference condition for specimens made from this material is 20% cold work after final heat treatment, supplying 50%-cold-worked material still allows the flexibility for further processing (annealing and reworking) for evaluation in a variety of conditions.

In return, 28 pieces of 10.5-mm-diam (0.41-in.) rod with total length of 28 m (1106 in.) and 10 pieces of 991- by 10.2- by 2.6-mm (39 x 0.40 x 0.104-in.) sheet of a low-nickel, high-manganese stainless steel, type EP 838, were received from the USSR.

Y-166807

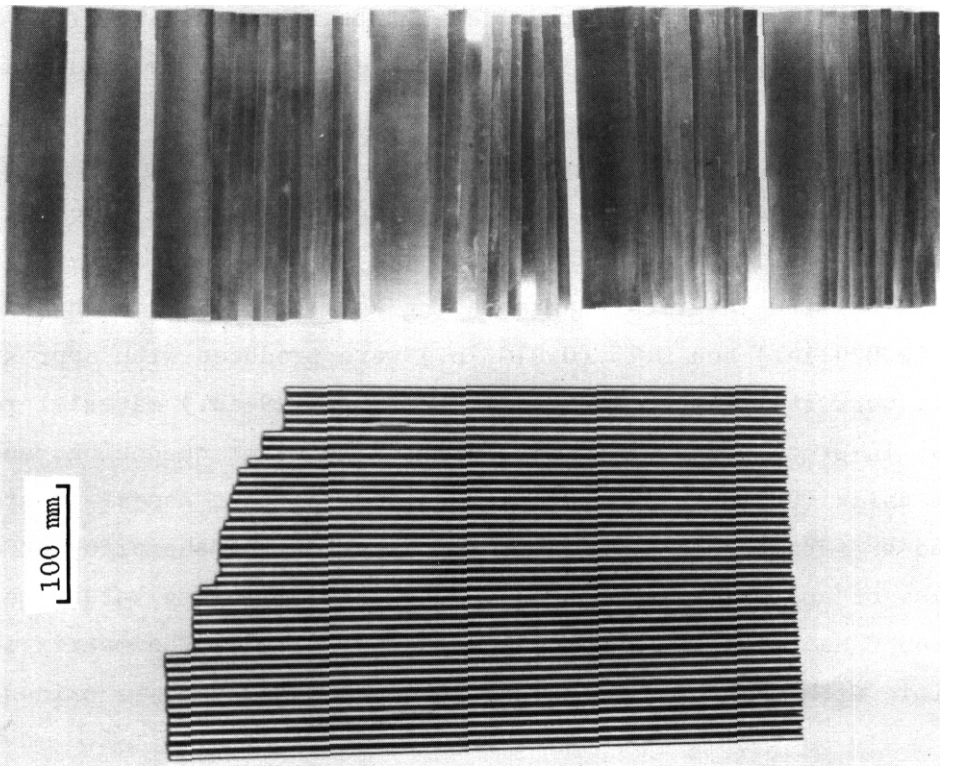

Fig. 3.1.1. The 7.9-mm-Diam (0.313-in.) Rod (Bottom) and the 1.9-mm-Thick (0.075-in.) Sheet (Top) of Type 316 Stainless Steel, Heat X-15893, Supplied to the USSR Under the U.S.-USSR Fusion Reactor Materials Agreement.

The composition of the steel EP 838 is shown below.

Element	Content (wt %)	Element	Content (Wt %)
C	0.02	Ce	0.01-0.2
Cr	11-13	B	0.0005
Mn	12-14	S	0.4
Si	0.06	P	0.4
Ni	4.4-4.8	O	0.001-0.002
Mo	0.3-0.6	N	0.05-0.09
Al	0.8-1.2	Fe	Balance

This steel is reported to be produced on an experimental commercial scale and has been designed for elevated-temperature and nuclear applications. The sheet and rod were hot rolled from double-melted ingot stock.

The first melting was by air induction followed by plasma remelting under a hydrogen-doped protective atmosphere. After hot rolling, the material was annealed at 1160°C, water quenched, cleaned, then cold worked 20%.

3.1.5 Additional Fabrication of the USSR Steel

To provide stock for radiation damage evaluation, a piece of as-received sheet stock was further processed without difficulty at ORNL by cold rolling with intermediate annealing at 1160°C. Final thicknesses of 0.7 mm (0.029 in.) and 0.25 (0.010 in.) were produced with approximately 20% cold work at finish. The 0.7-am-thick (0.029-in.) mterial received the last in-process anneal in air followed by water quenching, and the 0.25-am-thick (0.010-in.) material received the last anneal in argon followed by furnace cooling. The microstructure of the alloy at a thickness of approximately 0.9 mm (0.036 in.) following water quenching from 1160°C and pickling can be seen in Fig. 3.1.2. The matrix is austenitic with numerous inclusions that are assumed to be oxides.

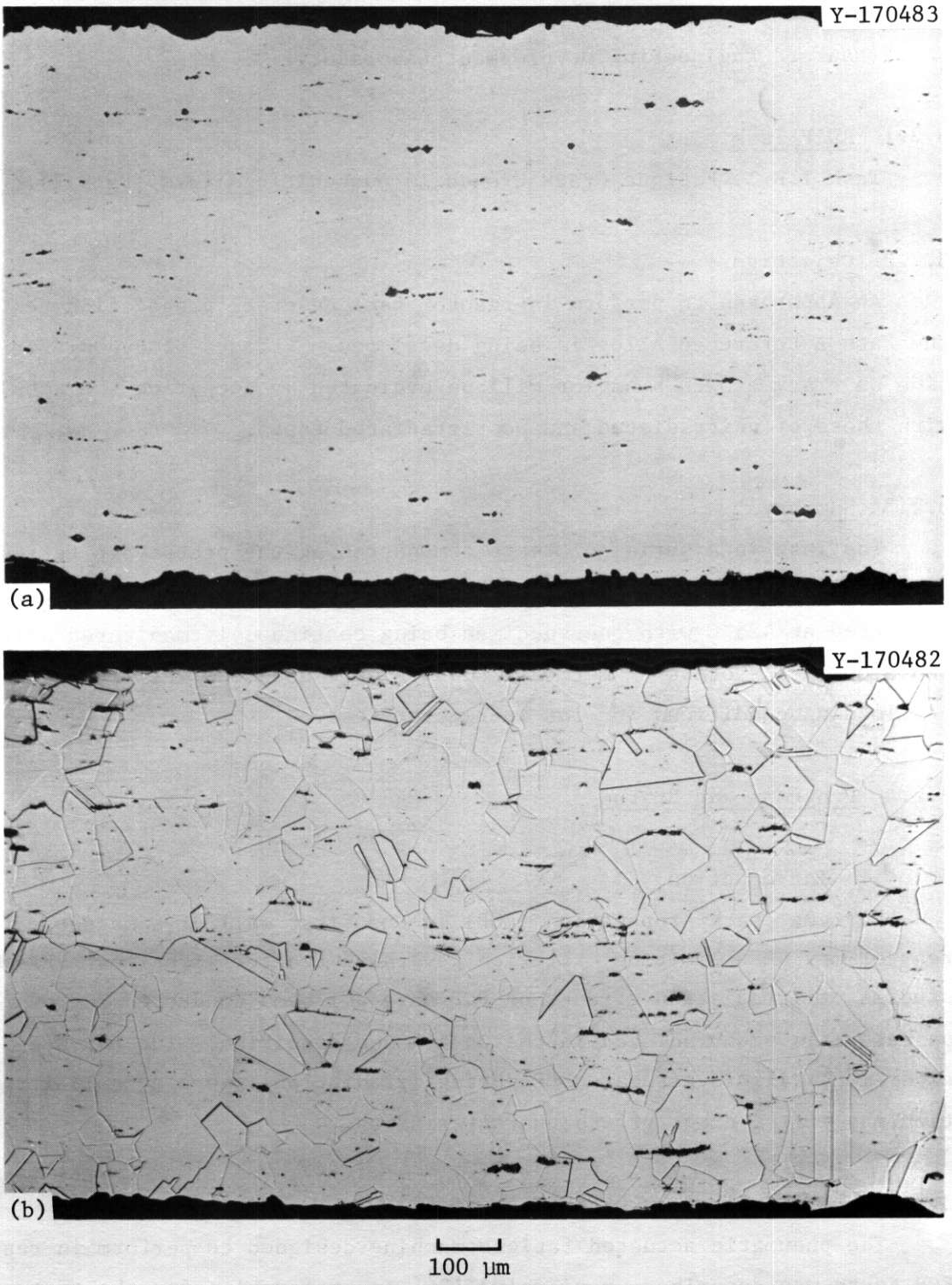

Fig. 3.1.2. Microstructure of Type EP 838 Stainless Steel from the USSR Following Water Quenching from 1160°C and Pickling. (a) As polished. (b) Etched in aqua regia.

3.2 FATIGUE CRACK GROWTH TESTING OF 316 SS FOR MFE-5 - A. M. Ermi (Hanford Engineering Development Laboratory)

3.2.1 ADIP Task

Task I.B.l, Fatigue Crack Growth in Austenitic Alloys (Path A).

3.2.2 Objective

An apparatus to perform in-reactor fatigue crack propagation tests on the Path A Reference Alloy is being developed. Effects of dynamic irradiation on crack growth behavior will be evaluated by comparing the results with those of unirradiated and postirradiated tests.

3.2.3 Summary

The last in a series of tests demonstrating the prototypic fatigue machine has been successfully completed. An eight-specimen chain test was conducted at 425°C with one specimen being continuously monitored using the electrical potential method. Results were used to finalize precracking and loading conditions for the in-reactor test.

3.2.4 Progress and Status

3.2.4.1 Introduction

Fatigue crack propagation (FCP) in the first wall of a magnetic fusion reactor may be a limiting criterion governing reactor lifetimes. Previous studies of irradiation effects on FCP have all been conducted out of reactor on materials preirradiated in the unstressed condition. The ORR-MFE-5 experiment will investigate FCP during irradiation, where dynamic irradiation may effect crack growth characteristics.

3.2.4.2 Eight-Specimen Chain Test at 425°C

The pneumatic actuated fatigue machine designed to perform in-reactor FCP tests was described previously.[1,2] In preparation for the test, a prototypic machine was constructed and various room temperature tests were performed.[3] The last planned test before the actual in-reactor and thermal control tests (both in sodium) was an eight-specimen chain test in helium

at 425°C.

The miniature center-cracked tension (CCT) specimens were of the reference alloy, 20% cold-worked 316 stainless steel. Initial crack lengths in the chain ranged from 4.5 to 10.0 mm. The crack length of one of the specimens was continuously monitored using the electrical potential (e.p.) method.[4] Test conditions included a frequency of 5.5 cycles/min, a maximum load of 350 lbs and a load ratio R = 0.10. A one meter electric kiln with nine independent temperature zones was used for the test.

After 132,836 cycles, one of the specimens separated, and the test was stopped. The seven remaining specimens were removed, and the final crack lengths were measured optically under a 150 lb load. These visual results and those obtained from the e.p. method are shown in Figure 3.2.1. The solid line is from a statistical analysis of only the initial and final crack length values.[2] The room temperature band from Reference 3 is included for comparison.

It has been shown that crack growth behavior in relatively inert environments below one-half the absolute melting temperature is, in general, quite close to that in a room temperature air environment.[5] Therefore, it is not surprising that the results of the 425°C test in helium lie on the upper bound of the room temperature band. Upon examination of the specimens, it was clear that some slight oxidation had occurred, thus accelerating the crack growth rates in comparison to previous room temperature helium chain tests using the prototype.[3]

3.2.4.3 Loading and Test Conditions for the In-Reactor FCP Test

As reported earlier!') the duration of the in-reactor test will be up to six months at temperature. Based on a cyclic frequency of one cycle/min and taking into account the scheduled reactor down times, the number of cycles which all eight specimens would see is up to 200,000. One of the problems in designing such a test is being able to choose the load and crack length combinations that will neither (a) result in seperation of a specimen much earlier than anticipated, or (b) result in undetectable crack growth after 200,000 cycles. Both of these cases are in reference to the thermal control test since accelerated or retarded crack growth behavior during

irradiation is the prime concern of the test.

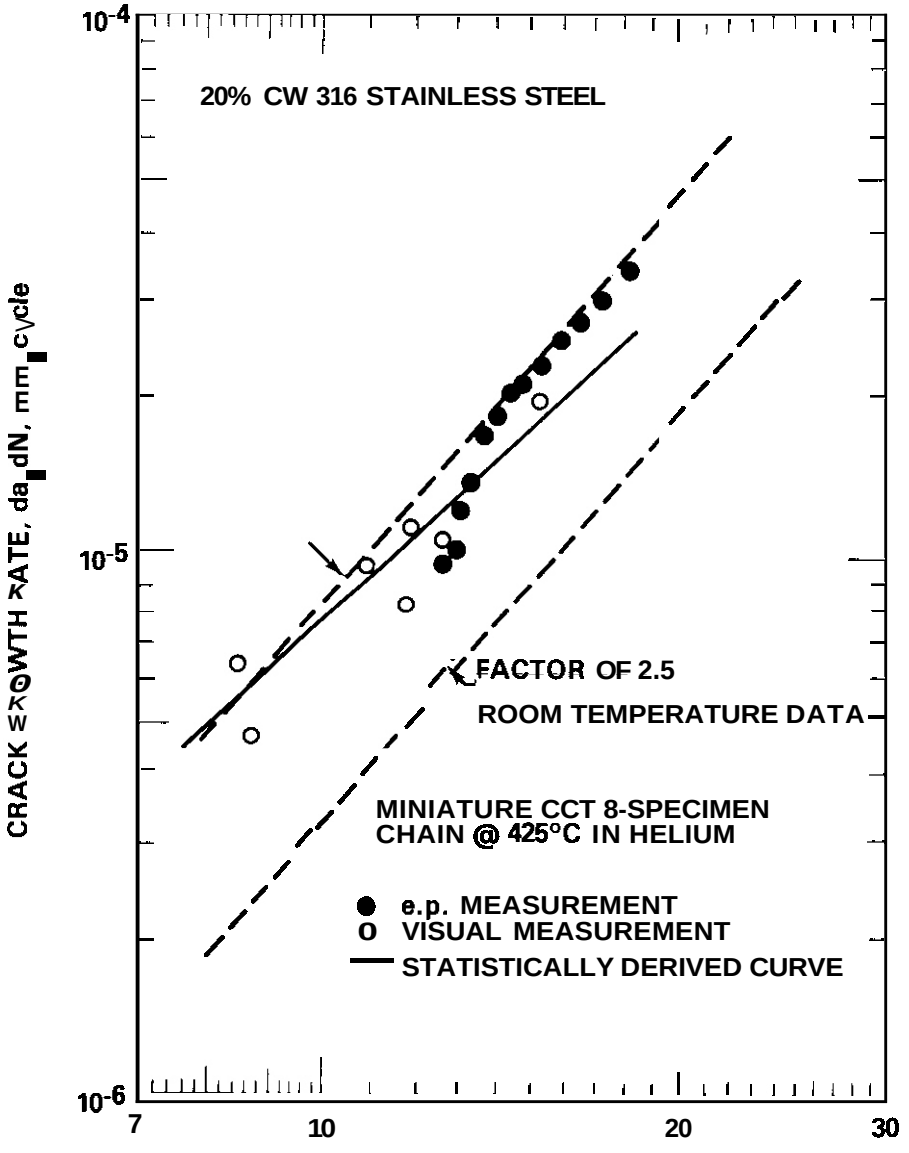

FIGURE 3.2.1 Comparison of the Prototype Eight-Specimen Chain Test at 425°C with Room Temperature Results from Reference 3.

Both the in-reactor and thermal control tests will be performed in static sodium at 425°C. Since prototypic studies using the specimen chain were not done under these conditions, the predicted effects of sodium on

crack growth must be based on results of other investigators. The consensus appears to be that in high purity, low oxygen sodium, crack growth rates at elevated temperatures ($\leq$600°C) are approximately the same as those in air at room temperature.[6-9] The upper bound of the room temperature band of Figure 3.2.1 should therefore represent the worst case insofar as maximum crack growth rates are concerned. A load of 335 lbs was selected which represents a 200,000 cycle test whose curve lies midway in the band. The worst case test would then accumulate about 125,000 cycles, or 62% of the targeted number of cycles, The fact that the test is to be conducted at one cycle/min should have little bearing since the frequency dependence disappears in low oxygen sodium below 600°C.[9] At the other extreme, the lower bound represents a test which would normally last ~320,000cycles. Still, significant and detectable crack growth would occur (~1.0 mm) on specimens with the smallest precracks if the test were to be halted after only 200,000 cycles.

The loading arrangement and initial crack lengths for the in-reactor test are outlined in Table 3.2.1. Specimen positions #3 through #7 are in the higher flux region, with the peak flux in the vicinity of the sixth specimen. Specimen #6 is triplicated (#1 and #3) while specimen #5 is duplicated (#2). The specimen with the largest initial crack length, #8, is located at the bottom of the chain. This specimen would completely seperate before any of the others, and would be sacrificed in the event that it breaks before the scheduled 200,000 cycles.

3.2.5 Conclusions

(a) Results of the final prototypic eight-specimen chain test at 425°C lie in the upper region of the room temperature crack growth band. This is considered the worst case of maximum growth rate that would be expected in sodium at 425°C.

(b) Based on the room temperature results, a load was chosen which will define a crack growth curve lying midway in the room temperature band.

TABLE 3.2.1

SPECIMEN LOADING ARRANGEMENT FOR THE ORR-MFE-5 EXPERIMENT

LOADING POSITION	SPECIMEN #	INITIAL CRACK LENGTH, 2a (mm)	ORR CORE POSITION C-7
1	AE-11	4.589	Top
2	AE-01	5.689	
3	AE-06	4.684	
4	AE-05	6.952	
5	AE-03	5.599	Center
6	AE-07	4.580	~ Peak Flux Position
7	AE-02	8.796	
8	AE-04	9.634	Bottom

3.2.6 Future Work

Fabrication of the in-reactor fatigue machine to be tested at ORNL is 80% complete. Insertion into the ORR is scheduled for later this summer. Specimen preparation for the thermal control test to be conducted at HEDL is underway.

3.2.7 References

1. A. M. Ermi, "Status of an In-Reactor Fatigue Crack Growth Experiment," *ADIP Quarterly Progress Report, June 30, 1979,* DOE/ET-0058/6, pp. 28-34.
2. A. M. Ermi, "Results of Prototypic Testing for the MFE-5 In-Reactor Fatigue Crack Propagation Experiment," *ADIP Quarterly Progress Report, September 30, 1979,* DOE/ET-0058/7, pp. 50-65.
3. A. M. Ermi, "Prototype Testing of MFE-5 In-Reactor Fatigue Crack Growth Experiment," *ADIP Quarterly Progress Report, March 31, 1980.*
4. J. L. Straalsund and D. A. Mervyn, "Adaptation of an Electrical Potential Technique to Measure Fatigue Crack Growth," *ADIP Quarterly Progress Report, December 31, 1978,* DOE/ET-0058/4, pp. 4-9.
5. L. A. James, "Fatigue Crack Propagation in Austenitic Stainless Steels," *Atomic Energy Review, 14, 1 (1976),* pp. 37-86.

6. P. Marshall, "The Fatigue Behavior of Annealed AISI *316* Stainless Steel in Air and High Temperature Sodium: Review and Preliminary Results," CEGB *Report RD/B/N3236 (1974)*.

7. E. K. Priddle and C. Wiltshire, "The Measurement of Fatigue Crack Propagation in Specimens Immersed in Liquid Sodium at Elevated Temperatures: Technique and Preliminary Results," *Int. J. Fracture, 11 (19751,* pp. 697.

8. L. A. James and R. L. Knecht, "Fatigue Crack Propagation Behavior of Type *304* Stainless Steel in a Liquid Sodium Environment," *Met. Trans., 6A (1975)*, pp. 109.

9. P. Marshall, "The Influence of Low Oxygen and Contaminated Sodium Environments on the Fatigue Behavior of Solution Treated **AISI** *316* Stainless Steel," **I.** *Mech. E., C101/77 (1977)*, pp. 27-36.

3.3 THE MICROSTRUCTURE AND MECHANICAL PROPEKTIES OF 20%-COLD-WORKED TYPES 316 STAINLESS STEEL AND 316 + 0.23 wt % Ti AFTEK HFIK IRRADIATION AT 55 to 375°C — P. J. Maziasz, M. L. Grossbeck, and F. W. Wiffen (ORNL)

3.3.1 ADIP Tasks

ADIP Tasks I.C.l, Microstructural Stability; I.C.2, Microstructure and Swelling in Austenitic Alloys; and I.B.13, Tensile Properties of Austenitic Alloys.

3.3.2 Objective

The objective of this investigation is to compare the effects of irradiation on titanium-modified type 316 and standard type 316 stainless steel. Low irradiation temperatures of 55 to 375°C are emphasized to determine any benefit of the titanium-modified material for Engineering Test Facility (ETF) applications.

3.3.3 Summary

Tensile testing at a strain rate of 0.0028/min indicates similar Levels of strength and postirradiation ductility for both 20%-cold-worked types 316 stainless steel (CW 316) and 316 + 0.23 wt % Ti (CW 316 + Ti) after High Flux Isotope Reactor (HFIK) irradiation at 55 to 375°C. The irradiations produced up to 13 dpa and 740 at. ppm He. Both irradiated steels show decreased strength properties and increased uniform elongation as irradiation and test temperatures increase. The HFIR irradiation increased the strength properties and decreased the ductility for CW 316. By contrast, both strength and ductility properties increased for CW 316 + Ti. All irradiated samples exhibited the ductile-transgranular fracture mode.

Microstructural examination for irradiations at 285 or 375°C reveals loops and cavities in all samples. Swelling of CW 316 increases as irradiation temperature decreases with values of about 0.12% at 375°C and 0.43% at 285°C. The CW 316 + Ti shows the same trend but with slightly lower swelling. The microstructure coarsens with decreasing

irradiation temperature in CW 316 but is refined with decreasing temperature in CW 316 + Ti. No precipitation is observed in CW 316 irradiated at 285°C. Fine gamma-prime precipitate particles are produced in CW 316 at 375°C, and fine MC particles are produced in CW 316 + Ti at both 375 and 285°C.

The CW 316 and CW 316 + Ti offer quite similar properties after HFIR irradiation at these temperatures and fluences. The latter has a slight advantage, particularly with respect to the properties of irradiated relative to unirradiated material. Flicrostructural examination of both materials irradiated at 55°C and at higher fluences at 375°C is needed before the comparison is complete.

3.3.4 Progress and Status

Cold-worked type 316 stainless steel is a candidate material for the first wall of the ETF. The irradiation conditions will include the incident flux of about 14-MeV (2.2-pJ) neutrons that simultaneously produce both displacement damage and helium, irradiation temperatures in the range 150 to 300°C, and integrated wall loadings up to 6 $MWyr/m^2$. Titanium-modified austenitic stainless steels have demonstrated advantages over unmodified steels in resisting both mechanical properties degradation and swelling at irradiation temperatures higher than those being considered for the ETF. This work considers HFIR irradiation of 20%-cold-worked types 316 (CW 316) and 316 + 0.23 wt % Ti (CW 316 + Ti) at temperatures of 55, 285, and 375°C and fluences producing up to 13 dpa and 740 at. ppm He to extend the material comparison.

3.3.4.1 Experimental Details

Tensile specimens irradiated at 285°C and above are from experiments HFIR-CTR-9 through -13. Tensile specimens irradiated at 55°C were from HFIR-CTR-16. The same heats of material were used in all experiments, and details of the experiments and specimen preparation as well as some results were reported previously.[1-4] The compositions of the materials are given in Table 3.3.1.

Table 3.3.1. Composition of Two Cold-Worked Austenitic Stainless Steels

Alloy	Content,[a] wt %										
	Cr	Ni	Mo	Mn	C	Ti	Si	P	S	N	B
316	18.0	13.0	2.58	1.90	0.05	0.05	0.80	0.013	0.016	0.05	0.0005
316 + Ti	17.0	12.0	2.50	0.5	0.06	0.23	0.40	0.01	0.013	0.0055	0.0007

[a]Balance iron.

Tensile specimens were machined from rod stock that had been annealed for 1 h at 1150°C, cold swaged to a 50% reduction in area, annealed 1 h at 1050°C, and then swaged another 20% before machining. The specimen geometry is shown in Fig. 3.3.1.

Tensile specimens in HFIK-CTR-16 were irradiated at the reactor coolant temperature of about 55°C. Specimens in HFIR-CTR-9 through -13 were irradiated at temperatures above the reactor coolant by using a helium gas gap. This work includes specimens irradiated at 285 and at 370 to 375°C. The irradiation temperatures are calculated according to early measurements of gamma heating by using SiC. Recent heating rate measurements and heat transfer calculations indicate the actual irradiation temperature to be 50 to 75°C higher[5,6] than the previously calculated temperatures.[7] However, relative comparison is valid since the precision of the temperature control is much better than its accuracy. Helium levels were calculated from an empirical relation determined by Wiffen et al.[8] based upon mass spectrographic analysis of HFIR-irradiated specimens and are accurate to better than 20%. Helium levels ranged from 180 to 740 at. ppm. Displacement damage (dpa) levels were calculated by Gabriel et al.[9] from the neutron fluxes and energy spectra in the HFIR. The dpa levels ranged from 5 to 13.

Postirradiation tensile testing was performed on an Instron machine. Tests were performed in air at a strain rate of 0.0028/min at test temperatures of 35, 300, and 350°C.

Transmission electron microscope (TEM) disks about 3 mm in diameter and 0.4 mm thick were cut from the undeformed shoulder of tested specimens

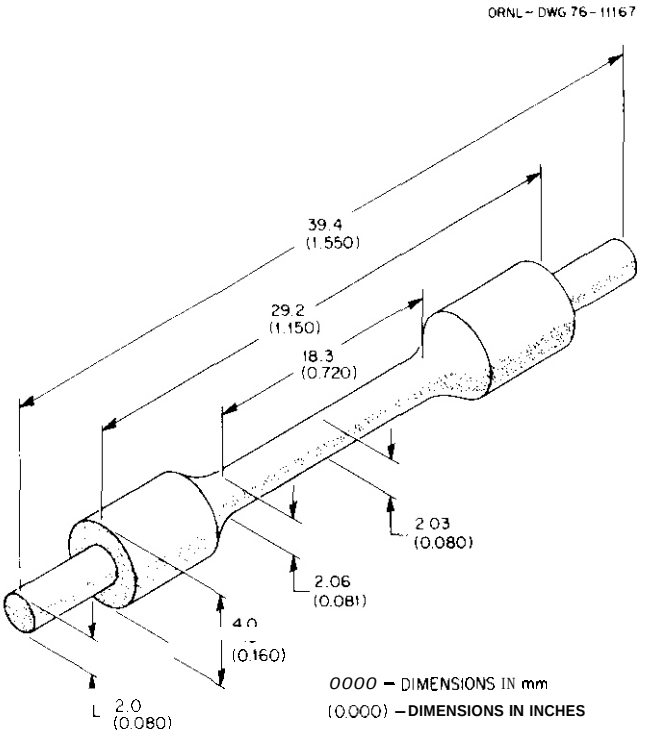

Fig. **3.3.1.** The HFIR–CTK Tensile Specimen. Transmission electron microscope disks are cut from either shoulder, which are at the same irradiation temperature as the gage.

(Fig. **3.3.1).** The disks were thinned to electron transparency by using standard thinning techniques.[10] The microstructures were examined with conventional TEM techniques. Cavity statistics were obtained for void volume fraction (swelling), and the precipitate phases were identified by selected area electron diffraction (SAD). The loop component of the microstructure is still being analyzed. Swelling determined by length change and by immersion density has been reported for these samples. 1

3.3.4.2 Mechanical Properties

The tensile properties of control and HFIX–irradiated CW **316** and CW 316 + Ti are presented in Table **3.3.2.** Ultimate tensile stress (UTS) and yield stress (YS) and uniform elongation (UE) and total elongation (TE) are plotted as a function of test temperature in Figs. 3.3.2 and **3.3.3,** respectively.

The unirradiated YS and UTS of CW **316** both decrease as the test temperature increases. The UTS decreases from 870 to 820 MPa at 35°C to

Table 3.3.2. Tensile Properties[a] of 20%-Cold-Worked Types 316 Stainless Steel (CW 316) and 316 t 0.23 wt % Ti (CW 316 + Ti)

Irradiation Parameters		Temperature, °C		Stress, MPa		Elongation, %	
(dpa)	(at. ppm lie)	Test	lrradiation	Yield	Ultimate Tensile	Uniform	Total
		20%-Cold-Worked Type 316 Stainless Steel					
		35		785	817	4.1	12.3
		35		836	864	7.9	17.8
		35		818	862	3.3	11.2
		300		708	747	1.4	6.0
		300		682	719	1.7	6.4
		350		527	633	12.0	17.0
		350		585	676	7.8	13.0
		450		496	641	12.0	18.0
		450		572	663	8.3	14.0
		450		542	645	10.0	16.0
4.9	180	35	55	960	967	0.4	9.1
8.5	380	35	55	943	950	0.4	14.7
10.8	520	35	55	948	954	0.4	12.0
8.8	380	35	55	945	949	0.3	11.:
7.7	390	300	285	998	998	0.2	5.1
4.9	180	350	370	780	848	4.5	8.5
7.7	390	350	370	855	917	4.2	8.7
8.5	380	350	375	611	752	3.3	6.8
13.0	740	350	375	594	731	3.3	6.4
13.0	740	350	375	688	800	4.6	8.3
		20%-Cold-Worked Type 316 + 0.23% Ti					
		350		759	779	0.56	5.7
		350		786	814	0.87	5.9
		450		710	765	2.1	6.9
6.9	290	35	55	960	965	0.4	9.7
10.5	490	35	55	993	1002	0.4	9.4
7.7	390	300	285	903	903	0.2	5.8
4.9	180	350	370	752	786	3.1	8.5
8.5	380	350	375	786	848	2.6	7.0
13.0	740	350	375	772	855	4.2	8.4
13.0	740	350	375	758	834	4.7	9.0

[a]Strain rate of 0.0028/min. Tests conducted in air.

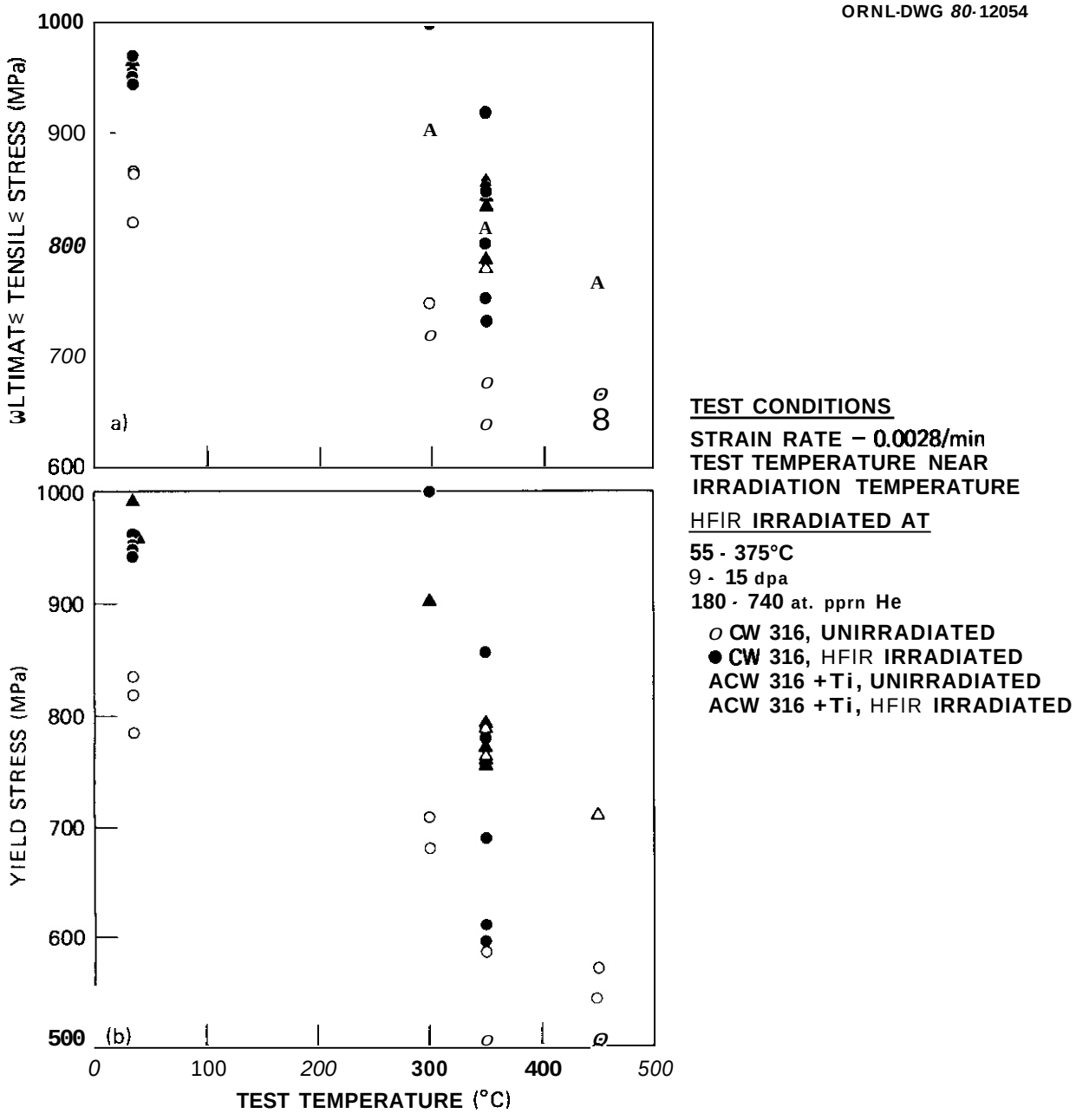

Fig. 3.3.2. (a) Ultimate Tensile Stress and (b) Yield Stress as Functions of Test Temperature for 20%-Cold-Worked Types 316 Stainless Steel and 316 + 0.23 wt % Ti Either Unirradiated or After HFIR Irradiation Near the Test Temperature.

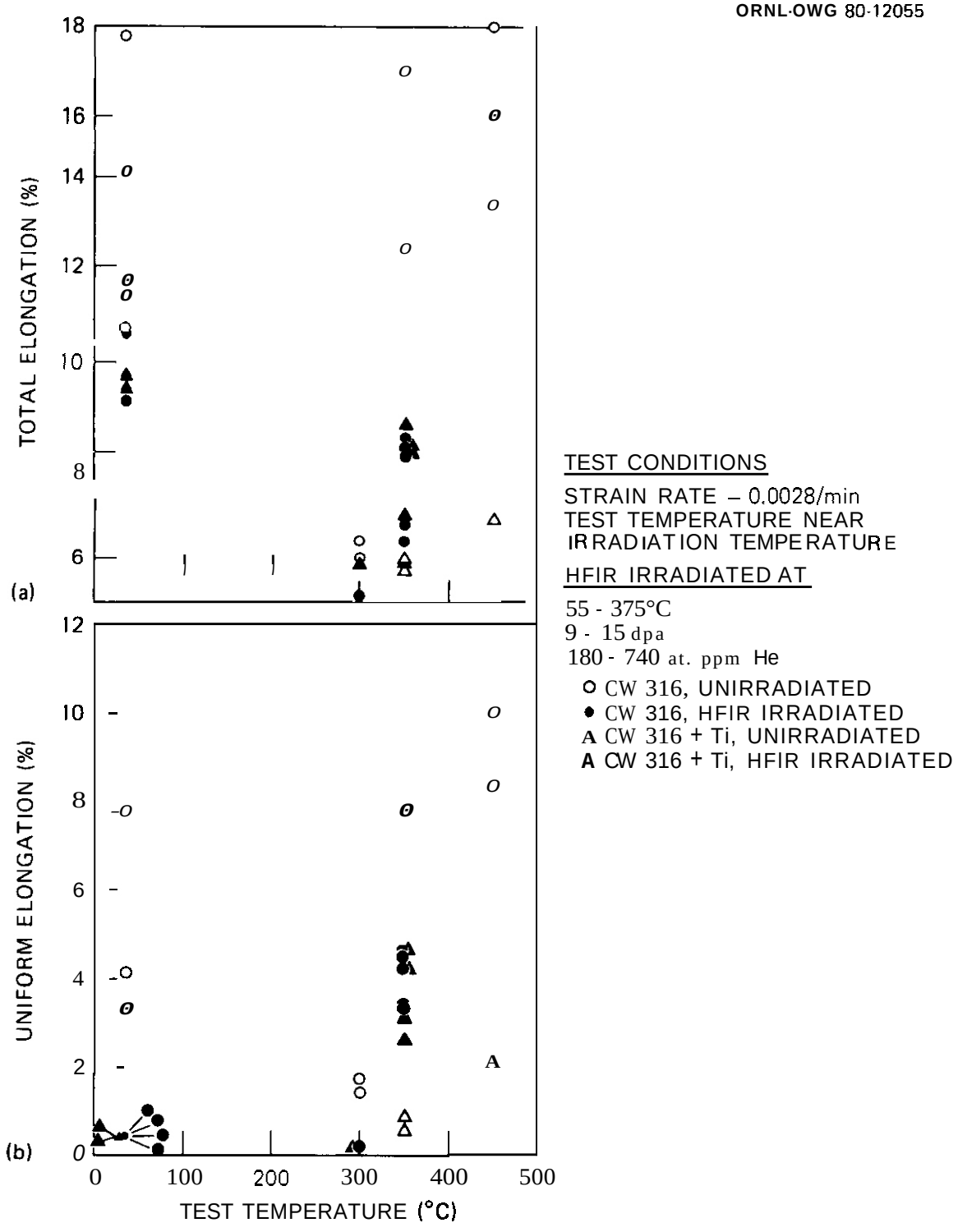

Fig. 3.3.3. (a) Total Elongation and (b) Uniform Elongation as Functions of Test Temperature for 20%-Cold-Worked Types 316 Stainless Steel and 316 + 0.23 wt % Ti Either Unirradiated or After HFIR Irradiation Near the Test Temperature.

from 670 to 640 MPa at 450°C. The YS follows the same trend. The YS is about 30 MPa lower than the UTS at 35°C and about 120 MPa lower at 450°C. Both the trend and magnitude of the UTS fall within the 95% confidence level for CW 316 in the *Nuclear Systems Materials (NSM) Handbook*,[11] but the YS is somewhat higher than the handbook values. These trends are outside the specimen-to-specimen scatter. By comparison, the YS and UTS of CW 316 are considerably increased by irradiation in the HFIR. Post-irradiation UTS and YS both appear to increase slightly with test and irradiation temperature until 300°C and then drop at 350°C. However, the data scatter considerably at 350°C, which does not exactly order with fluence and has been noted previously.[3,6] The UTS and YS are nearly equal from 35 to 300°C, and then the YS is less than the UTS by about 100 MPa at 350°C. The strength values at 35 and 300°C (950 and 1000 MPa) are among the highest reported for CW 316, either unirradiated[12] or after neutron irradiation.[13]

Unirradiated CW 316 + Ti has higher strength values than the CW 316 at test temperatures of 350 and 450°C (Table 3.3.2, Fig. 3.3.2). Both properties decrease with increasing test temperature, as for CW 316. The UTS is about 150 MPa higher and the YS about 175 to 200 MPa higher for CW 316 + Ti than the values for CW 316 tested at 350 to 450°C. The strength values for irradiated CW 316 + Ti are about the same or slightly higher than the unirradiated values at 350°C. The UTS and YS for irradiated CW 316 + Ti and irradiated CW 316 are similar from 35 to 350°C. The specimen-to-specimen scatter is considerably less for irradiated CW 316 + Ti than for CW 316 tested at 350°C.

The ductility of CW 316 is shown in Fig. 3.3.3(a) and (b) and Table 3.3.2. The data scatter considerably in TE for unirradiated material but not much more than noted in the NSM Handbook data.[11] The TE is low (about 6.5%) at a test temperature of 300°C but is about 12 to 18% at all other test temperatures from 35 to 450°C. The unirradiated UE shows similar scatter and increases somewhat with test temperature. The UE also shows the same minimum at 300°C as shown for TE. The postirradiation TE of CW 316 is less than the unirradiated values at test temperatures of 35 and 300°C and considerably less at 350°C (reduced by a factor of about 2). The UE and TE of irradiated CW 316 parallel the

temperature behavior of the unirrddiated properties. The UE is substantially reduced by irrddiation at all test temperatures. Both properties show less scatter after irradiation.

The unirrddiated ductility of CW 316 + Ti is considerably lower at 350 and 450°C than that of CW 316 (TE of 6–7%, compared with 15–18% for CW 316). However, irrddiation increases both the TE and the UE of CW 316 + Ti tested at 350°C. The postirradiation UE values are almost exactly the same for CW 316 + Ti and CW 316 at all test temperatures. The TE is slightly higher in CW 316 + Ti for the same comparison.

The fracture mode of all samples tested is ductile transgranular. Scanning electron microscopy images of the fracture surfaces of CW 316 irradiated and tested at 55°C and 375°C are shown in Fig. 3.3.4.

3.3.4.3 Microstructure and Swelling

The statistics for the cavity and precipitate particle components of the microstructures of CW 316 and CW 316 + Ti irradiated at either 285 or 375°C are presented in Table 3.3.3 and 3.3.4, respectively. The dislocation component of the microstructure is discussed qualitatively, but work is still in progress. Immersion density measurements for these samples are included in Table 3.3.3 and have been reported previously[1] for CW 316.

Thermally aged samples of CW 316 and CW 316 + Ti were examined after 2770 and 4400 h at temperatures ranging from 275 to 470°C. None of the aged samples showed any grain boundary or matrix precipitation or dislocation recovery from the initial cold-worked material. A representative microstructure of CW 316 + Ti aged 4400 h at 470°C shows both grain boundary and matrix in Fig. 3.3.5. These microstructures are unchanged from as-worked structures, showing the expected densely tangled cellular structures.

The low-magnification microstructures of both materials at irradiation temperatures of 285 and 375°C are shown in Fig. 3.3.6. Resolvable cavities can be seen at both irradiation temperatures in CW 316 but not in CW 316 + Ti. Grain boundary eta phase is observed in CW 316 irradiated at 375°C [Fig. 3.3.6(a)], but no grain boundary precipitation is observable in the other samples.

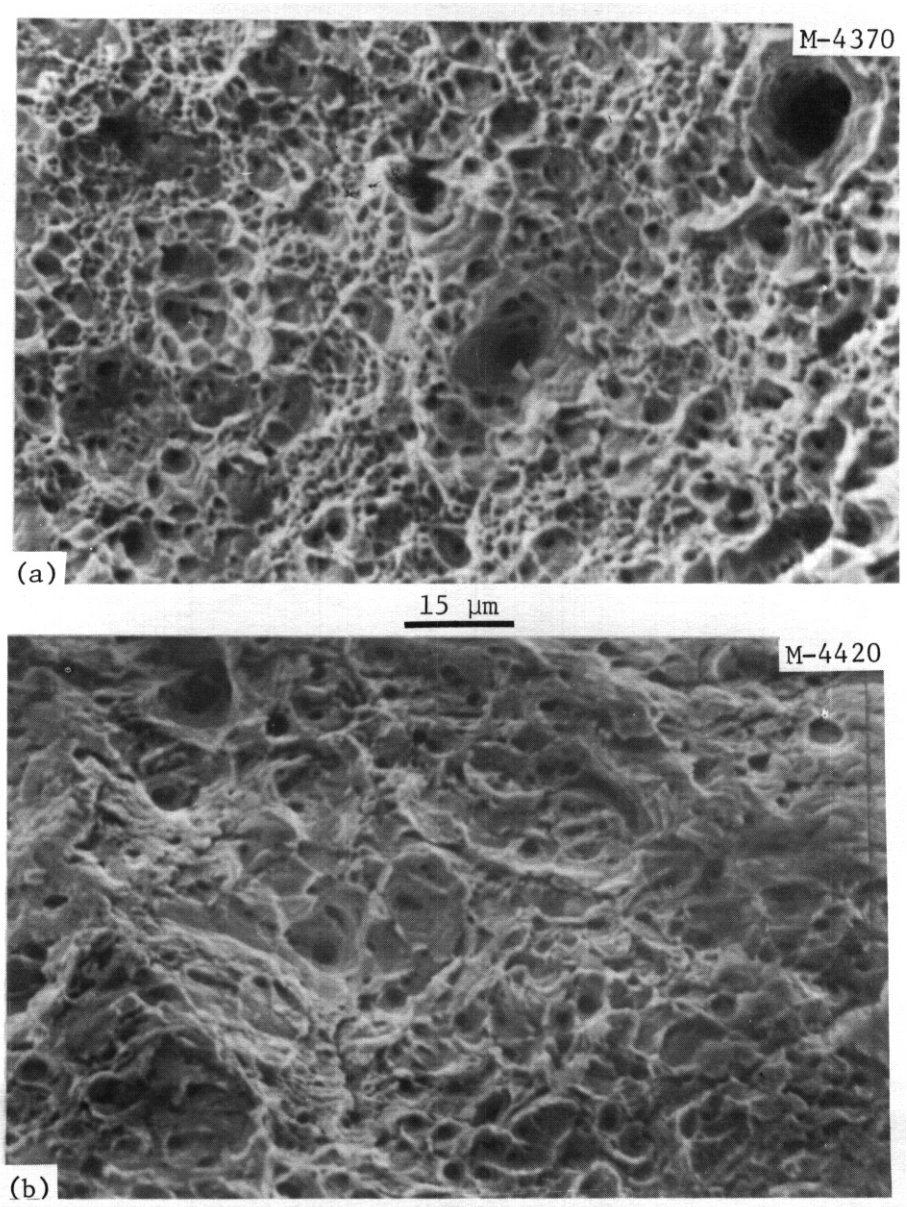

Fig. 3.3.4. Scanning Electron Micrographs of Fracture Surfaces of 20%-Cold-Worked Type 316 Stainless Steel After HFIR Irradiation at (a) 55°C to 520 at. ppm He and 10.8 dpa (Tensile Tested at 35°C) and (b) 375°C to 380 at. ppm He and 8.5 dpa (Tensile Tested at 350°C). Both indicate a ductile-transgranular failure mode.

Table 3.3.3. Quantitative Cavity Statistics for HFIR-Irradiated 20%-Cold-Worked Types 316 Stainless Steel and 316 + 0.23 wt % Ti

Irradiation Conditions			Swelling from Immersion Density (%)	Cavity Statistics[a]						
				Average Diameter, nm		Concentration, cavities/m^3		Volume Fraction Swelling, %		
Temperature (°C)	Helium (at. ppm)	Displacement Damage (dpa)		Mode 1	Mode 2	Mode 1	Mode 2	Mode 1	Mode 2	Total
			20%-Cold-Worked Type 316 Stainless Steel							
			+0.04		12.0					
			0	2.7	8.7	3.7	0.19	0.04	0.03	0.12
			20%-Cold-Worked Type 316 + 0.23 wt % Ti							
			−0.07	2.9		27		0.36		0.36
375	380	5	−0.13	3.1		4.6		0.03		0.03

[a]Cavity size distribution is bimodal. Mode 1 represents cavities with average diameters less than 5 nm. Mode 2 represents cavities with average diameters greater than 5 nm.

Table 3.3.4. Quantitative Precipitate Particle Statistics for HFIR-Irradiated 20%-Cold-Worked Types 316 Stainless Steel and 316 + 0.23 wt % Ti

Alloy	Irradiation Conditions			Precipitate Particle Statistics			
	Temperature (°C)	Helium (at. ppm)	Displacement Damage (dpa)	Phase	Average Size (nm)	Concentration (precipitate particles/m^3)	Volume Fraction (%)
316	375	380	8.5	Gamma prime	3	7×10^{22}	0.11
316 + Ti	375	380	8.5	MC	3.2	7.1×10^{22}	0.13

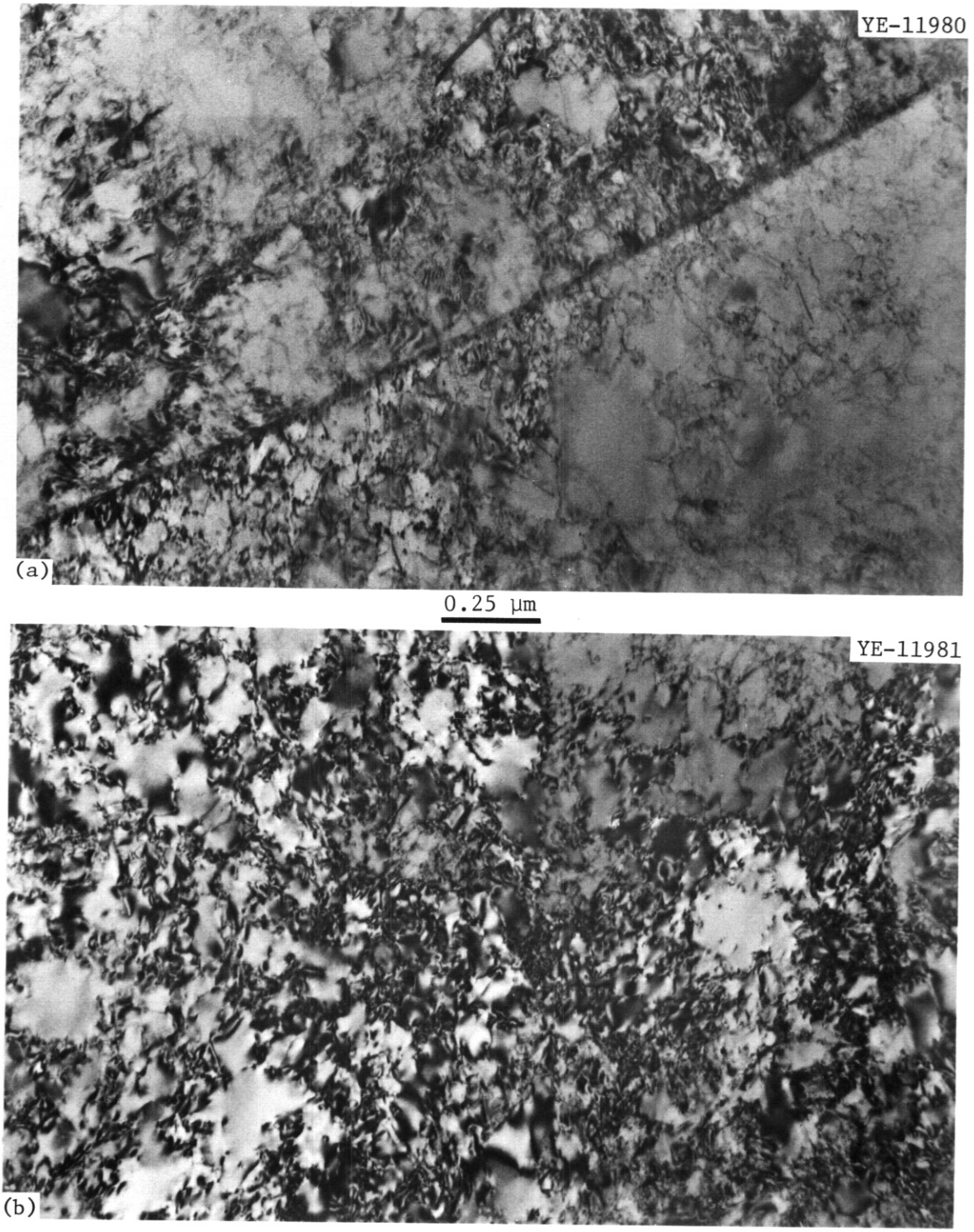

Fig. 3.3.5. Transmission Electron Micrograph of 20%-Cold-Worked Type 316 + 0.23 wt % Ti After Thermal Aging at 470°C for 4400 h. (a) Grain boundary. (b) Matrix. Precipitation is not observable, and recovery is not evident.

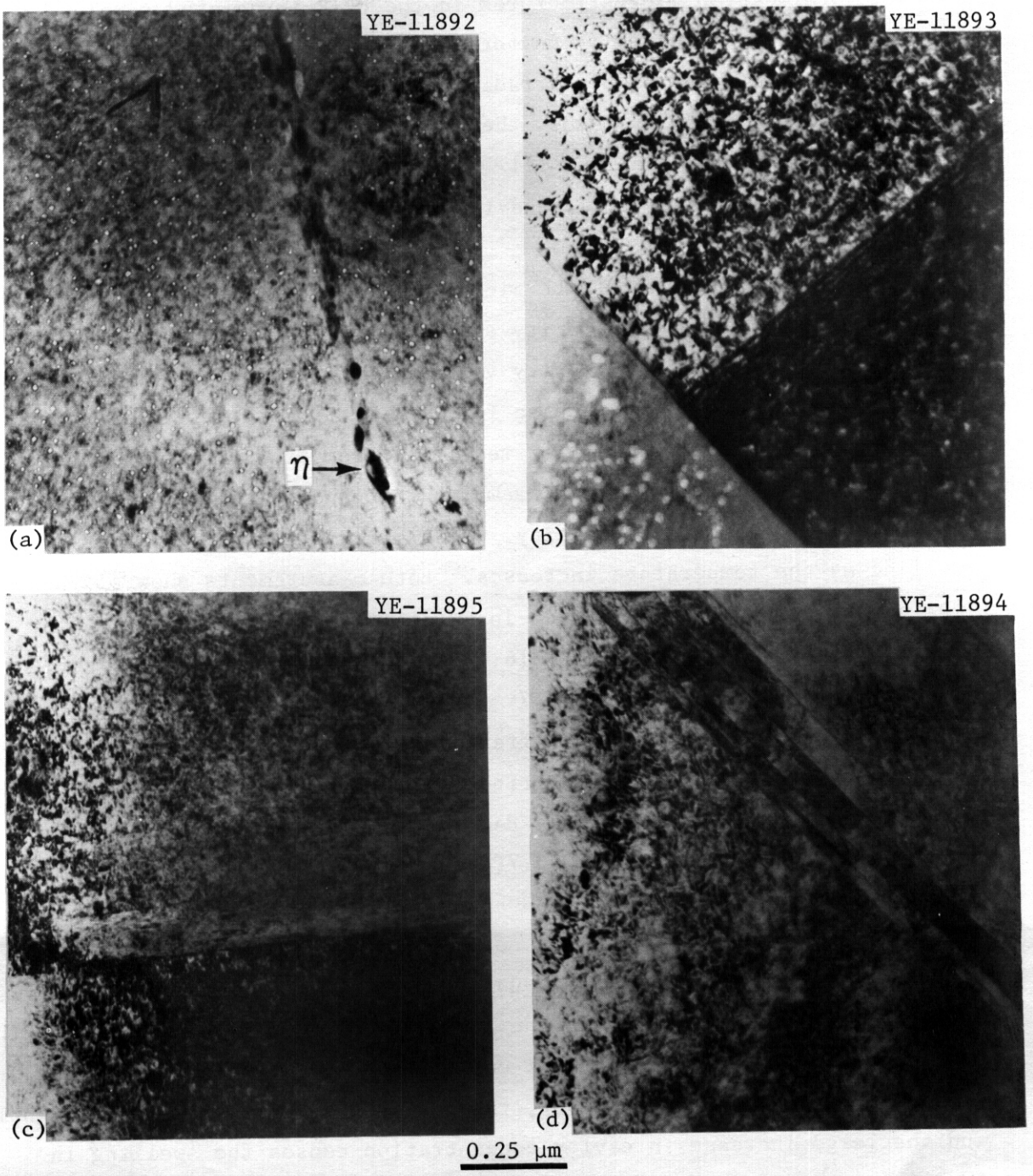

Fig. 3.3.6. Low-Magnification Microstructure of 20%-Cold-Worked Type 316 Stainless Steel Irradiated in the HFIR at (a) 375°C to 380 at. ppm He and 8.5 dpa and (b) 285°C to 390 at. ppm He and 7.7 dpa and of 20%-Cold-Worked Type 316 + 0.23 wt % Ti Irradiated at (c) 375°C to 380 at. ppm He and 8.5 dpa and (d) 285°C to 390 at. ppm He and 7.7 dpa.

The dislocation microstructures in the HFIR-irradiated samples are denser and more spatially uniform than in the thermally aged control material. The CW 316 irradiated at 375°C and the CW 316 + Ti irradiated at 285 and 375°C show the characteristic intergranular deformation bands parallel to <111> in the face-centered cubic (fcc) austenite [Fig. 3.3.6(a), (c), and (d)], whereas CW 316 irradiated at 285°C does not [Fig. 3.3.6(b)].

The cavity component of the microstructure is shown at higher magnification in Fig. 3.3.7, and cavity statistics are given in Table 3.3.3. All values of swelling from cavity volume fraction are less than 0.5% and are consistently higher than those for immersion density. Immersion density can reflect densification resulting from precipitation, and precipitation is observed in all samples that show either no swelling or densification by immersion density. Both materials show decreases in swelling as the temperature increases. Both measurements show slightly less swelling in CW 316 + Ti than in CW 316. The refinement in cavity distribution achieved in the CW 316 + Ti compared with CW 316 is reflected both in Table 3.3.3 and Fig. 3.3.7. The swelling increase with decreasing temperature occurs for totally different microstructural reasons in CW 316 and CW 316 + Ti. The cavity distribution coarsens considerably in CW 316 as the irradiation temperature is decreased. The bimodal cavity size distribution observed in Fig. 3.3.7(a) at 375°C appears to shift almost completely to the larger size mode as the temperature decreases. The effect within this mode is then a normal increase in cavity density with decreasing temperature but an unusual[14] increase in cavity size with decreasing temperature to cause the increase in swelling. By contrast the cavity distribution in CW 316 + Ti continues to refine with decreasing irradiation temperature. However, the cavity size decreases only slightly, and the large increase in cavity concentration causes the swelling in CW 316 + Ti to be greater at 375 than at 285°C.

The dislocation component of the microstructure produced by irradiation is very dense in all samples, as shown in Fig. 3.3.6. The dislocation microstructures of CW 316 and CW 316 + Ti are approximately the same before either aging or irradiation. The irradiated microstructures have

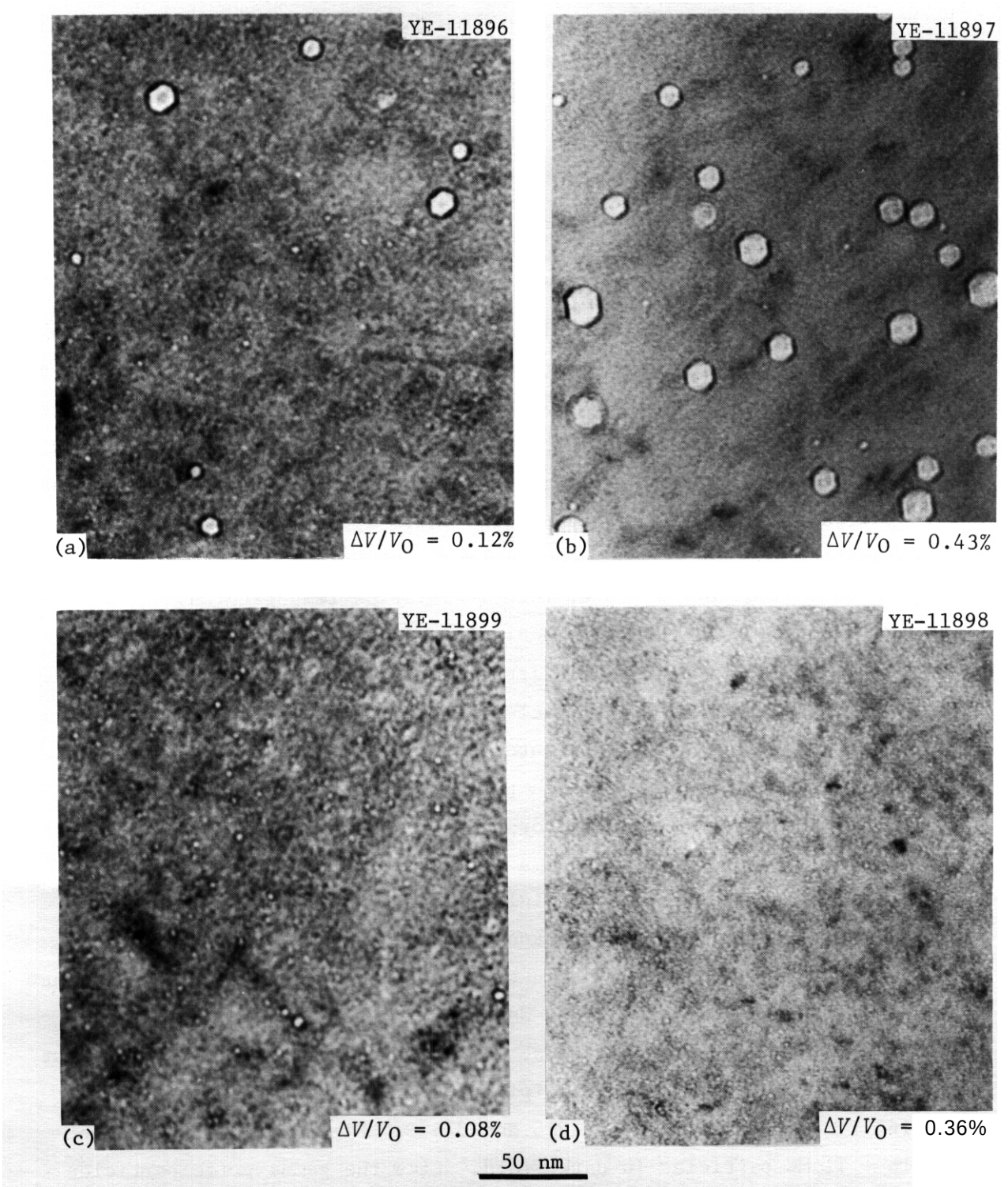

Fig. 3.3.7. Cavity Component of the Microstructure Produced by HFIR Irradiation in 20%-Cold-Worked Type 316 Stainless Steel Irradiated at (a) 375°C to 380 at. ppm He and 8.5 dpa and (b) 285°C to 390 at. ppm He and 7.7 dpa and in 20%-Cold-Worked Type 316 + 0.23% Ti Irradiated at (c) 375°C to 380 at. ppm He and 8.5 dpa and (d) 285°C to 390 at. ppm He and 7.7 dpa. $\Delta V/V_0$ = void volume fraction expressed in percent, where AV is change in volume and V_0 is original volume.

both a finer and a spatially more uniform dislocation density. Weak-beam dark field imaging of irradiated microstructures (Fig. 3.3.8) reveals the dislocation structure to be composed of both tangles and loops. These faulted loops appear to be Frank loops from their contrast behavior[15] and from the appropriate satellite streaks seen in reciprocal space near (200) matrix reflections[16] (Fig. 3.3.9). Loops have not been observed previously in HFIK-irradiated steel.[14] In general, there are about 7×10^{21} to 9×10^{21} loops/m^3 in both CW 316 and CW 316 + Ti irradiated at 375°C. The loops are about 30 to 35 nm in diameter in CW 316 and about 25 nm in CW 316 + Ti. In both materials the loop size increases as the irradiation temperature increases. In CW 316 the loop concentration clearly decreases with decreasing temperature, and some of the loops can be observed to be unfaulted in Fig. 3.3.8(b). In contrast, the loop concentration increases with decreasing irradiation temperature in CW 316 + Ti. The dislocation loop component of the microstructure is clearly refined in CW 316 + Ti compared with that of CW 316 at both irradiation temperatures.

Precipitation is observed in all irradiated samples except CW 316 irradiated at 285°C. The CW 316 irradiated in HFIK at 375°C has a fine distribution of gamma-prime particles, as shown in Fig. 3.3.10. The precipitate particles are distributed along the network component of the dislocation microstructure. Gamma prime has not been observed previously[17] in HFIK-irradiated (34-316. Its morphology and crystallographic habit (cube-on-cube) are similar to gamma prime observed by others in fast-reactor-irradiated austenitic stainless steels.[18-21] Care was taken to image in dark field by using the known location of the gamma-prime reflections [Fig. 3.3.10(b)], even when such reflections could not be seen in the diffraction pattern.[19-21] Gamma-prime precipitate particles are not evident in CW 316 irradiated at 285°C or in (34 316 + Ti irradiated at either temperature. Fine MC precipitate particles were observed in the CW 316 + Ti irradiated at bath 285 and 375°C. Figure 3.3.11 shows the CW 316 + Ti MC particles in dark field. Like the gamma-prime particles in CW 316, they are also distributed primarily on the network portion of the dislocation component of the microstructure. Table 3.3.4 shows that the size, concentration, and volume fractions of MC in CW 316 + Ti and

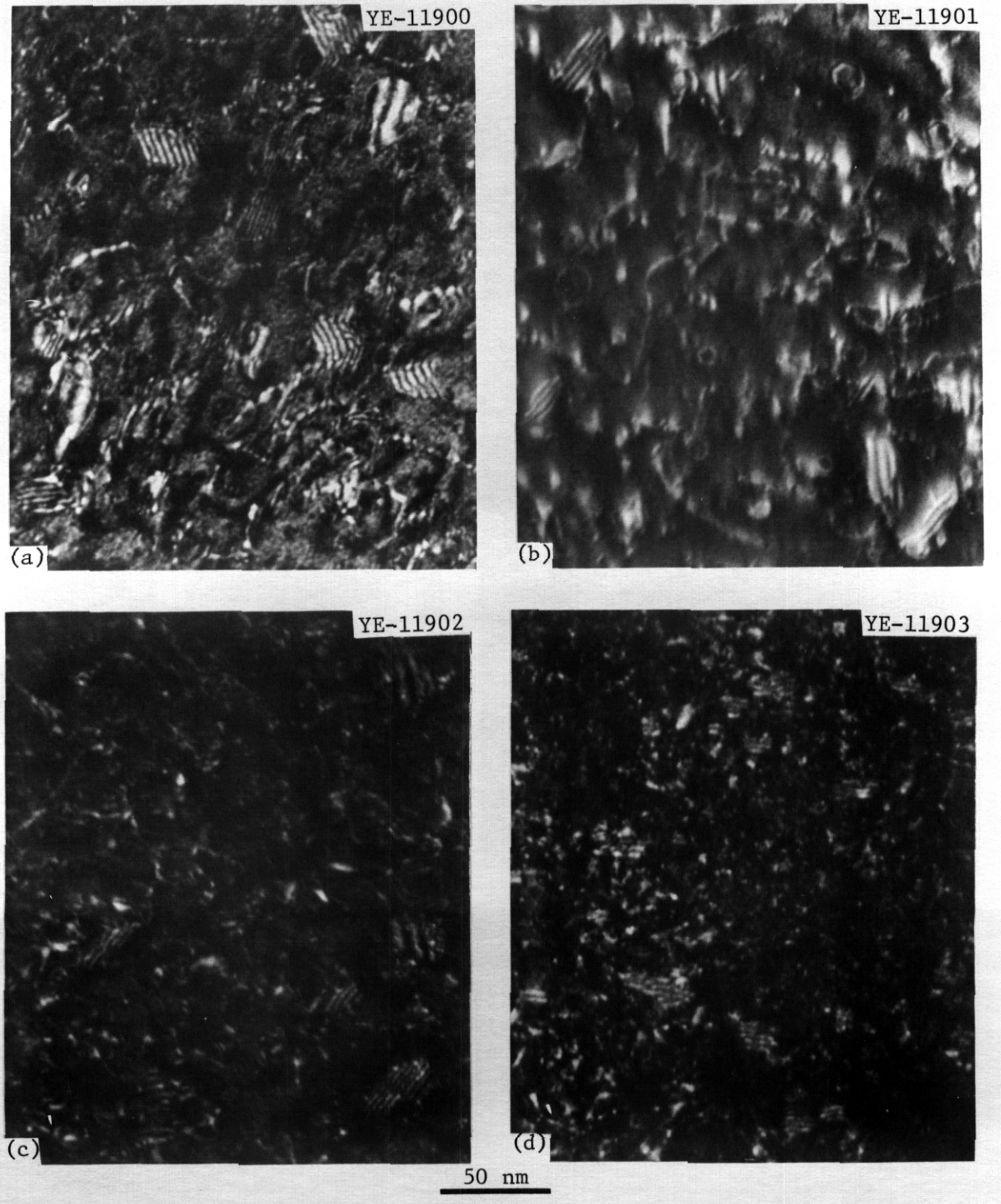

Fig. 3.3.8. The Dislocation Component of the Microstructure Produced by HFIR Irradiation of 20%-Cold-Worked Type 316 Stainless Steel Irradiated at (a) 375°C to 380 at. ppm He and 8.5 dpa and (b) 285°C to 390 at. ppm He and 7.7 dpa and of 20%-Cold-Worked Type 316 + 0.23 wt % Ti Irradiated at (c) 375°C to 380 at. ppm He and 8.5 dpa and (d) 285°C to 390 at. ppm He and 7.7 dpa. All pictures are about $g/3_g$ weak-beam dark field images taken with either g_{111} [(b), (d)] or g_{200} [(a), (c)].

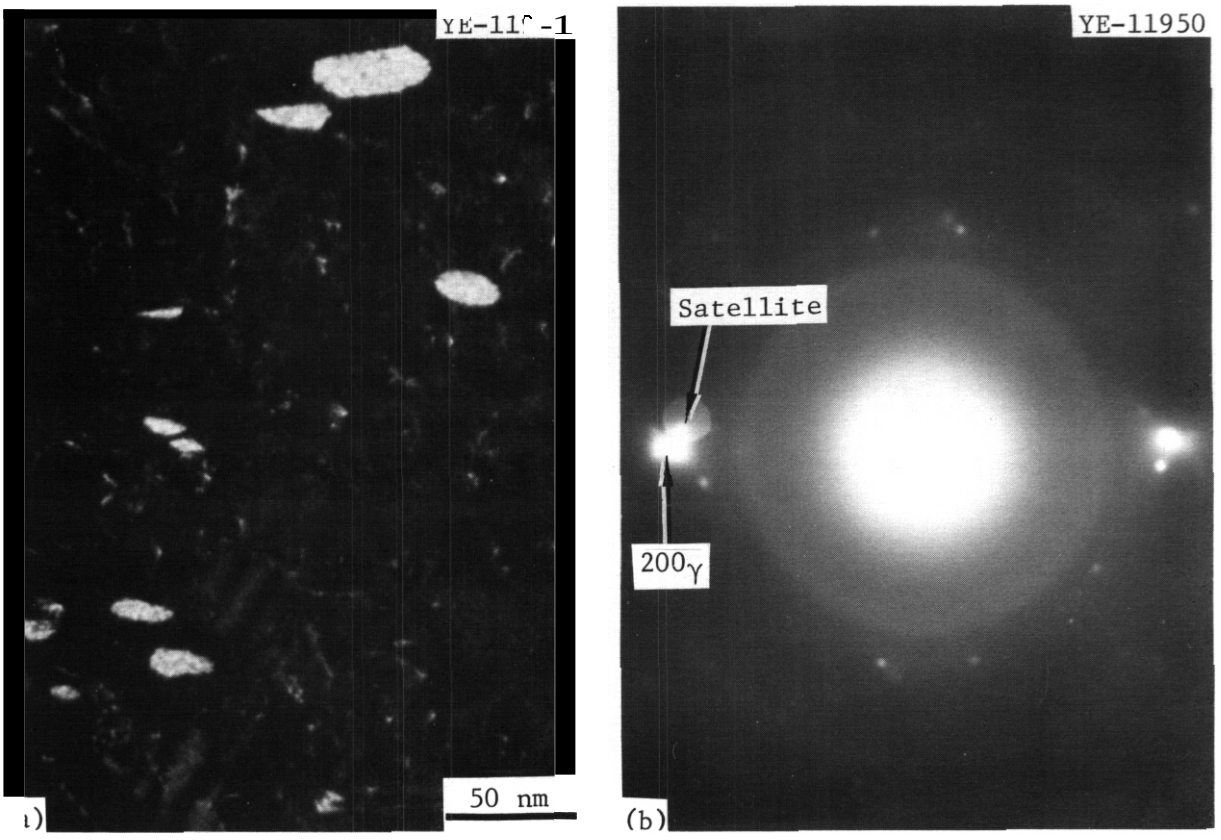

Fig. 3.3.9. (a) Selected Area Diffraction Shows (200) Matrix Reflections in Reciprocal Space with Satellite Streaks Resulting from Stacking Faults on (111) Planes. (b) Centered dark field imaging with one of the satellite streaks, clearly indicating that they come from the faulted plane of the loops. This helps confirm that the loops are Frank faulted loops. The sample is 20%-cold-worked type 316 stainless steel irradiated in the HFIR at 375°C.

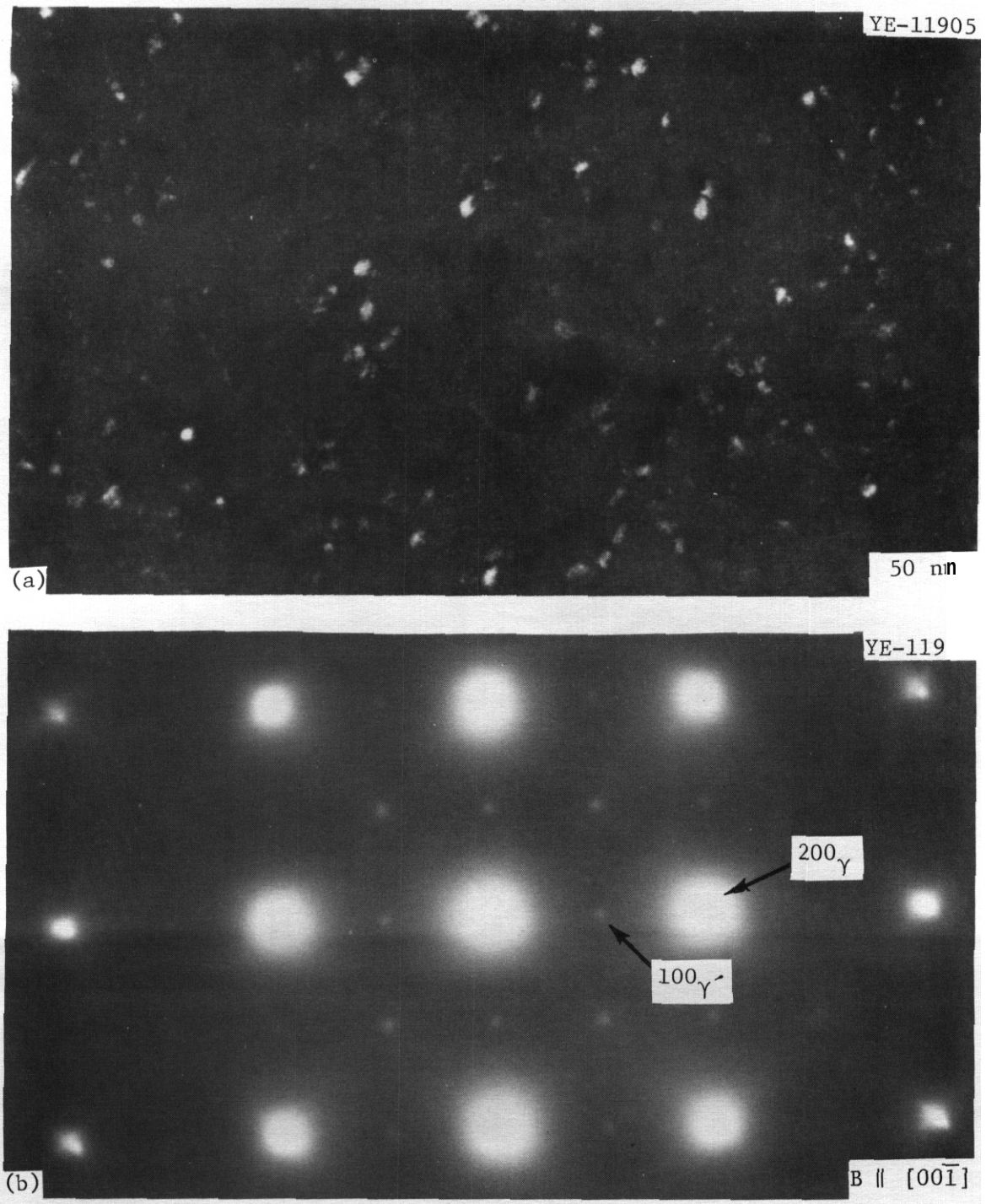

Fig. 3.3.10. (a) Centered Dark Field Image with Superlattice Reflection of Gamma Prime Formed by HFIR Irradiation of 20%-Cold-Worked Type 316 Stainless Steel at 375°C. (b) Selected area diffraction of coincident (001) planes of gamma prime and the austenite matrix, confirming the identification of the phase and indicating its cube-on-cube crystallographic habit.

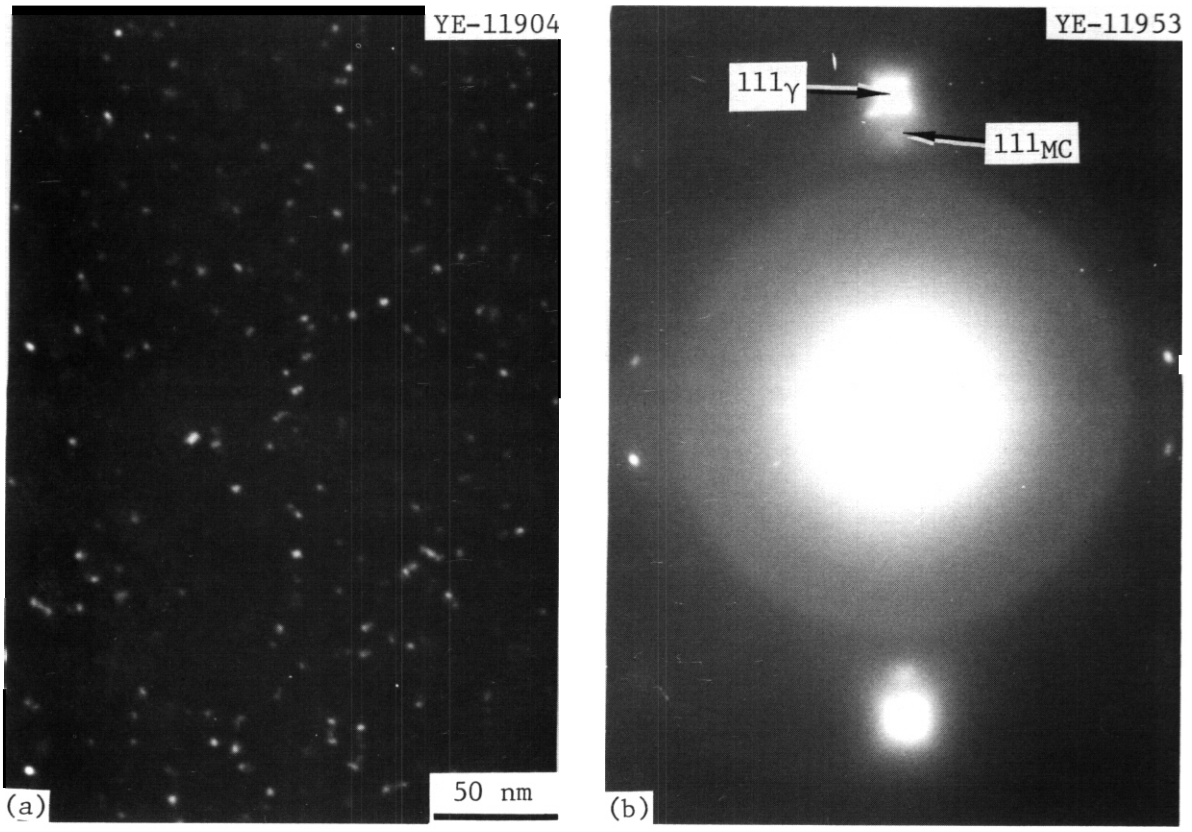

Fig. 3.3.11. Fine MC Particles Produced by HFIR Irradiation of 20%-Cold-Worked Type 316 + 0.23 wt % Ti at 375°C. (a) Centered dark field image of MC phase using (111) precipitate particle reflection. (b) Selected area diffraction showing parallel (111) reflections from the matrix and from the MC phase. The diffuse precipitate particle spot in reciprocal space is consistent with a fairly small MC particle size.

gamma prime in CW 316 are almost identical. However, comparison of Figs. 3.3.10(a) and 3.3.11(a) shows that the distributions differ, with gamma prime particles appearing to cluster, whereas most of the MC particles are discretely spaced along the dislocations. Precipitation of gamma prime during HFLK irradiatton is consistent with the temperatures at which gamma-prime formation is observed in type 316 alloys after fast-reactor irradiation.[18-21] However, precipitation of MC particles during HFIK irradiation occurs at much lower temperatures than observed in titanium-modified austenitic steels after either fast-reactor irradiation[22] or thermal aging (Fig. 3.3.6).

3.3.4.4 Discussion

The postirradiation mechanical properties of CW 316 and CW 316 + Ti are quite similar after HFIK irradiation at temperatures from 55 to 375°C to fluences producing up to 13 dpa and 740 at. ppm He. However, comparison with unirradiated material shows that the ductility of CW 316 is reduced by irradiation while that of CW 316 + Ti remains the same or increases. These trends can be seen more clearly when YS and TE after irradiation at about 375°C are plotted as a function of fluence by Grossbeck and Maziasz.[3] However, the high-strength, good ductility properties and the ductile-transgranular fracture mode together indicate that both materials have better properties than the same materials irradiated at higher temperatures and/or higher fluences.[3,4,6,13,23,24]

The increase in YS and UTS after irradiation at 285 and 375°C in both CW 316 and CW 316 + Ti correlate well with several features of the irradiation-produced microstructures. The generally increased dislocation density, the presence of a significant number of sessile Frank faulted loops, and the high concentration of small cavities in the irradiated microstructures all contribute to the observed strengthening. When strength increases, ductility usually decreases. Therefore, the reduction of UE and TE when the YS and UT increase in CW 316 after irradiation is not unusual. However, the increase in both strength and ductility parameters in irradiated CW 316 + Ti is unexpected. The strength parameters after irradiation at 285 and 375°C are lower in CW 316 + Ti

than in CW 316. However, this trend is qualitatively consistent with the precipitation differences between the alloys. Pickering[25] points out that C and N are the most potent solid-solution strengtheners in austenite with additional strengthening contributed by Si, Mo, Ti, and Nb. The CW 316 irradiated at 285°C has no precipitation and hence has its full complement of solid-solution strengtheners in addition to the other microstructural features that contribute to strengthening. In CW 316 irradiated at 375°C the gamma-prime precipitate particles mainly remove silicon from solution, little affecting the carbon that provides the more potent hardening. The CW 316 + Ti irradiated at 285°C has MC precipitation that removes C, Ti, Mo, and Nb, as discussed in Chapter 3.4 of this quarterly report. Fine MC carbide particles can provide dispersion strengthening, but the strengthening must be traded off against the loss of solid-solution strength as the precipitating elements are removed from the matrix. The trade-off appears about even in CW 316 + Ti irradiated at 375°C because unirradiated and irradiated values of YS and UT are equal.

The relative differences in YS and UTS of irradiated CW 316 and CW 316 + Ti do not appear to correlate well with the relative changes in other microstructural components. These data indicate a minor role of cavities (and possibly loops) in hardening at these conditions.

Both CW 316 and CW 316 + Ti exhibit modest levels of swelling at 285 and 375°C, measured by either immersion density or cavity volume fraction. We did not expect the swelling to be considerably higher at 285 than at 375°C. Although the swelling is less in the CW 316 + Ti than in CW 316, the trend of increased swelling with decreased irradiation temperature is the same. The microstructural reason for the greater swelling at 285 than at 375°C is different for each material – increased cavity size in CW 316 but increased cavity density in CW 316 + Ti. The cavity refinement in CW 316 + Ti relative to CW 316 results from the MC precipitation, an effect established earlier for 316 + Ti at higher temperatures.[26,27] The insensitivity of the total swelling to these drastic changes in microstructure indicates a dominant role of the amount of helium and the irradiation temperature on total swelling in cold-worked material at these conditions.

3.3.5 Summary

1. The YS and UTS of both CW 316 and CW 316 + Ti increase significantly on HFIK irradiation at 55 to 375°C at fluences producing up to 15 dpa and 740 at. ppm He. Postirradiation YS ranges from 700 to 1000 MPa and UTS from 800 to 1000 MPa for both materials, with CW 316 slightly stronger than CW 316 + Ti up to 350°C. The YS and UTS generally decrease as the test and irradiation temperatures increase.

2. Postirradiation UE and TE are similar for both CW 316 and CW 316 + Ti after irradiation at 55 to 375°C. Postirradiation TE ranges from 9 to 15% at 35°C and from 6.5 to 9% at 350°C but falls to 5 to 6% at 300°C. Postirradiation UE remains about constant at 0.2 to 0.5% at 35 to 300°C and increases to 2.5 to 4.5% at 350°C. Both UE and TE are substantially decreased by irradiation in CW 316 but are increased somewhat by irradiation in CW 316 + Ti.

3. The fracture mode of irradiated CW 316 and CW 316 + Ti remains ductile transgranular over the range of irradiation and test temperatures from 35 to 350°C.

4. Microstructural examination reveals measurable cavity swelling in both CW 316 and CW 316 + Ti irradiated at 285 and 375°C to fluences producing 7.7 to 8.5 dpa and 380 to 390 at. ppm He. The total swelling was 0.08 to 0.12% at 375°C and 0.36 to 0.43% at 285°C with slightly less swelling in CW 316 + Ti at both temperatures. The cavity microstructure is considerably refined in CW 316 + Ti compared with CW 316, particularly at 285°C.

5. The dislocation structure in all irradiated samples is significantly denser than in unirradiated, thermally aged control samples. The irradiated dislocation structure contains a substantial fraction of Frank faulted loops as well as a network tangle. The loop structure is much finer in CW 316 + Ti than in CW 316 at both 285 and 375°C.

6. Precipitation occurs in all samples except CW 316 irradiated at 285°C. Finely distributed gamma prime (~3 nm in diameter, 7×10^{22} precipitate particles/m^3) is produced in CW 316 irradiated at 375°C. Fine titanium-rich MC precipitate particles are produced during irradiation of CW 316 + Ti at 285 and 375°C. The fine MC is distributed on a scale similar to the gamma prime.

7. The mechanical properties, fracture mode, and swelling values are the same as or slightly better for CW 316 + Ti compared with CW 316 after irradiation at 50 to 375°C. The trend of improved rather than degraded postirradiation ductility compared with unirradiated values favors CW 316 + Ti over CW 316 for applications in this temperature range.

3.3.6 References

1. M. L. Grossbeck and P. J. Maziasz, "The Swelling of 20%-Cold-Worked Type 316 Stainless Steel Irradiated in HFIK to Helium Levels of 200–3700 at. ppm," *ADIP Quart. Prog. Rep. Jan.–Mar., 1978,* DOE/ET-0058/1, pp. 82–85.
2. F. W. Wiffen, "The Effects of Irradiation at About 55°C on Type 316 Stainless Steel," *ADIP Quart. Prog. Rep. Jan.–Mar., 1978,* DOE/ET-0058/1, pp. 89–93.
3. M. L. Grossbeck and P. J. Maziasz, "Tensile Properties of HFIK-Irradiated Types 316 and TiM 316 Stainless Steel at 200 to 1000 at. ppm He," *ADIP Quart. Prog. Rep. Sept. 30, 1975,* DOE/ET-0058/3, pp. 32-49.
4. M. L. Grossbeck and P. J. Maziasz, "Tensile Properties of HFIK-Irradiated Types 316 and 316 + 0.23% Ti Stainless Steel," *ADIP Quart. Prog. Rep. Dec. 31, 1978,* DOE/ET-0058/4, pp. 24–39.
5. M. L. Grossbeck and M. J. Kania, "HFIK Irradiation of Hourglass Fatigue Specimens," *ADIP Quart. Prog. Rep. June 30,* 2978, DOE/ET-0058/2, pp. 20–35.
6. M. L. Grossbeck and P. J. Maziasz, "Tensile Properties of Type 316 Stainless Steel Irradiated in a Simulated Fusion Reactor Environment," *J. Nucl. Mater.* *85* & 86(II,B): 883–87 (1979).
7. E. E. Bloom, J. W. Woods, and A. F. Zulliger, unpublished data, Oak Ridge National Labortory, September 1969.
8. F. W. Wiffen, E. J. Allen, H. Farrar IV, E. E. Bloom, T. A. Gabriel, H. T. Kerr, and F. G. Perey, "The Production Rate of Helium During Irradiation of Nickel in Thermal Spectrum Fission Reactors," to be submitted for publication.

9. T. A. Gabriel, B. L. Bishop, and F. W. Wiffen, *Calculated Irradiation Response of Materials Using Fission Reactor (HFIR, ORR, and FBR-II) Neutron Spectra*, ORNL/TM-6367 (August 1979).
10. C.K.H. DuBose and J. O. Stiegler, *Semiautomatic Preparation of Specimens for Transmission Electron Microscopy*, OKNL-4066 (Februray 1967).
11. *Nuclear Systems Materials Handbook*, Vol. 1, TIO-26666, pp. 2101-02.
12. D. Fahr, *Analysis of Stress-Strain Behavior of Type 316 Stainless Steel*, ORNL/TM-4292 (November 1973).
13. E. E. Bloom and F. W. Wiffen, "The Effects of Large Concentrations of Helium on the Mechanical Properties of Neutron-Irradiated Stainless Steel," *J. Nucl. Mater.* 58(2): 171-84 (November 1975).
14. P. J. Maziasz, F. W. Wiffen, and E. E. Bloom, "Swelling and Microstructural Changes in Type 316 Stainless Steel Irradiated Under Simulated CTK Conditions," pp. 259-88 in *Radiation Effects and Tritium Technology for Fusion Reactors*, CONF-750989, Vol. I (March 1976).
15. J. W. Edington, *Interpretations of Transmission Electron Micrographs, Monographs in Practical Electron Microscopy in Materials Science*, Philips Technical Library, Netherlands, 1975.
16. P. R. Okamoto and S. D. Harkness, "Stress-Biased Loop Nucleation in Irradiated Type 316 Stainless Steels," *J. Nucl. Muter.* 48: 204-06 (1973).
17. P. J. Maziasz, "The Precipitation Response of 20%-Cold-Worked Type 316 Stainless Steel to Simulated Fusion Irradiation," *J. Nucl. Mater.* 85 & 86(II,B): 913-17 (December 1979).
18. C. Cawthorne and C. Brown, "The Occurrence of an Ordered FCC Phase in Neutron Irradiated M316 Stainless Steel," *J. Nucl. Mater.* 66: 201-02 (1977).
19. H. R. Brager and F. A. Garner, "Swelling as a Consequence of Gamma Prime (γ') and $M_{23}(C,Si)_6$ Formation in Neutron Irradiated 316 Stainless Steel," *J. Nucl. Muter.* 73: 9-19 (1978).
20. E. H. Lee, A. F. Kowcliffe, and E. A. Kenik, "Effects of Si and Ti on the Phase Stability and Swelling Behavior of AISI 316 Stainless Steel," *J. Nucl. Mater.* 83: 79-89 (1979).

21. D. S. Gelles, "Gamma Prime Formation in AISI 316 Stainless Steel: An Example of Radiation-Enhanced Solute Segregation," pp. 130–45 in The *Metal Science* of *Stainless Steels*, E. W. Collings and H. W. King, Eds., The Metallurgical Society of AIME, New York, 1979.

22. E. H. Lee, P. J. Maziasz, and A. F. Kowcliffe, "Identification of Precipitation Phases Occurring in Austenitic Stainless Steels in Thermal and Irradiation Environments," paper to he presented at The Metallurgical Society of AIME Fall Meeting, Pittsburgh, October 5–9, 1980.

23. F. W. Wiffen, P. J. Maziasz, E. E. Bloom, J. O. Stiegler, and M. L. Grossheck, "The Behavior of Type 316 Stainless Steel Under Simulated Fusion Reactor Irradiation," pp. 146–58 in The *Metal Science of Stainless Steel*, E. W. Collings and H. W. King, Eds., The Metallurgical Society of AIME, New York, 1979.

24. J. A. **Horak**, E. E Bloom, M. L. Grossbeck, P. J. Maziasz, J. O. Stiegler, and F. W. Wiffen, "Swelling, Mechanical Properties and Microstructure of Type 316 Stainless Steel at Fusion Reactor Damage Levels," pp. 325–30 in *Proc. lrradiotion Behavior of Metallic Materials for Fast Reactor Core Components*, Corsica, France, June 4–8, 1979.

25. F. B. Pickering, "The Metallurgical Evolution of Stainless Steels," pp. 1–42 in *The Metallurgical Evolution of .Stainless Steels*, F. B. Pickering, Ed., American Society for Metals, Metals Park, Ohio, and **The** Metallurgical Society of AIME, New York, 1979.

26. P. J. Maziasz and E. E. Bloom, "Comparison of Titanium-Modified and Standard Type 316 Stainless Steel Irradiated in HFLK," ADIP *Quart. Prog. Rep. Jan.–Mar. 1978*, DOE/ET-0058/1, pp. 40–53.

27. P. J. Maziasz, B. L. **Cox**, T. K. Roche, and E. E. Bloom, "Time-Temperature-Precipitation Curve Determination of the Path A Prime Candidate Alloy for Microstructural Design," *ADIP Quart. Prog. Rep. Sept. 30*, 1979, DOE/ET-0058/7, pp. 103–27.

3.4 COMPOSITION AND MICKOSTKUCTURE OF PKECIPITATE PHASES IN AUSTENITIC STAINLESS STEELS — P. J. Maziasz (ORNL)

3.4.1 ADIP Task

ADIP Task I.C.l, Microstructural Stability, and Task I.C.2, Microstructure and Swelling in Austenitic Alloys.

3.4.2 Objective

The objective of this work is to characterize the precipitate phases that form in austenitic stainless steels during irradiation or thermal aging. This information will help identify compositional changes for further optimization of the Path A Prime Candidate Alloy (PCA).

3.4.3 Summary

The phases produced in type *316* stainless steel by thermal aging at 750°C or below are eta (η), tau (τ), Laves, and sigma (σ). Thermal aging of type *316* + *0.23* wt % Ti *(316* + Ti) produces titanium-rich MC in addition to varying combinations of the above-mentioned phases. The compositions of the thermally produced phases are unique and distinguishable. Relative *to* the matrix, MC is enriched in Mo, V, Ti, and Nb; tau ($M_{23}C_6$) is enriched in Mo and Cr; Laves is enriched in Si, Mo, and Cr; eta is enriched in Si, Mo, Cr, and Ni; and sigma is enriched in Mo and Cr. All these phases produced by thermal aging are depleted in Fe and, with the exception of eta, depleted in Ni. Only tau and MC are depleted in Si. The thermally produced phases in type *316* nucleate heterogeneously on grain boundaries, matrix dislocations, or the interfaces of other precipitate phases (sympathetic nucleation). In general, the increase of available nucleation sites can account for the enhancement of eta, laves, and sigma phases in thermally aged 20%-cold-worked as compared with solution-annealed type *316* stainless steel. Precipitation of tau, eta, and Laves together considerably reduces the Si and Mo contents of the austenite matrix during thermal aging.

Irradiation can enhance laves, eta, and MC formation and retard or eliminate formation of tau phase relative to thermal aging. The phases produced during irradiation appear compositionally similar to their thermal

counterparts (excluding the irradiation-induced phases) but with small, systematic composition perturbations. The enrichment or depletion behavior with respect to specific elements remains similar to the thermal behavior. The exception is Laves phase, which can be enriched in Ni when produced during irrddiation at lower temperatures. In general, the phases enhanced during irradiation are those considerably enriched in Si, Mo, and Ni. The exception is MC, which is clearly enhanced during High Flux Isotope Reactor (HFIK) irradiation and yet incorporates little or no Si or Ni.

Those precipitate phases that have no corresponding thermally produced counterparts in the same material are considered to be induced by the irradiation. These include G phase, gamma prime, and the phosphorus-rich rod phase. However, these phases play either a minor role (gamma prime) or are not formed at all during HFIK irradiation of types 316 or 316 + Ti.

The current strategy in fusion alloy design for Path A materials is to encourage and stabilize fine-scale MC precipitation, while reducing or eliminating the formation of other phases. It appears that the Si content of the matrix should be held low to discourage Laves and eta Eormation during irradiation. Molybdenum is involved in eta, Laves, and sigma but also in MC and should be varied to determine the effect on MC stability. Finally, systematic combinations of V and Nb with the normal Ti addition should be considered to determine their effects on MC stability.

3.4.4 Progress and Status

Numerous papers report and discuss the enhancement and alteration of precipitation in stainless steel during neutron irradiation and the potential effects of precipitates on void or bubble swelling.[1-10] Precipitation produced during irradiation can also affect other properties, such as strength or ductility,[8] which is discussed in Chapter 3.3 of this quarterly report. Many investigators have reported that phases produced in stainless steel during irradiation are considerably altered in composition compared with the same phases produced by thermal aging. Recently, however, proper phase identification and quantitative x-ray

energy dispersive spectroscopy (EDS) of matrix-free precipitate particles suspended on extraction replicas have shown that many of the phases produced during either Experimental Breeder Reactor (EBR)-II or HFIK irradiation are compositionally quite similar to the same phases produced during thermal aging. The comparison began with finding eta phase in thermally aged type 316 and then its proper identification[11] in either EBR-II- or HFIK-irradiated type 316. The comparison is now extended to tau ($M_{23}C_6$), laves, and MC.

3.4.4.1 Experimental Details

Alloy compositions, determined by quantitative chemical analysis of bulk material, are given in Table 3.4.1. The details of specimen fabrication for 20%-cold-worked or solution-annealed types 316 stainless steel (CW 316 or SA 316) or 316 + Ti (CW 316 + Ti or SA 316 + Ti) have been reported in Chapter 3.3 of this quarterly report and elsewhere.[6-8,12-14] Fabrication details for producing homogeneous Path A PCA have also been reported.[15] Specimens of type 316 and/or type 316 + Ti have been irradiated in the HFIK at temperatures ranging from 370 to 700°C to fluences producing up to about 4000 at. ppm He and 60 dpa.[6-8,12] Several specimens of the same heat of type 316 have been irradiated[13] in EBR-II at 500 to 615°C to fluences producing about 9 dpa and about 4 to 5 at. ppm He. Samples for conventional transmission electron microscopy (CTEM) were obtained from a variety of samples: 3-mm-diam disks cut from rod stock or punched from sheet for thermally aged material and disks cut from the gage or shoulder of buttonhead tensile specimens or

Table 3.4.1. Composition of Three Austenitic Stainless Steels

Alloy	Content,[a] wt %												
	Cr	Ni	Mo	Mn	Si	Ti	C	P	S	N	B	V	Nb
316	18.0	13.0	2.6	1.9	0.8	0.05	0.05	0.013	0.016	0.005	0.0005	0.01	0.0005
316 + Ti	17.0	12.0	2.5	0.5	0.4	0.23	0.06	0.01	0.013	0.006	0.0007	0.01	0.01
PCA[b]	14.0	16.2	2.3	1.8	0.4	0.24	0.05	0.01	0.003	0.01	0.0005	c	E

[a] Balance iron plus trace impurities.

[b] PCA = Prime Candidate Alloy.

[c] Not detectable.

from the gage of sheet tensile specimens for irradiated material. One disk from each specimen was thinned to electron transparency with a standard two-stage dimpling and electropolishing method.[16] A second disk from several samples was used for extracting precipitates on an electron transparent carbon film. The specimen surface is prepared by electropolishing with 5 vol % perchloric acid in methanol followed by lightly electroetching with 10 vol % hydrochloric acid in ethanol to obtain surface relief. A 50- to 200-nm-thick carbon film was vacuum deposited on the surface and removed by further electropolishing. The carbon film is then floated in methanol and suspended on a beryllium grid. The replicas thus produced contain well-separated, matrix-free precipitates as recommended for quantitative x-ray EDS analysis.[17] The x-ray microanalysis was performed in a JEM 100CX (120-kV) analytical electron microscope (AEM) optimized for x-ray EDS.[18] A beryllium double-tilt holder and gimble were used to further reduce the system x-ray background signal. The EDS was performed[18] in the CTEM rather than the scanning transmission electron microscope (STEM) mode to maximize excited volume and minimize contamination, which is important when analyzing for Si. Precipitate phase particles were identified both in-foil and on replicas by multizone tilting and selected area diffraction (SAD) or convergent beam electron diffraction (CBED) and compared with available literature data.[19,20] The matrix was analyzed in the CTEM mode on elliptical areas about 0.5 × 1 μm adjacent to the foil edge (between precipitate particles in aged samples). In all cases the foil thickness was about 20 to 100 nm. The x-ray spectra were collected and analyzed with a PDP 11/34 computer. After appropriate background subtraction, integral intensities were measured by fitting Gaussians and were converted into quantitative compositional information via the standardless analysis technique, employing programs developed by Zaluzec.[21,22] Overlapping peaks were deconvoluted by using appropriate subtraction and the following constants:[17,18,21,22] Cr (K_β/K_α) = 0.138; Mo $[L_\alpha/(L_\alpha + L_\beta)]$ = 0.735 and $(L_\alpha + L_\beta)/K_\alpha$ = 3.06; Nb $[L_\alpha/(L_\alpha + L_\beta)]$ = 0.735 and $(L_\alpha + L_\beta)/K_\alpha$ = 3.17; Ti (K_β/K_α) = 0.09; V (K_β/K_α) = 0.10. Peaks analyzed contained from 100 to 100,000 counts with a statistical significance of 10 to 0.03%. respectively, for the reported weight percent.

3.4.5 Results

The information will be presented for each phase separately and then for the matrix analyses performed. Precipitate phases occurring during reactor irradiation can be considered to be enhanced by irradiation. However, those precipitate phases that have no corresponding thermally produced counterparts in the same material are considered to be induced by the irradiation and are treated elsewhere.[23] These include G phase, gamma prime, and the phosphorus-rich rod phase. However, these phases play either a minor role (gamma prime) or are not formed at all during HFIR irradiation of types 316 or 316 + Ti. The phases considered in this work are eta, tau ($M_{23}C_6$), Laves, MC, sigma, and chi. A summary of phases present for both the thermal aging and irradiation exposure is given in Table 3.4.2. A summary of the crystallographic information and volumetric misfit relative to the untransformed austenite for the various phases is given in Table 3.4.3.

Table 3.4.2. Phases Present After Thermal Aging or Irradiation of Types 316 Stainless Steel or 316 + Ti

Material[a]	Thermal Aging			Neutron Irradiation			
	Conditions		Phases	Conditions			Phases
	Time (h)	Temperature (°C)		Reactor[b]	Temperature (°C)	Damage Level (dpa)	
SA 316	10,000	600	Tau	HFIK	550	42	Eta, *tau*, Laves
	10,000	650	Tau, eta, Laves, sigma				
20% CW 316	10,000	600	Tau, eta, Laves, sigma	HFIR	380	49	Eta
	10.000	650	Tau, eta, Laves, sigma	HFIR	460	54	Eta, Laves
				EBR-II	500	9	Tau, eta
SA 316 + Ti	1	1050	MC	HFIR	600	30	Tau, Laves, MC
PCA	1	1050	MC				

[a] SA = solution annealed; CW = cold worked; PCA = Prime Candidate Alloy.

[b] HFIR = High Flux Isotope Reactor; EBR = Experimental Breeder Reactor.

Table 3.4.3. Crystallographic Data and Calculated Volume Misfit for Various Precipitate Phases in Type 316 Austenitic Stainless Steel

Phase	Crystal Structure[a]	Lattice Parameter (nm)	Solute[b] (atoms/unit cell)	Misfit Parameter,[c] $(\delta - \delta_m)/\delta_m$
Austenite, gamma	(cubic, Fm3m, A1)	$a_0 = 0.36$[d]	4	0
Tau ($Cr_{23}C_6$)[e]	(cubic, Fm3m, $D8_4$)	$a_0 = 1.06$[d,f]	92	0.10
Eta (Fe_3W_3C)	(cubic, Fd3m, $E9_3$)	$a_0 = 1.07$[g,h]	96	0.09
Laves (Fe_2Mo)	(hexagonal, $P6_3/mmc$, C14)	$a_0 = 0.47$[d,f] $c_0 = 0.77$ $c/a = 1.64$	12	−0.05
Sigma (Fe, Cr)	(tetragonal, P4/mnm, $D8_b$)	$a_0 = 0.88$[d] $c_0 = 0.46$ $c/a = 0.52$	30	0.02
Chi (a–Mn)	(cubic, $I\bar{4}3m$, 1\12)	$a_0 = 0.89$[d,f]	58	0.04
Ti–rich MC (TIC)	(cubic, Fmlm, Bl)	$a_0 = 0.43$[a,f]	4	0.7
Gamma prime (Ni_3Si)	(cubic, Pmlm, $L1_2$)	$a_0 = 0.35$[a]	4	−0.08
P–rich rods (Fe_2P)	(hexagonal, P321, C22)	$a_0 = 0.604$[i] $c_0 = 0.36$ $c/a = 0.6$	b	−0.38
G phase ($Ti_6Ni_{16}Si_7$)	(cubic. Fm3m, A1)	$a_0 = 1.1$[j]	116	0.04

[a]For each phase (lattice system, space group, structure type) where lattice system is the Bravais lattice type — space group is given by the short form of the point group symmetry elements in the Hermann-Mauguin short notation; structure type is the Strukturbericht notation for the element or pure compound that is the prototype structure for that crystal class. Source: C. J. Smithells, Ed., Metals Reference *Rook,* 5th ed., Butterworths, London, 1976, pp. 108–77.

[b]The total number of atoms per unit cell of the structure minus the number of interstitial carbon or nitrogen atoms (if any).

[c]δ is the volume per solute atom in the precipitate structure; δ = (volume/unit cell)/(solute atom/unit cell); δ_m = volume per solute atom in the austenite matrix.

[d]Source: B. Weiss and R. Stickler, "Phase Instabilities During High–Temperature Exposure of 316 Austenitic Stainless Steel," *Metall.* Trans. 3: 851–66 (1972).

[e]Either prototype compound or compound appropriate to steel.

[f]Source: K. W. Andrews, P. J. Bryson, and S. R. Koewn, Interpretation of Electron Diffmction Patterns, 2d ed., Plenum Press, New York, 1971.

[g]Source: H. Hughes, "A New Silicide in a 12 Percent Chromium Steel," Nature 183: 1543 (1959).

[h]Source: P. J. Maziasz. "The Formation of Diamond–Cubic Eta (η) Phase in Type 116 Stainless Steel Exposed to Thermal Aging or Irradiation Environment," *Scr.* Metall. 13: 621–26 (July 1979).

[i]Source: J. Bentley and J. M. Leitnaker, "Stable Phases in Aged Type 321 Stainless Steel," pp. 70–91 in *The Metal Science* of Stainless *Steels,* E. W. Collings and H. W. King, Eds., The Metallurgical Society of AIME, New York, 1979.

[j]Source: E. H. Lee, A. F. Rowcliffe, and E. A, Kenik, "Effects of Si and Ti on the Phase Stability and Swelling Behavior of AISI 316 Stainless Steel," *J. Nucl.* Mater. 83: 79 (1979).

3.4.5.1 Tau Phase

The designation tau (τ) is chosen following Stadelmaier[24] because the stoichiometry of this phase in steel is not well known. Efforts are under way by Zaluzec and Maziasz[25] to measure the C content in tau produced during thermal aging by using quantitative electron energy loss spectroscopy (EELS). However, with reference to the literature, tau and "$M_{23}C_6$" can be used interchangeably.

Tau phase is face-centered cubic (fcc) with a lattice parameter of about 1.06 nm when formed in stainless steel (Table 3.4.3). The lattice parameter determined by SAD in this work agrees within ±0.05 nm. Tau phase has approximately a +10% volume misfit with respect to untransformed austenite on the basis of crystal structure and lattice parameters. Tau phase is generally formed after thermal aging at 560°C and above in either SA 316 or CW 316 examined in this work or in similar steels examined by others.[26-28] The crystallographic habit relationship is cube-on-cube, as shown by SAD in Fig. 3.4.1. However, tau can sometimes appear to have a twinned crystallographic habit with respect to the surrounding matrix if it nucleates cube-on-cube with stacking faults or deformation bands in cold-worked material. Figure 3.4.1(b) shows the appropriate (001) diffraction pattern from a single tau particle that is necessary to distinguish fcc tau phase from diamond-cubic eta phase.

Figure 3.4.2 indicates that intragranular tau phase produced on thermal aging has a variety of morphologies while always maintaining the same cube-on-cube crystallographic habit. Typical morphologies and distributions of tau phase produced at grain boundaries in thermally aged type 316 are shown in Fig. 3.4.3. The grain boundary particles are usually oriented cube-on-cube with only one of the grains at the boundary and grow into the supersaturated matrix or that grain.

In thermally aged, titanium-modified austenites, tau phase is generally reduced,[29] as in type 316 + Ti, or eliminated,[15] as in Path A PCA. This is generally consistent with observations of others for titanium-modified compared with unmodified austenitic stainless steels.[26,30-32]

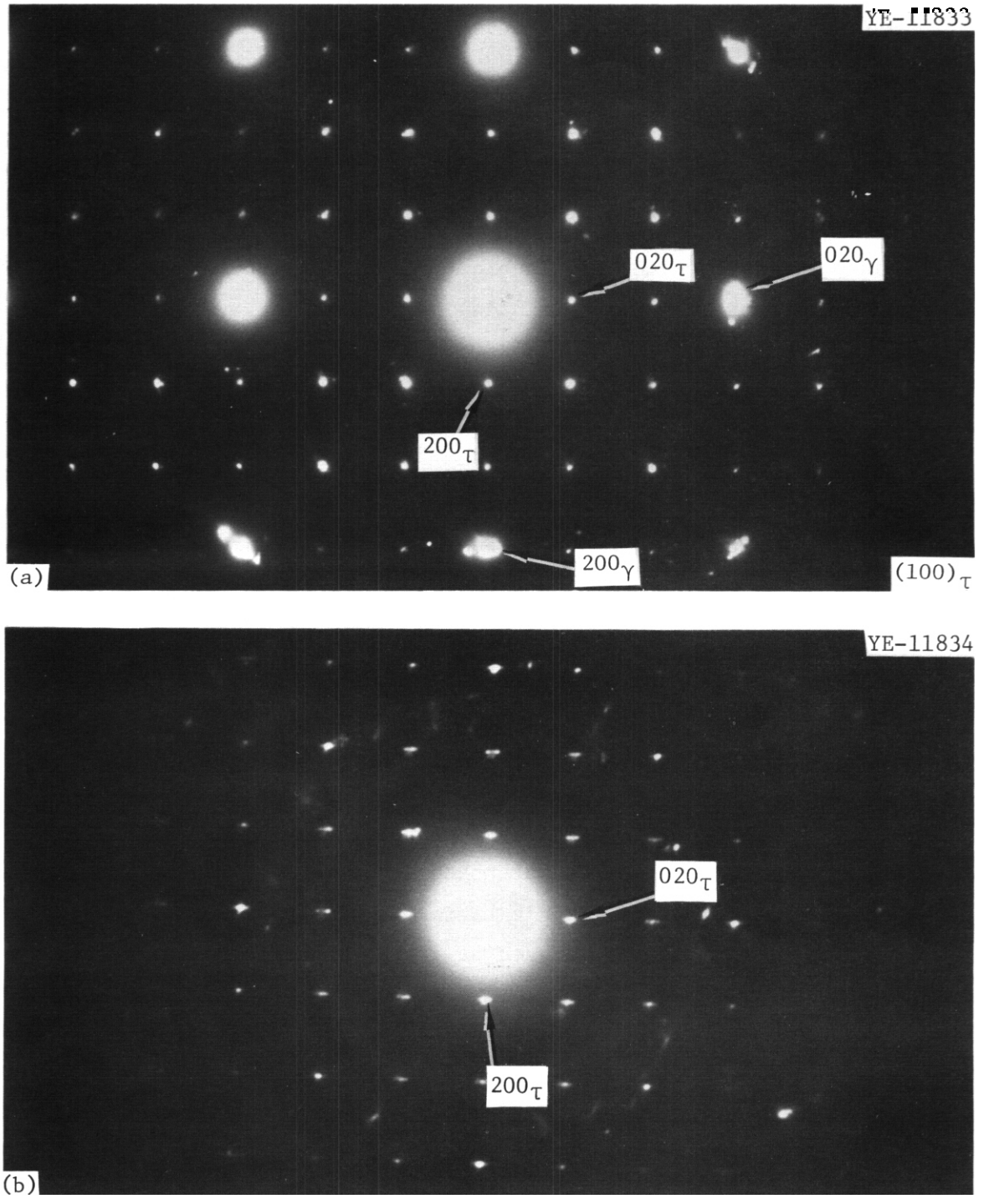

Fig. 3.4.1. (a) Selected Area Diffraction (SAD) of *(001)* Zone Axis for Austenite Matrix Plus Intragranular Tau Phase Particles in 20%-Cold-Worked Type 316 Thermally Aged for 10,000 h at 650°C and (b) SAD from a Single Particle of the Same Phase in the Same Crystallographic Orientation on a Carbon Extraction Replica.

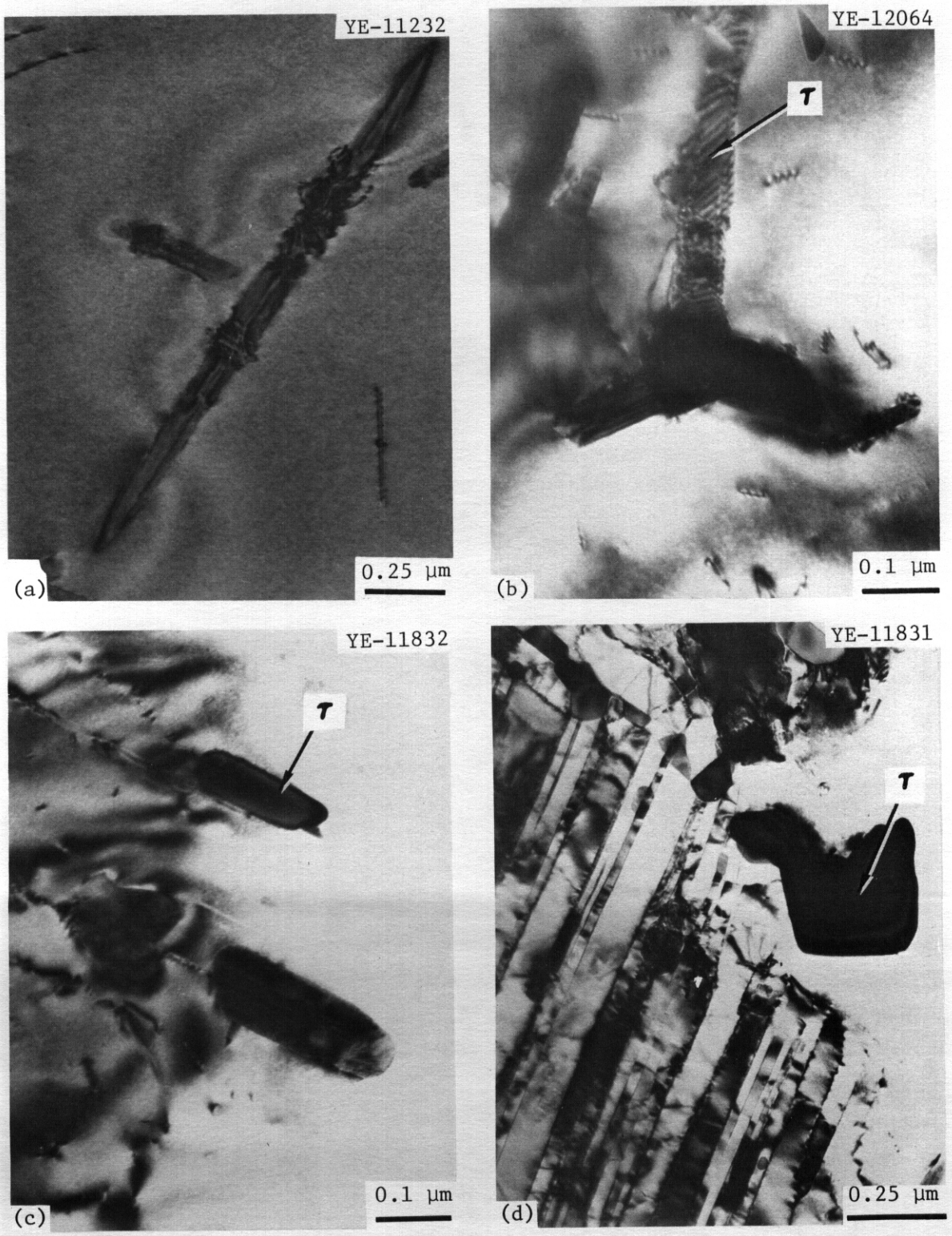

Fig. 3.4.2. Bright Field Images of the Various Morphologies of Tau Produced by Thermal Aging of Type 316. (a) Long <110> axis sword or laths in solution-annealed type 316 aged 10,000 h at 600°C. (b) Wide laths or rectangular particles in solution-annealed type 316 aged 10,000 h at 650°C. (c) Blocky or rounder shaped particles in 20%-cold-worked type 316 aged 10,000 h at 650°C. (d) Large rectangular plate particle of tau in 20%-cold-worked type 316 aged same as (c).

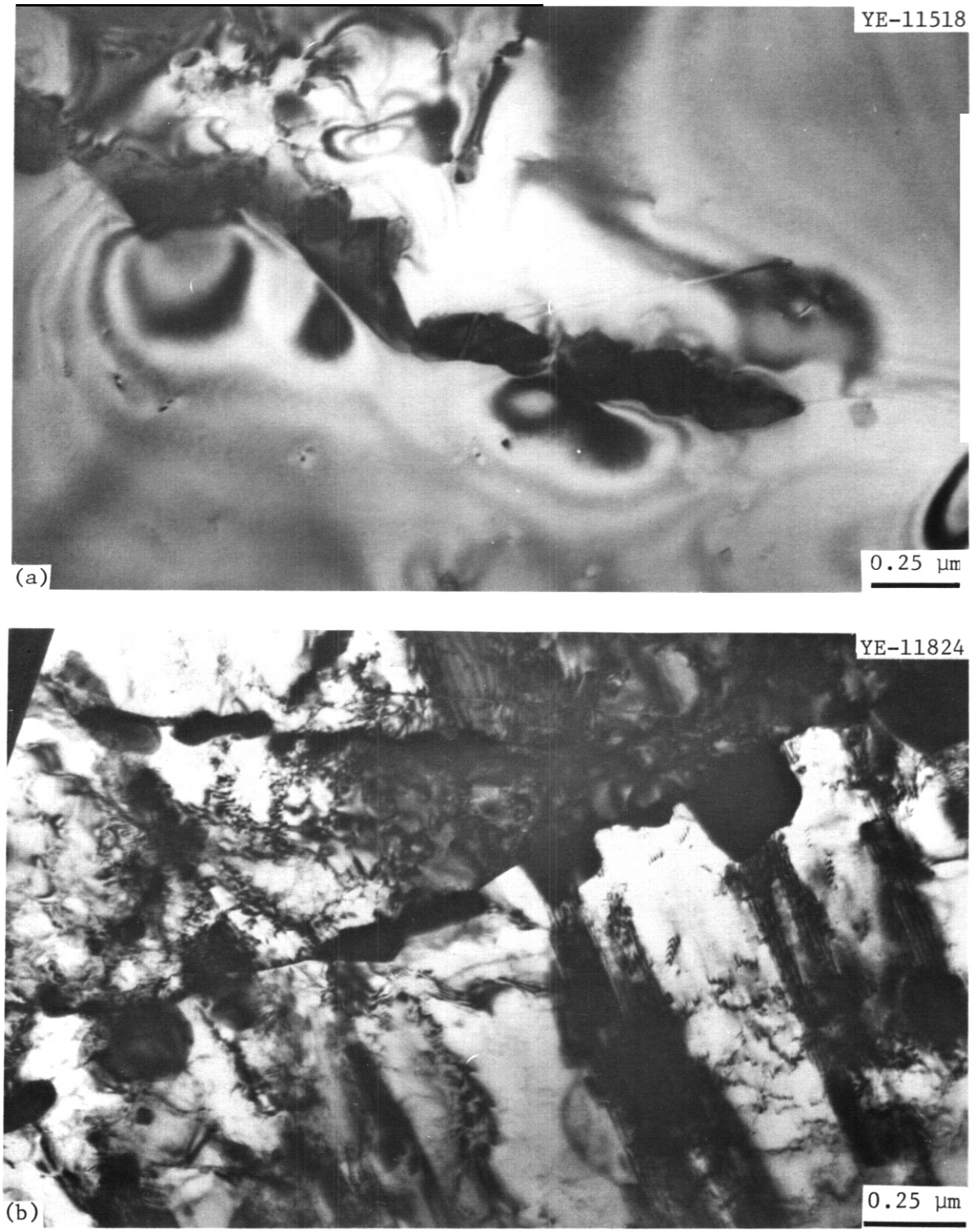

Fig. 3.4.3. Typical Grain Boundary Tau Phase Produced by Thermal Aging in (a) Solution-Annealed Type 316 Aged 10,000 h at 600°C and (b) 20%-Cold-Worked Type 316 Aged 10,000 h at 600°C.

Tau phase, in either CW *316* or SA *316*, appears at somewhat lower temperatures for EBR-II irradiation compared with thermal aging.[13] Figure *3.4.4* shows grain boundary microstructures produced in SA *316* and CW *316* at 500°C and in SA *316* at 625°C during irradiation to a fluence of *8.4* dpa (irradiation time ~*3400* h). The amount of tau phase appears reduced after EBR-II irradiation when compared with type *316* thermally aged at 600°C [Figs. 3.4.3(a) and 3.4.4]. Tau phase is again produced both at the grain boundaries and in the matrix of the same heat of material irradiated in EBR-II at *680* to 750°C. Tau phase is not observed at all[7,29] after HFIR irradiation at 550°C or below in CW *316* or CW *316* + Ti. It is observed primarily at the grain boundaries[8] of SA *316* + Ti irradiated in the HFIR at 600°C and at the grain boundaries and in the matrix[6] of SA *316* irra-diated in the HFIR at 550°C. It appears in anomalously large particles' in CW *316* after HFIR irradiation at 600°C. This sample recrystallized during the irradiation. Tau is always observed to have its characteristic cube-on-cube crystallographic habit after thermal aging or irradiation in either EBR-II or HFIR.

The compositional measurements on a number of tau phase particles produced either thermally or during neutron irradiation are given in Table *3.4.4*, and a characteristic x-ray EDS spectrum is shown in Fig. *3.4.5*. Matrix measurements for both unaged controls and the matrix between precipitate particles after thermal aging are given in Table *3.4.5* for comparison. Tau on the average is low in Si, Fe, and Ni and considerably enriched in Cr and Mo, relative to the bulk alloy composition. Occasional particles show a large enrichment of Ti or V, which have very low concentrations in the austenite matrix. The composition of the phase is the same whether it is produced in SA *316* or CW *316* and shows no systematic temperature dependence outside the particle-to-particle compositional variation. An average composition for tau produced by thermal aging in weight percent is *0.5 Si—14* Mo—64.5 Cr—0.5 Mn—15.5 Fe—4.0 Ni, neglecting the occasional V and Ti. The composition of tau produced in type *316* + Ti is very nearly similar, except that TI appears regularly at several weight percent.[29] Quantitative microprobe analysis of tau produced thermally in either type *316* or closely related austenites[27,33]

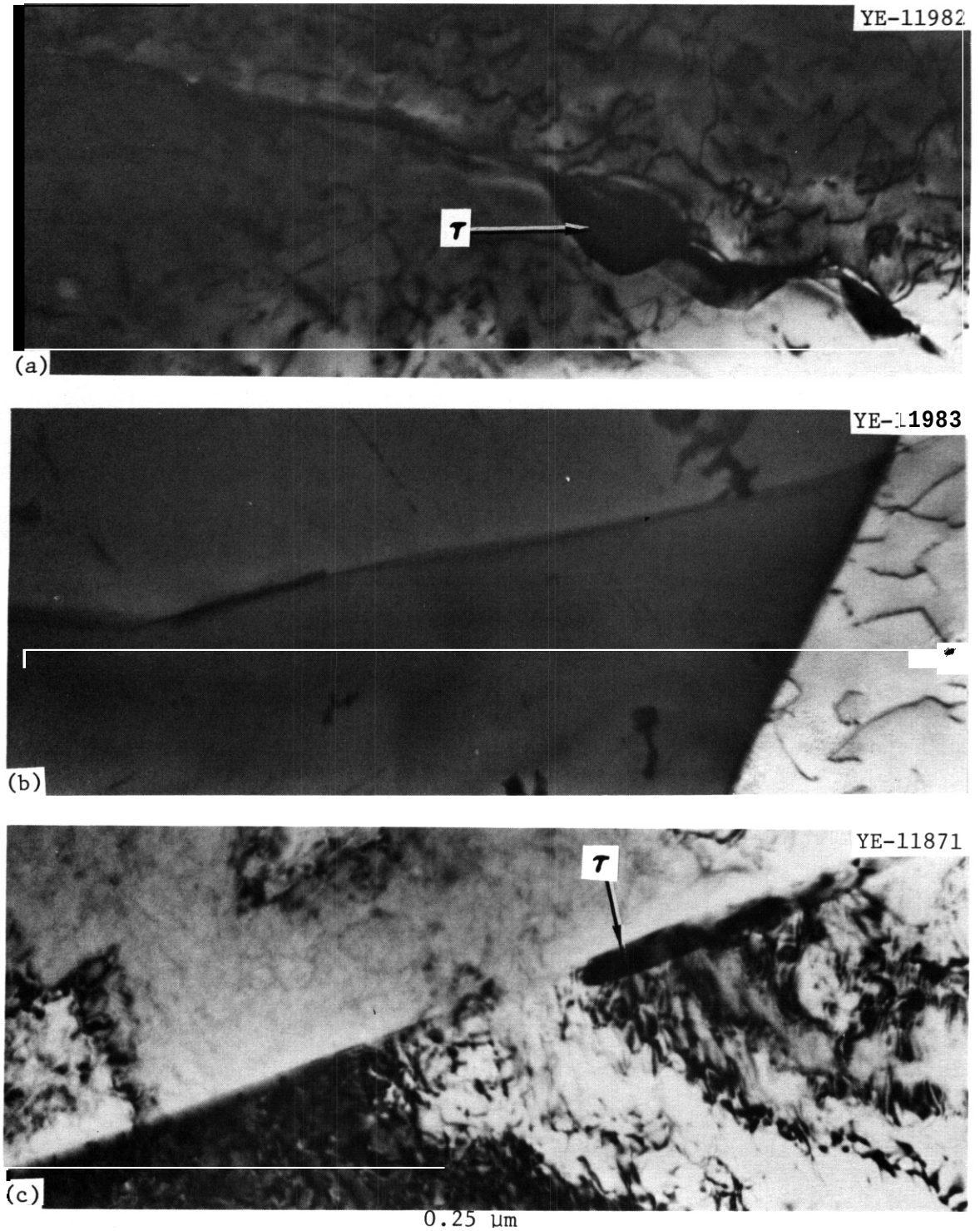

Fig. 3.44. Typical Grain Boundary Microstructures Produced During EBR-II Irradiation of (a) Solution-Annealed Type 316 Irradiated at 500°C, (b) Solution-Annealed Type 316 Irradiated at 625°C, and (c) 20%-Cold-Worked Type 316 Irradiated at 500°C. All samples were irradiated to a fluence of 8.4 dpa, which corresponds to an exposure time of about 3400 h

Table 3.4.4. X-Ray Energy Dispersive Spectroscopy Compositional Information[a] from Tau ($M_{23}C_6$) Phase Produced by Either Thermal Aging or Neutron Irradiation

Content,[b] wt %							
Si	Mo	Ti	V	Cr	Mn	Fe	Ni
SA Type 316 Aged 10,000 h at 600°C (Grain Boundary)							
c	9.0	0.8	c	58.3	0.5	27.4	4.0
0.2	9.7	0.2	c	67.4	c	19.5	3.0
0.2	10.6	0.4	c	67.0	c	18.3	3.5
SA Type 316 Aged 10,000 h at 600°C (Matrix)							
0.3	16.0	3.0	c	62.0	c	17.0	1.7
c	14.8	0.2	c	65.0	c	17.0	3.0
c	19.7	c	c	67.0	c	12.3	1.0
c	16.6	c	c	66.0	c	14.6	2.8
SA Type 316 Aged 10,000 h at 650°C (Matrix)							
2.0	24.5	c	c	51.7	c	18.3	3.5
c	16.5	c	c	66.6	1.7	11.2	4.0
c	15.3	c	c	68.4	0.6	13.0	2.7
2.0	17.0	1.0	2.3	55.3	c	13.0	9.4
20% CW Type 316 Aged 10,000 h at 600°C (Matrix)							
0.8	12.4	c	c	63.4	2.2	16.0	5.3
c	9.7	c	c	73.0	0.4	13.5	3.4
0.4	12.3	c	c	61.0	1.4	20.0	5.0
0.6	12.6	c	c	60.2	1.6	18.0	7.0
2.0	16.2	c	0.5	64.3	0.3	9.4	7.2
20% CW Type 316 Aged 10,000 h at 650°C (Matrix)							
1.3	12.7	c	c	71.0	c	8.0	7.0
c	8.5	0.4	c	74.3	0.3	13.2	3.3
20% CW Type 316, EBR-II Irradiated at 500°C to 9 dpa (Grain Boundary)							
3.0	12.4	0.6	0.5	54.4	0.2	16.8	12.3
1.0	12.0	1.0	1.0	56.5	1.8	23.0	3.5
2.3	12.8	0.4	0.4	59.0	1.0	14.8	9.2
[illegible]e 316 + Ti, HFIR Irradiated at 600°C to 30 dpa (Grain Boun[illegible]							
0.5	10.0	0.6	2.0	56.0	c	25.8	4.8
1.0	11.0	c	c	64.7	c	18.0	4.7

[a]Column headings are aging or irradiation conditions. Terms in parentheses indicate locations of analyzed precipitate particles. SA = solution annealed; CW = cold worked.

[b]Normalized weight percent.

[c]Not detectable.

Table 3.4.5. X-Ray Energy Dispersive Spectroscopy Compositional Information[a] on the Austenite Matrix Before or After Thermal Aging

Content,[b] wt %							Precipitate Phases
Si	Mo	Ti	Cr	Mn	Fe	Ni	
Type 316, SA Control							
1.3	4.0	c	18.0	2.6	61.1	13.0	None
1.5	3.4	c	18.1	2.5	61.1	13.4	
Type 316, 20% CW Control							
1.0	2.5	c	19.4	1.6	63.1	12.4	
1.2	3.8	c	18.3	1.7	62.3	12.7	None
1.2	3.3	c	18.3	1.7	63.7	11.8	
Type 316 + Ti, SA Control							
0.5	2.3	0.2	18.8	0.6	65.0	12.5	
0.2	2.4	0.2	19.3	0.6	66.0	11.4	MC, Ti(C,N)S
0.3	3.1	0.3	19.7	0.6	63.3	12.7	
Path A PCA (Homogenized), SA Control							
0.4	2.6	0.2	16.0	2.3	62.7	15.8	
0.6	2.6	0.1	16.0	1.7	62.0	17.0	Ti(C,N)S
0.5	2.7	0.2	16.6	1.4	61.6	17.0	
Type 316, SA, Thermally Aged 10,000 h at 600°C							
2.0	3.4	c	19.0	2.0	61.0	12.6	
1.3	3.0	c	18.2	1.8	62.7	13.0	Tau
1.3	4.0	c	18.3	2.0	62.2	12.2	
Type 316, SA, Thermally Aged 100 h at 650°C							
1.9	3.6	c	18.7	1.5	61.7	12.6	None
1.2	3.1	c	19.0	1.3	62.7	12.6	
Type 316. SA, Thermally Aged 10,000 h at 650°C							
0.9	1.4	c	18.6	1.5	65.6	12.0	Tau, eta, Laves,
0.8	1.5	c	18.5	2.0	64.2	13.0	and sigma
Type 316, 20% CW, Thermally Aged 10,000 h at 600°C							
1.1	1.2	c	18.3	2.2	64.8	12.4	
0.7	3.1	c	19.5	1.8	62.5	12.3	Tau, eta, Laves,
0.6	2.1	c	19.6	1.9	63.0	12.8	and sigma
Type 316, 20% CW, Thermally Aged 10,000 h at 650°C							
0.9	0.4	c	18.7	1.9	63.6	14.4	
0.8	0.9	c	19.5	1.7	64.0	13.1	Tau, eta, Laves,
1.5	0.2	c	19.3	2.4	62.6	14.0	and sigma

%ut-in headings indicate aging conditions. SA = solution annealed; CW = cold worked; PCA = prime candidate alloy.

[b] Normalized weight percent.

[c] Not detectable.

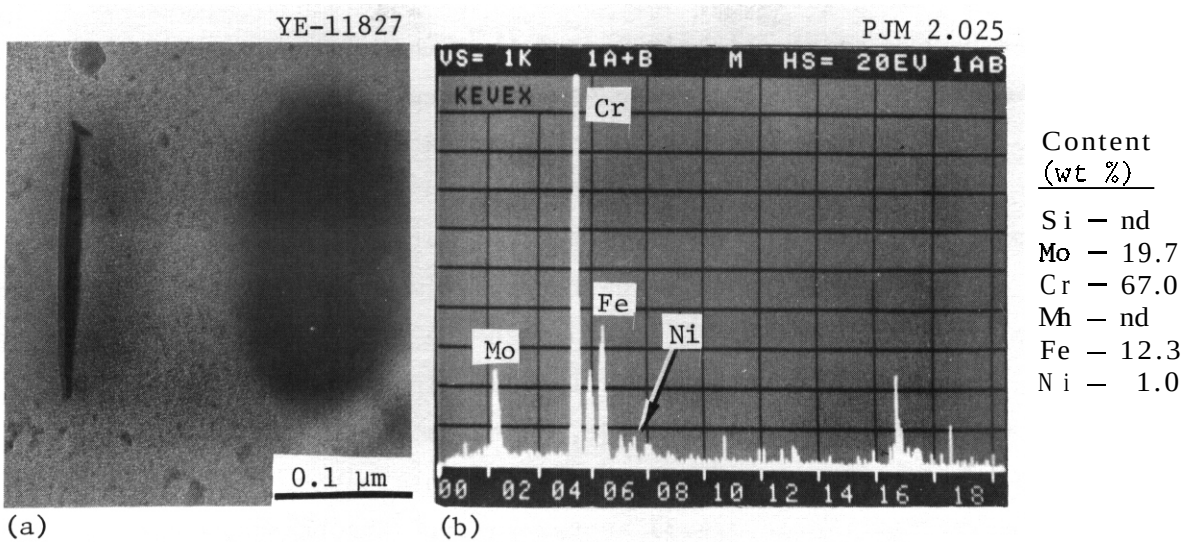

Fig. 3.4.5. Characteristic X-Ray Energy Dispersive Spectroscopy (EDS) Spectrum of Tau Phase Extracted from Solution-Annealed Type 316 Aged for 10,000 h at 600°C and Analyzed Quantitatively. (a) Bright field image of the lath tau precipitate. (b) EDS spectrum and precipitate composition. nd = not detectable.

agrees well with the composition measurements in this work. However, those investigators did not measure the Si concentration. Other composition measurements[34,35] of tau phase in several heats of type 316 using replicas and the same quantitative x-ray EDS techniques also agree well with compositions reported in Table 3.4.4.

Tau phase produced during EBR-II irradiation of CW 316 or HFIR irradiation of SA 316 + Ti has a composition similar to thermally produced tau phase (Table 3.4.4). The Si and Ni concentrations are slightly higher in tau phase produced by EBR-II irradiation compared with that produced thermally. However, the composition of tau phase produced by HFIR irradiation is the same as that produced thermally, despite the fact that the comparison is between types 316 and 316 + Ti. Tau phase produced in type 316 during irradiation appears to concentrate 0.5 to 2 wt % of both V and Ti more regularly than does the thermally produced phase.

3.4.5.2 Eta Phase

Eta (η) phase has a diamond-cubic crystal structure with a lattice parameter of about 1.07 nm (Table 3.4.3). Selected area diffraction

measurements using ratios of interplanar spacings always shows the lattice parameter of eta to be slightly larger than that for tau, which is consistent with Table 3.4.3. Eta phase was only recently found in this heat of type 316 thermally aged at 600 to 650°C by Maziasz[11] and in several other heats of type 316 aged at the same conditions by Steeds and co-workers.[34-37] Eta is most difficult to identify when intimately mixed with tau phase because only subtle diffraction differences [missing 200 reflection on (001) zone for diamond cubic] distinguish the two phases (Figs. 3.4.1 and 3.4.6). Eta phase is morphologically indistinguishable from tau phase, and the two often form side by side, as shown in Fig. 3.4.7. Eta phase also has the same cube-on-cube crystallographic habit, nucleation sites, and volume misfit (Table 3.4.3) as tau phase. Eta phase is found primarily at the grain boundaries in thermally aged SA 316 in a narrow temperature range centered about 650°C. Eta phase is produced[29] at the

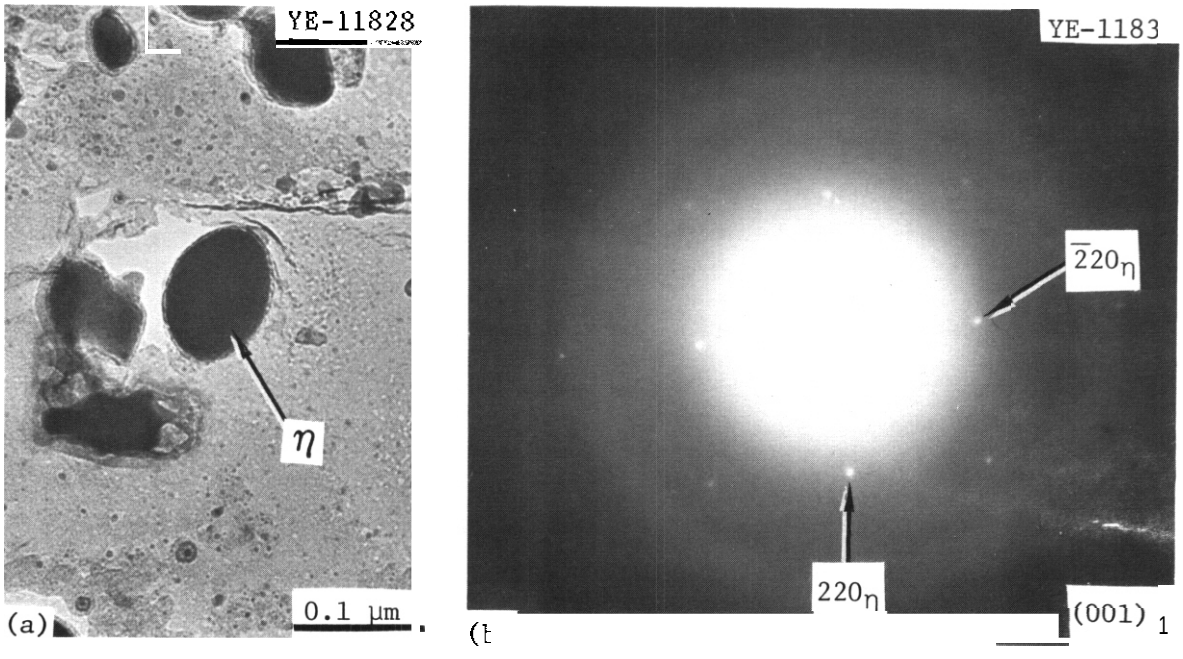

Fig. 3.4.6. (a) Bright Field Image of Eta Phase Particle Extracted from 20%-Cold-Worked Type 316 Aged 10,000 h at 650°C. (b) Selected area diffraction on (001) zone axis. The missing 200 reflections unambiguously confirm diamond-cubic structure (compare with Fig. 3.4.1).

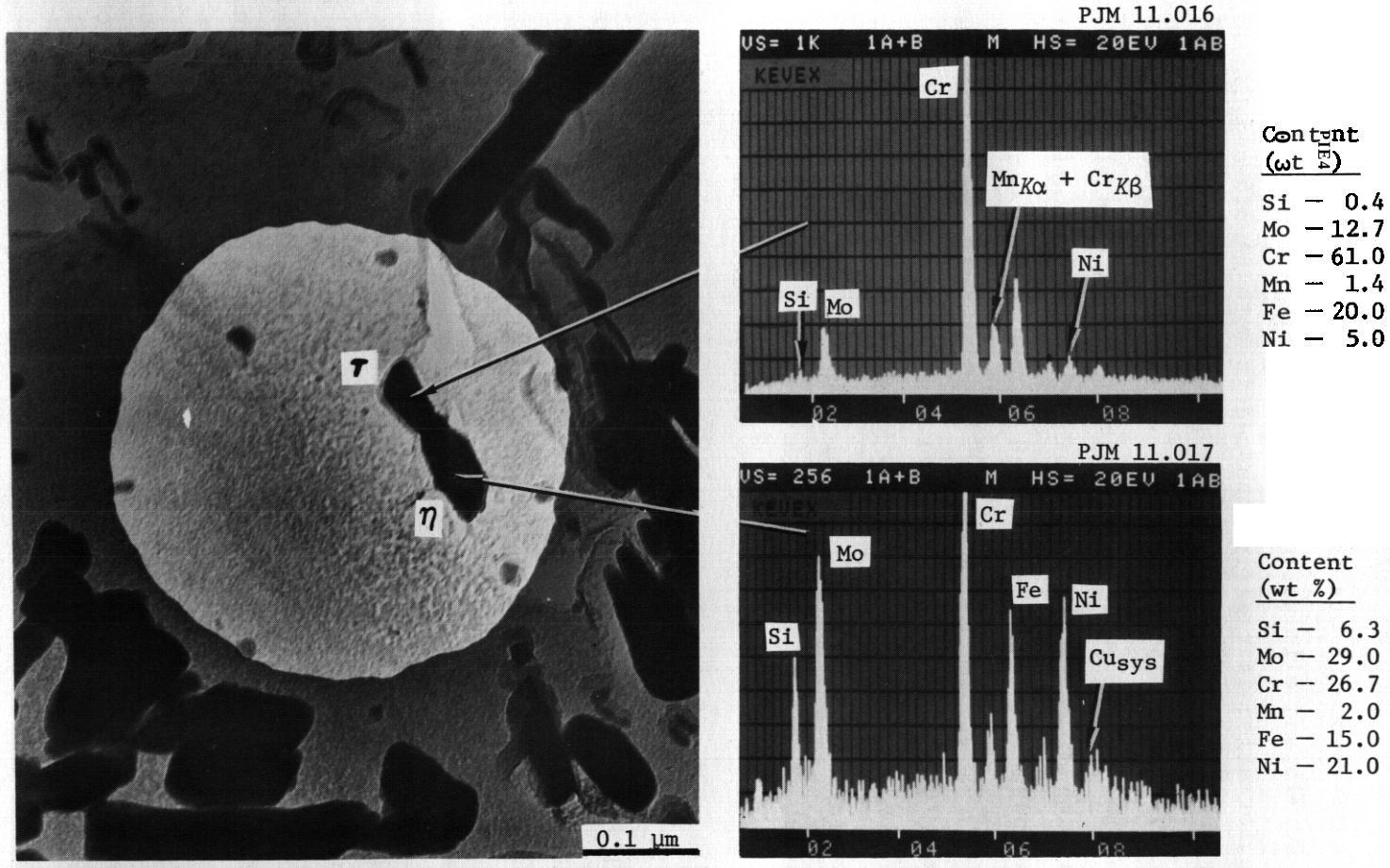

Fig. 3.4.7. Bright Field Image of Side-by-Side Particles of Tau and Eta Phases Extracted from 20%-Cold-Worked Type 316 Aged 10,000 h at 600°C. They are morphologically indistinguishable but separable by selected area diffraction (SAD). Their respective x-ray spectra, however, are clearly different and can be used for identification. [See P. J. Maziasz, "The Formation of Diamond Cubic Eta (η) Phase in Type 316 Stainless Steel Exposed to Thermal Aging or Irradiation Environments," *Scr. Metall.* 13: 621–26 (1979)]. The circle image is the shadow of the smallest SAD aperture so that one can appreciate the difficulty of properly identifying an intimate mixture of the two phases by SAD. Cu_{sys} indicates copper detected in the microscope and not from specimen.

grain boundaries on thermal aging from 560 to 650°C and in the matrix from 600 to 650°C in CW 316. The relative amount of eta in the combination eta plus tau can be as much as 50% in CW 316 aged at 600 to 650°C. As with tau, thermally produced eta is considerably reduced[29] in CW 316 + Ti compared with CW 316 and eliminated in Path A PCA.[15]

Eta phase formation is clearly enhanced in both SA 316 and CW 316 either by fast reactor irradiation at 600 to 650°C or below[11,13,23,29,38,39] or by HFIR irradiation at 550°C or below.[7,11,13,29] Eta almost completely replaces tau as the matrix phase in EBR-II-irradiated type 316 and replaces tau in the matrix and at the grain boundaries in HFIR-irradiated type 316. Eta phase is primarily confined to the grain boundaries in CW 316 + Ti irradiated in the HFIR at 550°C or below.[29] As during thermal aging, eta phase formation appears to have an upper temperature limit during neutron irradiation. Eta phase produced during irradiation can have several variations in crystallographic habits in addition to the normal cube-on-cube variant. Figure 3.4.8 shows the clear diamond-cubic structure of eta phase and a stereographic representation of the crystallographic habit as determined by SAD. Because the orientation relation in Fig. 3.4.8(b) does not exactly match the matrix and precipitation planes, it can have a multiplicity of small variations of the same general habit and give the appearance of being randomly oriented. Figure 3.4.9 again shows the diamond-cubic crystal structure of eta phase produced by HFIR irradiation of CW 316.

The x-ray EDS compositional measurements of extracted eta phase particles are presented in Table 3.4.6. A characteristic spectrum for eta phase produced in thermal aging is shown in Fig. 3.4.7. Eta phase is considerably enriched in Si, Mo, Ni, and to a lesser extent Cr, compared with the unprecipitated matrix (Table 3.4.4). Eta is depleted in Fe and contains Mn at about the matrix level or less. It can contain several weight percent of either Ti or V, and their enrichments are somewhat more regular than in thermally produced tau phase. An average composition of eta precipitated in thermal aging in weight percent is 7 Si—23.5 Mo—2 (V and/or Ti)—31 Cr—0.5 Mn—11 Fe—25 Ni. As with tau phase, there is some particle-to-particle scatter, but within this scatter the composition

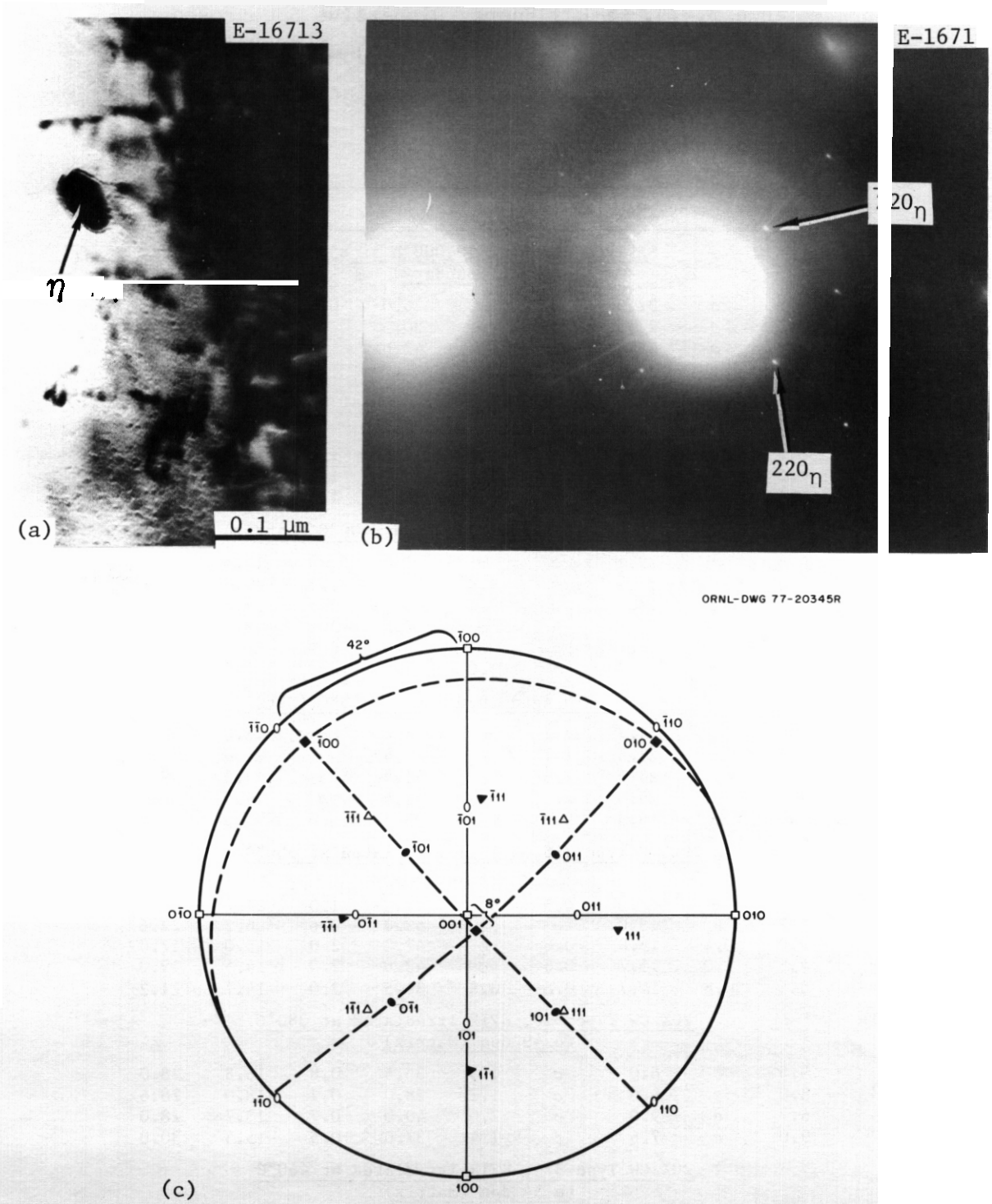

Fig. 3.4.8. Clear Selected Area Diffraction (SAD) Identification of Eta Phase Produced in 20% Cold Worked Type 316 Irradiated in EBR-II to 8.4 dpa at 500°C. (a) Bright field image. (b) SAD on (001) zone axis. (c) Stereographic representation of the unusual crystallographic habit represented with superimposed matrix and precipitate stereographic projections.

Table 3.4.6. X-Ray Energy Dispersive Spectroscopy Compositional Information[a] from Eta Phase Particles Produced by Either Thermal Aging or Neutron Irradiation

Content,[b] wt %								
Si	P	Mo	Ti	V	Cr	Mn	Fe	Ni
SA Type 316 Aged 10,000 h at 650°C (Grain Boundary)								
6.3	c	32.3	c	c	26.0	0.1	17.3	18.3
5.3	c	27.5	1.7	c	30.5	c	7.2	27.8
3.8	c	22.6	1.0	c	42.6	c	15.6	14.4
8.0	c	35.0	c	c	21.7	c	13.2	22.0
20% CW Type 316 Aged 10,000 h at 600°C (Grain Boundary)								
6.8	c	17.2	c	2.2	32.0	1.6	10.6	29.7
8.3	c	17.2	c	2.4	33.0	1.2	6.8	31.0
6.4	c	15.0	c	2.6	36.0	1.8	13.2	25.0
20% CW Type 316 Aged 10,000 h at 600°C (Matrix)								
8.3	c	29.4	c	c	25.0	c	13.6	23.7
5.6	c	27.7	c	1.3	28.0	1.5	12.5	23.4
6.0	c	17.0	c	2.0	35.5	2.6	13.6	23.4
7.0	c	19.0	c	c	31.5	2.2	12.0	28.3
6.3	c	29.2	c	c	26.6	2.0	15.0	21.0
9.3	c	29.0	c	1.0	31.4	c	2.6	26.7
20% CW Type 316 Aged 10,000 h at 650°C (Matrix)								
8.0	c	24.7	2.2	c	31.0	c	3.8	30.3
5.6	c	25.5	1.7	c	24.4	c	25.0	17,8
8.8	c	23.6	2.8	c	31.8	c	3.3	29.7
4.6	c	15.0	2.5	6.4	41.5	c	9.4	20.6
7.0	c	15.3	2.8	0.7	35.7	1.0	7.0	30.6
20% CW Type 316, EBR-II Irradiated at 500°C to 9 dpa (Matrix)								
4.7	c	18.0	0.5	0.2	42.5	1.0	11.2	22.0
4.8	c	13.0	c	c	52.8	0.6	6.2	22.6
4.0	0.4	13.8	0.6	c	47.2	2.0	15.0	17.0
4.6	1.0	15.7	0.6	c	42.6	2.0	14.5	19.0
5.5	0.8	14.7	0.8	0.8	39.5	2.0	14.7	21.2
20% CW Type 316, HFIR Irradiated at 380°C to 49 dpa (Matrix)								
9.5	c	8.0	c	1.5	35.4	0.8	16.8	28.0
8.0	c	6.0	c	1.2	38.0	0.2	18.0	28.6
6.7	c	9.0	c	2.0	40.0	0.7	13.7	28.0
9.0	c	7.6	c	1.4	37.0	0.5	15.5	30.0
20% CW Type 316, HFIR Irradiated at 460°C to 54 dpa (Matrix)								
2.3	c	7.4	c	3.1	33.7	0.4	22.0	31. I

[a] Column-in headings are aging or irradiation conditions. Terms in parentheses indicate locations of analyzed precipitate particles. SA = solution annealed; CW = cold worked.

[b] Normalized weight percent.

[c] Not detectable.

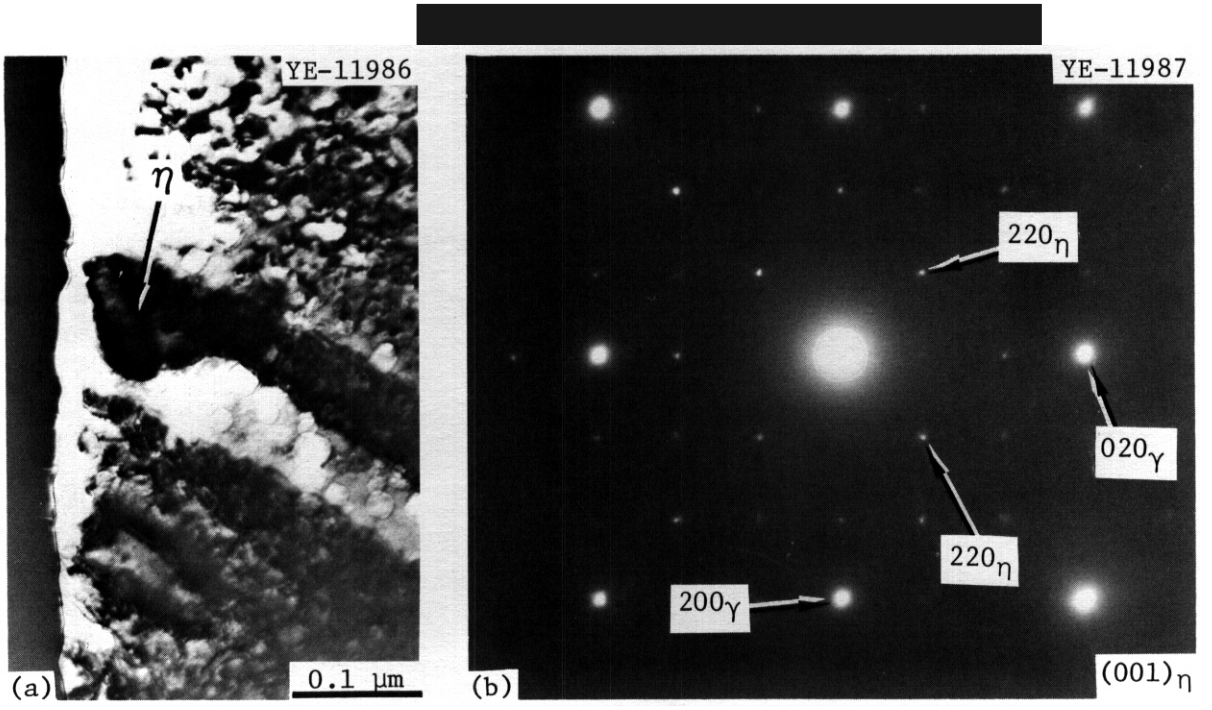

Fig. 3.4.9. Selected Area Diffraction (SAD) Identification of Eta Phase Produced in 20%-Cold-Worked Type 316 Irradiated in the HFIR to 48 dpa at 380°C. (a) Bright field image of eta particle in austenite matrix. (b) SAD on (001) zone axis.

shows little or no systematic temperature dependence and no significant difference between solution-annealed and cold-worked conditions for type 316. The composition of eta agrees well with similar measurements made on eta in other thermally aged steels.[34,35,37] The composition of eta produced thermally in CW 316 + Ti is perturbed to much higher Mo and Ti concentrations and lower Cr and Ni concentrations[29] compared with CW 316.

Table 3.4.6 also shows the composition of eta phase produced during either EBR-II or HFIR irradiation of type 316, and characteristic spectra are shown in Fig. 3.4.10. The eta phase produced by EBR-II irradiation is quite similar to the averaged thermally produced eta phase composition. This trend has been noted previously[11,39] and is supported by a much larger base of EBR-II data presented by Lee et al.[23] Several EBR-II-produced particles show detectable P, which is undetected in the thermal phase particles. Eta phase produced by HFIR irradiation of CW 316 is also similar to thermally produced eta but is systematically much lower in

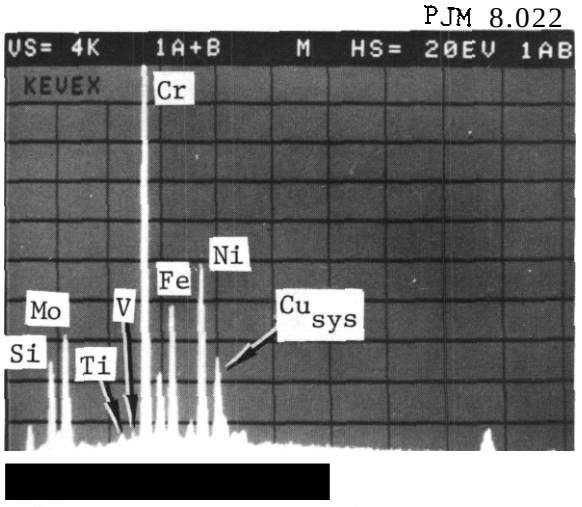

Content (wt %)

Si – 5.5
Mo – 14.5
Ti – 1.0
V – 1.0
Cr – 40.0
Mn – 2.0
Fe – 15.0
Ni – 21.0

(a)

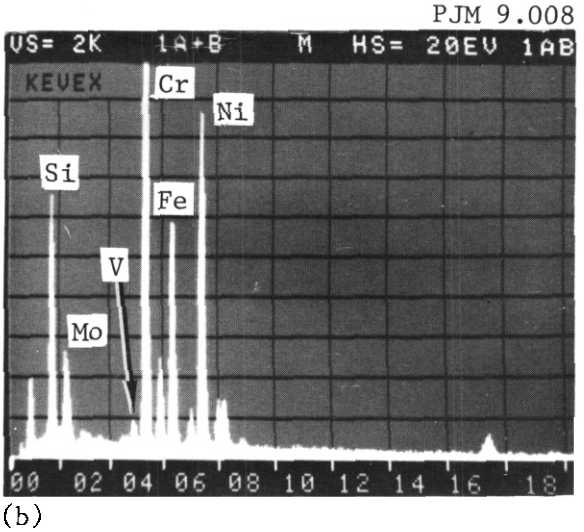

Content (wt %)

Si – 9.5
Mo – 8.0
V – 1.5
Cr – 35.5
Mn – 1.0
Fe – 16.5
Ni – 28.0

(b)

Fig. 3.4.10. Characteristic X-Ray Energy Dispersive Spectroscopy Spectra of Extracted Eta Phase Particles Produced by (a) EBR-II Irradiation of 20%-Cold-Worked Type 316 to 8.4 dpa at 500°C and by (b) HFIR Irradiation of 20%-Cold-Worked Type 316 to 48 dpa at 380°C. The quantitative chemical analyses are also shown, Cu_{sys} indicates copper detected in the microscope and not from specimen.

Mo and higher in Ni and/or Si concentrations (Figs. 3.4.7 and 3.4.10). Eta phase produced in the HFIR also shows a more regular enrichment of V than does thermal eta.

3.4.5.3 Laves Phase

Laves phase has a hexagonal crystal structure with lattice parameters a_0 = 0.47 nm and c_0 = 0.77 nm (a nearly ideal *c-to-a* ratio of 1.64), as shown in Table 3.4.3. Laves phase appears to have a small but negative volume misfit with respect to untransformed austenite. Laves forms in SA 316 aged at 650°C and above and in CW 316 aged at 600°C and above, consistent with the observations of others.[26-28] Laves has two basic morphological variants. One variant has a blocky shape, while the other has a long, narrow lath shape. Both are shown in Fig. 3.4.11. The individual particles appear to be made up of many thin crystallites joined by internal faults, similar to the internal twins in martensite plates. These can be seen inside the particles shown in Fig. 3.4.11(c) and appear to be responsible for the thin particle streaking of the Laves reflections in reciprocal space, as observed in SAD, because the particles themselves are not that thin.

The two morphological variants of Laves phase correlate quite well with two general, inexact crystallographic habit relationships that have many variations themselves. These are summarized stereographically in Figs. 3.4.12 and 3.4.13 for the lath and blocky morphological variants, respectively. Laves phase was observed in SA 316 and CW 316 to differ systematically. In SA 316 the Laves lath variant correlates with a crystallographic habit that generally has the basal (00.1) plane of Laves located near a (123) type plane of the austenite [Figs. 3.4.12(a)]. Obviously this relationship can have many permutations. The blocky variant correlates with a habit relationship that has (00.1) Laves coincident with a (113) type plane in the austenite and (11.0) Laves coincident with (110) austenite. This results in better overall plane matching for the two phases [Fig. 3.4.13(a)]. Figure 3.4.11(c) shows many of the Laves particles to be clustered about tau phase particles.

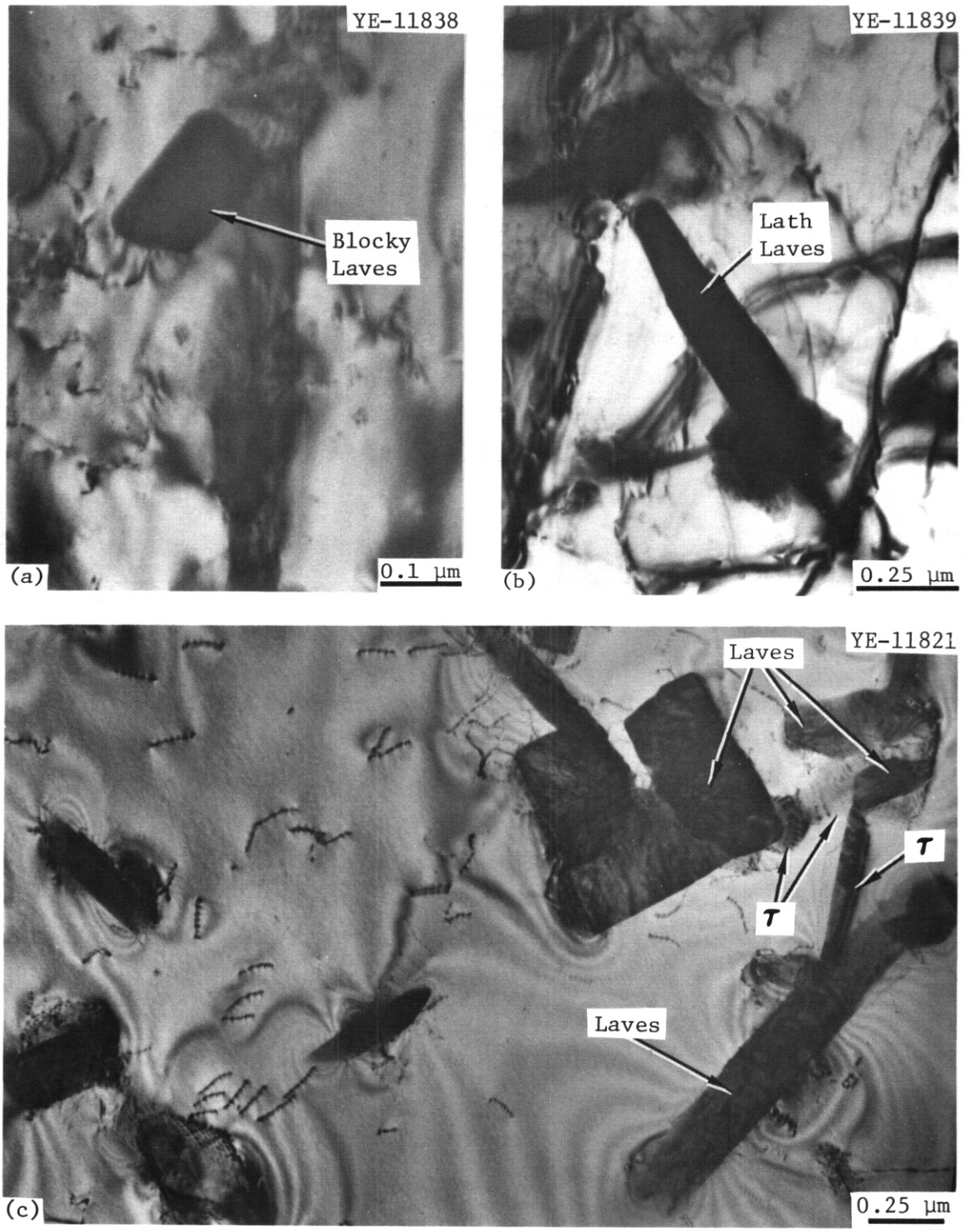

Fig. 3.4.11. The Basic Laves Phase Morphologies in Thermally Aged Type 316. (a) The blocky morphological variant of Laves in 20%-cold-worked type 316 aged 10,000 h at 600°C. (b) The lath morphological variant of Laves in 20%-cold-worked type 316 aged 10,000 h at 650°C. (c) Laves phase particles nucleated sympathetically on intragranular tau in solution-annealed type 316 aged 10,000 h at 650°C.

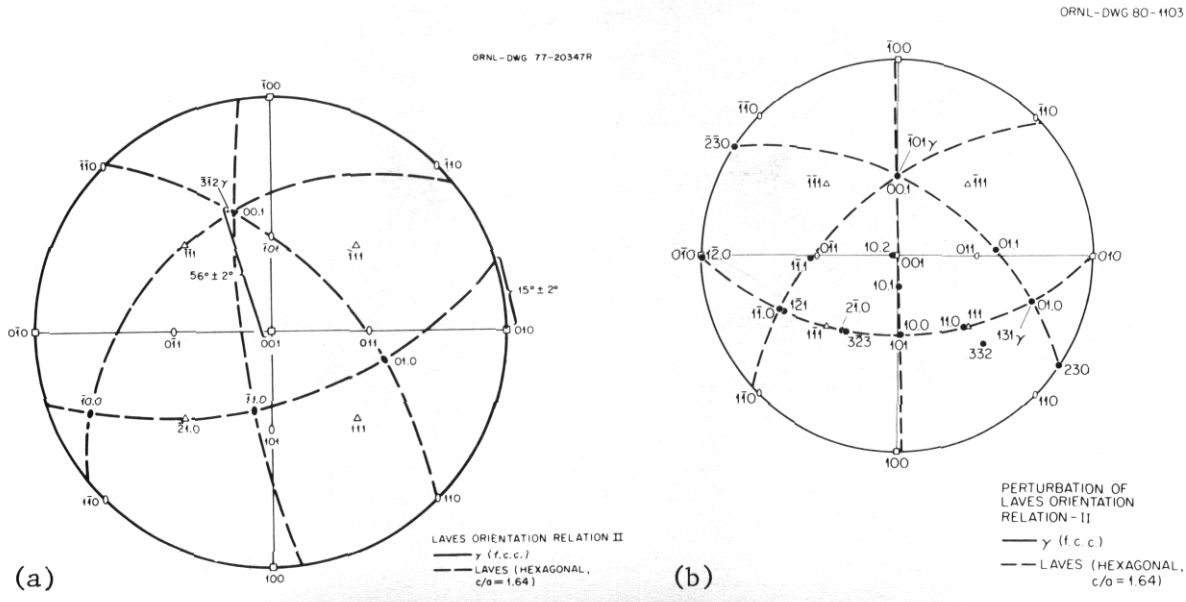

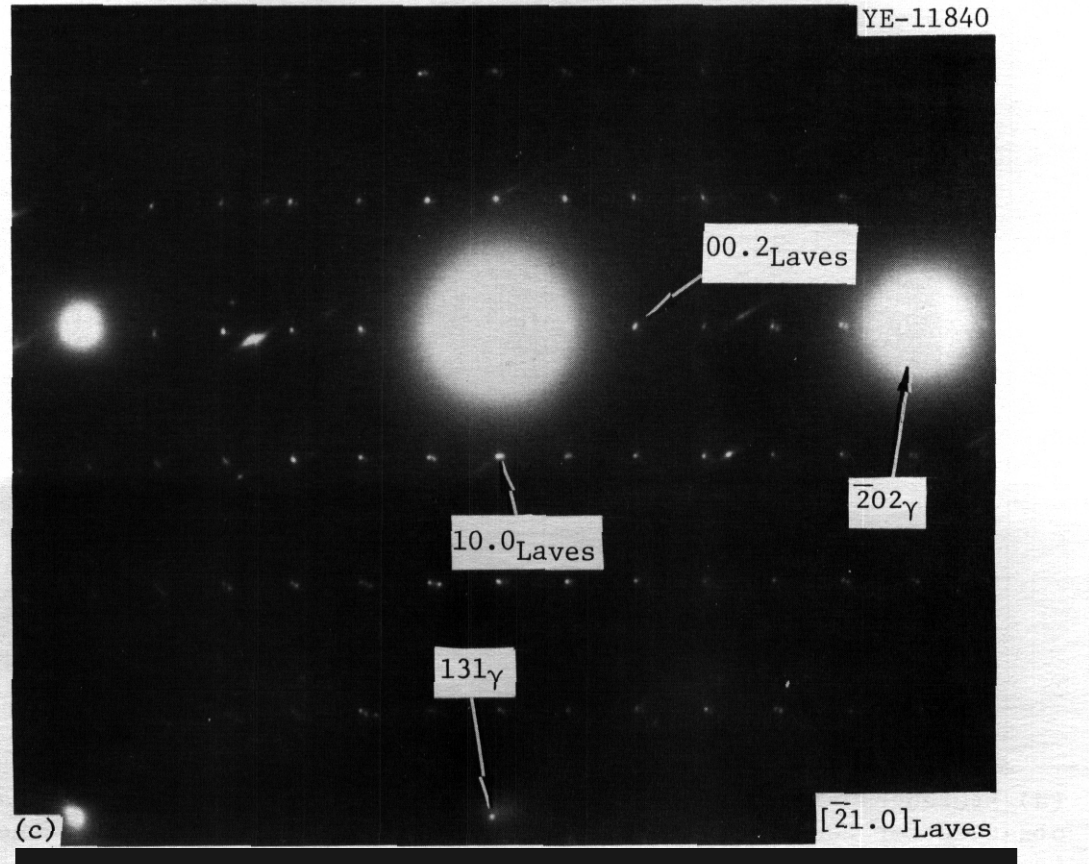

Fig. 3.4.12. Crystallography of the Lath-Shaped Laves Phase. (a) Stereographic representation of the general crystallographic habit observed for the lath-shaped morphological variant of Laves phase produced in thermally aged solution-annealed type 316. (b) and (c) Stereographic representation and selected area diffraction evidence, respectively, of the perturbation of the crystallographic habit caused by formation of Laves laths in 20%-cold-worked type 316.

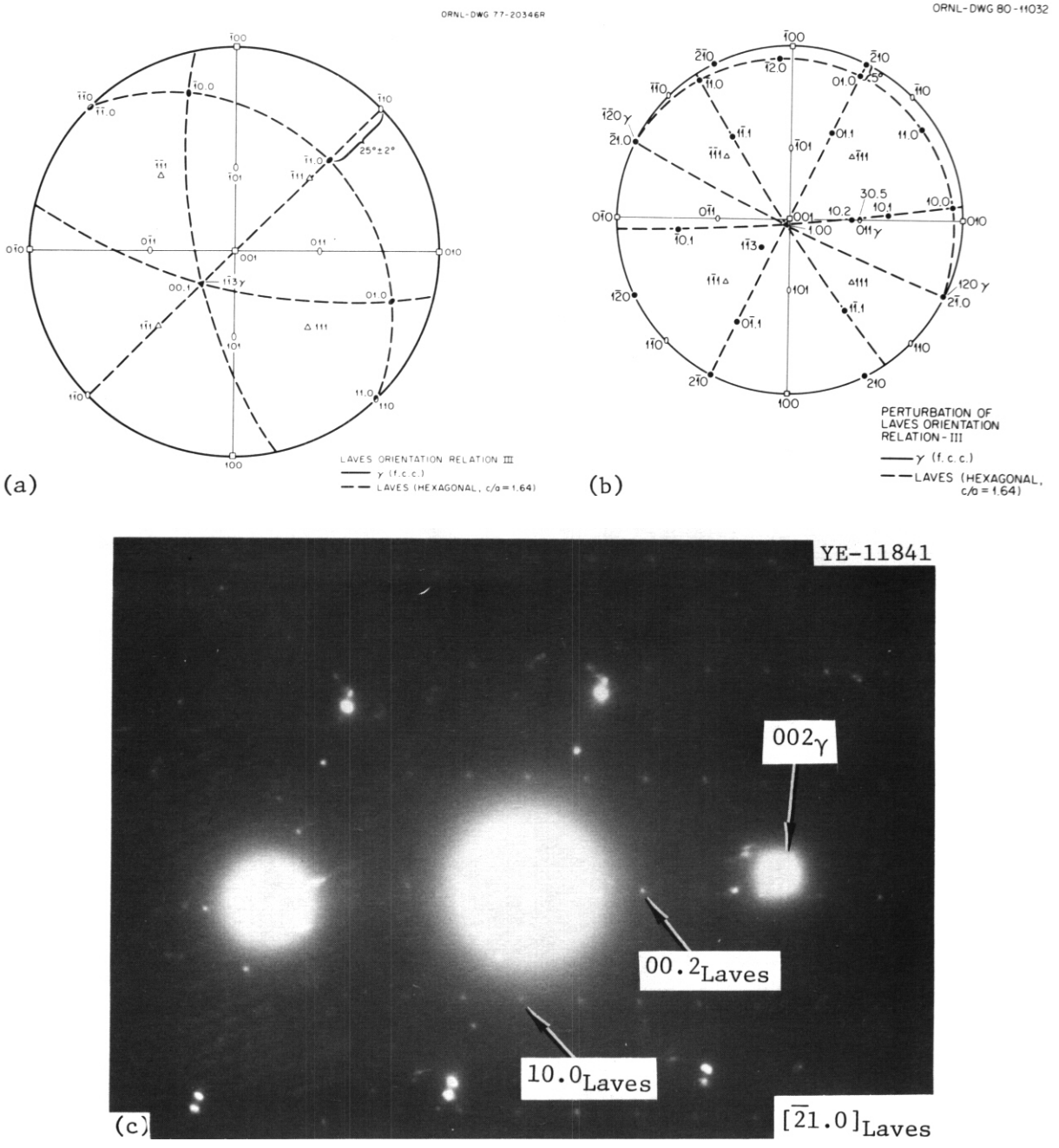

Fig. 3.4.13. Crystallography of the Blocky Variation of Laves Phase. (a) Stereographic representation of the general crystallographic habit observed for the blocky morphological variant of Laves produced thermally in solution-annealed type 316. (b) and (c) Stereographic representation and selected area diffraction evidence, respectively, of the perturbation of the crystallographic habit caused by formation of blocky Laves phase in 20%-cold-worked type 316.

The tau-austenite interface may influence the habit relationship for Laves sympathetically nucleated in SA 316. Figures 3.4.12(b) and 3.4.13(b) show the habit relations for both morphological variants of Laves formed in CW 316. These stereograms show better plane matching between the Laves phase and the austenite matrix in the cold-worked material than in the solution-annealed case. This would certainly correlate with the easier nucleation and hence enhancement of Laves phase in CW 316 compared with Laves in SA 316.

The amount of intragranular Laves appears reduced during thermal aging for SA 316 + Ti or CW 316 + Ti compared with type 316, but the reduction is not nearly as much as for tau or eta phases. Laves occurs at the grain boundaries of SA 316 + Ti, which is not an ordinary occurrence for Laves in type 316 (Fig. 3.4.14). Laves also forms in the 20%-cold-worked Path A PCA after thermal aging, but the amount seems considerably reduced compared with type 316.

Laves phase is generally enhanced by neutron irradiation in both types 316 and 316 + Ti. Laves appears at the same or slightly lower temperatures after EBR-II or HFIR irradiation of SA 316 compared with thermal aging. In CW 316 the irradiation temperatures at which Laves is formed in either reactor are definitely lower than the temperatures of formation during thermal aging. In both reactor environments the relative amounts of Laves phase in type 316 appear increased after irradiation compared with the amount after thermal aging. Laves phase produced by HFIR irradiation in type 316 + Ti appears at the same temperature as in HFIR-irradiated type 316. However, the relative amounts appear to vary. For instance, more Laves appears to be produced[8,10] in SA 316 + Ti than in SA 316 at 575 to 600°C, but slightly less appears to be produced[29] in CW 316 + Ti than in CW 316 irradiated at 470°C.

The x-ray EDS compositional measurements for extracted Laves particles are given in Table 3.4.7, and a characteristic x-ray EDS spectrum for thermally formed Laves is shown in Fig. 3.4.15. Compared with the unprecipitated matrix (Table 3.4.4), thermal Laves is considerably enriched in Si and Mo. The Cr and Mn occur at about the same level as in the matrix, and Laves is depleted of Fe and Ni. Laves contains

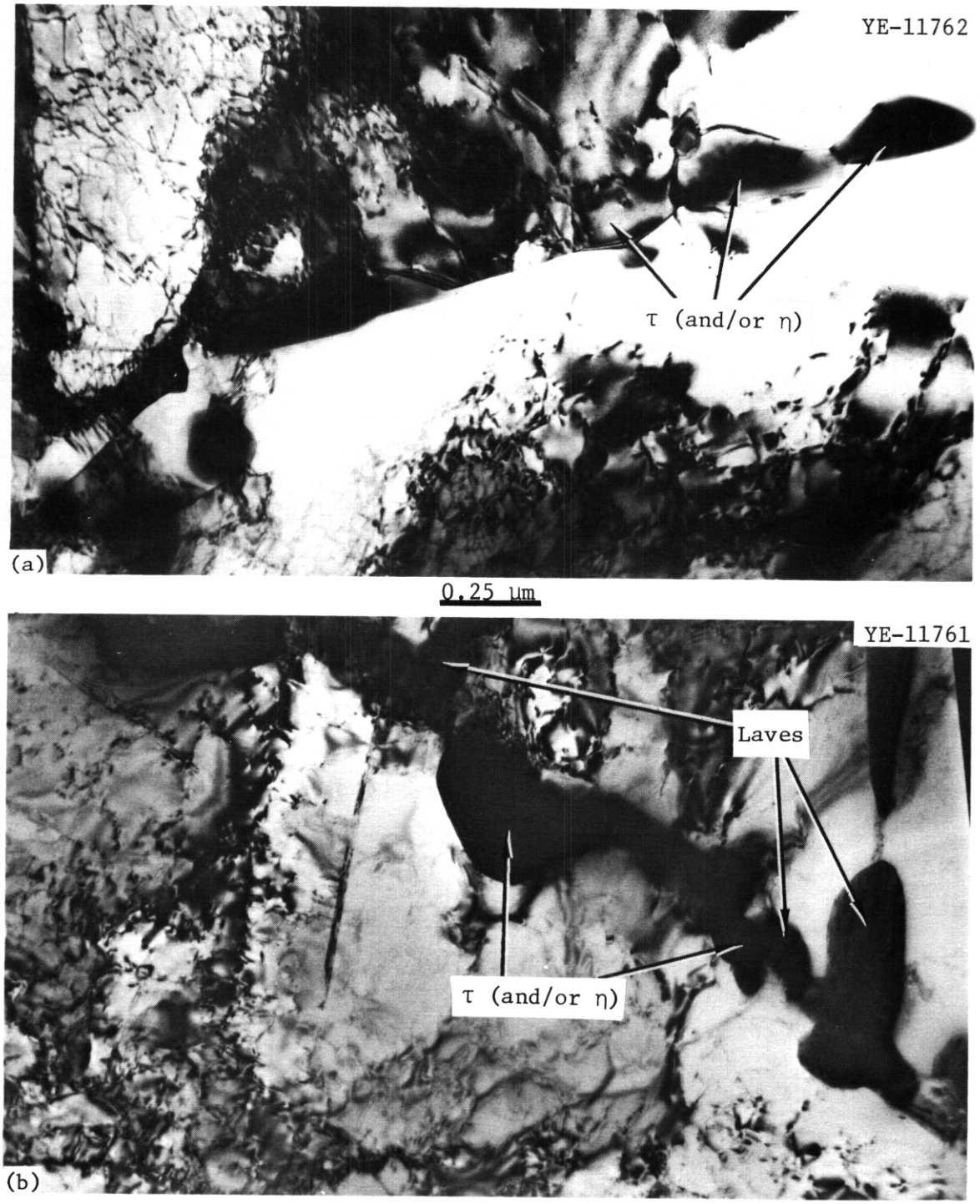

Fig. 3.4.14. Typical Grain Boundary Precipitation Produced by Thermal Aging at 700°C for 2770 h of (a) 20%-Cold-Worked Type 316 and (b) 20%-Cold-Worked Type 316 + Ti. The basic difference is the formation of Laves phase at the grain boundaries in the type 316 + Ti in addition to the tau and/or eta found at grain boundaries of both steels.

Table 3.4.7. X-Ray Energy Dispersive Spectroscopy Compositional Information[a] from Laves Phase Produced by Either Thermal Aging or Neutron Irradiation

Content, wt %							
Si	Mo	Ti	V	Cr	Mn	Fe	Ni
SA Type 316 Aged 10,000 h at 650°C (Matrix)							
5.0	43.6		c	13.2	0.5	32.7	5.0
5.0	42.7	c	c	12.2	1.0	34.3	4.8
4.7	46.2	c	c	10.4	c	34.3	4.4[a]
20% CW Type 316 Aged 10,000 h at 600°C (Matrix)							
3.6	39.0	c	c	15.0	0.3	35.5	6.5
1.3	40.3	c	c	13.6	0.5	37.0	7.3
4.6	39.2	c	c	14.2	2.0	34.0	6.0
6.4	38.4	c	c	14.2	1.2	33.3	6.7
4.6	40.2	c	c	14.6	1.4	32.3	7.0
4.6	39.0	c	c	14.7	1.3	34.0	6.5
20% CW Type 316 Aged 10,000 h at 650°C (Matrix)							
4.5	47.0	c	0.2	11.7	0.5	31.6	4.5
7.4	69.0	c	c	3.8	c	17.0	2.8[d]
3.5	38.7	c	1.0	15.7	1.7	34.0	5.4[d]
3.2	39.0	c	1.0	13.0	1.7	36.0	6.0[d]
4.0	43.0	c	0.5	13.0	1.4	33.0	5.0[d]
SA Type 316, HFIR Irradiated at 550°C to 42 dpa (Matrix)							
4.8	42.4	c	1.0	13.5	0.4	30.6	7.3
20% CW Type 316, HFIR Irradiated at 460°C to 54 dpa (Matrix)							
3.8	19.0	22	0.7	21.7	1.0	31.0	20.5
1.6	13.0	27	0.7	26.0	1.0	32.2	22.8
SA Type 316 + Ti, HFIR Irradiated at 600°C to 30 dpa (Matrix)							
4.0	33.3	2.0	1.7	17.0	0.6	34.4	7.0
5.0	31.0	1.5	1.5	15.3	0.3	35.3	10.0
3.6	30.0	0.6	1.0	16.0	0.1	40.0	8.4
4.4	31.4	1.0	1.0	16.6	1.0	36.0	8.4

%ut-in headings are aging or irradiation conditions. Terms in parentheses indicate locations of analyzed precipitate particles. SA = solution annealed; CW = cold worked.

[b] Normalized weight percent.

[c] Not detectable.

[d] Blocky shaped morphological variant of Laves phase. All other particles are the lath-shaped morphological variant of Laves phase.

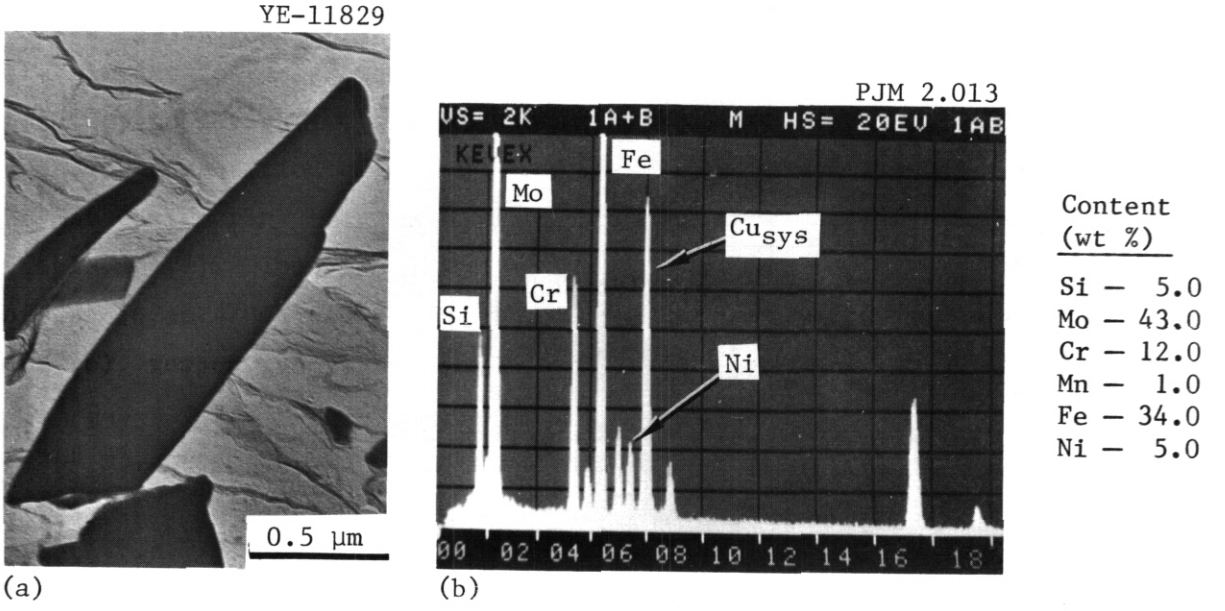

Fig. 3.4.15. Characteristic X-Ray Energy Dispersive Spectroscopy (EDS) Spectrum of Laves Phase Extracted from Solution-Annealed Type 316 Aged 10,000 at 650°C and Analyzed Quantitatively. (a) Bright field image of extracted precipitate particle. (b) EDS spectrum and composition information.

detectable V only in CW 316 at 650°C. An average Laves composition in weight percent is 4.5 Si—43 Mo—13 Cr—1 Mn—33 Fe—5.5 Ni. Laves has much more Mo and more Fe than either eta or tau. It also has less Cr than either. The individual particle compositions in Table 3.4.7 are quite close to average composition and do not show significant temperature, morphology, or pretreatment dependence. These measurements agree well with measurements by others[27,35] on Laves composition in different heats of type 316. The compositional measurements for Laves in aged CW 316 + Ti are similar to these except that they show a more systematic enrichment of Ti up to several weight percent.[29]

The composition of Laves phase produced in SA 316 or CW 316 and SA 316 + Ti during HFIR irradiation is similar to that produced thermally (Table 3.4.7). The x-ray spectra of Laves produced during HFIR irradiation of CW 316 at 470°C and SA 316 + Ti at 600°C are compared in Fig. 3.4.16(a) and (b), respectively. The Laves produced during irradiation at 470°C in

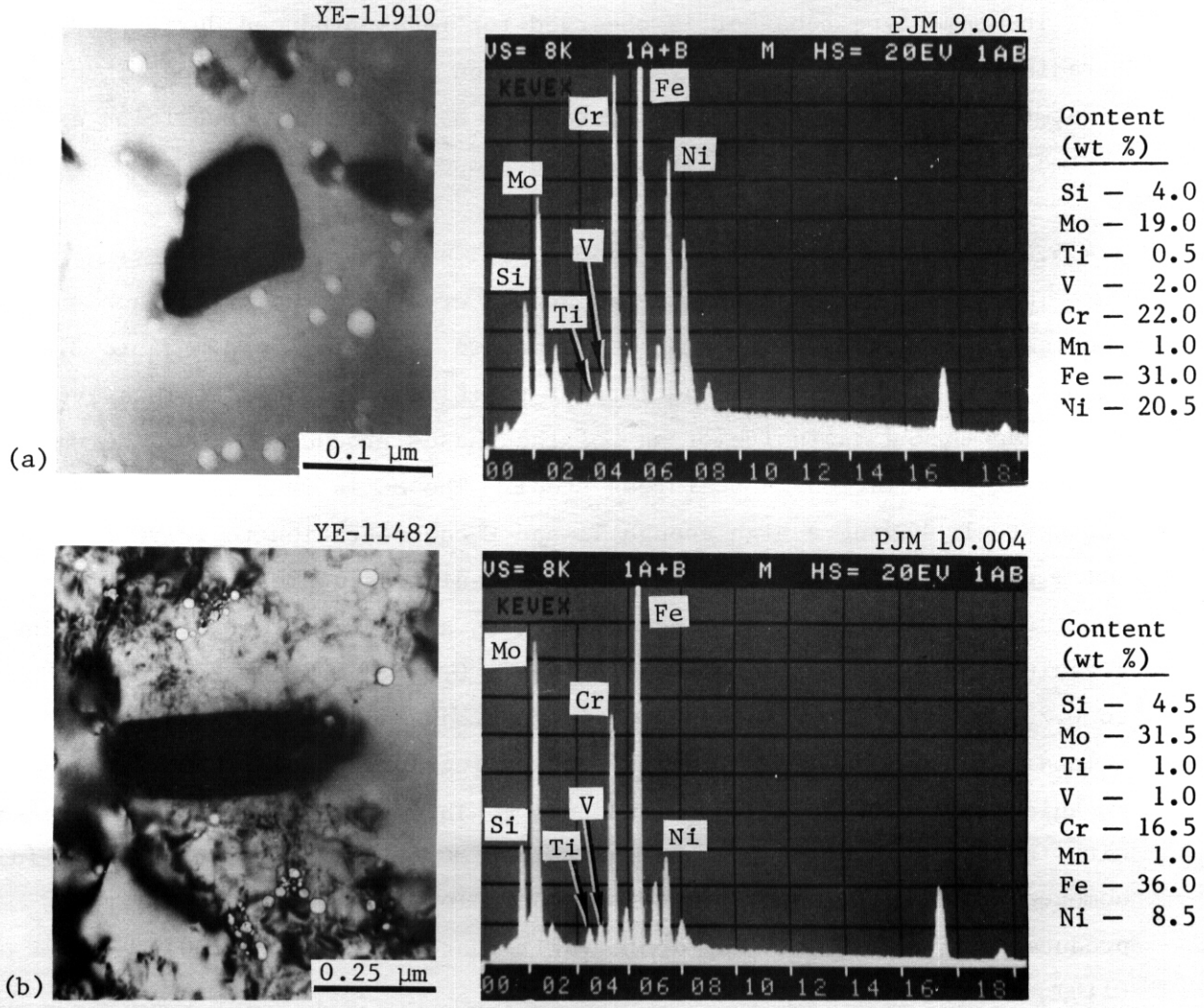

Fig. 3.4.16. Bright Field Images and Characteristic X-Ray Energy Dispersive Spectroscopy Spectra of Laves Phase Extracted from (a) 20%-Cold-Worked Type 316 Irradiated in the HFIR at 460°C to 54 dpa and (b) Solution-Annealed Type 316 + Ti Irradiated in the HFIR at 600°C to 30 dpa and Analyzed Quantitatively.

CW 316 is much lower in Mo and higher in Ni and Cr than thermally produced Laves (compare Figs. 3.4.15 and 3.4.16). It also has a consistently higher (Ti + V) level. However, Laves produced in either SA 316 or SA 316 + Ti by irradiation at 550 to 650°C is very close to the thermally produced Laves composition.

The same type behavior is observed for Laves produced during EBR-II irradiation. That is, the Laves composition is lower in Mo and higher in Ni at the low irradiation temperatures and has the same composition as thermal Laves at the higher irradiation temperatures.[29]

3.4.5.4 Titanium-Rich MC Phase

The titanium-rich MC phase has an fcc crystal structure with a lattice parameter of about 0.43 nm, as shown in Table 3.4.3. Table 3.4.3 also indicates that MC has the largest positive volume misfit relative to untransformed austenite of any of the phases produced either thermally or during irradiation in stainless steel. The MC is observed only in those steels having a high enough Ti and C concentration to drive the $xTi + C \rightarrow Ti_xC$ reaction forward. For austenitic stainless steels with about 0.05 wt % C, this Ti concentration is about 0.15 to 0.35 wt %. The titanium-modified steels in this work have 0.05 to 0.06 wt % C and 0.20 to 0.25 wt % Ti. The MC phase particles produced during thermal aging maintain an exclusive cube-on-cube crystallographic habit relationship at aging temperatures of 850°C and below. This habit is always associated with the equiaxed morphological variant of MC (Fig. 3.4.17). At 900°C in homogeneous Path A PCA, a rod-shaped morphological variant of MC is produced[40] with a crystallographic habit that has $(332)_\gamma \parallel (001)_{MC}$ and $(1\bar{1}0)_\gamma \parallel (1\bar{1}0)_{MC}$, as shown in Fig. 3.4.18.

In thermally aged SA 316 + Ti, MC is the predominant intragranular phase at 560°C and above. Intragranular MC is always observed at dislocations, and both the size and spatial distribution for cold-worked material are much refined compared with solution-annealed material (Fig. 3.4.17). The MC precipitates together with tau, Laves, and eta at the grain boundaries in SA 316 + Ti or CW 316 + Ti. However, in Path A PCA, MC becomes the dominant grain boundary phase, occurring with occasional Laves phase particles (compare Figs. 3.4.14 and 3.4.19).

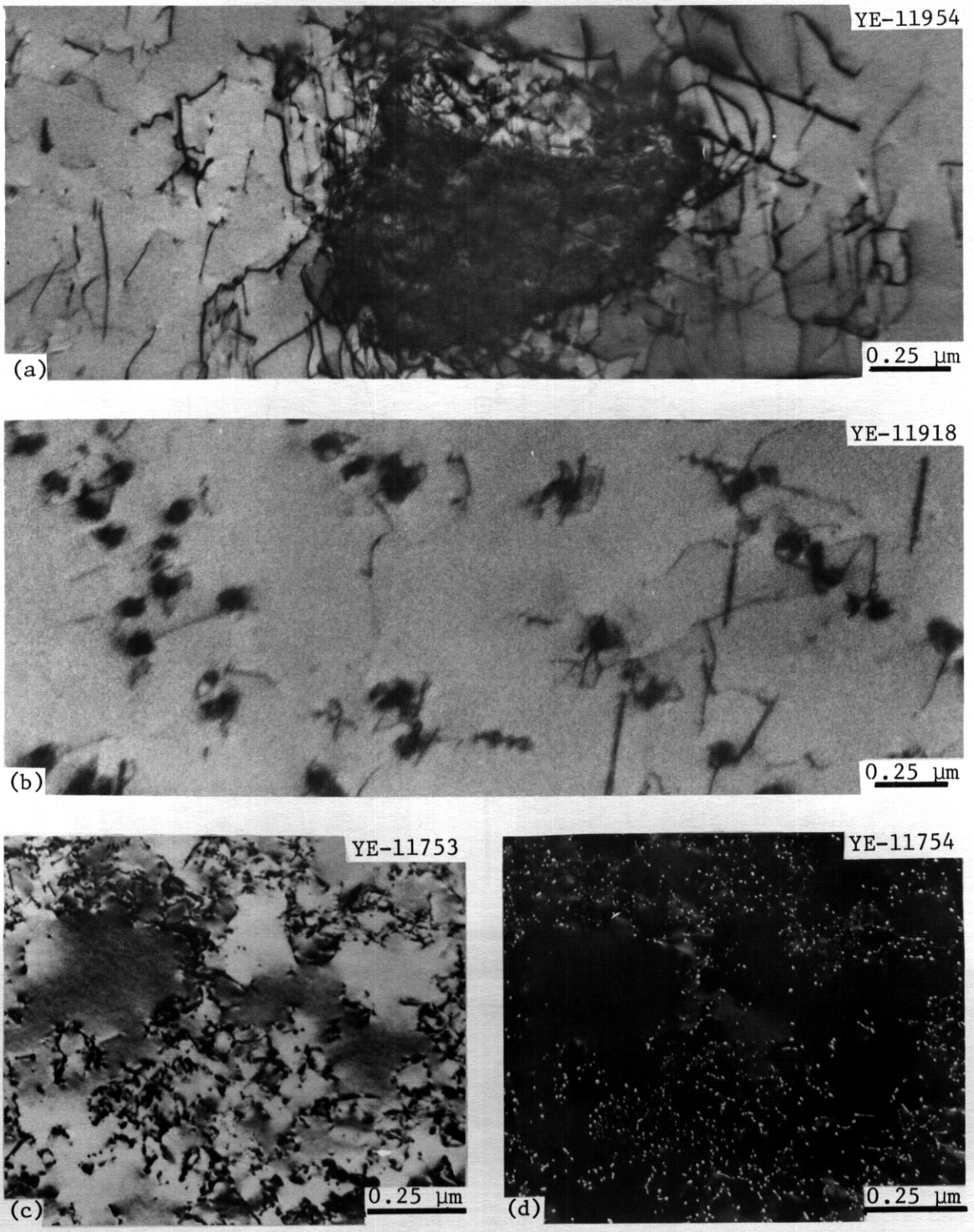

Fig. 3.4.17. The Variation in Size and Distribution of the Cube-on-Cube Variant of MC That Can Be Produced Thermally in Titanium-Modified Material. (a) Large particle in solution-annealed Path A PCA aged 24 h at 900°C. (b) Smaller particles produced in solution-annealed type 316 + Ti aged 2770 h at 700°C. (c) and (d) Bright field and centered dark field images, respectively, of very fine particles on the dislocation network in cold-worked Path A PCA aged 0.5 h at 750°C.

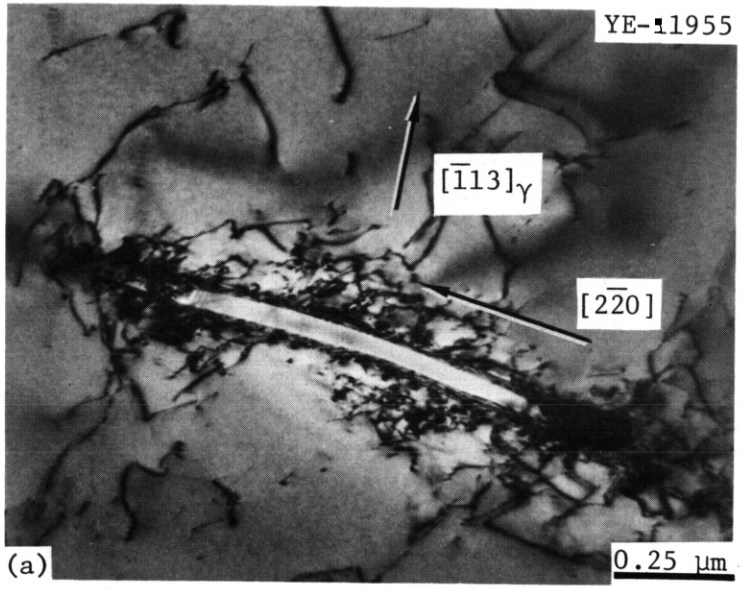

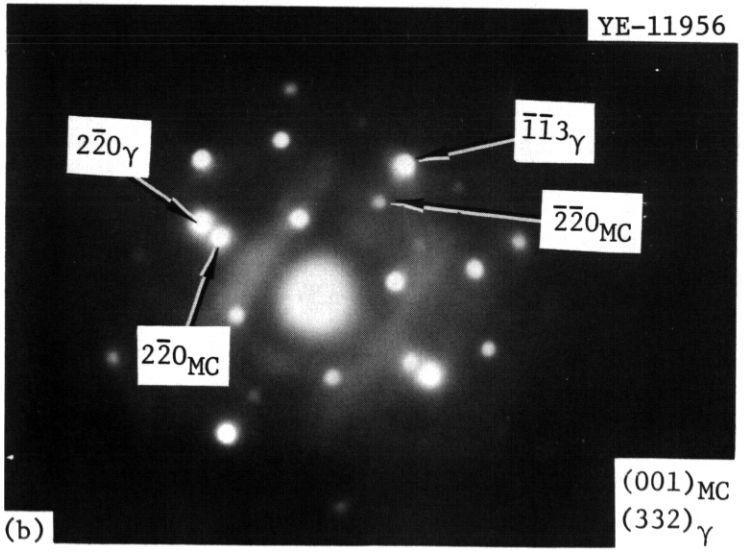

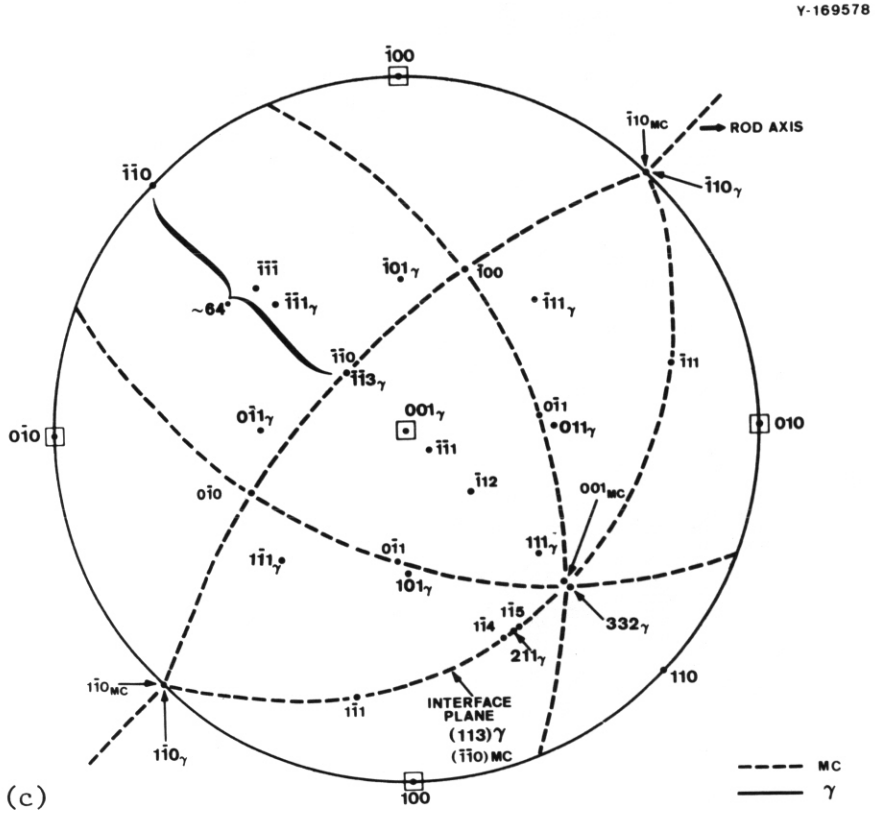

Fig. 3.4.18. (a) Bright Field Image of the Rod-Shaped Morphological Variant of MC Produced in Solution-Annealed Path A PCA Aged 24 h at 900°C. (b) and (c) Selected area diffraction and stereographic representation, respectively, of the crystallographic habit relationship for the rod variant of MC.

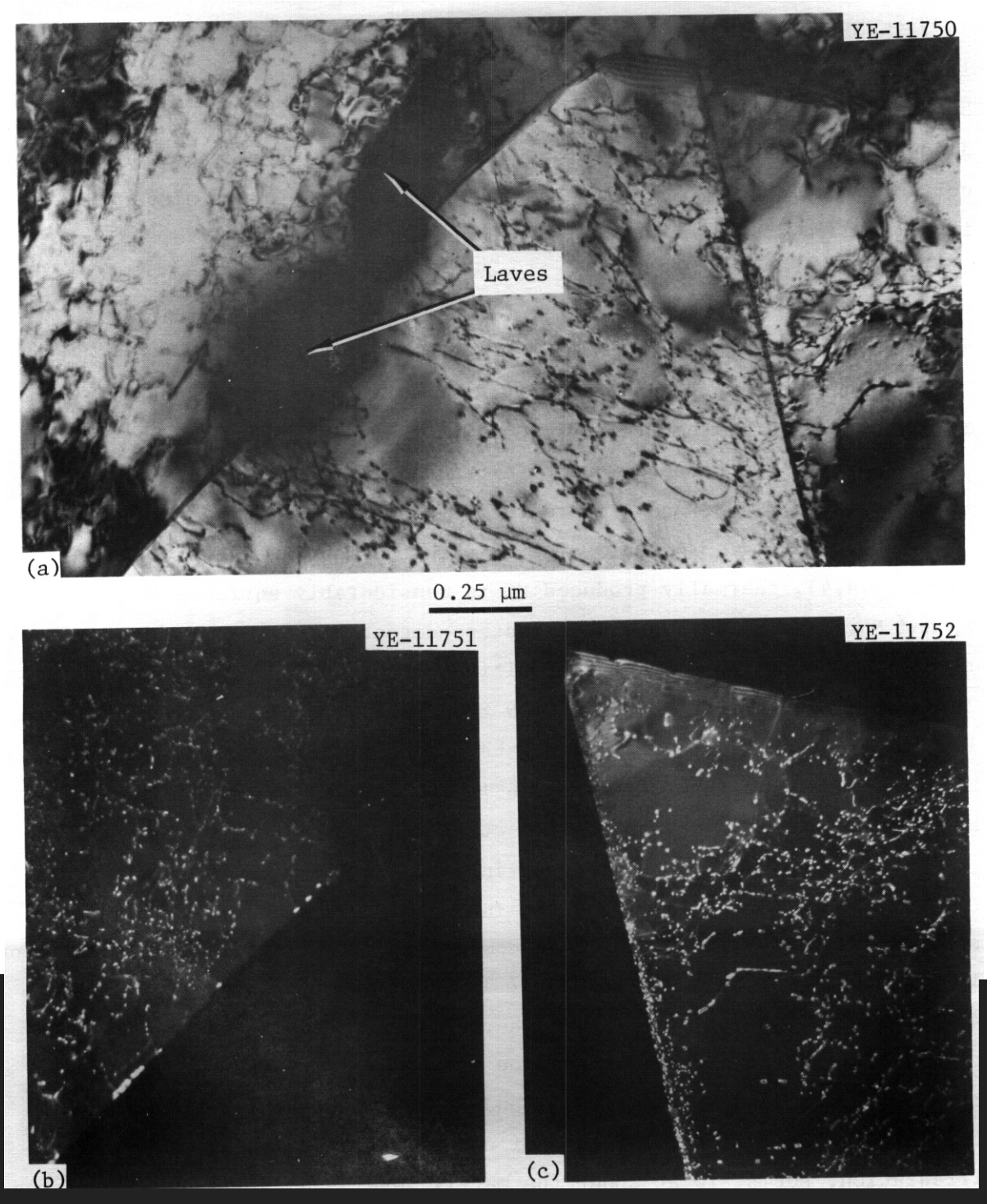

Fig. 3.4.19. Grain Boundary Precipitation of MC in 25%-Cold-Worked Path A PCA Aged 166 h at 750°C. (a) Bright field image showing grain boundary and occasional Laves particle. (b) and (c) Centered dark field

The MC phase formation appears considerably enhanced by HFIR irradiation in CW 316 + Ti. No MC is observed in material thermally aged below 560°C, but MC clearly forms at 280°C and above[29] in the HFIR, as discussed in Chapter 3.3 of this quarterly report. By comparison, MC does not form[23] below 500°C in titanium-modified austenitic stainless steels irradiated in EBR-II. The MC is observed in SA 316 + Ti after HFIR irradiation at 600 to 680°C, but lower irradiation temperatures have not yet been examined. At least in SA 316 + Ti, the rod-shaped variant appears to be the dominant form of MC after irradiation.[8,10] In general, the amount of precipitation after HFIR irradiation appears about the same or slightly greater than that produced by thermal aging.

The x-ray EDS compositions of extracted MC phase particles are given in Table 3.4.8, and a characteristic spectrum for thermally produced MC is shown in Fig. 3.4.20. Compared with the matrix of type 316 + Ti (Table 3.4.4), thermally produced MC is considerably enriched in Mo, Ti, V, and Nb. The phase contains almost no detectable Si, Ni, or Mn and very little Fe or Cr. An average composition of the MC in weight percent is 20 Mo—66 Ti—2.5 V—1 Cr—1 Fe—0.5 Ni—9 Nb. For the same condition (1 h at 1050°C), MC produced thermally in Path A PCA is about 10 wt % higher in Mo and lower in Ti than MC in SA 316 + Ti. It also contains slightly higher levels of Cr, Mn, and Fe but still very little or no Si and Ni.

The composition of MC produced in SA 316 + Ti by HFIR irradiation at 600°C to about 30 dpa is also given in Table 3.4.8, and a spectrum is shown in Fig. 3.4.21. The average composition of MC after HFIR irradiation in weight percent is 0.4 Si—38 Mo—37 Ti—6.5 V—5.5 Cr—7.5 Fe—3 Ni—1.6 Nb. Although qualitatively similar to thermally produced MC, the composition of the MC produced during irradiation unmistakably tends toward having more Mo, V, Cr, and Fe and less Ti and Nb as compared with that produced thermally. The detectable Si and Ni concentrations also increase after irradiation, but Si is at about the matrix level, and Ni is still depleted relative to the matrix. Further work on longer time thermal aging of SA 316 + Ti or Path A PCA indicates that the MC composition generally progresses toward a lower Ti level and higher levels of Mo, Cr, and Fe as the precipitation process continues.[38,40]

Table 3.4.8. X-Ray Energy Dispersive Spectroscopy Compositional Information[a] from MC Phase Produced Either by Thermal Aging or Neutron Irradiation

Content,[b] wt %								
Si	Mo	Ti	V	Cr	Mn	Fe	Ni	Nb
SA Type 316 + Ti Aged 1 h at 1050°C (Matrix)								
c	16.1	69.2	2.8	0.4	c	1.2	c	10.3
c	22.0	66.0	1.3	0.8	c	c	c	9.4
c	23.5	62.0	3.3	1.5	c	1.6	0.8	7.3
c	17.3	68.6	2.0	1.0	c	1.8	0.5	8.8
Path A PCA Aged 1 h at 1050°C (Matrix)								
c	37.4	49.0	2.6	1.0	1.3	7.7	1.0	c
c	28.6	54.6	3.7	3.0	2.4	7.0	0.7	c
c	24.2	61.0	4.6	2.3	1.5	5.6	0.8	c
c	32.8	46.3	2.0	6.5	c	5.5	1.4	5.4
SA Type 316 + Ti, HFIR Irradiated at 600°C to 30 dpa (Matrix)								
0.3	35.0	34.5	7.0	7.0	c	10.6	5.6	c, d
c	39.6	36.6	6.4	6.3	1.0	8.0	2.0	c, d
1.2	40.8	37.5	6.5	5.2	0.3	5.6	2.8	c, d
c	38.2	42.4	6.4	4.8	c	4.6	1.2	2.3[d]
c	44.4	30.0	7.0	5.4	c	9.5	3.7	c
0.5	36.5	30.0	7.3	6.5	c	9.9	5.5	3.8
0.6	33.3	46.0	5.3	3.4	c	4.6	1.3	5.5

[a] Cut-in headings are aging or irradiation conditions. Terms in parentheses indicate locations of analyzed precipitate particles. SA = solution annealed; PCA = Prime Candidate Alloy.

[b] Normalized weight percent.

[c] Not detectable.

[d] Rod-shaped morphological variant of MC. All other particles are equiaxed or rectangular-shaped morphological variants of MC that have an exclusive cube-on-cube crystallographic habit.

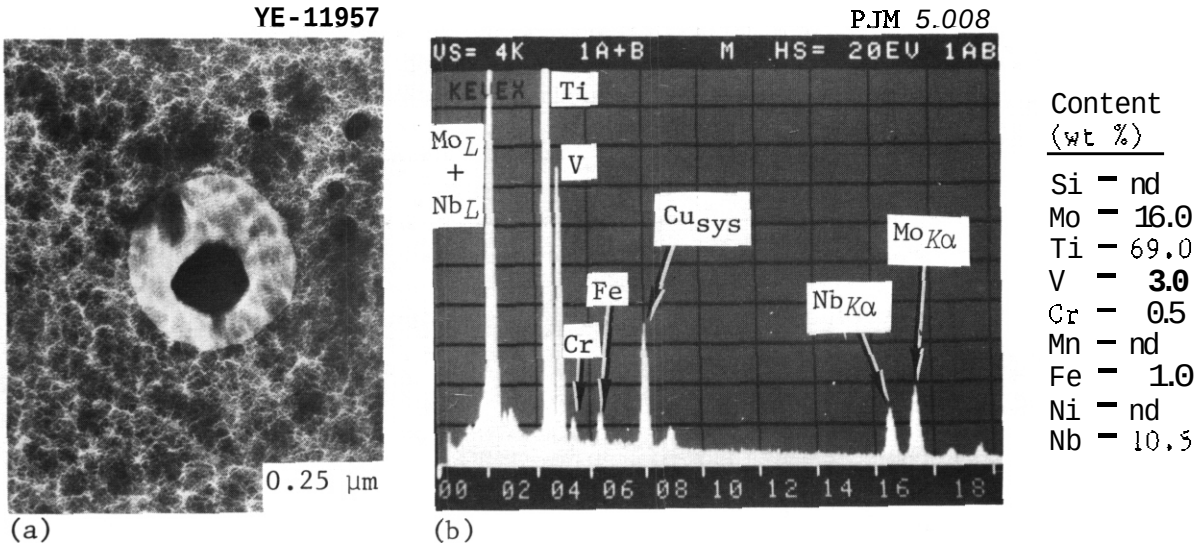

Fig. 3.4.20. Characteristic X-Ray Energy Dispersive Spectroscopy (EDS) Spectrum of Cube-on-Cube Variant of MC Extracted from Type 316 + Ti Solution Annealed for 1 h at 1050°C and Analyzed Quantitatively. (a) Bright field image of precipitate particle. (b) EDS spectrum and composition. nd = not detectable. Cu_{sys} indicates copper detected in the microscope and not from specimen.

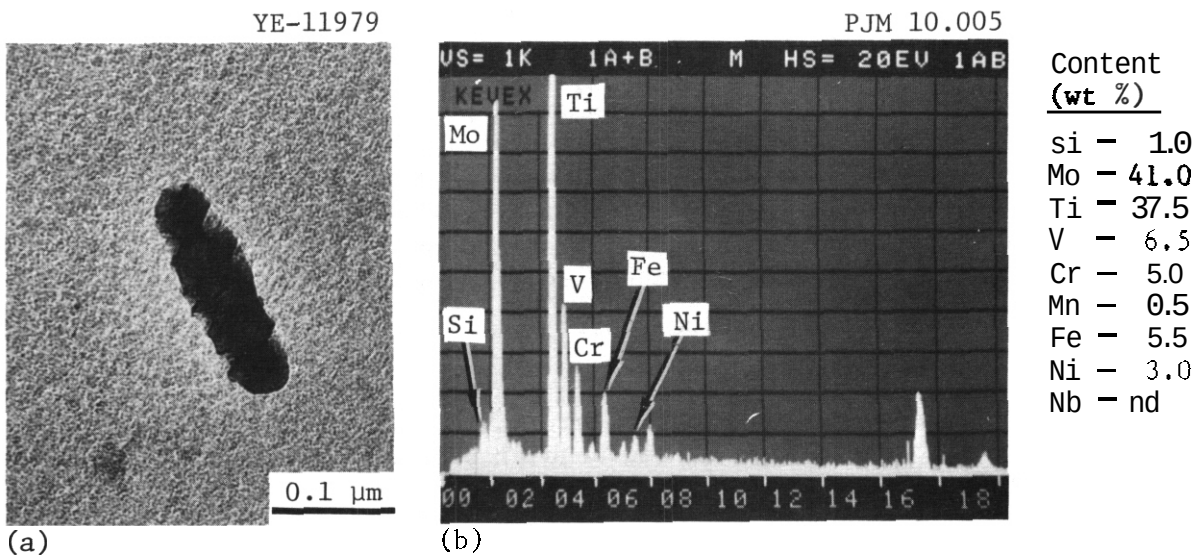

Fig. 3.4.21. Characteristic X-Ray Energy Dispersive Spectroscopy (EDS) Spectrum of Rod Variant of MC Extracted from Solution-Annealed Type 316 + Ti Irradiated in the HFIR at 600°C to a Fluence of 30 dpa and Analyzed Quantitatively. (a) Bright field image of precipitate particle. (b) EDS spectrum and composition. nd = not detectable.

3.4.5.5 Sigma, Chi and $Ti_4C_2S_2$ Phases

These phases are treated together because they generally occur as coarse particles and usually form at higher temperatures and/or longer times than the phases treated previously. Sigma (σ) and chi ($\times$) occur naturally from supersaturated solutions, whereas $Ti_4C_2S_2$ forms either near the solvus or in the melt. From Table 3.4.3, sigma has a tetragonal crystal structure with lattice parameters a_0 = 0.88 nm, c_0 = 0.46 nm, and c/a = 0.52 for the composition normally formed in steel.[27] Chi is body-centered cubic (bcc) with a_0 = 0.89 nm. The $Ti_4C_2S_2$ is a hexagonal phase with a_0 = 0.32 nm, c_0 = 1.12 nm, and c/a = 3.5. Sigma and chi have almost no volume misfit relative to untransformed austenite. The $Ti_4C_2S_2$ phase is found as an angular inclusion in titanium-modified austenites, very coarsely distributed and generally at grain boundaries.

Sigma phase is observed in SA 316 after thermal aging at 650 to 900°C but only after aging for several thousand hours, particularly at the lower temperatures. In solution-annealed material, sigma is confined to the grain boundaries. In CW 316 sigma is observed at 600°C (after 10,000 h) and above and occurs at intragranular deformation bands, at the interfaces between recrystallized and unrecrystallized material, and at grain boundaries. Sigma phase particles have a variety of morphologies that appear "glob-like" rather than sharply facetted. However, sigma does have several well-defined crystallographic habit relationships.[6,27,41] The most common has $(001)_\sigma \parallel (111)_\gamma$ with $(110)_\sigma \parallel (110)_\gamma$.

Chi phase is generally intragranular after aging at temperatures above 700 but below 900°C in either CW 316 or SA 316. It is not a dominant thermal phase in any of the materials observed in this work.

Sigma phase formation is somewhat slower for thermally aged SA 316 + Ti compared with SA 316 but appears enhanced in amount for CW 316 + Ti as compared with CW 316. In contrast, considerable enhancement of sigma phase in both SA 316 + Ti and CW 316 + Ti was found by Grot and Spruiell[30] in another heat of type 316 + Ti.

Irradiation of either types 316 or 316 + Ti generally results in lower temperatures of formation and enhanced amounts of sigma and chi.

Sigma appears after HFIR irradiation at 600°C and above in SA 316 and at 550°C and above in CW 316. The particles are very large (several micrometers) and generally form at grain boundaries. More sigma particles[29] are produced in CW 316 + Ti than in CW 316 during irradiation at 550°C. Chi phase is a dominant portion of the intragranular precipitation in both types 316 and 316 + Ti irradiated above 600 to 650°C.

The x-ray EDS composition of thermally produced sigma is given in Table 3.4.9, and a characteristic spectrum is shown in Fig. 3.4.22. An average composition in weight percent is 1.3 Si-6 Mo-36 Cr-1 Mn-50.7 Fe-5 Ni. The composition depends very little on either temperature or pretreatment microstructure. Other work[38] confirms this trend up to 850 to 900°C. Sigma formed in type 316 + Ti shows little difference from the average composition given above. These trends and compositions are in good

Table 3.4.9. X-Ray Energy Dispersive Spectroscopy Compositional Information[a] from Sigma and $Ti_4C_2S_2$ Produced Thermally

Content,[b] wt %									
S	Si	Mo	Ti	V	Cr	Mn	Fe	Ni	Nb
Sigma, SA Type 316 Aged 10,000 h at 650°C (Grain Boundary)									
C	1.3	7.0	C	C	35.1	0.6	50.4	5.0	C
C	1.3	5.8	C	C	35.2	1.0	51.4	5.3	C
20% CW Type 316 Aged 10,000 h at 600°C									
C	1.3	5.4	C	C	37.7	2.2	48.5	5.0	C
C	1.2	5.4	C	C	34.2	2.7	51.5	5.0	C
20% CW Type 316 Aged 10,000 h at 650°C									
C	1.5	6.7	C	C	34.8	C	51.7	5.3	C
C	1.4	6.0	C	C	37.2	C	50.4	4.8	C
$Ti_4C_2S_2$, SA Type 316 + Ti Aged 1 h at 1050°C									
18.7	C	1.4	54.6	2.0	4.5	0.4	15.0	2.4	1.0
25.5	C	2.0	65.0	3.5	0.4	C	1.4	C	2.2

%ut-in headings are aging conditions. Terms in parentheses indicate locations of analyzed precipitate particles. SA = solution annealed; CW = cold worked.

[b]Normalized weight percent.

[c]Not detectable.

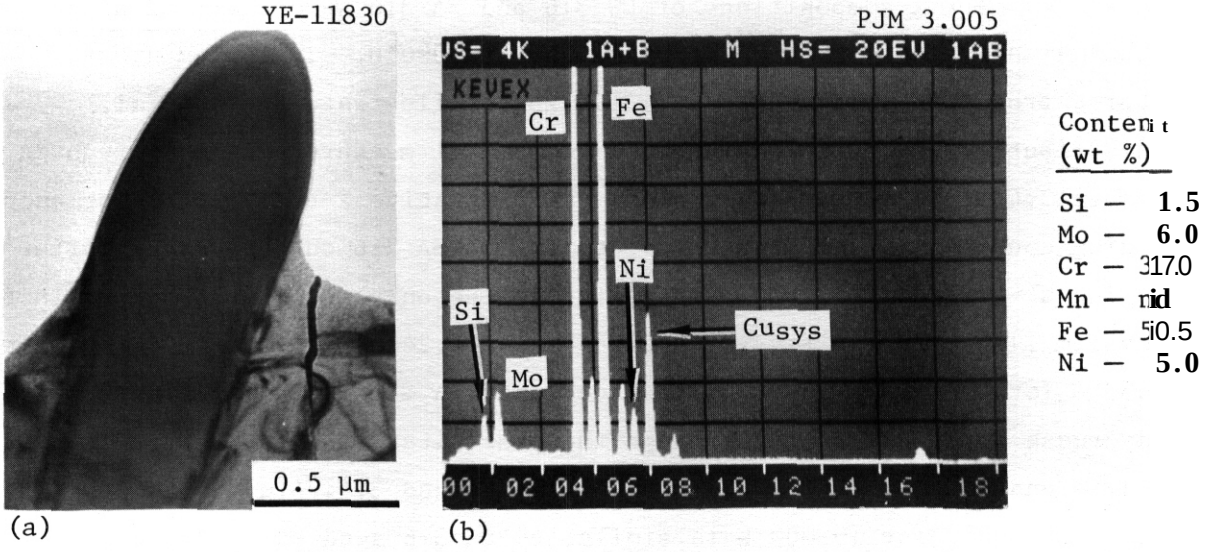

Fig. 3.4.22. Characteristic X-Ray Energy Dispersive Spectroscopy (EDS) Spectrum of Sigma Phase Produced in 20%-Cold-Worked Type 316 by Aging for 10,000 h at 650°C and Analyzed Quantitatively. (a) Bright field image of precipitate particle. (b) EDS spectrum and composition. nd = not detectable. Cu_{sys} indicates copper detected in microscope and not in specimen.

agreement with x-ray EDS measurements made by others.[27,34,41] Composition measurements for $Ti_4C_2S_2$ are included in Table 3.4.9 and show that, except for almost completely replacing S by Mo, the composition is somewhat similar to that for MC reported in Table 3.4.8.

3.4.5.6 Compositional Changes in the Austenite Matrix After Precipitation During Thermal Aging

Measurements of the matrix composition made in thin foils of unaged control material are given in Table 3.4.5. Comparison of x-ray EDS compositions in Table 3.4.5 with quantitative bulk chemistry results in Table 3.4.1 indicates generally good agreement between the two. Both the Mo and Si concentrations appear a little higher by x-ray EDS in type 316, and Cr appears a little higher in the PCA than values indicate for the same elements in Table 3.4.1. The measurements on control samples of type 316 (Table 3.4.5) provide the baseline for a relative comparison of compositional changes after thermal aging. The area-to-area variations for the control samples of type 316 suggest the limit of compositional change that can be attributed to thermal aging.

The matrix compositions of CW 316 and SA 316 were examined after thermal aging at either 600 or 650°C for 10,000 h. Typical microstructures produced are shown in Fig. 3.4.23 to illustrate the spatial distribution of precipitation. Compositional measurements are given in Table 3.4.5, and Fig. 3.4.24 shows representative x-ray spectra for each aging condition. The matrix composition of SA 316 changes little after aging at 600°C for 10,000 h where tau is the only precipitate phase in the system [Table 3.4.2, Figs. 3.4.23(a) and 3.4.24(c)]. The SA 316 aged at 650°C for 10,000 h shows a slight decrease in Si and a significant decrease in Mo concentration when the precipitate phases are primarily Laves and tau [Table 3.4.2, Figs. 3.4.23(b) and 3.4.24(e)]. The CW 316 aged at 600°C for 10,000 h is similar to SA 316 aged at 650°C. The CW 316 aged at 650°C shows low Si and the lowest matrix Mo concentration. In CW 316 aged at 650°C, the Ni concentration appears to increase slightly, with the change being outside the normal area-to-area variation. Both cold-worked samples contain significant amounts of eta and some sigma, in addition to the intergranular tau and Laves. Figure 3.4.23 shows that the interparticle spacing of precipitates decreases significantly in CW 316 as compared with SA 316. The matrix regions affected by the precipitates may overlap, leaving the matrix seriously depleted of the precipitating elements. Figure 3.4.25 shows a matrix region adjacent to an eta particle in SA 316 aged at 650°C and gives an idea of how different local matrix regions next to precipitates may be during thermal aging. This region is rich in Cr and Mn and seriously depleted in Ni, Si, and Mo. For the phases formed in thermal aging this could only be caused by eta phase, which is rich in Ni. However, it can be seen that the matrix composition is not far from that of sigma phase with the exceptions of Mo and Mn (Table 3.4.8).

3.4.6 Discussion

Several general conclusions can be drawn from the data presented. First, the phases produced during neutron irradiation are compositionally very similar to their thermal aging counterparts. Second, phase instability can be controlled during thermal aging and during irradiation

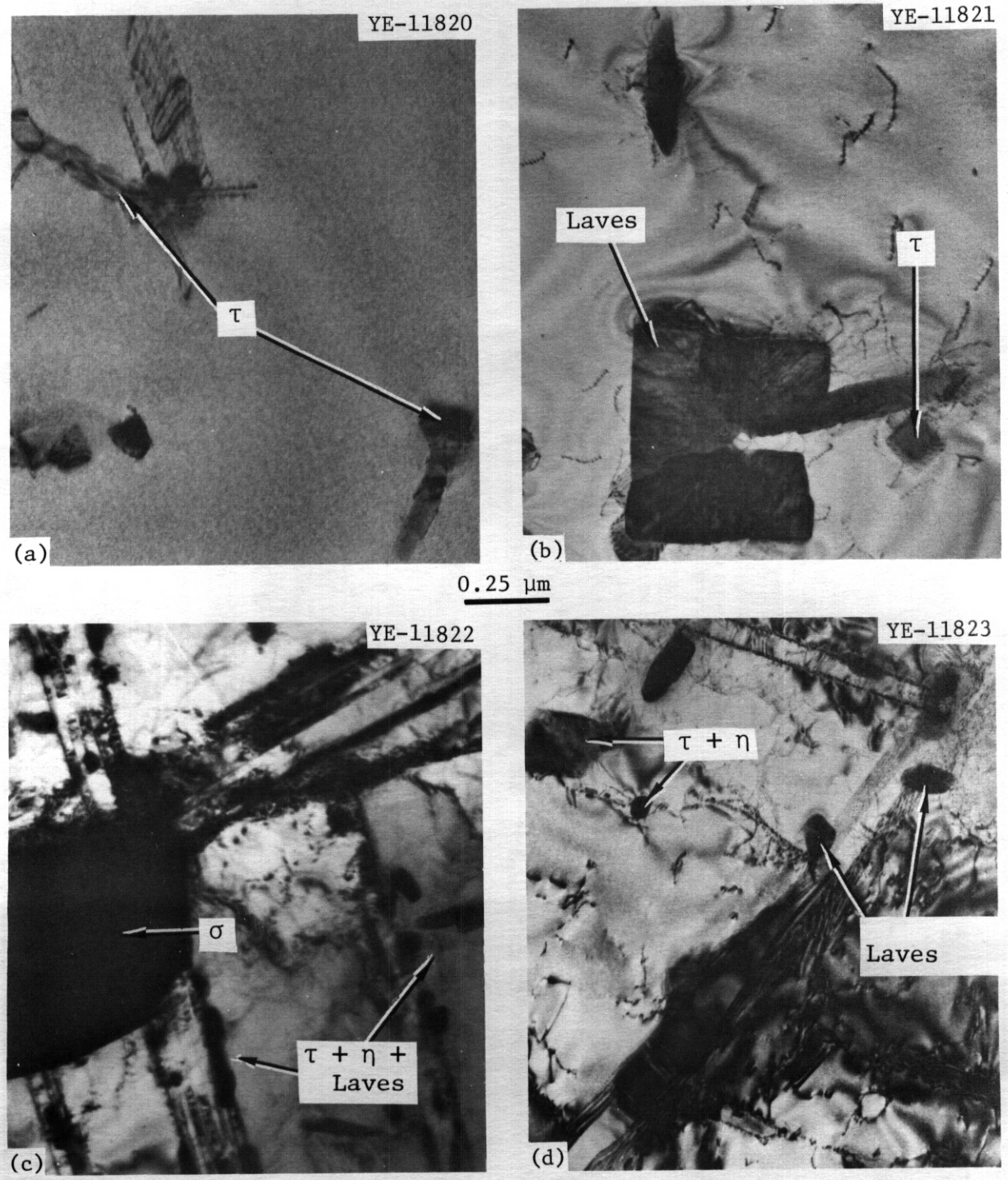

Fig. 3.4.23. Representative Microstructures Produced by Thermal Aging for 10,000 h. (a) Solution-annealed Type 316 at 600°C. (b) Solution-annealed type 316 at 650°C. (c) 20%-cold-worked type 316 at 600°C. (d) 20%-cold-worked type 316 at 650°C. This gives an idea of the spatial distribution of precipitate phases in order to interpret the matrix composition measurements.

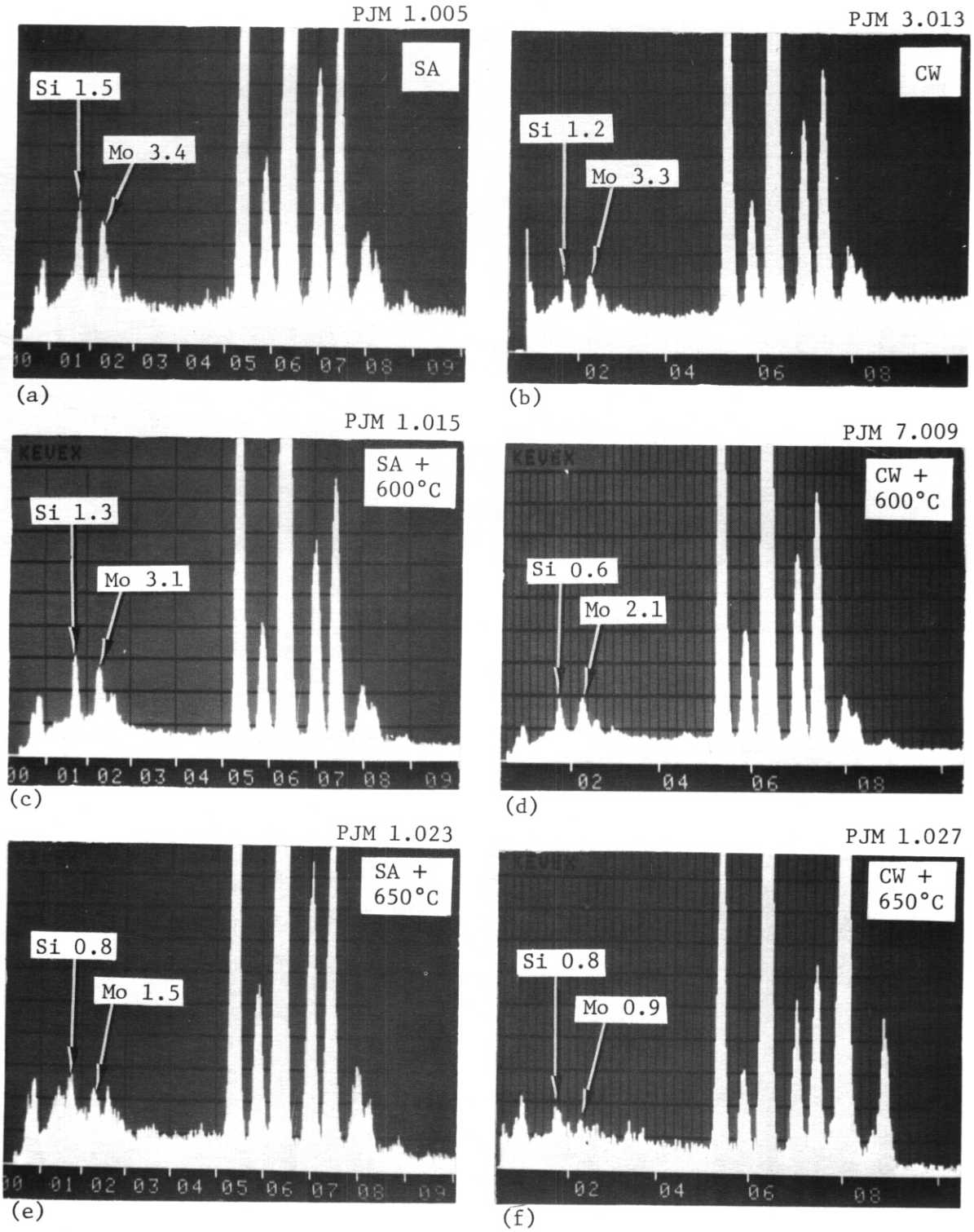

Fig. 3.4.24. Changes in Matrix Composition Caused by Thermal Aging for 10,000 h and Represented by Analyzed X-Ray Energy Dispersive Spectroscopy Spectra. (a) Solution-annealed type 316 control. (b) 20%-cold-worked type 316 control. (c) Solution-annealed type 316 aged at 600°C. (d) 20%-cold-worked type 316 aged at 600°C. (e) Solution-annealed type 316 aged at 650°C. (f) 20%-cold-worked type 316 aged at 650°C. All element compositions are in weight percent.

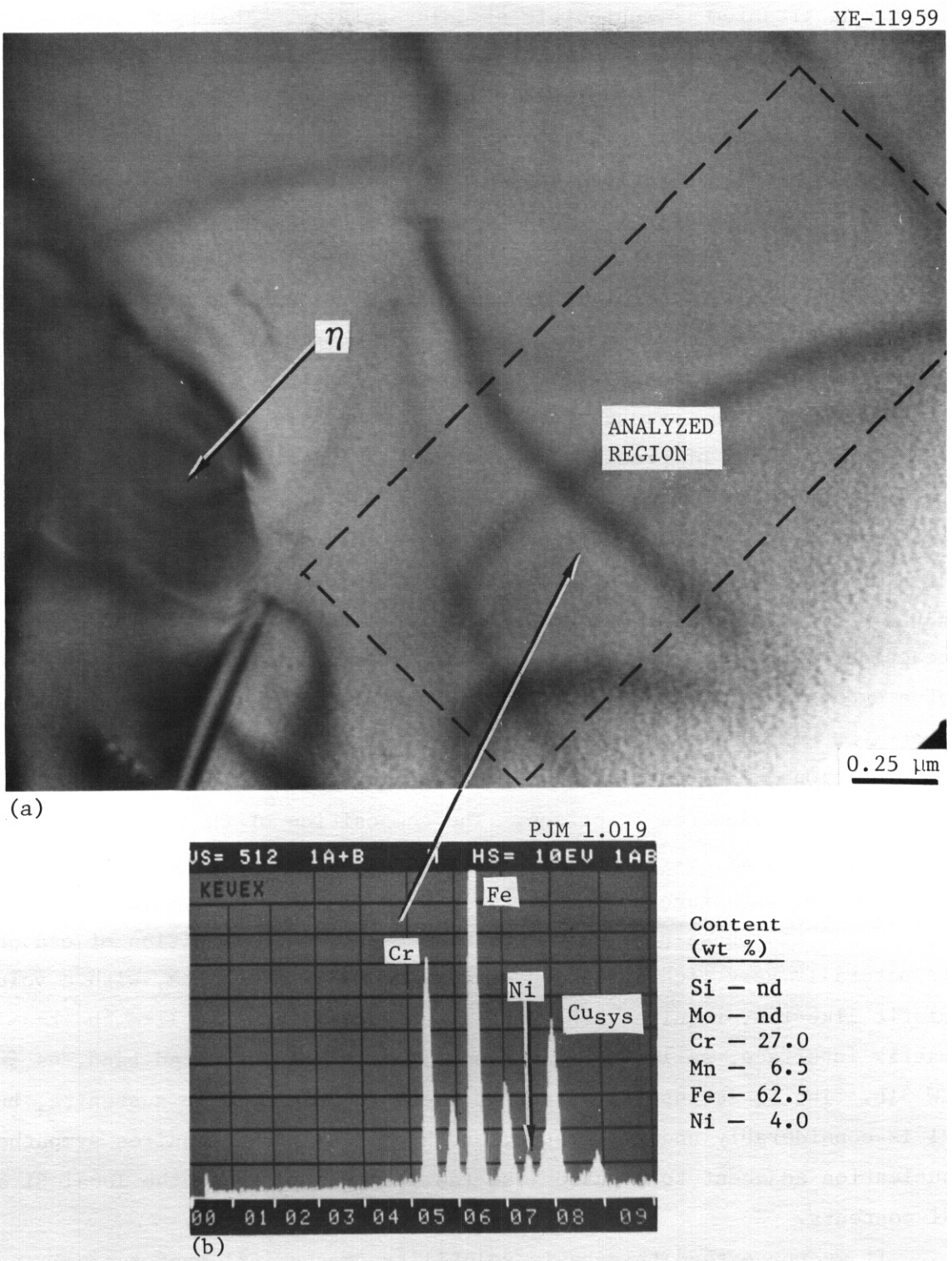

Fig. 3.4.25. An Unusual Matrix Region Near Eta Phase Particles That Is Very Low in Si, Mo, and Ni in Solution-Annealed Type 316 Aged 10,000 h at 650°C and Analyzed by Quantitative X-Ray Energy Dispersive Spectroscopy (EDS) Microanalysis. (a) Bright field image of precipitate particle. (b) EDS spectrum and composition. nd = not detectable. Cu_{sys} indicates copper detected in microscope and not in specimen.

by adding titanium to austenitic stainless steels. Third, Si and Mo are the substitutional solute elements most involved in thermal precipitation in type 316; for precipitation during irradiation, Ni is also active.

Many aspects of precipitation do change during irradiation, including nucleation sites, formation temperatures, morphology, size, and spatial distribution. However, the results examined here indicate that the phase compositions for thermally stable phases are similar to the compositions of the same phases precipitating under irradiation. The irradiation can also induce phases to form that are not the stable or naturally forming phases during thermal aging.' These phases, including gamma prime, G, and phosphorus-rich phases, have been treated elsewhere.[23]

Many aspects of precipitation during irradiation can be understood by considering the solute affinity of the thermal phases and combining this with the effects of point defect supersaturations and radiation-induced solute segregation. A good place to begin is by comparison of eta and tau phase. Thermally, tau phase formation is driven by the chemical reaction 23 Cr + 6 C → $Cr_{23}C_6$ with considerable substitutional solubility of elements like Fe and Mo for Cr and possibly deviations from stoichiometry as well. The phase usually nucleates at heterogeneities (dislocations, faulted bands, or grain boundaries) and develops an incoherent, dislocated interface. The composition of this phase indicates little solubility for Ni and Si. Therefore, tau rejects these solutes ahead of the interface as the particle grows. The side-by-side formation of eta and tau phase particles results because the composition of eta phase is naturally very rich in Si and Ni compared with tau. Eta, with a volume misfit like tau, requires a heterogeneous nucleation site like the tau-matrix interface, as in SA 316, or some portion of a faulted band, as in CW 316. The Si is supersaturated at these temperatures in austenite, but Ni is considerably undersaturated, and hence eta phase requires sympathetic nucleation adjacent to a phase like tau that can increase the local Si and Ni contents.

If we now extend this basic solubility or chemical preference behavior of the thermal phases and include the effects of radiation-induced solute segregation,[42-46] the enhancement of eta and retardation

of tau becomes an expected result. Enrichment of Si and Ni can be expected at any point defect recombination site or at sinks for interstitials. This segregation would encourage eta phase formation while resisting tau phase formation. Eta phase is not often observed thermally as discrete particles but is almost always observed sympathetically with tau or sometimes Laves. This behavior is consistent with eta being eliminated when tau is eliminated, as in thermally aged type 316 + Ti. Eta phase is often observed as discrete particles in either EBR-II- or HFIK-irradiated type 316, because solute segregation serves to build up the Si and Ni contents of the matrix. This same reasoning can be extended to Laves formation[29] and helps considerably in understanding formation of the radiation-induced phases that have no thermal counterparts in type 316, like G phase, phosphorus-rich rod phase, or gamma prime.[23]

However, not all phases enhanced by irradiation are Ni and Si rich. The outstanding exception is the MC phase. It incorporates almost no Ni and Si on formation during thermal aging and very little of either solute when formed during irradiation. Enhanced MC formation appears to result from the very large negative free energy driving force,[47,48] its large positive volume misfit, and the effect of vacancies in stabilizing oversized misfit phases.[49-51] The free energy driving force for titanium-rich MC formation is on the order of —10 kJ/mol °C and is the largest for the phases formed on thermal aging in stainless steel. The volume misfit, from Table 3.4.3, is also the largest observed for the phases formed in steel. Precipitate stability theory[49-51] indicates that the supersaturation of vacancies produced during irradiation should help to stabilize the oversized misfit phases. The oversized misfit demands that the phase absorb vacancies during growth, and this is the idea employed by Silcock and Tunstall[52] to explain stacking fault precipitation of MC at Frank partial dislocations. These combined ideas explain enhanced MC precipitation during irradiation. However, the effects of solute segregation of Ni and Si during irradiation do not cooperate with the growth of MC precipitate particles that have very low solubilities for Ni and Si. This indicates there may be some circumstances in which solute segregation

during irradiation could reduce MC precipitation as it does tau phase. A goal of alloy development then should be to encourage MC precipitation by maintaining the lowest acceptable Si level in the matrix.

The compositional behavior of individual phases, when combined with their volume misfit properties, correlates well with their effect on one another, on the surrounding matrix, and on their sink behavior during irradiation. The MC precipitate particles are able to prevent or reduce tau formation on thermal aging because of their competition for C. Since eta phase nucleates sympathetically with tau, it is consistent that it be reduced as well. The MC rejects Si but enriches in Mo and Ti, and these effects must be traded off in order to determine MC's effect on Laves formation. From the standpoint of volume misfit, Laves being slightly undersized and MC being oversized would be consistent with coprecipitation. The MC precipitation in itself should not have much direct effect on sigma phase precipitation because the only interaction appears to be competition for Mo.

For thermally aged SA 316 and CW 316, the compositional changes in the matrix are consistent with both the phases formed and their compositions. The SA 316 aged at 600°C for 10,000 h precipitates tau particles that are spaced about 0.5 to 2 μm apart. They affect the average matrix composition little. All the other aging conditions produce eta and Laves, together with tau, and reduce the average matrix concentration of Si and Mo.

The MC has been shown to be an effective helium trap, and fine dispersions of MC are a goal of alloy development in austenitic stainless steel. Its vacancy-absorbing and nickel- and silicon-rejecting behavior are consistent with it being a vacancy-biased sink during irradiation. These concepts are quite successful in explaining MC helium trapping.[10] The other phases in steel have little usefulness during irradiation and can often be associated with detrimental effects, increased swelling (eta, Laves), or embrittlement (eta, sigma). The Path A PCA appears to be a considerable improvement over type 316 alloys because the increased Ni and decreased Cr discourages both tau and sigma formation. Reduction of Si would reduce Laves formation and reduce formation of the undesirable radiation-induced phases.[23] Maintaining low P and Mn levels also will

suppress the potential for formation of the phosphorous-rich rod phase and manganese-stabilized G phase, respectively. Finally, systematic variation of Mo and combination of V and Nb with the Ti addition may maximize the MC stability.

3.4.7 Conclusions

1. Tau, eta, Laves, and sigma phases are produced during thermal aging of type 316 alloys at temperatures below 700 to 750°C. The MC phase is produced in addition to varying amounts of the above phases when the austenite is modified by the addition of 0.2 to 0.3 wt % Ti. The basic composition of these phases is given in Table 3.4.10.

Table 3.4.10. Composition of Phases Produced by Thermal Aging of Type 316 Stainless Steel

Precipitate Phase	Content,[a] wt %								
	Si	Mo	Cr	Mn	Fe	Ni	V	Ti	Nb
Tau	0.5	14	64.5	0.5	15.5	4.0	c	c	c
Eta	7	23.5	31	0.5	11	25	2	c	c
Laves	4.5	43	13	1	33	5.5	c	c	c
Ti-MC[b]	c	20	1	c	1	0.5	2.5	66	9
Sigma	1.5	6	36	1	50.7	5			

[a]Averaged compositions.

kormed only in titanium-modified steels.

[c]Not detectable.

2. The eta, Laves, and sigma phase formations are enhanced in CW 316 compared with SA 316 during thermal aging. The eta and tau are reduced, but sigma is enhanced in thermally aged type 316 + Ti, when compared with type 316. The eta and tau are eliminated in thermally aged Path A PCA.

3. Eta and Laves phase formation are enhanced by HFIR irradiation of either SA 316 or CW 316 and CW 316 + Ti relative to thermal aged material. Tau phase formation is reduced or eliminated in both. The MC formation is enhanced by HFIR irradiation of type 316 + Ti.

4. Compositionally the thermal phases behave as follows with respect to the matrix:

- eta is rich in Si, Mo, Cr, and Ni and poor in Fe;
- tau is rich in Mo and Cr and poor in Fe, Si, and Ni;
- Laves is rich in Si and Mo and poor in Fe and Ni;
- sigma is rich in Mo and Cr and poor in Fe, Ni, and Si;
- MC is rich in Ti, Elo, Nb, and V and poor in Cr, Fe, Si, and Ni.

All the phases contain from nearly zero to the matrix average content of Mn. Laves, eta, and tau can have occasional enrichment of V and/or Ti.

5. With respect to relative amounts of Si, Mo, Cr, Fe, Ni, and Ti(+Nb/+V), the compositions of the thermal phases order as follows:

- Si: eta, Laves > sigma > tau > MC;
- Mo: Laves > MC, eta > tau > sigma;
- Cr: tau > sigma > eta > Laves > MC;
- Fe: sigma > Laves > eta, tau > PIC;
- Ni: eta > Laves, sigma > tau > MC;
- Ti (and/or Nb, V): MC > eta, tau > Laves, sigma.

6. The compositions of Laves, tau, eta, and MC produced during irradiation are similar to those of the same phases produced during thermal aging. The enrichment or depletion relative to the matrix does not change except for Laves produced at lower temperatures, which become Ni rich. Some of the phases show slight increases in Si or Ni content and, except for MC, show a more systematic enrichment of Ti and V at lower irradiation temperatures.

7. The SA 316 aged for 10,000 h at 600°C shows little matrix compositional change when tau phase precipitates. The CW 316 aged at 600°C and SA 316 and CW 316 aged at 650°C show a measurable reduction in matrix Si and a considerable reduction of matrix Mo concentrations when eta, Laves, and sigma precipitate in addition to tau phase.

8. Further development of Path A alloys to produce maximum MC stability should consider the following:

- reduce Si to the lowest necessary or convenient level;
- systematically evaluate small changes in Mo content for the effect on MC;

- determine the minimum necessary Mn level;
- consider combinations of V and Nb with Ti to evaluate their effect on MC formation and stability.

3.4.8 References

1. E. E. Bloom and J. O. Stiegler, "Effect of Irradiation on the Microstructure and Creep-Rupture Properties of Type 316 Stainless Steel," pp. 360–82 in *Effects of Radiation on Substructures and Mechanical Properties on Metals Alloys, Amer. Soc. Test. Mater. Spec. Tech. Publ.* 529, American Society for Testing and Materials, Philadelphia, September 1973.
2. H. R. Brager and J. L. Straalsund, "Defect Development in Neutron Irradiated Type 316 Stainless Steel," ***J. Nucl.*** *Mater.* 46: 134–58 (1973).
3. H. R. Brager and F. A. Garner, "Swelling as a Consequence of Gamma Prime (γ') and $M_{23}(C,Si)_6$ Formation in Neutron Irradiated 316 Stainless Steel," ***J. Nucl.*** *Mater.* 73: 9–19 (1978).
4. J. I. Bramman, K. Q. Bagley, C. Cawthorne, and E. J. Fulton, "Void Formation in Cladding and Structural Materials Irradiated in DFR," pp. 125–38 in *Radiation-Induced Voids in Metals, AEC Symp. Ser.* 26, J. W. Corbett and L. C. Ianiello, Eds., Washington, D. C., 1972.
5. J. I. Bramman et al., "Void Swelling and Microstructural Changes in Fuel Pin Cladding and Unstressed Specimens Irradiated in DFR," pp. 497–507 in *Radiation Effects in Breeder Reactor Structural Materials,* M. L. Bleiberg and J. W. Bennett, Eds., The Metallurgical Society of AIME, New York, 1977.
6. P. J. Maziasz, "Precipitation Response of Austenitic Stainless Steel to Simulated Fusion Irradiation," pp. 160–80 in *The Metal Science of Stainless Steels,* E. W. Collings and H. W. King, Eds., The Metallurgical Society of AIME, New **York,** 1979.
7. P. J. Maziasz, "The Precipitation Response of 20%-Cold-Worked Type 316 Stainless Steel to Simulated Fusion Irradiation," *J. Nucl. Mater.* 85 & 86(II,B): 713–17 (1979).

8. P. J. Maziasz and E. E. Bloom, "A Comparison of the Properties Response of Types 316 and 316 + Ti Stainless Steels After HFIR Irradiation," to be submitted for publication.
9. E. H. Lee, A. F. Rowcliffe, and E. A. Kenik, "Effects of Si and Ti on the Phase Stability and Swelling Behavior of AISI 316 Stainless Steel," *J. Nucl. Mater.* 83(1): 79-89 (1979).
10. P. J. Maziasz, "Helium Trapping at Ti-Rich MC Particles in Neutron-Irradiated Type 316 Stainless Steel," to be submitted for publication.
11. P. J. Maziasz, "The Formation of Diamond-Cubic Eta (η) Phase in Type 316 Stainless Steel Exposed to Thermal Aging or Irradiation Environments," *Scri. Metall.* 13(7): 621-26 (1979).
12. P. J. Maziasz, F. W. Wiffen, and E. E. Bloom, "Swelling and Microstructural Changes in Type 316 Stainless Steel Irradiated Under Simulated CTK Conditions," pp. 259-88 in *Radiation Effects and Tritium Technology for Fusion Reactors,* CONF-750989, Vol. I (March 1976); also ORNL/TM-5396 (May 1976).
13. P. J. Maziasz, B. L. Cox, and J. A. Horak, "The Effect of Preinjected Helium on the Microstructure and Tensile Properties of EBR-II-Irradiated 20%-Cold-Worked Type 316 Stainless Steels," *ADIP Quart. Prog. Rep. Mar. 31, 1980,* DOE/ER-0045/2, pp. 35-57.
14. M. L. Grossbeck and P. J. Maziasz, "Tensile Properties of HFIR-Irradiated Types 316 and TiM 316 Stainless Steel at 200 to 1000 at. ppm He," *ADIP Quart. Prog. Rep. Sept. 30, 1978,* DOE/ET-0058/3, pp. 32-49.
15. P. J. Maziasz, B. L. Cox, T. K. Roche, and E. E. Bloom, "Time-Temperature-Precipitation Curve Determination of the Path A Prime Candidate Alloy for Microstructural Design," *ADIP Quart. Prog. Rep. Sept. 30, 1979,* DOE/ET-0058/7, pp. 103-27.
16. C.K.H. DuBose and J. O. Stiegler, *Semiautomatic Preparation of Specimens for Transmission Electron Microscopy,* OWL-4066 (February 1967).

17. N. J. Zaluzec, "Quantitative X-Ray Microanalysis in an AEM: Instrumental Considerations and Applications to Materials Science," pp. 121–67 in *Introduction to Analytical Electron Microscopy*, J. J. Hren, J. I. Goldstein, and D. C. Joy, Eds., Plenum Press, New York, 1979.

18. J. Bentley, N. J. Zaluzec, E. A. Kenik, and R. W. Carpenter, "Optimization of an Analytical Electron Microscope for X-Ray Microanalysis: Instrumental Problems," pp. 581–94 in *Scanning Electron Microscopy, (Proc., Washington, D.C., April 16–20, 19791* SEM Inc., AMF O'Hare, Illinois, 1979.

19. K. W. Andrews, P. J. Bryson, and s. R. Koewn, *Interpretation of Electron Diffraction Patterns*, 2d ed., Plenum Press, New York, 1971.

20. C. J. Smithells, Ed., *Metals Reference Book*, 5th ed., Butterworths, London, 1976, pp. 104–77.

21. N. J. Zaluzec, *An Analytical Electron Microscope Study of the Omega Phase Transformation in a Zirconium-Niobium Alloy*, ORNL/TM-6705 (June 1979). PH.D. Thesis, University of Illinois, 1978.

22. N. J. Zaluzec, unpublished computer programs, Oak Ridge National Laboratory, 1979.

23. E. H. Lee, P. J. Maziasz, and A. F. Rowcliffe, "Identification of Precipitate Phases Occurring in Austenitic Stainless Steels in Thermal and Irradiation Environments," paper to be presented at The Metallurgical Society of AIME Fall Meeting, Pittsburg, October 5–9, 1980.

24. H. H. Stadelmaier, "Metal-Rich Metal-Metalloid Phases," pp. 141–80 in *Developments in the Structuml Chemistry of Alloy Phases*, Plenum Press, New York, 1969.

25. N. J. Zaluzec and P. J. Maziasz, unpublished data, Oak Ridge National Laboratory, 1980.

26. D. V. Edmonds and R.W.K. Honeycombe, "Precipitation in Iron-Base Alloys," pp. 121–60 in *Precipitation Processes in Solids*, The Metallurgical Society of AIME, New York, 1978.

27. B. Weiss and R. Stickler, "Phase Instabilities During High Temperature Exposure of 316 Austenitic Stainless Steel," *Metall. Trans.* 3: 851–66 (1972).

28. J. E. Spruiell, J. A. Scott, C. S. Ary, and K. L. Hardin, "Microstructural Stability of Thermal-Mechanically Pretreated Type 316 Austenitic Stainless Steel," *Metall. Trans.* 4: 1533–44 (1973).

29. P. J. Maziasz, J. A. Horak, B. L. Cox, and M. L. Grossbeck, "The Influence of Both Helium and Neutron Irradiation on Precipitation in 20%-Cold-Worked Austenitic Stainless Steel," paper to be presented at the Metallurgical Society of AIME Fall Meeting, Pittsburg, October 5–9, 1980.

30. A. S. Grot and J. E. Spruiell, "Microstructural Stability of Titanium-Modified Type 316 and Type 321 Stainless Steel," *Metall. Trans.* 6A: 2023–30 (1975).

31. M. M. McDonald and J. M. Leitnaker, "Stabilities of Intermetallic Phases," *Metals and Ceramics Division Materials Science Program Annu. Prog. Rep. June 30, 1979,* ORNL–5589, pp. 199–200.

32. J. M. Leitnaker and J. Bentley, "Precipitate Phases in Type 321 Stainless Steel After Aging 17 Years at 600°C," *Metall. Trans.* 8A: 1605–13 (1977).

33. M. Waldenström, "An Experimental Study of Carbide–Austenite Equilibria in Iron–Base Alloys with Mo, Cr, Ni and Mn in the Temperature Range 1173 to 1373°K," *Metall. Trans.* 8A: 1963–77 (1977).

34. C. J. Bolten et al., "Properties and Microstructure of 316 Stainless Steel," pp. 1183–92 in *Mechanical Behavior of Materials,* Vol. 2, K. J. Miller and R. F. Smith, Eds., Pergamon Press, Oxford, England, 1979.

35. L. P. Stoter, Ph.D. Thesis, University of Bristol, England, 1979.

36. K. E. Cooke, N. Evans, L. Stoter, and J. W. Steeds, "Accurate Crystallographic Information from Precipitates in 316 and Related Stainless Steel," *Inst. Phys. Conf. Ser.* 41: 195–200 (1978).

37. N. S. Evans, Ph.D. Thesis, University of Bristol, England, 1979.

38. P. J. Maziasz, unpublished data, Oak Ridge National Laboratory, 1980.

39. T. M. Williams and J. M. Titchmarsh, "The Occurrence of a Silicon-Rich Phase of the M_6C Type in Neutron–Irradiated FV 548 Steel," *J. Nucl. Mater.* 87: 398 (1979).

40. P. J. Maziasz and R. W. Carpenter, "MC Precipitate Characterization in Austenitic Stainless Steel," paper presented at EMSA Pacific Regional Meeting, San Francisco, Aug. 4-8, 1980.

41. J. Bentley and J. M. Leitnaker, "Stable Phases in Aged Type 321 Stainless Steel," pp. 70-91 in *The Metal Science of Stainless Steels*, E. W. Collins and H. W. King, Eds., The Metallurgical Society of AIME, New York, 1979.

42. P. R. Okamoto and H. Wiedersich, "Segregation of Alloying Elements to Free Surfaces During Irradiation," *J. Nucl. Mater.* 53: 336-45 (1974).

43. R. A. Johnson and N. Q. Lam, "Solute Segregation in Metals Under Irradiation," *Phys. Rev. B* 13: 4364-75 (1976).

44. R. A. Johnson and N. Q. Lam, "Solute Segregation Under Irradiation," *J. Nucl. Mater.* 69 & 70: 424-33 (1978).

45. P. R. Okamoto and L. E. Rehn, "Radiation-Induced Segregation in Binary and Ternary Alloys," *J. Nuct. Mater.* 83: 2-23 (1979).

46. H. Wiedersich, P. R. Okamoto, and N. Q. Lam, "A Theory of Radiation Induced Segregation in Concentrated Alloys," *J. Nucl. Mater.* 83: 98-108 (1979).

47. J. M. Leitnaker and R. E. Gehlbach, *Thermodynamics* of *Precipitation Reactions in Titanium-Modified Stainless Steel*, ORNL/TM-4343 (July 1974).

48. S. R. Shatynski, "The Thermochemistry of Transition Metal Carbides," *Oxid. Met.* 13: 105-18 (1979).

49. K. C. Russell, "The Role of Excess Vacancies in Precipitation," *Scr. Metall.* 3: 313-16 (1969).

50. S. I. Maydet and K. C. Russell, "Precipitate Stability Under Irradiation: Point Defect Effects," *J. Nucl. Mater.* 64: 101-14 (1977).

51. K. C. Russell, "The Theory of Phase Stability Under Irradiation," *J. Nucl. Mater.* 83: 176-87 (1979).

52. J. M. Silcock and W. J. Tunstall, "Partial Dislocations Associated with NbC Precipitation in Austenitic Stainless Steels," *Philos. Mug.* 10: 361-89 (1964).

4. PATH B ALLOY DEVELOPMENT — HIGHEK STRENGTH Fe–Ni–Cr ALLOYS

5. PATH C ALLOY DEVELOPMENT — REACTIVE AND REFKACTORY ALLOYS

5.1 THE EFFECT OF HYDROGEN ON FLAW GROWTH OF TITANIUM ALLOY Ti-6242s -

G. W. Wille and P. S. Pao (McDonnell Douglas Corporation)

5.1.1 ADIP Task

Task 1.B.3, Fatigue Crack Growth in Reactive/Refractory Alloys (Path C).

5.1.2 Objective

The objective of this study is to develop quantitative data to determine the effects of both internal and external hydrogen on fatigue crack growth of Ti-6242s alloy at temperatures and hydrogen pressures of interest for fusion reactors.

5.1.3 Summary

Machining of the specimens is complete. Calibration of equipment to monitor crack growth is complete. The environmental test chamber for fatigue testing has been set up.

5.1.4 Progress and Status

Machining of the modified-WOL specimens is complete.

The environmental test chamber has been set up for fatigue tests of the Ti-6242s specimens in hydrogen environment. This is shown in Figure 5.1.4-1.

The crack growth during testing in the environmental test chamber will be monitored using an electrical potential means for measurement. This technique is based on the principle that the electrical resistance to an AC current passing through the specimen increases with crack extension. A correlation can therefore be made between the electrical potential across the specimen and the crack length. The calibration tests were conducted on duplicate Ti-6242s specimens. The crack length vs. normalized potential is shown in Figure 5.1.4-2. The calibration equation is based on least-square linear regression analysis is:

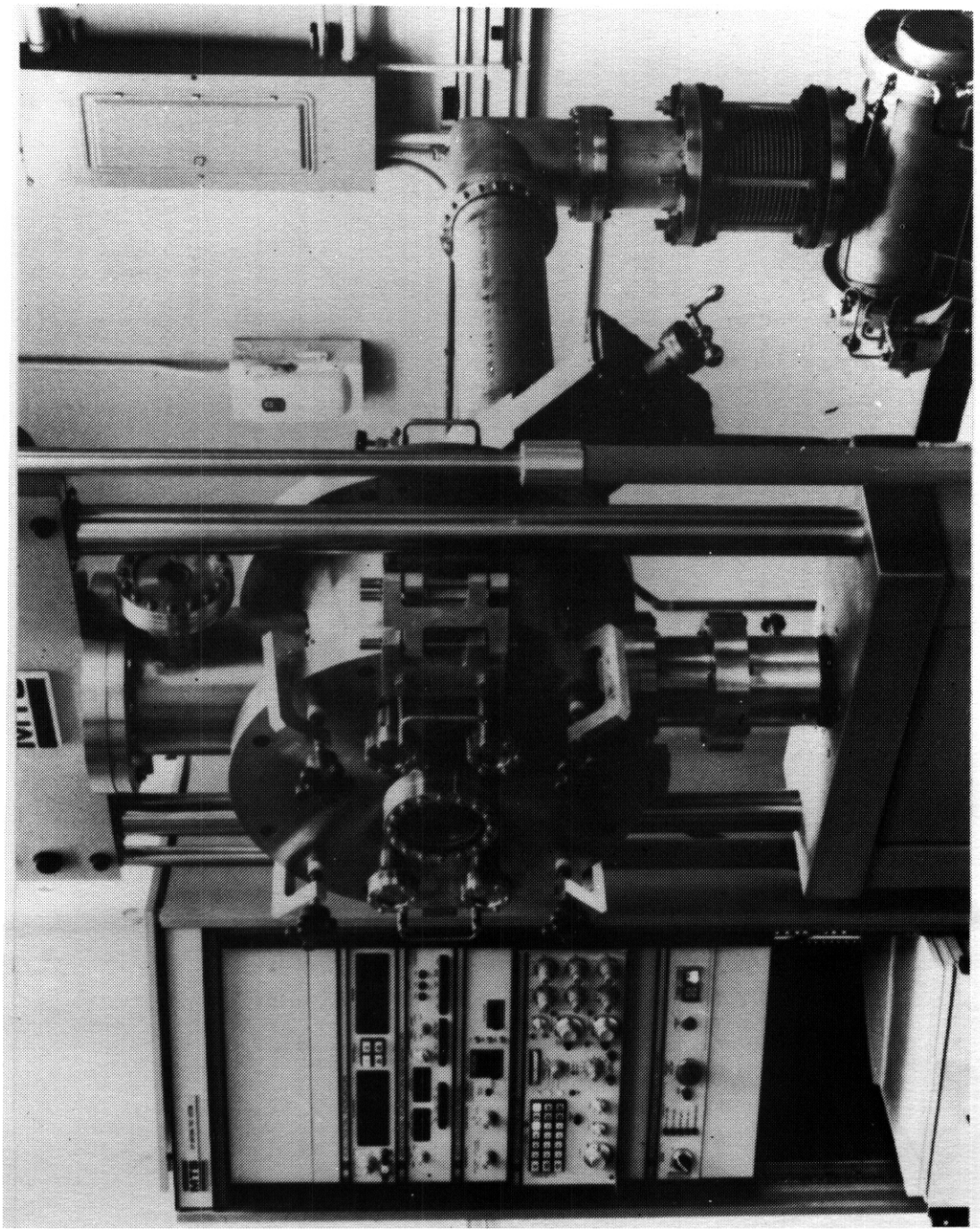

FIGURE 5.1.4-1 ENVIRONMENTAL TEST CHAMBER IN FATIGUE TEST UNIT

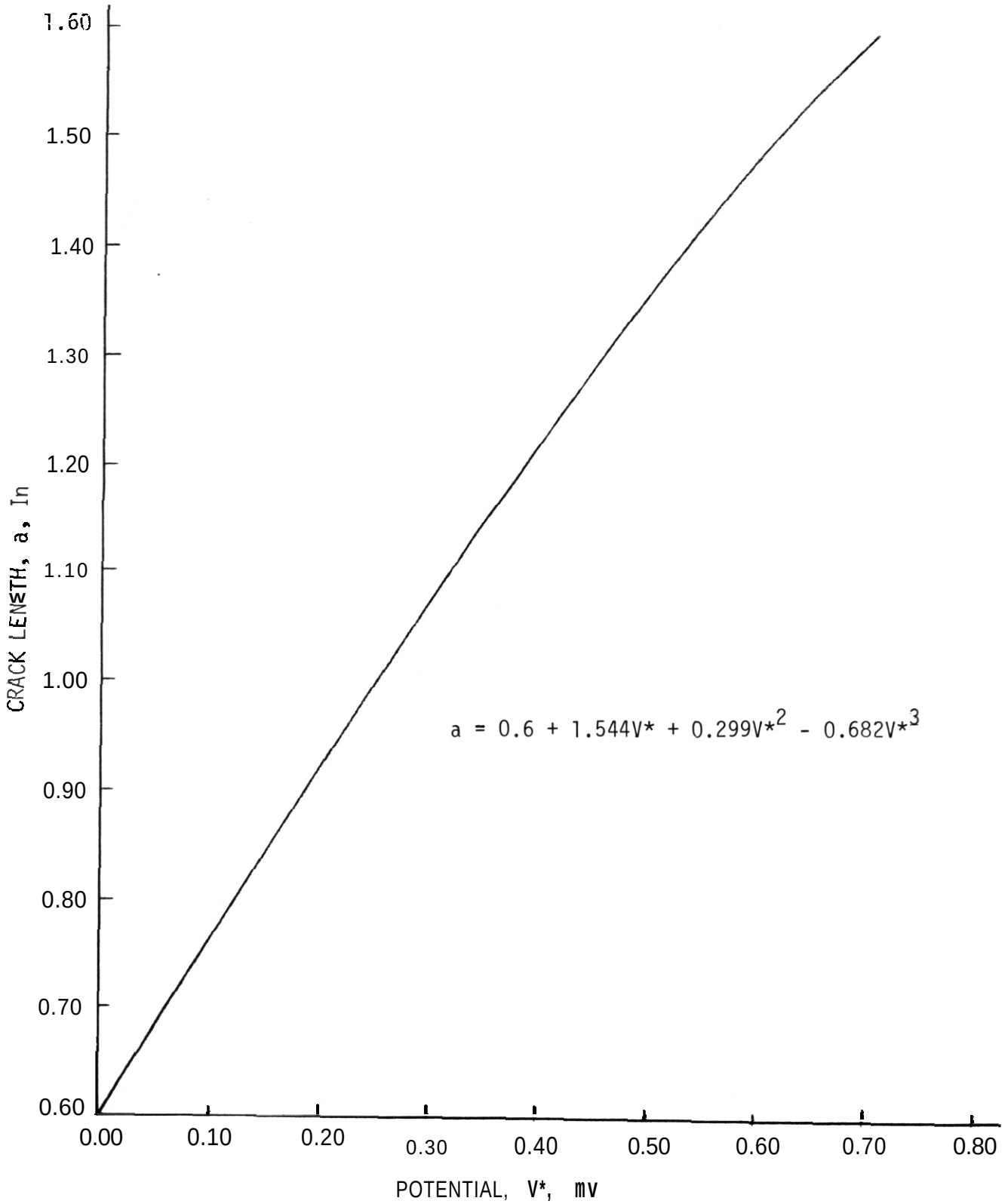

FIGURE 5.1.4-2 CALIBRATION CURVE FOR AC POTENTIAL SYSTEM

$$a = 0.6 + 1.55\ V^{*} + 0.299\ V^{*2}$$

where $V^{*} = \frac{(V-V_r)}{V_r}$ = normalized potential at crack length, a

V_r = reference potential at starter notch

V = potential during fatigue testing

a = crack length

The accuracy of this calibration is better than 0.5% in the range 0.6 inch $\leq a \geq$ 1.6 inch.

5.1.5 Conclusions

1. Machining of specimens is complete
2. Calibration of equipment to monitor crack growth is complete.
3. The environmental test chamber for fatigue testing has been set up.

5.2 TENSILE PKOPERTIES OF HELIUM-INJECTED AND REACTOR-IRRADIATED V–20 Ti — M. P. Tanaka, J. A. Horak, and E. E. Bloom (ORNL)

5.2.1 ADIP Tasks

ADLP Task I.B.15, Tensile Properties of Reactive and Refractory Alloys.

5.2.2 Objective

The objective of this work is to determine the effect of preinjected helium followed by neutron irradiation on the microstructure and mechanical properties of V–20% Ti. These results will be used for the evaluation of the potential use of V–20% Ti in fusion reactor service.

5.2.3 Summary

Sheet tensile specimens of annealed V–20% Ti alloy have been pre-injected with 90 and 200 at. ppm He by use of 60-MeV (9.6-pJ) alpha particles at the Oak Ridge Isochronous Cyclotron (ORIC). Some of the samples were then irradiated in row 7 of the Experimental Breeder Reactor (EBR-II) at temperatures of 400, 525, 575, 625, and 700°C to neutron fluences of 2×10^{26} to 4×10^{26} neutrons/m^2 (>0.1 MeV).

Tensile properties and fractography of the injected and the irradiated specimen have been compared with those of the control specimen. This comparison showed that the helium injection increased the strength at test temperatures below 500°C and decreased the elongation above 500°C. The loss of ductility (reduction of elongation) depended on the amount of injected helium. The loss of ductility resulting from the neutron irradiation was much greater when the specimens were irradiated and tested at temperatures above 600°C.

5.2.4 Progress and Status

The details of the helium implantation of samples used in this study were reported by Horak.[1] Briefly, sheet specimens 191 by 25.4 by 0.254 mm of vacuum-annealed (0.5 h at 900°C) V–20% Ti were injected with 60-MeV alpha particles at the ORIC. The beam energy was degraded with a variable thickness foil to give uniformly distributed helium contents of

90 and 200 at. ppm He. After the injection, tensile specimens with a length of 31.75 mm and a gage section 12.7 by 1.02 by 0.254 mm were stamped from the sheet with a precision die.

The tensile specimens were irradiated in row 7 of EBR-II, in experiment X-287, to neutron fluences 2×10^{26} to 4×10^{26} neutrons/m^2 (>0.1 MeV). The irradiation temperatures of 700, 625, and 575°C were attained in heat-pipe capsules. The irradiation temperatures of 525 and 400°C were attained in gamma-heated capsules with gas gap temperature control. Some of the specimens were immersed in static sodium; the others were encapsulated in helium-filled subcapsules. Comparisons will establish effects resulting from interstitial impurity mass transfer.

The tensile specimens were tested at a strain rate of 6.67×10^{-4}/s at temperatures near the neutron irradiation temperature. Tests were conducted in a cold-wall, resistance-heated furnace contained in an ion pumped vacuum chamber. The vacuum during testing was below 40 μPa (3×10^{-7} torr).

Tensile results on control, helium-preinjected, and neutron-irradiated specimens are tabulated in Table 5.2.1. The data are also shown graphically in four figures that follow. Engineering stresses reported are based on pretest specimen dimensions.

The yield stress, ultimate stress, and total elongation of the control and helium-injected material are shown graphically in Fig. 5.2.1. Helium injection has increased the yield stress and ultimate stress for test temperatures of 525°C and lower. The increase in strength was dependent on the amount of injected helium. At test temperatures 500 to 700°C, the helium did not greatly affect the strength properties. However, the elongation was reduced. The reduction of the total elongation in the preinjected specimen depended on the injected helium content. The value of the elongation at 700°C in the specimen injected with 200 at. ppm He was 8.7%, which was less than half that of the control specimen. The fracture surfaces of the specimen containing 0 and 200 at. ppm He tested at 625°C are shown in Fig. 5.2.2. Cracks along grain boundaries can clearly be seen in the helium-containing sample but are not seen for the control material. The fracture surface shows many exposed grain boundaries, consistent with a grain separation fracture mode.

Table 5.2. Helium Contents, Irradiation Conditions, and Tensile Properties of V–20% Ti

Preinjected Helium[a] (at. ppm)	Irradiation Conditions[b]			Test Temperature (°C)	Tensile Properties[d]			
	Temperature (°C)	Fluence[c] (>0.1 MeV) (neutrons/m^2)	dpa		Strength, MPa		Elongation, %	
					0.2% Yield	Ultimate	Uniform	Total
0				25	546	661	12.0	19.6
0				400	387	588	11.4	13.3
0				525	400	668	13.0	14.7
0				575	407	681	14.1	19.0
0				625	384	619	12.3	19.9
0				700	345	499	13.4	19.2
50				400	475	641	7.9	10.1
50				525	443	701	16.6	18.2
50				575	405	658	13.0	21.5
50				625	387	597	10.3	18.1
50				700	330	531	10.9	13.3
200				400	515	649	12.8	15.1
200				525	468	708	16.7	18.2
200				575	433	653	15.1	17.3
200				625	410	644	14.1	15.6
200				700	362	455	8.3	8.7
0	625	2 to 4 × 10^{26}	~20	625	361	475	1.8	3.1
0	700	2 to 4	~20	700	399	453	3.0	4.9
50	400	2 to 4	~20	400	629	777	4.9	7.0
200	400	2 to 4	~20	400	656	814	6.7	8.2
200	625	2 to 4	~20	625	386	575	4.9	5.7

[a]Nominal value.

[b]Blank spaces indicate control specimen.

[c]Measurement on fluence monitor is in progress.

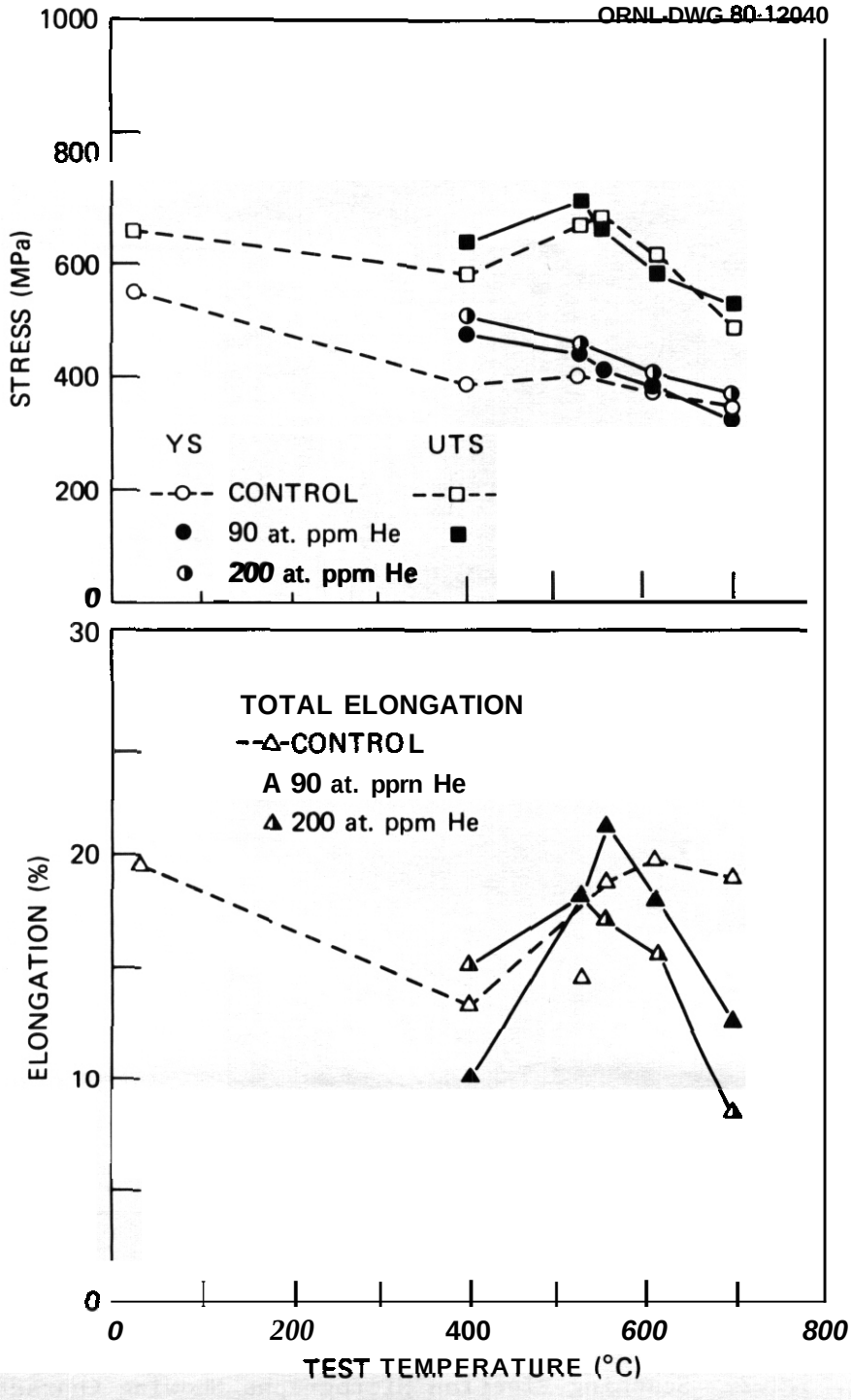

Fig. 5.2.1. Tensile Properties of V–20% Ti Injected with up to 200 at. ppm He and Tensile Tested at 625°C. These samples were not neutron irradiated. The strain rate was 6.67×10^{-4}/s. YS = yield stress; UTS = ultimate tensile stress.

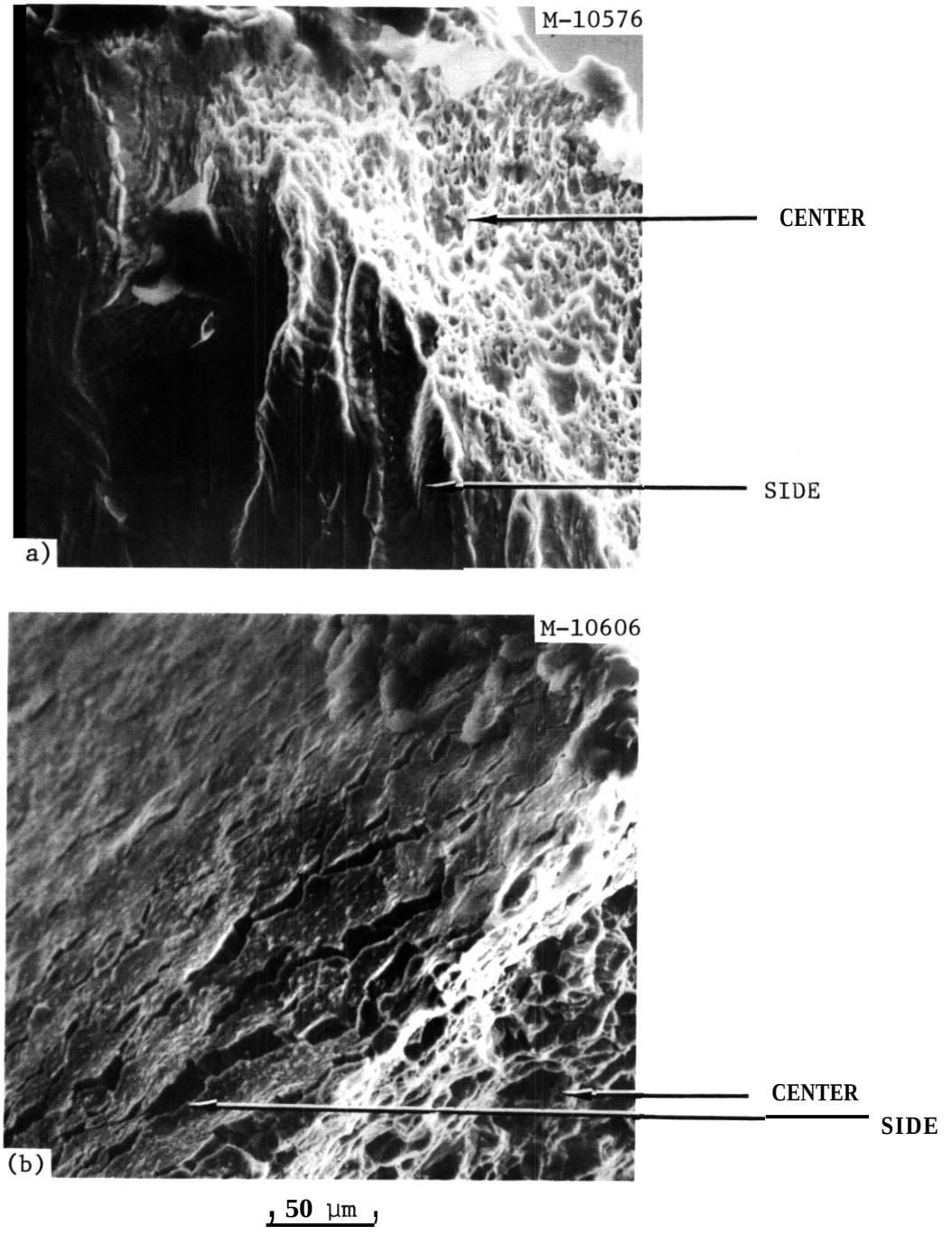

Fig. 5.2.2. Scanning Electron Micrographs Showing Characteristic Fracture Surfaces Observed in V–20% Ti Containing (a) 0 and (b) 200 at. ppm He and Tested at 625°C. These samples were not neutron irradiated.

The yield stress, ultimate stress, and elongation of the neutron-irradiated specimens are shown in Figs. 5.2.3 (no preinjected helium), 5.2.4 (90 at. ppm preinjected helium), and 5.2.5 (200 at. ppm preinjected helium). In each case the results for neutron-irradiated specimens are

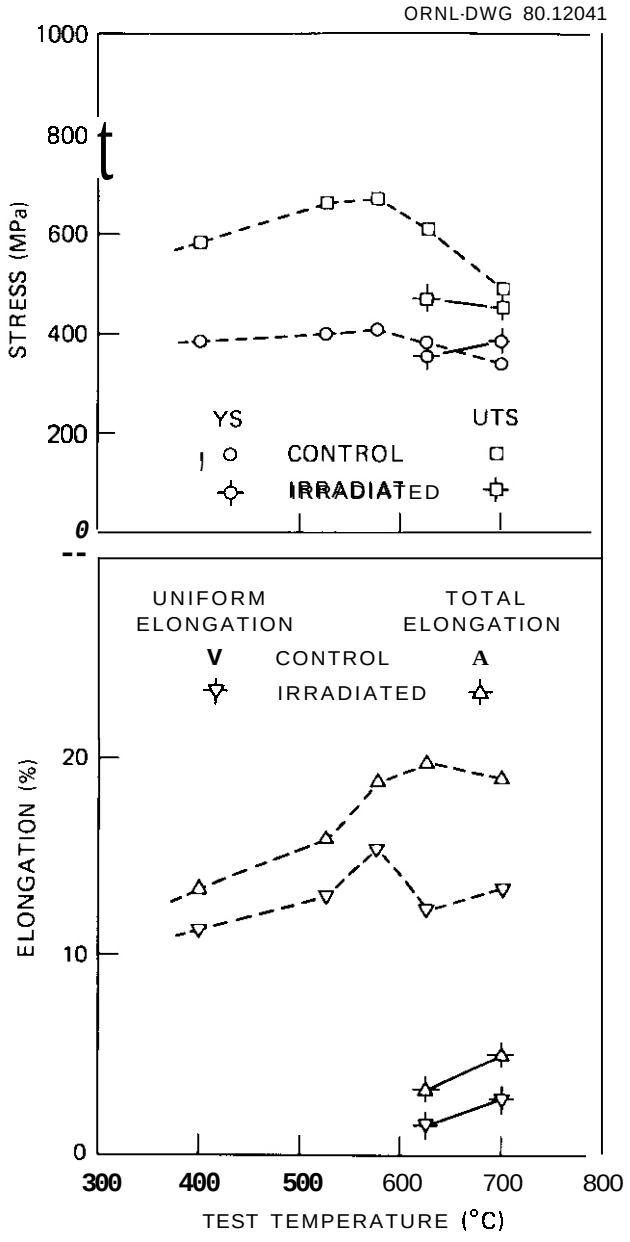

Fig. 5.2.3. Tensile Properties of V-20% Ti Irradiation in the EBR-II. These samples were not helium injected. YS = yield stress; UTS = ultimate tensile stress.

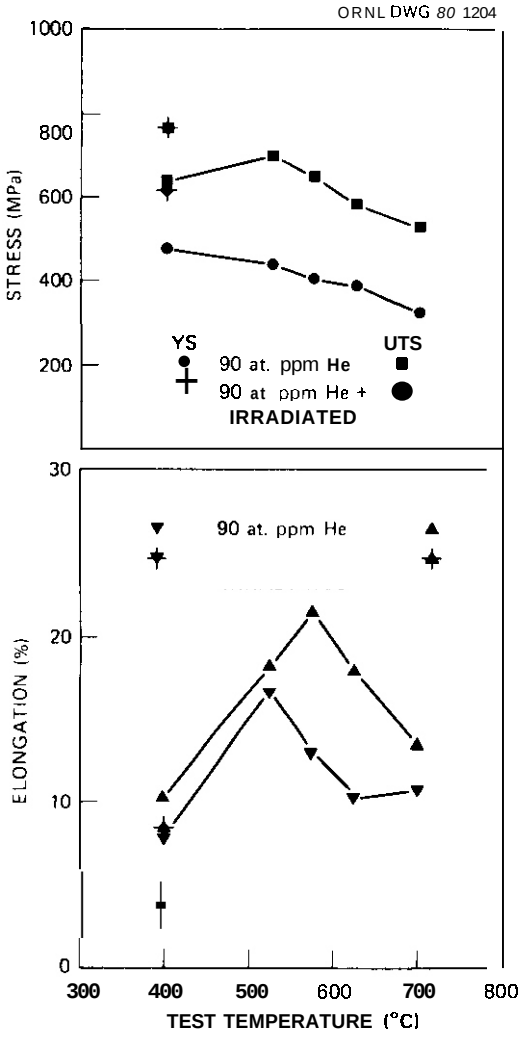

Fig. 5.2.4. Tensile Properties of V–20% Ti That Was Injected with 90 at. ppm He and Irradiated in EBR-II to 20 dpa. The irradiated specimens were tested near the irradiation temperature at a strain rate of 6.67×10^{-4}/s. YS = yield stress; UTS = ultimate tensile stress.

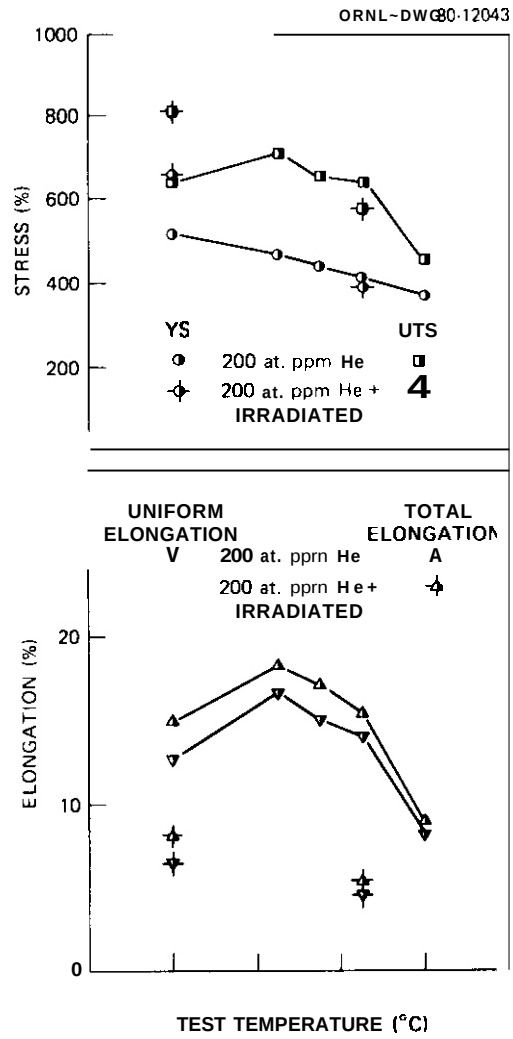

Fig. 5.2.5. Tensile Properties of V–20% Ti That was Injected with 200 at. ppm He and Irradiated in EBR-II. YS = yield stress; UTS = ultimate tensile stress.

compared with those of control samples containing the same level of helium but without neutron irradiation. The results are limited at present, but some trends are clear. For the lowest irradiation and test temperature of 400°C, neutron irradiation has produced a significant increase in yield and ultimate tensile stress and decrease in uniform and total elongation. The decrease in total elongation results primarily from a decrease in uniform strain. The necking or nonuniform strain is little changed. At 625 and 700°C the strength properties are not significantly altered. However, the elongation is significantly reduced compared with the control specimens at these higher temperatures. We cannot draw conclusions from these limited data regarding effects of the preinjected helium.

5.2.5 Future Work

Tensile tests and scanning electron microscopy examination of the rest of the irradiated specimens are now in progress. Electron microscopy examination is also planned to determine the damage structure (bubble size, dislocation structure, and void distribution) for the injected and the irradiated specimens.

5.2.6 Reference

1. J. A. Horak, "Helium Implantation in Potential CTR Structural Materials," *Controlled Thermonuclear Materials Technology Annu. Prog. Rep. June 30, 1975,* ORNL–5082, p. 40.

5.3 FATIGUE BEHAVIOR OF UNIRRADIATED PATH C ALLOYS — K. C. Liu (ORNL)

5.3.1 ADIP Task

ADIP Task I.B.3, Fatigue Crack Growth in Reactive and Refractory Alloys.

5.3.2 Objective

The objective of this work is to develop baseline fatigue and crack growth information for the Path C refractory metal scoping alloys in the unirradiated condition.

5.3.3 Summary

Results of exploratory fatigue tests on annealed Nb–1% Zr showed that this alloy has about the same fatigue resistance at room temperature and at 650°C. It was also shown that the fatigue lifetime of Nb—1% Zr is superior by a factor of about 10 in comparison with average values obtained for 20%-cold-worked type 316 stainless steel tested at low strain ranges.

Fatigue tests of the ADIP heat of V—15% Cr—5% Ti are presently under way. Test results obtained to date indicate that at room temperature this alloy has marginally better fatigue resistance than Nb-1% Zr. Only one fatigue test on V—15% Cr—5% Ti at 650°C has been completed. This data point fell below the average trend curve of Nb—1% Zr.

5.3.4 Progress and Status

5.3.4.1 Status of Cyclic Fatigue Testing of Nb—1% Zr

Exploratory fatigue tests on unirradiated Nb—1% Zr (not the ADIP heat) were discontinued to initiate scheduled fatigue tests on three vanadium-based alloys from the ADIP heat. Since these tests were exploratory, only a limited number of tests were performed, primarily to check out the long-term operational capabilities of the testing system and its associated control instrument and to examine the vacuum capability needed for Path C alloys testing at high temperature. In spite of such limitations, useful information on the fatigue behavior of Nb—1% Zr was obtained.

Miniature hourglass-shaped fatigue specimens, which were described in detail previously,[1] were used. Tests were performed under fully reversed strain control, using a triangular waveform beginning in compression at a strain rate of 4×10^{-3}/s. Tests results obtained are summarized in Table 5.3.1 and are also represented in Fig. 5.3.1. An average trend curve for unirradiated 20%-cold-worked type 316 stainless steel tested at 430°C is also included in Fig. 5.3.1 for comparison.

Table 5.3.1. Fatigue Lifetime of Nb-1% Zr

Specimen[a]	Test Temperature[b] (°C)	Total Strain Range (%)	Cyclic Lifetime (cycles)
ANZ 111	650	2.0	2,848
ANZ 110	650	1.0	38,420
ANZ 112	650	0.6	1,042,187
ANZ 102	RT	2.0	3,308
ANZ 101	UT	1.0	31,402
CNZ 1	UT	1.0	19,148
CNZ 2	UT	0.5	967,447

[a] ANZ = annealed 1 h at 1400°C in vacuum; CNZ = cold worked.

[b] RT = room temperature.

These limited data suggest that the fatigue behavior of annealed Nb-1% Zr at 650°C is about the same as that at room temperature. Cold-worked Nb-1% Zr appears to be less fatigue resistant than the annealed material, probably because of the reduced ductility.

Figure 5.3.2 shows the peak-to-peak stress amplitude or the stress range for the hysteresis loops as a function of number of cycles for Nb-1% Zr cycled at a total strain range of 1.0%. Continuous cycle tests at room temperature resulted in cyclic softening throughout the test for the cold-worked specimens. Under the same test condition, cyclic softening also occurred in an annealed specimen but practically ceased after 200 to 300 cycles when a stable hysteresis loop was established. However, an annealed specimen tested at 650°C showed a brief initial hardening followed by a gradual cyclic softening until it reached a stable condition at about 1000 cycles.

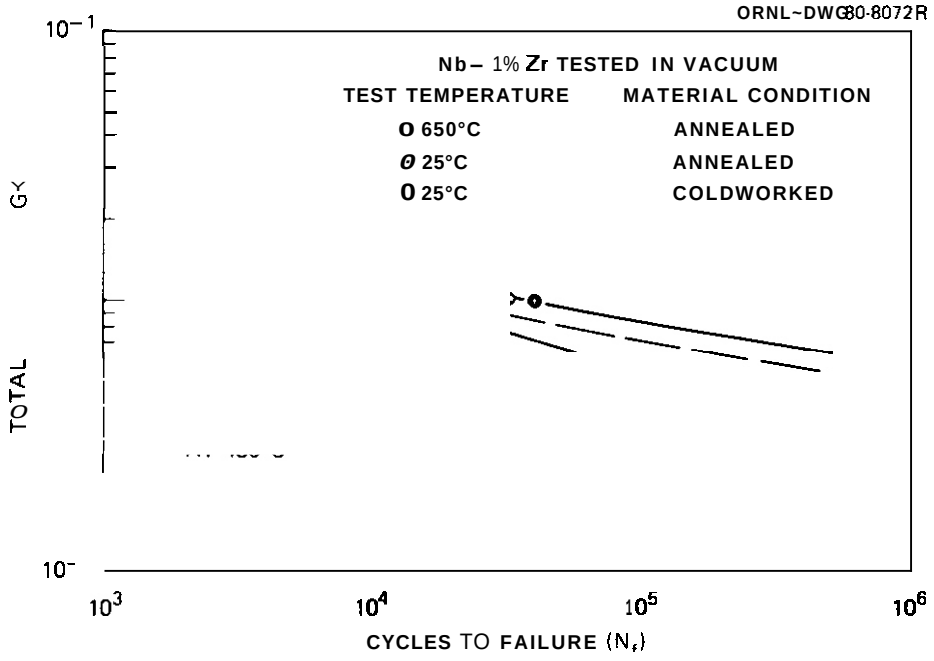

Fig. 5.3.1. Cyclic Fatigue Data for Nb–1% Zr Tested at 25 and 650°C in Vacuum. A trend curve for 20%–cold–worked type 316 stainless steel tested in vacuum at 430°C is shown for comparison.

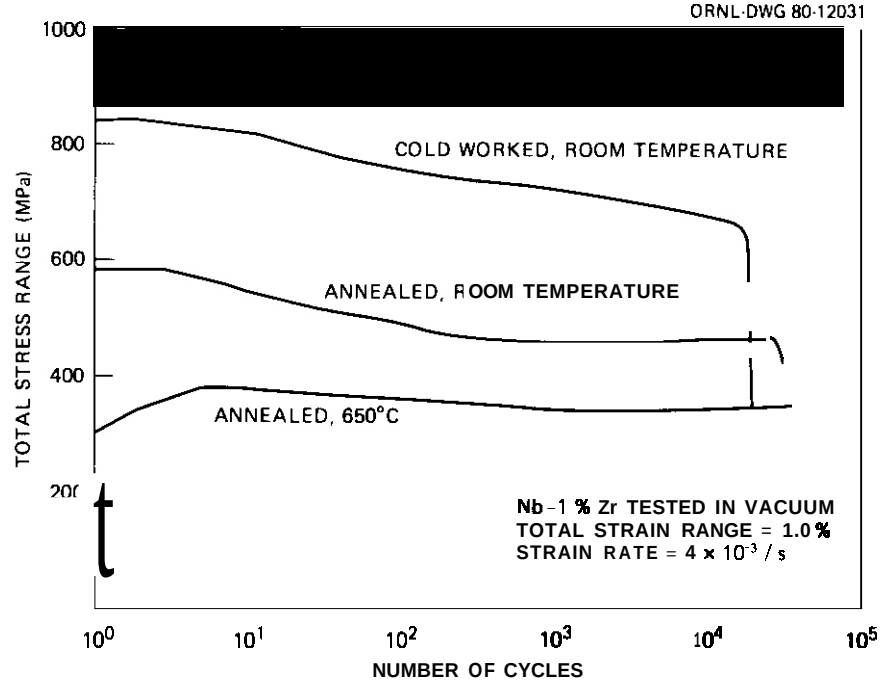

Fig. 5.3.2. Cyclic Stress–Strain Behavior of Nb–1% Zr Tested at 25 and 650°C. All the tests were cycled at ±0.5% strain.

The correlation between such behavior and the cyclic fatigue lifetime is somewhat complex. However, it is reasonable to postulate that high stress amplitude in the cold-worked specimen was a result of the cold-worked structure that has reduced the ductility and fatigue lifetime.

5.3.4.2 Status of Cyclic Fatigue Testing of V-15% Cr-5% Ti

Fatigue tests on V-15% Cr-5% Ti from the ADIP heat have been initiated, and four tests have been completed to date. A fifth test at 650°C is currently under way. Specimens were made from 6.4-mm-diam bars, which were annealed at 1200°C in a vacuum less than 10 μPa for 1 h before machining. Specimens that passed inspections were then stress relieved at the same temperature for 0.5 h. The method of testing, including the test waveform and strain rate as described in the preceding section, was adopted to develop a set of consistent baseline data for Path C alloys. The test condition was altered for strain ranges no greater than *0.6%*. For these tests initial strain control at a strain rate of 4×10^{-3}/s was changed to load control at a higher strain rate of 4×10^{-2}/s after stable elastic cycling was established. This reduces testing time by a factor of about 10.

A matrix of 12 cyclic fatigue tests, as shown in Table 5.3.2, is being followed. Results of completed tests are summarized in Table 5.3.3 and also are presented in Fig. 5.3.3.

Table 5.3.2. Test Schedule[a] for V-15% Cr-5% Ti

Temperature (°C)	Total Strain Range, %			
	2.0	1.0	0.6	0.4
Room Temperature	*	*	*	*
550	*	*	*	*
650	*	*	*	*

[a]Asterisks indicate that tests are scheduled for these temperatures and strain ranges.

Table 5.3.3. Fatigue Lifetime[a] of V—15% Cr—5% Ti (Heat CAM-835B-3)

Specimen	Test Temperature[b] (°C)	Total Strain Range (%)	Cyclic Lifetime (cycles)
AV 53	RT	2.0	4,345
AV 51	RT	1.0	109,125
AV 52"	RT	0.6	>2,047,000
AV 54	650	2.0	1,874
AV 55[d]	650	0.6	>82,000

[a]All tests in vacuum of ≤13 μPa.

[b]RT = room temperature.

"Testing time exceeded 31 d, discontinued temporarily.

[d]Test in progress.

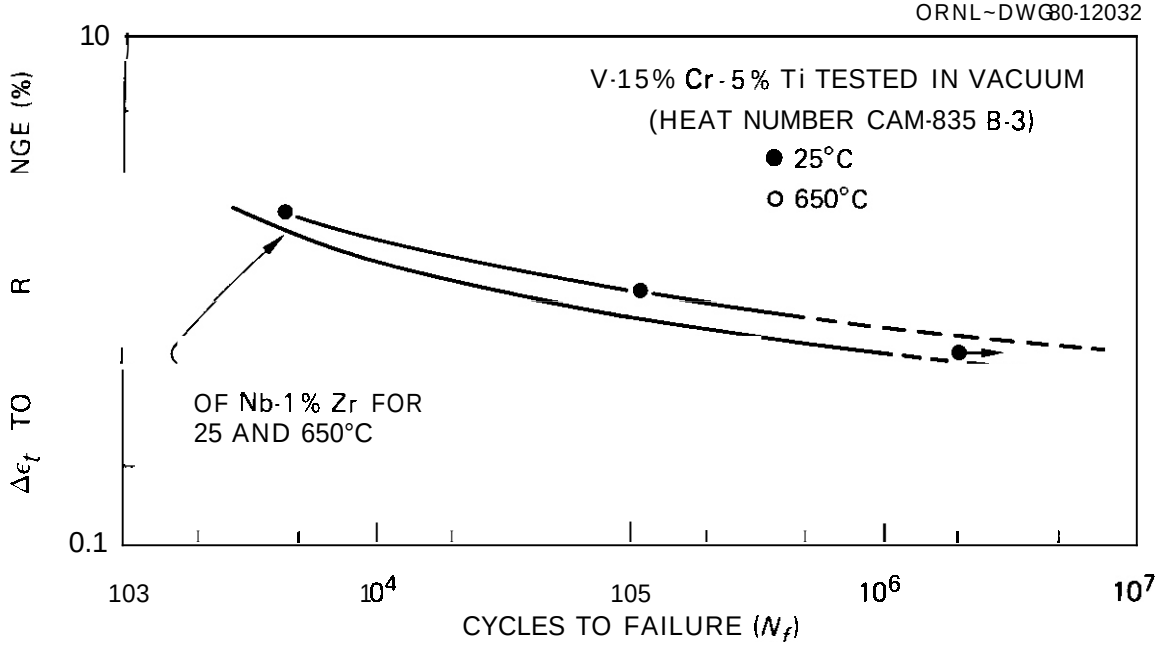

Fig. 5.3.3. Cyclic Fatigue Data for V—15% Cr—5% Ti Tested at 25 and 650°C in Vacuum. An average trend curve for Nb—1% Zr tested at 25 and 650°C is included for comparison.

Examination of Fig. 5.3.3 shows that three room temperature data points fell consistently above the average trend curve for Nb–1% Zr discussed in the preceding section. The test of specimen AV-52 was discontinued after it exceeded 2×10^6 cycles because the testing time had exceeded 31 d with no indication of imminent failure. Alloy V–15% Cr–5% Ti at room temperature appears to have better fatigue resistance than does Nb–1% Zr. However, a single test conducted at a total strain range of 2% indicated that V–15% Cr–5% Ti at 650°C was less fatigue resistant than Nb–1% Zr. A careful examination of the fractured specimen showed that a slight indication of plastic instability had developed near the fracture zone. It is possible that the synergistic effects of the plastic instability from strain cycling at high strain range and the fatigue crack propagation had accelerated the failure. Data scatter is of course another possibility.

Unlike Nb–1% Zr, which exhibited cyclic softening under continuous fatigue tests, —15% Cr–5% Ti appeared to be a cyclic hardening material at strain ranges in excess of about 0.6%, as shown in Fig. 5.3.4. All

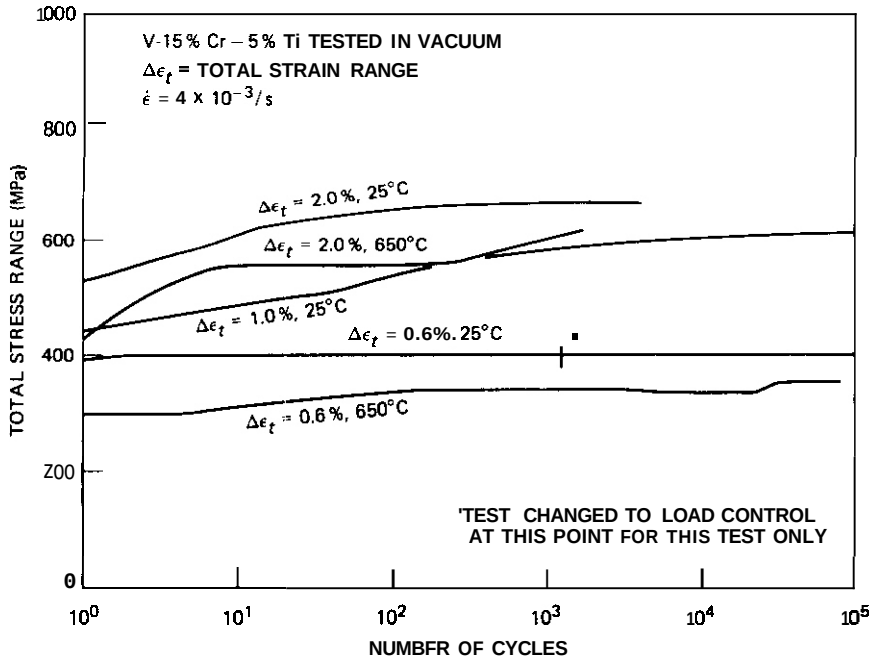

Fig. 5.3.4. Cyclic 'Stress–Strain Behavior of V–15% Cr–5% Ti Tested at 25 and 650°C.

tests at room temperature demonstrating cyclic hardening indicated that strain hardening in V—15% Cr—5% Ti increases monotonically as the number of cycles increases, whereas at 650°C more stability after initial hardening was demonstrated.

5.3.5 Conclusions

Limited data obtained to date indicated that annealed Nb—1% Zr has about the same fatigue resistance at room temperature and at 650°C. It was encouraging to see that three data points for V—15% Cr—5% Ti tested at room temperature fell above the average curve of Nb—1% Zr. However, one test datum at 650°C fell substantially below the same curve. No conclusion will be made until more high-temperature data become available for further evaluation.

5.3.6 Reference

1. K. C. Liu, "Mechanical Property Testing of Unirradiated Path C Alloys," *ADIP Quart. Prog. Rep. Sept. 30, 1979*, DOE/ET-0058/7, pp. 141—43.

6. PATH D ALLOY DEVELOPMENT — INNOVATIVE MATERIAL CONCEPTS

6.1 DEVELOPMENT OF IRON-BASE ALLOYS WITH LONG-RANGE-ORDERED CRYSTAL STRUCTURE — C. T. Liu (ORNL)

6.1.1 AUIP Task

ADIP Task I.B.12, stress-rupture properties of special and innovative materials, and Task I.K. 16, tensile properties of special and innovative materials.

6.1.2 Objective

The objective of this study is to develop a unique class of high-temperdturr alloys — ductile long-range-ordered (LRO) alloys based on $(Fe,Ni)_3V$ — and to evaluate their potential for use as structural naterials for fusion energy systems.

6.1.3 Summary

The iron-base LRO alloys with compositions $(Fe,Ni)_3V$ are being developed for fusion energy applications. The alloys have excellent high-temperature strength and good ductility and fabricability in the ordered state. Studies of phase relations indicate that sigma phase precipitates from the disordered solid solution (gamma) at temperatures above the critical ordering temperature (T_c). Below T_c, atom ordering takes place in the alloys through the peritectoid reaction $\gamma + \sigma \rightarrow \gamma'$, where γ' is the cubic ordered phase (Ll_2-type) formed on the face-centered cubic (fcc) lattice. The sigma phase region can he reduced or eliminated by adding small amounts of titanium. Tensile tests as a function of temperature indicate that the LRO alloys with base compositions show a ductility minimum around T_c. However, modifying the alloys with titanium significantly improves their ductility at elevated temperatures. The tensile properties of the base and titanium-modified alloys are not affected by long-term aging at 550°C. Preliminary evaluation of material prepared by using commercially produced ferrovanadium as feed material indicates this as a promising approach to lowering the alloy production cost.

6.1.4 Progress and Status

6.1.4.1 Introduction

Long-range-ordered alloys generally offer significant advantages over conventional or disordered alloys for high-temperature structural applications.[1,2] This is based largely on relatively slow solid-state diffusion processes and unique dislocation dynamics of ordered lattices. The main difficulty limiting the use of LRO alloys is their low ductility and fabricability in the ordered state. Recently, our work on cobalt-base LRO alloys with compositions $(Co,Fe)_3V$ has overcome this limitation.[3] We have demonstrated that the ductility of the ordered alloys can be controlled by adjusting alloy composition and ordered crystal structure. The alloys with cubic ordered structure ($L1_2$-type) are ductile and fabricable with tensile elongation in excess of 30% at room temperature. Alloys with lower cobalt contents would offer the potential of higher tritium breeding ratios, lower levels of structural activation, and lower alloy production costs. For these reasons we are developing cobalt-free, iron-base LRO alloys for fusion applications at temperatures to 700°C.

6.1.4.2 Alloy Preparation and Fabrication

The iron-base LRO alloys were prepared according to the composition $(Fe,Ni)_3V$. Table 6.1.1 lists the nominal composition of the alloys we have prepared so far. The base alloys $(Fe,Ni)_3V$ are also modified with less than 1% Ti for further improvement in metallurgical and mechanical properties.

The alloys LRO-35, -37, -38, -39, and -41 currently being evaluated were made by arc melting or electron-beam melting and drop casting into a 25- by 13- by 140-mm rectangular mold. The ingots were clad in molybdenum cover sheets and rolled to a total thickness reduction of 80% at 1100°C. After breakdown by hot rolling, the alloy plates were cold rolled from 2.5 to 0.76 mm with an intermediate anneal at 1100°C. The as-rolled sheets were of good quality with no indication of edge or end cracks (Fig. 6.1.1). Thus, titanium additions do not affect the good fabricability of the iron-base LRO alloys.

Table 6.1.1. Alloy Composition of the Iron-Base Long-Range-Ordered Alloys Currently Being Evaluated

Alloy	Base Composition (wt %)	Ti-Modified Composition (wt %)	Critical Ordering Temperature, T_c (°C)
LRO-16	Fe—31.0 Ni—23.0 V		670
-35		Fe—31.8 Ni—22.5 W. 4 Ti	690
-39		Fe—31.8 Ni—22.0 W. 9 Ti	
LRO-40	Fe—35.7 Ni—22.9 V		
-41		Fe—35.7 Ni—22.0 W. 9 Ti	
LRO-20	Fe—39.5 Ni—22.9 V		700
-37		Fe—39.5 Ni—22.4 W. 4 Ti	720
-38		Fe—39.5 Ni—22.0 W. 9 Ti	

Y-153908

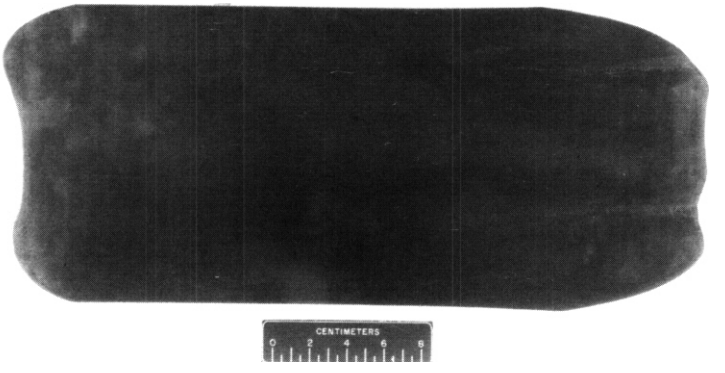

Fig. 6.1.1. Alloy Sheet of LRO-37 Produced by Cold Rolling from 2.5 to 0.8 mm at Room Temperature.

6.1.4.3 Ordered Structure and Phase Relationships

The phase relationships and ordered structure in the iron-base LRO alloys were studied by quenching and aging in the temperature range from 300 *to* 1200°C. Figure **6.1.2** shows the phase relationships in the base alloy LRO-20 (Fe—39.5% Ni—22.9 V) and **in** the titanium-modified alloy LRO-37 (Fe—39.5% *Ni-22.4%* V—0.4% Ti) determined by x-ray diffraction and metallographic examination. **The** disordered fcc solid solution (gamma phase) existing in the LRO-20 at high temperatures was retained at room temperature on quenching from above 750°C. The gamma phase decomposes into $\gamma + \sigma$ in a narrow temperature range, 710 to 750°C. Below 710°C atom ordering takes place in the alloy through the peritectoid reaction $\gamma + \sigma \rightarrow \gamma'$, where γ' is the cubic ordered phase (Ll_2 type). The gamma prime can also be produced by aging the quenched gamma at temperatures below T_c. The existence of sigma phase in the base alloy is not desirable because, in some cases, the retention of sigma phase below T_c would lower the ductility and weaken atomic order in the alloys. The sigma phase

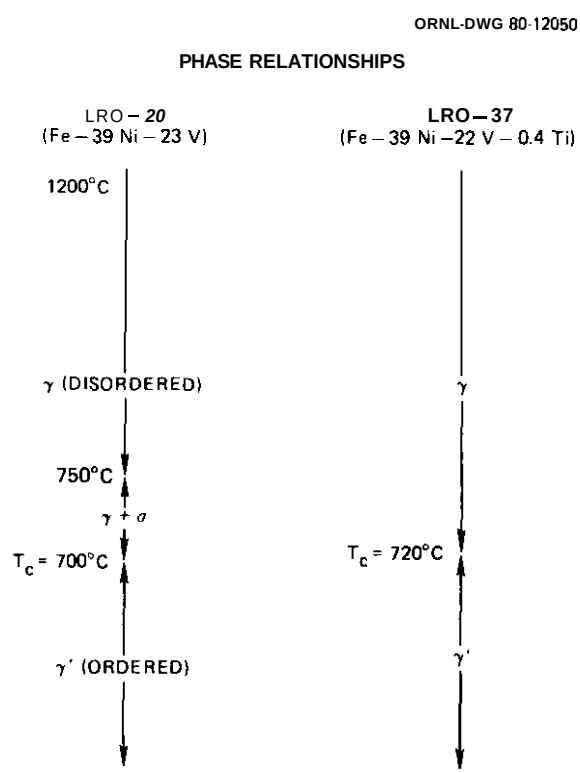

Fig. 6.1.2. Phase Relationships of the Base Alloy LRO-20 and the Titanium-Modified Alloy **LRO-37.**

region can be substantially reduced or completely eliminated (depending on nickel content) by adding small amounts of titanium. As indicated in Fig. 6.1.2, the sigma phase formation is completely eliminated in **LRO-37** containing *0.4%* Ti. We currently adjust nickel and titanium concentration for control of sigma phase formation in iron-base **LRO** alloys.

The T_c was estimated from measurement of thermal expansion, x-ray diffraction, and measurement of mechanical properties. Adding small amounts of titanium appears to increase the critical ordering temperature. As shown in Fig. 6.1.2 and Table 6.1.1, the T_c of the titanium-modified alloy is higher than that of base alloy by about **20°C.**

6.1.4.4 Tensile Properties

Tensile properties of titanium-modified alloy **LRO-37** and the base alloy **LRO-20** were determined on sheet specimens at a strain rate of 3.3×10^{-3}/s. Figure 6.1.3(a) shows a plot of yield strength as a function of test temperature. The yield strength of the titanium-modified alloy, like the base alloy, increases with temperature and reaches a maximum near T_p, which is about **720°C.** The positive temperature dependence of the strength makes the **LRO** alloys much stronger than conventional alloys at elevated temperatures. For instance, the yield strength of the ordered alloys reaches 400 MPa, which is about **4** times that of annealed type 316 stainless steel at **650°C.** The strength of the **LRO** alloys decreases sharply above T_c as a result of loss of long-range order.

Figure 6.1.3(b) compares the ductility of the base alloy **LRO-20** with the titanium-modified alloy **LRO-37.** Both alloys are ductile with tensile elongation in excess of **35%** at temperatures below **450°C.** Above **450°C** the ductility of the base alloy **LRO-20** decreases substantially with temperature and reaches a minimum of 14.6% near T_c. In comparison, the ductility of the titanium-modified alloy is much less dependent on temperature and shows only a moderate drop near T_c. The ductility minimum of the titanium-modified alloy is **28.3%** at **720°C.** Thus, alloying with titanium additions significantly improves the ductility of the iron-base alloys at elevated temperatures.

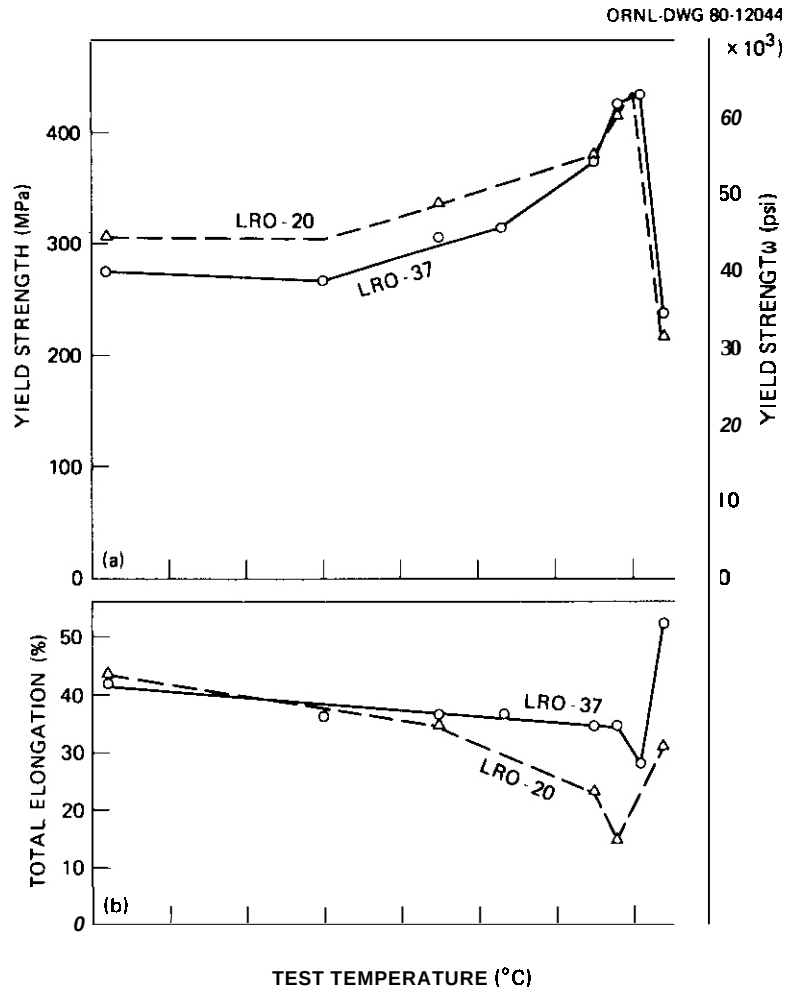

Fig. 6.1.3. Plot of Yield Strength and Total Elongation of the Base Alloy LRO-20 and the Titanium-Modified Alloy LRO-37 as a Function of Test Temperature.

6.1.4.5 Long-Term Aging Study

To evaluate the structural stability and mechanical properties of iron-base LRO alloys, specimens of the base alloy LRO-20 and titanium-modified alloy LRO-35 (Fe–31.8% Ni–22.5% Y–0.4% Ti) were encapsulated in vacuum and aged at 550°C. The tensile properties of the aged specimens were determined at room temperature after 2000 h at temperature. Table 6.1.2 shows the tensile properties of the aged material and compares them with the properties of control material. The comparison indicates that long-term aging at 550°C has little adverse effect on the tensile properties of the iron-base LRO alloys. Characterization of the structure of the aged material is in progress.

Table 6.1.2. Room Temperature Tensile Properties of Long-Range-Ordered Alloys Aged 2000 h at 550°C in Vacuum

Alloy	Condition[a]	Strength, MPa (ksi)		Total Elongation (%)
		Yield	Tensile	
LRO–20	Control	309 (44.9)	1054 (153.0)	43.8
LRO–20	Aged	336 (48.8)	1188 (172.5)	40.8
LRO–35	Control	270 (39.2)	1124 (163.1)	42.1
LRO–35	Aged	309 (44.8)	1216 (176.5)	40.3

[a]Control indicates no aging treatment.

6.1.4.6 Preparation of Iron-Base LRO Alloys by Using Ferrovanadium

The iron-base LRO alloy currently being developed at ORNL contains 22 to 23 wt % V. The material cost of the alloys would be lowered by a factor greater than 20 if commercially produced ferrovanadium can be used in place of pure vanadium as feed material. The commercial ferrovanadium generally contains 80 to 85% V and 10 to 15% Fe with impurities such as 1 to 4% O and less than 2% Al and Si. To study the feasibility of using ferrovanadium, two 400-g alloy ingots of LRO–37 were prepared with as-received and electron-beam-purified ferrovanadium. The fabricability was then checked by hot rolling at 1100°C followed by a 50% cold roll at room temperature. Both ingots were successfully rolled to 0.6-mm sheets with excellent quality. This result demonstrates that preparation of iron-base LRO alloys with ferrovanadium does not impair their fabricability and ductility. The evaluation of their mechanical properties is in progress.

6.1.5 Conclusions and Future Work

The iron-base LRO alloys with compositions listed in Table 6.1.1 are being developed for possible fusion energy applications. The LRO alloys have excellent high-temperature strength and good ductility and fabricability in the ordered state. Alloying with less than 1% titanium

significantly improves the metallurgical and mechanical properties of the iron-base LRO alloys. The sigma phase with tetragonal crystal structure is observed in the base alloys at temperatures above T_c. The sigma phase region can be reduced or completely eliminated by titanium additions. The base alloys show a ductility minimum around T_c; however, modification of the alloys with titanium significantly improves their ductility at elevated temperatures. The tensile properties of the base and titanium-modified alloys are little affected by long-term aging at 550°C.

Our program is continuing to develop and characterize the iron-base ordered alloys for fusion energy applications.

6.1.6 References

1. N. S. Stoloff and K. G. David, "The Mechanical Properties of Ordered Alloys," *Prog. Mater. Sci.* 13(1): 1–84 (1966).
2. B. H. Kear, C. T. Sims, N. S. Stoloff, and J. H. Westbrook, Eds., *Ordered Alloys — Structuml and Physical Metallurgy, Proc. 3d Bolton Landing Conference, Lake George, N. Y., Sept. 8–10, 1969,* Claitor's Publishing Division, Baton Rouge, La., 1970.
3. C. T. Liu and H. Inouye, "Control of Ordered Structure and Ductility of $(Fe,Co,Ni)_3V$ Alloys," *Metall. Tmns.* 10A(10): 1515–25 (1979).

6.2 THE EFFECT OF 4-MeV NICKEL ION IRRADIATION ON THE MICROSTRUCTURE OF $(Fe,Ni)_3V$ LONG-RANGE-ORDERED ALLOYS — D. N. Braski (ORNL)

6.2.1 ADIP Task

ADIP Task I.C.5, Microstructure and Swelling in Special and Innovative Materials.

6.2.2 Objective

The objective of this research is to define the response of a new class of $(Fe,Ni)_3V$ long-range-ordered (LRO) alloys to both neutron and ion irradiation with the overall goal of evaluating the potential use of this alloy class as structural material for fusion energy systems.

6.2.3 Summary

The unirradiated microstructure of $(Fe_{61}Ni_{39})_3V$ contains a relatively uniform distribution of small MC-type precipitate particles and large, widely scattered islands of sigma phase. Essentially the same alloy, except for a 0.4 wt % Ti addition, contained scattered inclusions with MC-type precipitate particles decorating the dislocations at the inclusion-matrix interfaces.

Irradiation of $(Fe_{61}Ni_{39})_3V$ at 525, 570, 625, and 680°C with 4-MeV (0.6-pJ) nickel ions to 70 dpa with the simultaneous injection of helium and hydrogen produced cavities, a high density of dislocation loops, and a redistribution of MC-type precipitate particles. The alloy remained ordered throughout the irradiation except at 680°C, which was above its critical ordering temperature of about 670°C. The irradiation also produced a high density of dislocations in the titanium-modified alloy but only a few small cavities at 525 and 570°C. No cavities were observed at either 625 or 680°C. The MC-type particles precipitated in the modified alloy at all bombardment temperatures. As the bombardment temperature was increased, the precipitate particle size also increased. However, the number of these particles decreased. The mechanism by which titanium enhanced the resistance of $(Fe_{61}Ni_{39})_3V$ to ion damage is unclear.

6.2.4 Progress and Status

6.2.4.1 Introduction

The relative resistance of $(Fe,Ni)_3V$ LRO alloys to radiation damage has been studied experimentally by bombarding them with 4-MeV nickel ions. The effects of the bombardment on the microstructures of these alloys have been evaluated by transmission electron microscopy (TEM) and will be correlated later with results obtained from neutron (reactor) irradiation of the same materials. This report summarizes the qualitative TEM results for the iron-base alloy LRO-16G, which was bombarded to 70 dpa with simultaneous injection of helium and hydrogen at temperatures of 525, 570, 625, and 680°C. We will also report the effect of adding 0.4 wt % Ti on the resistance of the alloy to radiation. The quantitative TEM results concerning swelling, etc. will be presented and will be compared with similar data collected for a cobalt-base LRO alloy and 20%-cold-worked type 316 stainless steel in a later report.

6.2.4.2 Experimental Procedure

Ingots (about 0.3 kg) of two iron-base LRO alloys (see Table 6.2.1 for composition) were arc melted under argon. The molybdenum-wrapped ingots were then hot rolled at 1100°C to a thickness of about 1 mm. The thickness of the sheet was further reduced to about 0.6 mm by cold rolling. Disks with 3-mm diameters were electrical-discharge machined from the sheet and heat-treated to the ordered condition. The LRO-16G disks were

Table 6.2.1. Alloy Compositions

Alloy	Content						
	Wt %				Nominal wt ppm		
	Fe	Ni	V	Ti	C	N	O
LRO-16G	46.0	31.0	23.0		21	106	95
LRO-35F	45.3	31.8	22.5	0.4	63	100	100

annealed at 1130°C for 15 min, were quenched in water, and were aged in a vacuum furnace at 605°C for 5.5 d. The LRO–35F disks were annealed at 1200°C in an attempt to avert sigma phase formation; were quenched in water; and were aged at 650°C for 3 d, then at 600°C for 30 h, and finally at 500°C for 60 h. Both sides of the disks were ground flat with 600–grit emery paper, and one side of each disk was polished to a mirror finish with vibratory polishing equipment.

The disks were bombarded in the ORNL dual ion beam facility[1] with 4–MeV nickel ions to a dose of 70 dpa at 525, 570, 625, and 680°C. Helium and hydrogen ions were simultaneously injected at levels of 8 and 28 at. ppm/dpa, respectively. The TEM specimens were prepared by electro–polishing 0.50 ± 0.15 μm of material away from the polished (bombarded) surface to reach the calculated damage layer. The polishing solution contained 125 ml of concentrated H_2SO_4 and 875 ml of methanol. Then each specimen was jet polished from the side opposite that which was bombarded, using the same solution and a current density of about 65 kA/m^2 until perforation occurred. The TEM specimens were examined in a 120-kV electron microscope with a eucentric double–tilt specimen stage.

6.2.4.3 Results

The composition of LRO–16G given in Table 6.2.1 may also be expressed in chemical notation as $(Fe_{61}Ni_{39})_3V$. Its crystal structure is ordered face–centered cubic (fcc) or Ll_2. The microstructure of LRO–16G before ion irradiation (Fig. 6.2.1) consisted of about 10-nm-diam MC–type precipitate particles dispersed in the ordered matrix and at grain boundaries. An approximately 0.25-μm zone denuded of precipitate particles was observed on both sides of all grain boundaries. These particles have not yet been analyzed, but similar ones in the cobalt–base alloys were VC or V(C,N,O), in which N and O may substitute for C in the precipitate particle lattice. The precipitate particles exhibit interstitial strain contrast as a result of the MC lattice parameter being substantially larger than that of the matrix. Large islands of sigma phase were also present in the microstructure, as shown in Fig. 6.2.2. The islands were not single cyrstals but were composed of many tiny grains that were often

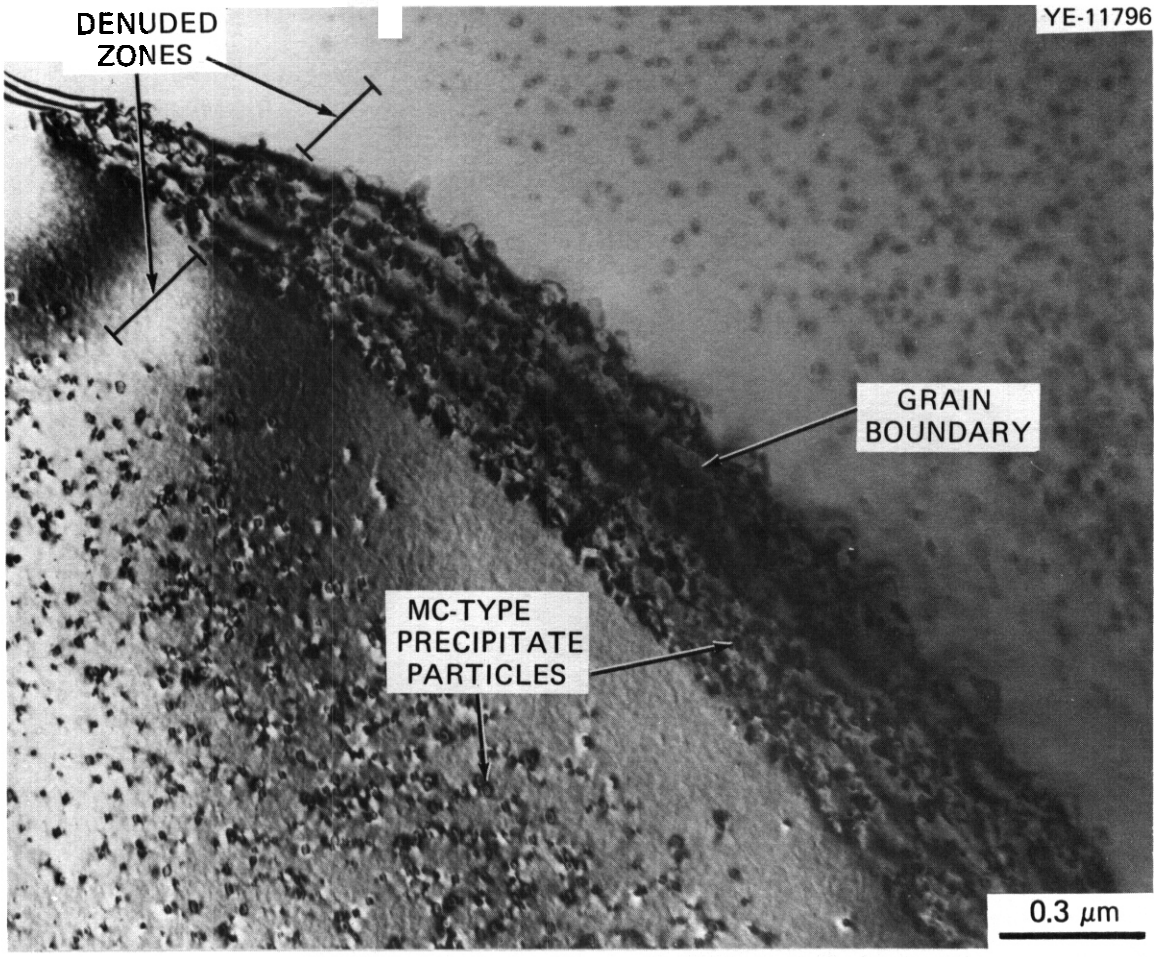

Fig. 6.2.1. The LRO-16G Microstructure Before Ion Irradiation.

heavily faulted. A zone denuded of precipitate particles was also observed at the sigma phase boundary. Selected area electron diffraction confirmed that the sigma phase had a tetragonal structure with c = 0.46 nm and a = 0.88 nm, which agrees with the x-ray data for sigma phase found in this system of alloys.[2] After irradiation with nickel ions, the microstructure contained a high density of small dislocation loops and dislocation segments, as shown in the micrograph in Fig. 6.2.3, which was taken under dynamical or "two-beam" imaging conditions. When the imaging conditions were changed to obtain kinematical conditions, numerous cavities were observed at all four bombardment temperatures, as shown in Fig. 6.2.4. With increasing temperature the average cavity size increased (Fig. 6.2.4). There was a narrow range of sizes for both 525 and 570°C

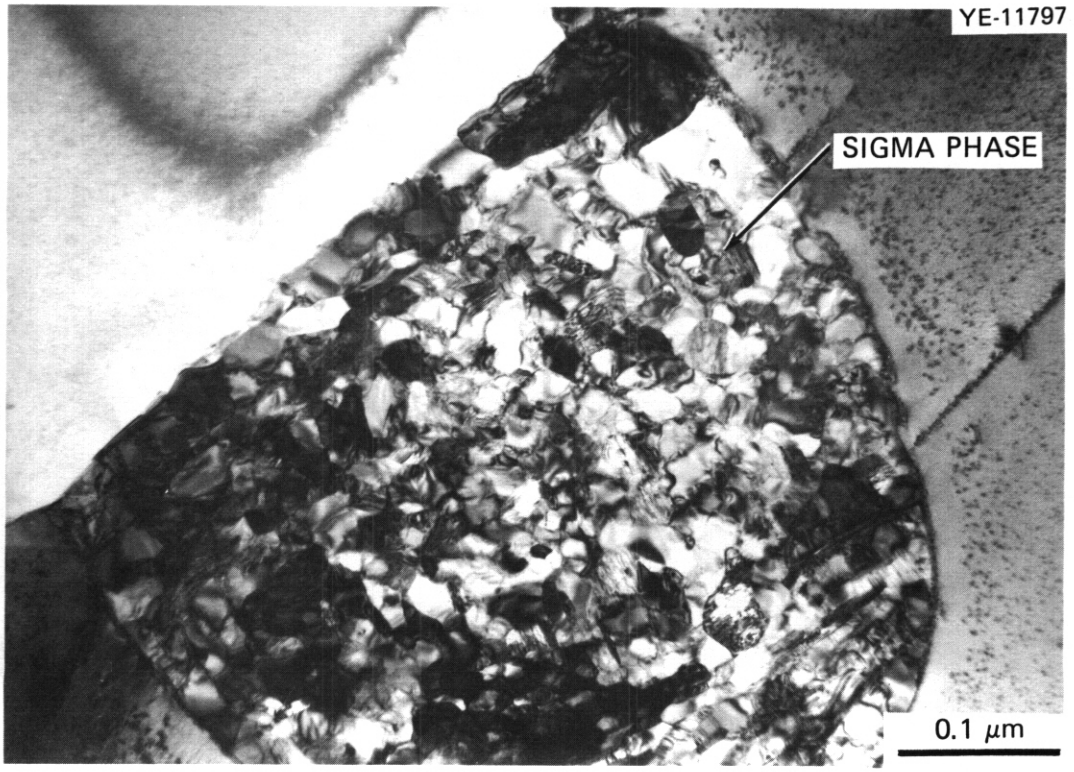

Fig. 6.2.2. Large Isolated Sigma Phase Particle in LRO-16G Before Ion Irradiation.

(Fig. 6.2.5), but a bimodal distribution was produced at 625 and 680°C. Of course the wide distribution of the larger cavities was indicative of the greater swelling that occurred in LRO-16G at the higher bombardment temperatures. At 625 and 680°C the large cavities (Fig. 6.2.4) were faceted, while the cavities with diameters no greater than about 10 nm were spherical. This could be an indication that the large cavities were more "void-like" and contained less helium and hydrogen than needed to balance the surface tension forces. Conversely, the small spherical bubbles would then be considered "bubble-like" and may contain enough gas to balance the bubble surface tension. This interpretation is based on studies of bubble faceting[3] and of annealing of stainless steel implanted with helium.[4] The LRO-16G alloy remained ordered after 70 dpa at all temperatures except 680°C. In this case the disordering was not caused by the irradiation but resulted from the bombardment temperature being about 10°C above the critical ordering temperature for the alloy. At 625°C the large cavities were coated with MC precipitate particles, as shown in the

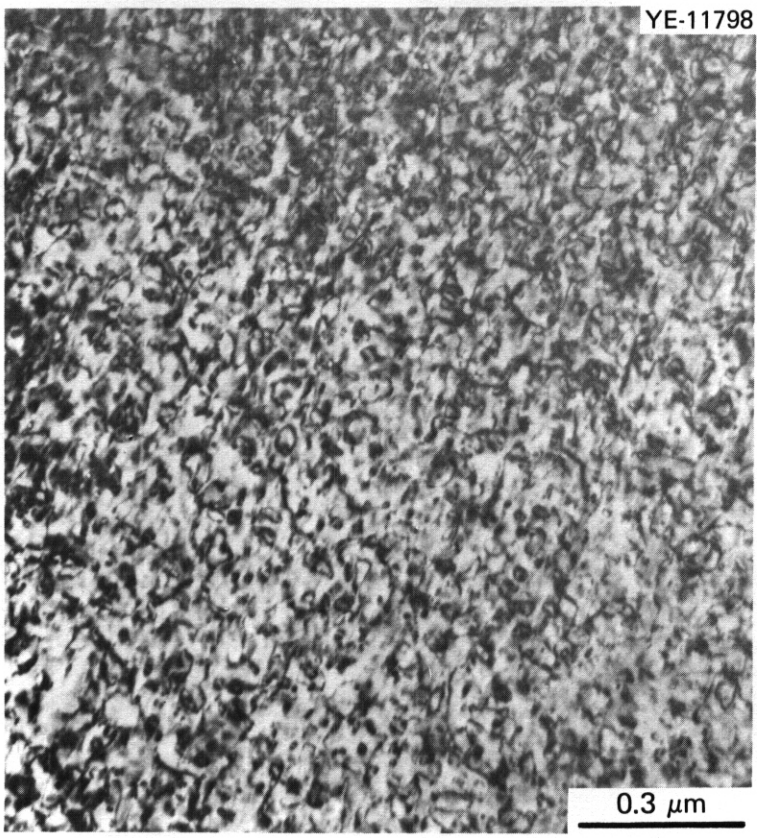

Fig. 6.2.3. Microstructure of LRO-16G after 70 dpa from Nickel Ions with Simultaneous Injection of 8 at. ppm/dpa He and 28 at. ppm/dpa H at 525°c, Showing Small Dislocation Loops and Segments.

bright and dark field micrographs in Fig. 6.2.6. After comparing this observation with the original MC precipitate particle distribution shown in Fig. 6.2.1, one must conclude that the irradiation has caused their redistribution. Redistribution of precipitate particles in alloys from both ion and neutron irradiation has been observed by other investigations.[5]

The ordered alloy LRO-35F had the same composition as LRO-16G except for an 0.4 wt % addition of titanium (Table 6.2.1). Furthermore, it was examined after identical ion irradiation conditions. The effect of the small titanium additions was quite significant. To begin with, the unirradiated microstructure differed in that the small MC-type precipitate particles were not nearly as uniformly distributed in the matrix, and sigma phase was absent. Instead, there were a few large scattered inclusions with interfacial dislocations that were decorated with tiny

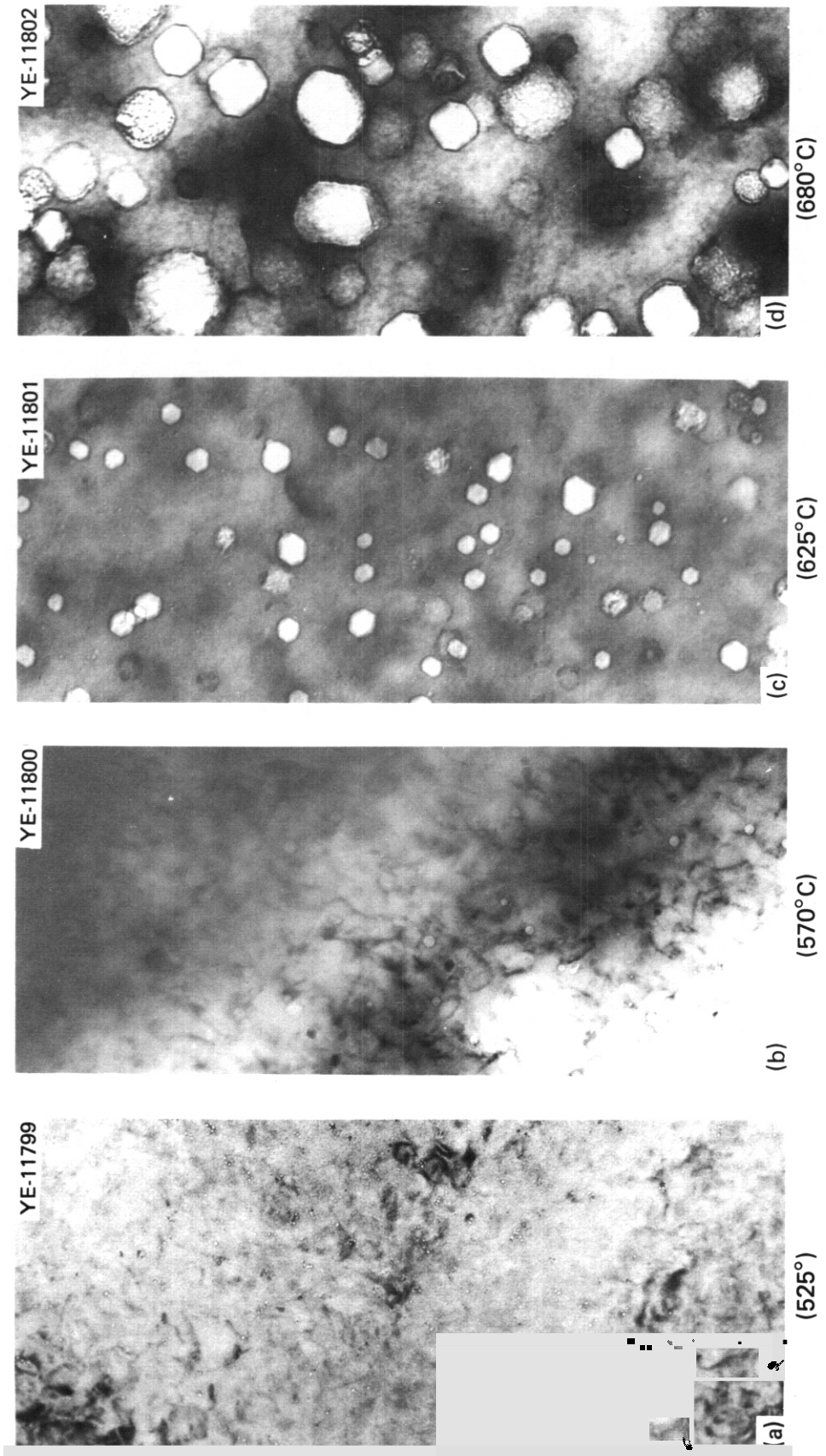

Fig. 6.2.4. Cavities in LRO-16G After 70 dpa from Nickel Ion Irradiation with 8 at. ppm/dpa He and 28 at. ppm/dpa H Simultaneously Injected at (a) 525, (b) 570, (c) 625, and (d) 680°C.

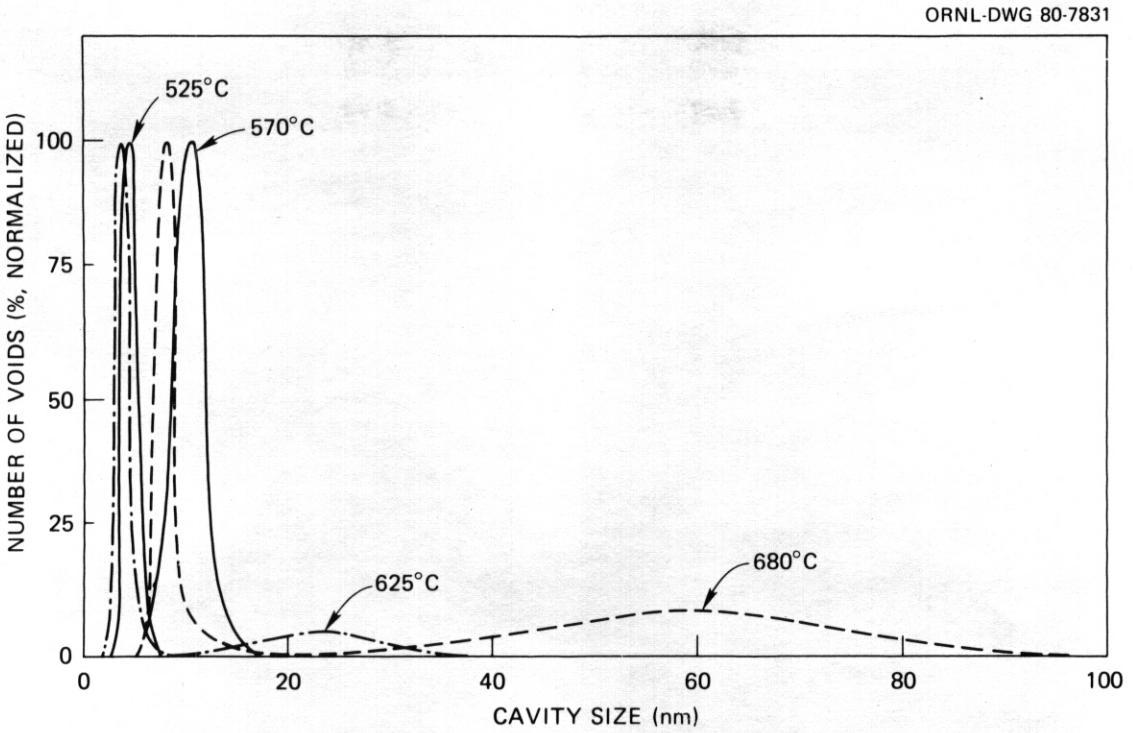

Fig. 6.2.5. Cavity Size Distribution in LRO-16G after 70 dpa from Nickel Ion Irradiation with Simultaneous Injection of 8 at. ppm/dpa He and 28 at. ppm/dpa H.

MC-type precipitate particles, as shown in Fig. 6.2.7. The circular patches seen in the micrograph were artifacts on the foil surfaces caused by electropolishing.

After irradiation, the LRO-35F microstructure contained a high density of loops and dislocation segments, as was observed in the LRO-16G specimens. A relatively uniform distribution of MC-type precipitate particles was also observed. The bright and dark field micrographs in Fig. 6.2.8 show that, as higher bombardment temperatures are reached, the dislocation density decreases, while the precipitate particles become larger and less numerous.

A small number of cavities with diameters of about 3.5 nm was observed in the LRO-35F specimens irradiated at 525 and 570°C. No cavities were observed in specimens irradiated at 625 and 680°C. After irradiation at 680°C, the LRO-35F microstructure was disordered because, as in LRO-16G, 680°C was above the critical ordering temperature. From

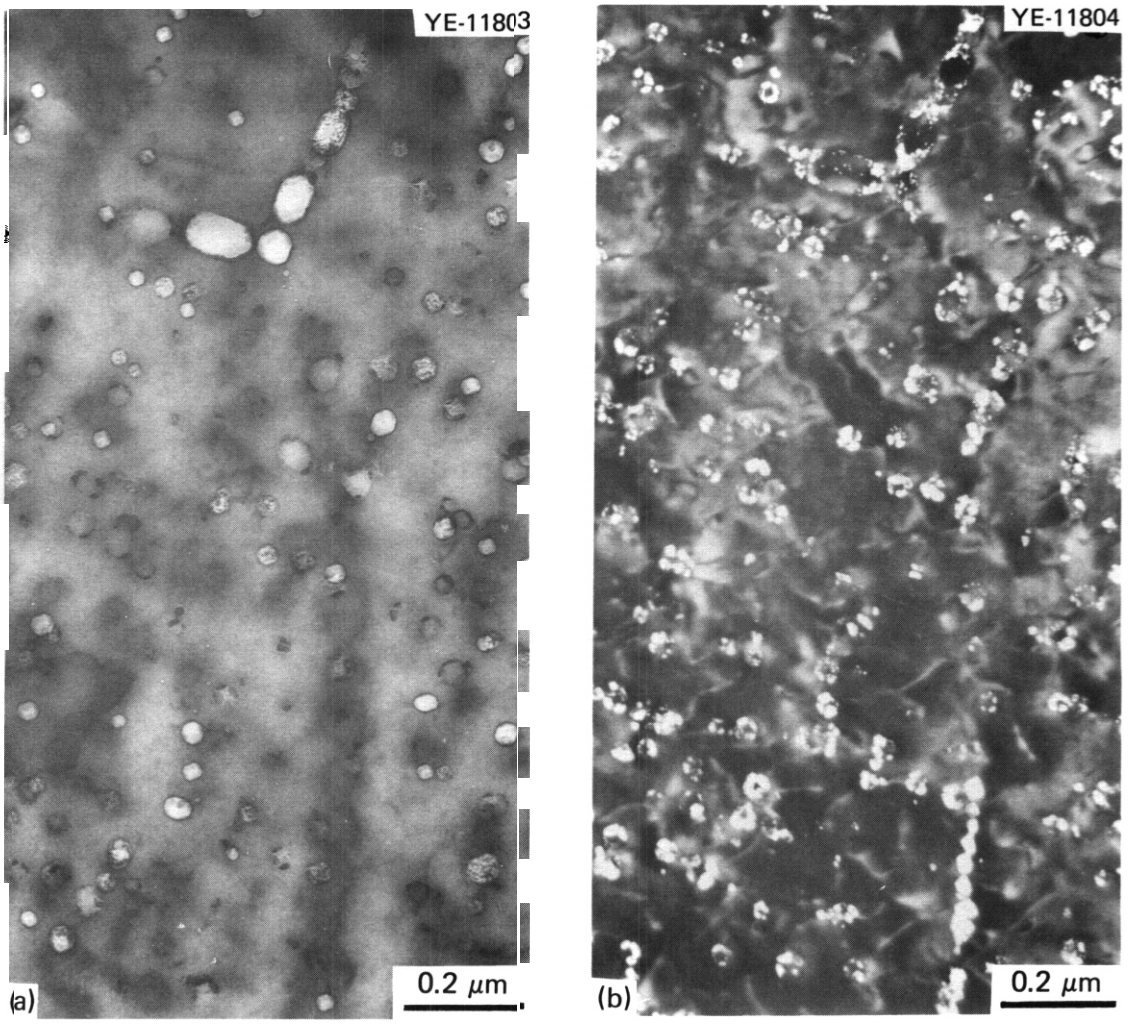

Fig. 6.2.6. The Decoration of Cavities in LRO-16G Irradiated to 70 dpa from Nickel Ions with Simultaneous Injection of 8 at. ppm/dpa He and 28 at. ppm/dpa H at 625°C. (a) Bright field. (b) Dark field using (220) precipitate reflection.

these results we find that the 0.4 wt % addition of titanium has produced an ordered alloy more resistant to swelling under nickel ion damage. The mechanism whereby titanium accomplishes this improved microstructural response to irradiation is not clear at this time.

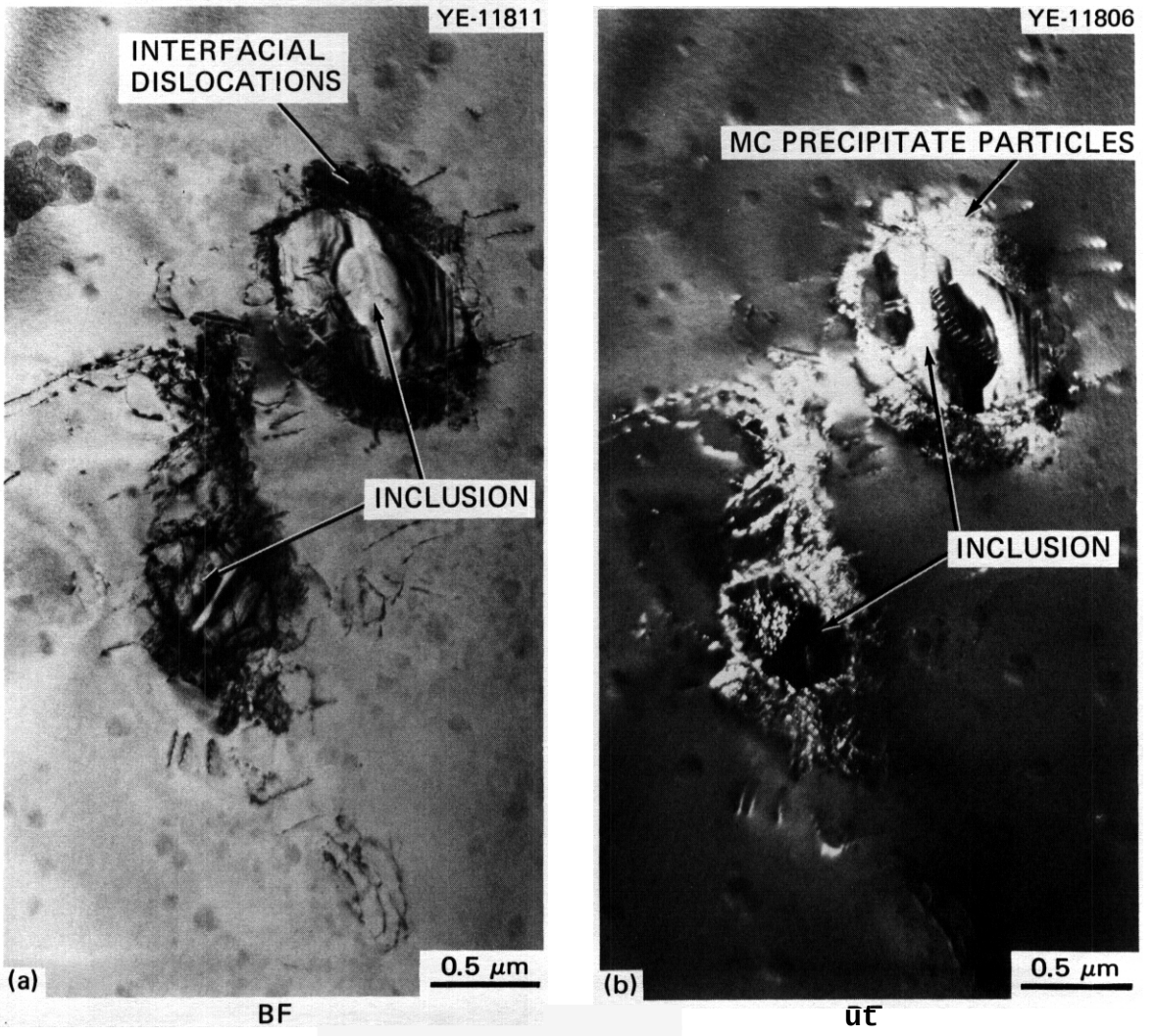

Fig. 6.2.7. The LRO-35F Microstructure Before Ion Irradiation, Showing MC-Type Precipitate Particles on Interfacial Dislocations. (a) Bright field. (b) Dark field using (200) precipitate reflection.

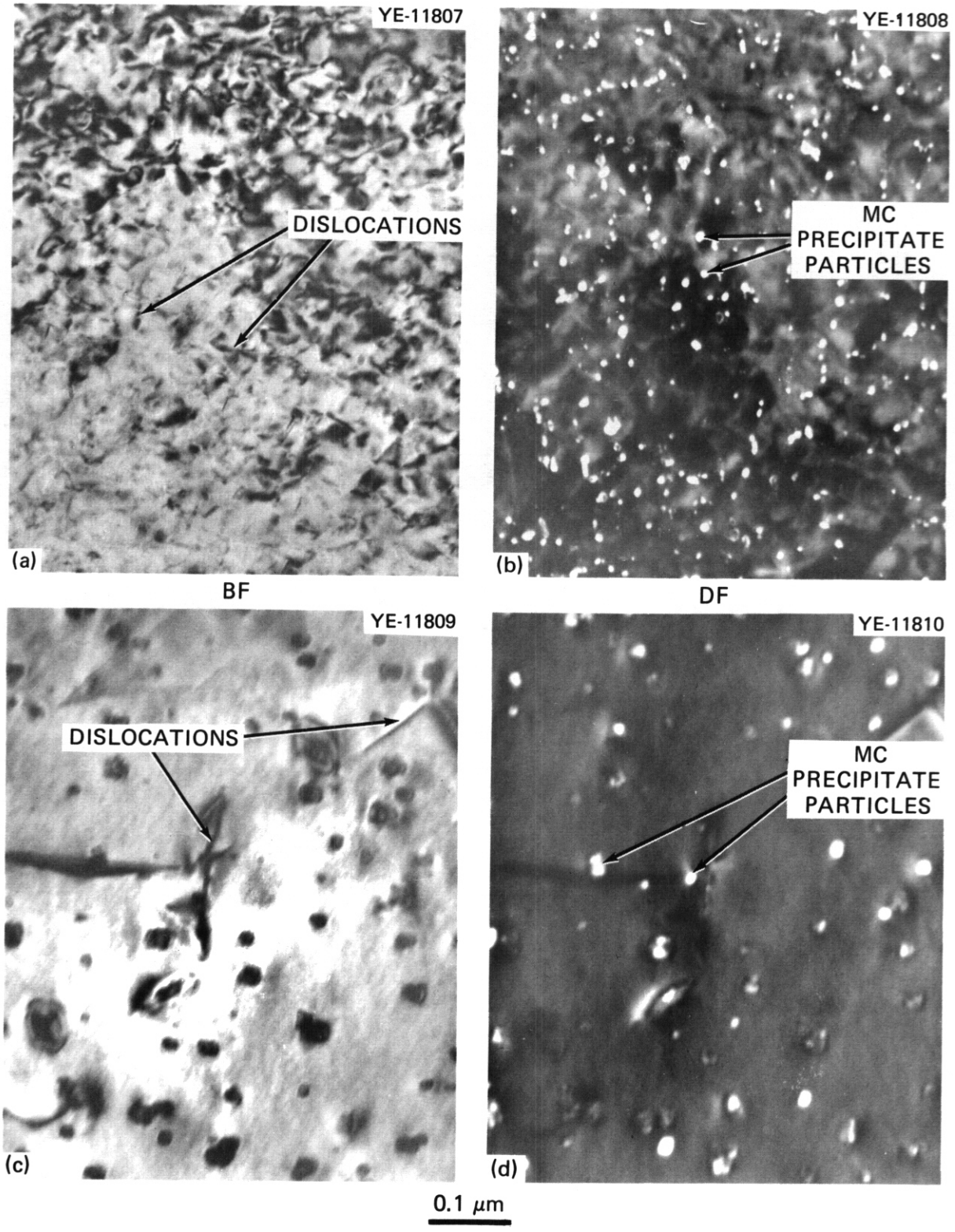

Fig. 6.2.8. Bright and Dark Field Images of the LRO-35F Alloy After Nickel Ion Irradiation to 70 dpa with Simultaneous Injection of 8 at. ppm/dpa He and 28 at. ppm/dpa H at (a) 525°C (Bright Field), (b) 525°C [Dark Field Using (220) Precipitate Reflection], (c) 680°C (Bright Field), and (d) 680°C [Dark Field Using (200) Precipitate Reflection].

6.2.5 Conclusions and Future Work

The addition of 0.4 wt % Ti to the base $(Fe_{61}Ni_{39})_3V$ LRO alloy markedly improved its resistance to swelling under nickel ion irradiation for the conditions used in the experiment. The mechanism whereby this improvement was accomplished is not clear at this time.

Future work will include the quantification of the microstructural data already collected for LRO-16G and LRO-35F and comparison of the results with those for a cobalt-base LRO alloy and type 316 stainless steel (20% cold worked) under the same irradiation conditions. Other ion irradiation experiments are being planned for an iron-base LRO alloy with composition modified to reduce formation of sigma phase. Other studies will concentrate on establishing the role of titanium in this class of alloys. Finally, the effects of neutron irradiation on the microstructure of the iron-base LRO alloys will be evaluated.

6.2.6 References

1. M. B. Lewis, N. H. Packan, G. F. Wells, and R. A. Buhl, "Improved Techniques for Heavy Ion Simulation of Neutron Radiation Damage," *Nucl. Instrum. Methods* 167(2): 233 (1979).
2. C. T. Liu and H. Inouye, "Control of Ordered Structure and Ductility of $(Fe,Co,Ni)_3V$ Alloys," *Metall. Trans.* 10A(10): 1515–25 (1979).
3. R. S. Nelson, D. J. Mazey, and R. S. Barnes, "The Equilibrium Shape and Size of Holes in Solids," *Philos. Mag.* 11: 91 (1965).
4. D. N. Braski, H. Schroeder, and H. Ullmaier, "The Effect of Tensile Stress on the Growth of Helium Bubbles in an Austenitic Stainless Steel," *J. Nucl. Mater.* 83(2): 265–77 (1979).
5. A. L. Chang and M. Baron, "Particle Redistribution and Phase Stability in Ion and Neutron Irradiated Gamma Prime Strengthened Fe-Cr-Ni Based Alloys," *J. Nuct. Mater.* 83(1): 214–22 (1979).

6.3 PROPERTIES OF RAPIDLY SOLIDIFIED NUCLEAR GRADE 316 STAINLESS STEEL — K. Genssler and N. J. Grant (MIT)

6.3.1 ADIP Task

Tasks I.B.16 and I.B.12, Tensile and Stress-Rupture Properties.

6.3.2 Objective

The objective of this study is to investigate the mechanical properties of Nuclear grade 316 stainless steel which was structure refined by rapid solidification (RS). Emphasis was given to the properties at temperatures expected in the first wall of fusion systems. The properties of rapidly solidified material were compared with the properties of ingot material.

6.3.3 Summary

Nuclear grade 316 stainless steel was processed by rapid solidification. Mechanical testing (room temperature and high temperature tensile, Charpy impact, low cycle fatigue and stress rupture testing) showed that the rapidly solidified alloy in all instances either matches or exceeds to an important degree the mechanical properties of ingot material; rational exceptions include long term creep at 650°C due to the much finer grain size of the RS alloy.

6.3.4 Progress and Status

6.3.4.1 Introduction

Thermomechanical treatments for the purpose of grain refinement face restrictions when wrought stainless steels are used. Typical recrystallization temperatures of 750 to 1000°C are usual. Problems of carbide precipitation, and also of σ phase formation complicate grain size control. Nevertheless, recrystallized grains as small as 3 μm are readily achieved, but carbides do precipitate from solution.[1]

The purpose of this study was to investigate the properties of a Nuclear grade type 316 stainless steel which was structure refined by rapid solidification. Emphasis was given to mechanical properties at

temperatures expected in the first wall of fusion systems. Hardness, room temperature tensile, high temperature tensile, stress-rupture, notch bar impact and low cycle fatigue properties of rapidly solidified material were studied and were compared with the properties of ingot material.

6.3.4.2 Production of Rapidly Solidified Alloy

Production of rapidly solidified (RS) alloy included rapid solidification by using the roller quenching technique, consolidation of rapidly solidified foils by hot extrusion and different thermomechanical treatments.

Nuclear grade 316 stainless steel was provided by ORNL as a bar 10 cm in diameter; it was designated as MFE Reference Heat (Heat No. X-15893).

Rapid solidification was performed in a roller quenching apparatus.* Material was melted in an argon atmosphere using induction melting. A fine stream of molten metal was rapidly solidified in contact with two counter-rotating rolls. Obtained foils were typically 75 to 100 μm thick and 5-10 cm long. The estimated cooling rate was 10^5 to 10^6°C/sec. The alloy solidified dendritically with secondary dendrite arm spacing of 2 μm. Foils were cold compacted to obtain a billet and then heated in the range 1040-1080°C and extruded. The reduction of area was 30:1 resulting in a 1.3 cm diameter bar.

The RS extruded material with a 16 μm equiaxed grain size was subjected to various thermomechanical treatments (TMTs), in part because the 30:1 extrusion ratio results in insufficient hot work to guarantee a structure which will not show small delaminations during mechanical testing.

6.3.4.3 Mechanical Testing

Room temperature tests were run on an Instron Machine at a constant crosshead speed of 0.13 cm/min. High temperature tensile tests were run at 400°, 500° and 650°C on a Riehle testing machine using a Satec power positioning furnace and Satec temperature controller. Charpy impact tests were performed at room temperature on a Tinius Olson Machine with

a linear hammer velocity at the instant of striking of 4.21 cm/sec. Constant load stress rupture tests were run at 650°C using a flexible load train and simple lever arm type frames. Low cycle fatigue testing was performed at 400° and 650°C on an MTS model 10.1×10^3 kg servo-hydraulic fatigue machine.

Different processing conditions are summarized in Table 6.3.1 and include as received ingot material, rapidly solidified (RS) and extruded (Extr) material, and RS material subjected to different thermomechanical treatments (TMTs). Thermomechanical treatments comprised swaging (60% CW) and heat treatments at temperatures of 940°, 1040" and 1090°C followed by water quenching (WQ).

Table 6.3.1. Processing Variables of Nuclear Grade 316 Stainless Steel

Treatment Designation	Processing Condition	Grain Size (μm)
1	RS + Extr	16.0
2	RS + Extr + 62% CW + 940°C, 1/2 hr + WQ	9.6
3	RS + Extr + 62% CW + 1040°C, 1/2 hr + WQ	12.0
4	RS + Extr + 62% CW + 1090°C, 1/2 hr + WQ	16.0
5	HRAP ingot material	68.0

TMT with heat treatment at 1040°C resulted in the best combination of strength and ductility. Therefore, mechanical tests, except for low cycle fatigue and Charpy impact testing, were carried out in this TMT condition. Low cycle fatigue and Charpy tests were performed on material in the as-extruded condition. Ingot material was tested in the as-received, solution treated condition.

Rockwell hardness, grain size and room temperature tensile properties of Nuclear grade 316 stainless steel for several processing conditions are shown in Table 6.3.2. High temperature tensile properties are shown in Table 6.3.3. It follows that properties of RS material are not only considerably higher than those of ingot material

Table 6.3.2. Room Temperature Properties and Structure of Nuclear Grade 316 Stainless Steel

Processing Condition Variable	Ingot No. 5*	RS + Extr No. 1	RQ + Extr No. 2	RQ + Extr No. 3	RQ + Extr No. 4
Grain Size (μm)	68.0	16	9.6	12.0	16.0
Hardness, R_B	75.0	84	88.0	86.0	81.0
0.2% YS (KSI)	42.75	-	55.8	53.5	48.0
(MPA)	295.0	-	384.0	369.0	331.0
UTS (KSI)	87.50	-	109.75	106.75	103.25
(MPA)	603.0	-	757.0	736.0	712.0
Elong., Pct.	74.7	-	52.6	54.2	62.1
R.A., Pct.	77.1	-	61.5	-	69.6

*See Table ℘ 3 1

Table 6.3.3. Tensile Properties of Nuclear Grade 316 Stainless Steel at 400°C, 500°C and 650°C

Processing Condition	Test Temperature °C	0.2% Y.S. KSI	(MPA)	UTS KSI	(MPA)	Elongation %	R.A. %	Y.S. Ratio
Ingot, No. 5*	400	27.65	(191)	68.40	(472)	54.0	71.5	0.65
RS + Extr, No. 3		36.50	(252)	85.20	(587)	40.0	58.5	0.68
Ingot, No. 5	500	23.80	(164)	66.40	(458)	53.5	70.5	0056
RS + Extr, No. 3		33.40	(230)	82.60	(570)	40.5	55.5	0062
Ingot, No. 5	650	23.00	(159)	53.00	(365)	52.0	74.°	0.54
RS + Extr, No. 3		32.45	(224)	63.10	(435)	45.5	57.⊟	0.61

*See Table 6.3.1

but also higher than those reported by other investigators who achieved the same grain size by TMTs only.' These results are attributed to better use of solid solution strengtheners in RS material. Hardness and tensile properties are shown to depend on grain size. Strength values increase with decreasing grain size while ductility remains high and decreases only slightly. A straight line relationship has been observed when plotting YS and UTS versus elongation for the ingot material and RS and cold worked material which was annealed at 980°, 1040" and 1090°C. In testing at 400-650°C, it was possible to relate yield strength and test temperature for as-received ingot and RS material; the slopes for both processing conditions are almost the same indicating that the strength improvements are retained throughout the temperature range of 400-650°C.

Stress rupture properties of ingot material and RS materials at 650°C are shown in Figure 6.3.1. The RS material is stronger than ingot material at short rupture times; however, long term creep data at 650°C confirm that the fine grain size of the RS alloy is weaker than the much coarser ingot product. On the other hand, the normal grain boundary embrittlement of the ingot product in creep rupture tests at 650°C is absent in the RS alloy. As shown in Figure 6.3.1, the ingot product follows *a* normal pattern of decreased elongation, 44% at short rupture times and 8% at approximately 500 hr. rupture life. RS material with fine grain size and refined structure shows a much smaller decrease in elongation, from 45% to 25% for comparable rupture times (a similar trend may be observed in the RS material as a function of grain size). This ductility behavior may be an important feature in subsequent irradiation testing wherein the absence of other embrittling factors may be critical.

Charpy impact properties were examined at room temperature as we are interested only in the temperature range of ductile fracture. These tests revealed delamination of RS material which was not thermomechanically treated. Despite delamination problems, Charpy impact values were of the same order as those of ingot material. It is therefore reasonable to assume that the thermomechanical treatment would yield higher Charpy impact values.

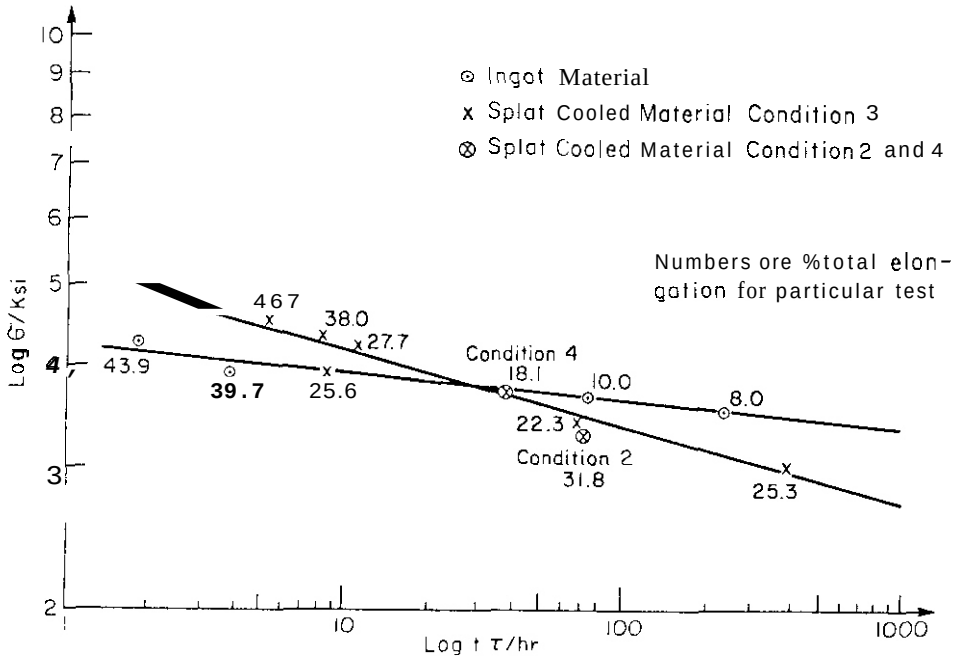

Figure 6.3.1. Stress Rupture Data of Nuclear Grade 316 Stainless Steel. Log Stress versus Log Rupture Life at 650°C.

Figure 2 shows the low cycle fatigue (LCF) properties of ingot material and splat cooled material at 650°C. LCF properties of RS material at 400° and 650°C improved considerably for low level of plastic deformation close to the fatigue limit, but were not better for large plastic deformation, where stress levels are high. This may be due to the fact that LCF is essentially a process of stage II crack propagation and as such does not depend on grain size.[3] As plastic deformation decreases, the amount of stage I crack initiation as a fraction of total life also increases, thus LCF properties become more grain size dependent, and result in a higher endurance limit for the RS material. Close examination of the crack initiation sites shows that stage I microcracks extend only over the length of the grain size for both ingot and RS material.

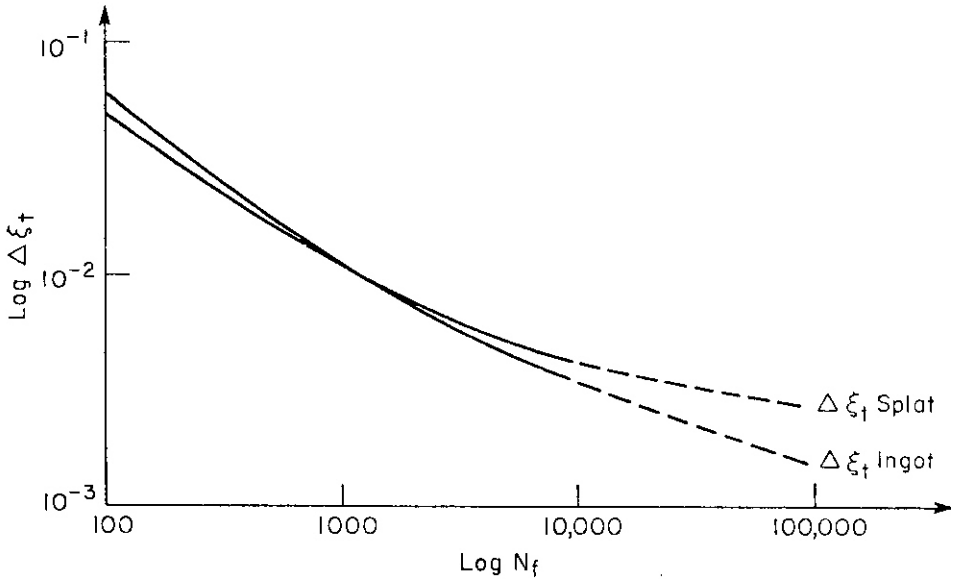

Figure 6.3.2. Low Cycle Fatigue Data of Nuclear Grade 316 Stainless Steel. Total Strain as a Function of Number of Cycles to Failure at 650°C.

6.3.5 Conclusions

A Nuclear grade type 316 stainless steel was processed by rapid solidification at an estimated cooling rate of 10^5°C/sec. The alloy solidified dendritically with a secondary dendrite arm spacing of 2 μm and recrystallized to a 16 μm equiaxed grain size during subsequent extrusion at 1050°C. To avoid longitudinal delamination, the RS and extruded material was thermomechanically treated at three different temperatures resulting in three different grain sizes.

Hardness, room temperature tensile properties and high temperature tensile properties were considerably higher than those of ingot material, and also higher than those of other investigations which achieved the same grain size by thermomechanical treatments alone.

Charpy impact values were of the same order of magnitude as those of ingot material although delaminations were observed on the fracture surface of RS material due to limited amounts of hot work.

RS material is stronger than ingot material at short rupture times at 650°C; long term creep data confirmed that the fine grain size of

the RS alloy is weaker than the coarse ingot material. However, the normal grain boundary embrittlement of the ingot product is absent in the RS product.

LCF properties of RS material at 400° and 650°C were improved considerably for low level of plastic deformation close to the fatigue limit but were not better at high stress levels.

6.3.6 References

1. J. A. Scott and J. E. Spruiell, "Grain Refinement of Wrought Austenitic Stainless Steels by Rapid Heating," *Metall. Trans.* 5: 255-59 (1974).
2. J. P. Durand, R. M. Pelloux and N. J. Grant, "Properties of Splat-Quenched 7075 Aluminum Type Alloys," *Mater. Sci. Eng.* 23: 247-256 (1976).
3. R. M. Pelloux, "Influence of Grain Size on Fatigue," pp. 231-43 in *Proceedings of the 16th Sagamore Army Materials Research Conference*, 1969, Syracuse University Press, Syracuse, New York, 1970.

6.4 OPTIMIZATION OF STRUCTURE AND PROPERTIES OF PRIME CANDIDATE ALLOY (PCA) BY RAPID SOLIDIFICATION — J. Megusar, L. Arnberg, J. B. Vander Sande and N. J. Grant (MIT)

6.4.1 ADIP Task

Tasks I.C.5 and I.B.12, Microstructure and Swelling and Stress Rupture Properties of Special and Innovative Materials.

6.4.2 Objective

The objective of this study is to show the potential of rapid solidification in optimizing the structure and properties of Path A Prime Candidate Alloy for use as a structural material for fusion energy systems. Samples of rapidly solidified and thermomechanically treated Path A-1 and Path A-2 alloys have been included in alloy development irradiation experiments.

6.4.3 Summary

A high density of heterogeneous nucleation sites for helium trapping was provided by reducing the grain size, by increasing the TiC content and surface area and by controlling the dislocation structure by rapid solidification and subsequent thermomechanical treatments. Thermomechanical treatments were developed which resulted in higher strength and elongation in stress rupture testing at 650°C than in a 20% cold worked reference state. While rapid solidification allowed for a controlled TiC precipitate size, density and distribution, coarsening may effectively limit the applications of TiC dispersion strengthened austenitic stainless steel at higher irradiation temperatures.

6.4.4 Progress and Status

6.4.4.1 Introduction

Rapid solidification of alloys allows a degree of manipulation of composition and microstructure which is unattainable by other alloy preparation methods.[1] Fine grained material containing fine second phase particles and inclusions are obtained. The uniformity of com-

position and ease of attaining highly supersaturated solid solutions in rapidly solidified alloys allow for control of precipitate number densities, sizes and interface structures. An alloy designed to resist swelling should contain a maximum number of heterogeneous helium trapping sites such as dislocation cores, grain boundaries and matrix/particle interfaces.

Rapid solidification and subsequent thermomechanical treatments were used to optimize the structure and properties of Path A PCA alloy. In addition, the amount of carbon and titanium in the original Path A PCA alloy has been doubled since it has been shown[2] that TiC carbides are preferred sinks for accomodating helium in comparison with dislocations and other precipitate phases in 316 type stainless steel.

6.4.4.2 Production of Rapidly Solidified Alloys

PCA alloy was provided by ORNL as a 10 cm diameter bar; it was designated as Path A-1 alloy after rapid solidification. Path A-2 alloy was prepared by adding extra titanium and carbon to PCA alloy to approximately double the TiC content (0.081% C, 0.60% Ti).

Rapid solidification was performed in a roller quenching apparatus.[3] Material was melted in an argon atmosphere using an induction melting unit. A fine stream of molten metal was rapidly solidified in contact with two counter-rotating rolls. Obtained foils were typically 75 to 100 μm thick and 5-10 cm long. The estimated cooling rate was 10^5-10^6°C/sec.

Consolidation of RS foils was performed by hot extrusion. Foils were cold compacted to obtain an 85%dense billet and then heated in the range 1040-1080°C and extruded. The reduction of area was 30:1 resulting in a 1.3 cm diameter round bar.

The RS and extruded material was subjected to various thermomechanical treatments (TMTs) which included swaging of the as extruded bar to 60% R.A. with subsequent annealing in the temperature range 650-1000°C.

6.4.4.3 Stress Rupture Properties

The following TMTs were selected for the RS and extruded Path A-1 and Path A-2 alloys based on the recrystallization results and the

results from TEM studies: i) 60% CW + 850°C, 1/2 hr. (annealed); ii) 60% CW + 700°C, 1/2 hr. (recovered); iii) 60% CW + 850°C, 1/2 hr. + 20% CW (cold worked). The latter would serve as the reference state since the 20% CW condition is *so* designated for the **fusion** alloy development program.

As shown in Figure *6.4.1,* the Path A-1 alloy recovery annealed at 700°C shows the highest values of stress rupture strength at 650°C; the bottom curve corresponds to Path A-1 which was annealed at 850°C (recrystallized) and the curve in the middle corresponds to 20% CW condition. Path A-1 recovered at 700°C has significantly superior rupture strength and higher ductility at rupture in the preirradiated condition when compared with the reference 20% CW state. The stress rupture curve for Path A-2 annealed at 850°C lies, as expected, slightly above the curve for Path A-1 alloy; the elongation values at rupture are comparable for both alloys.

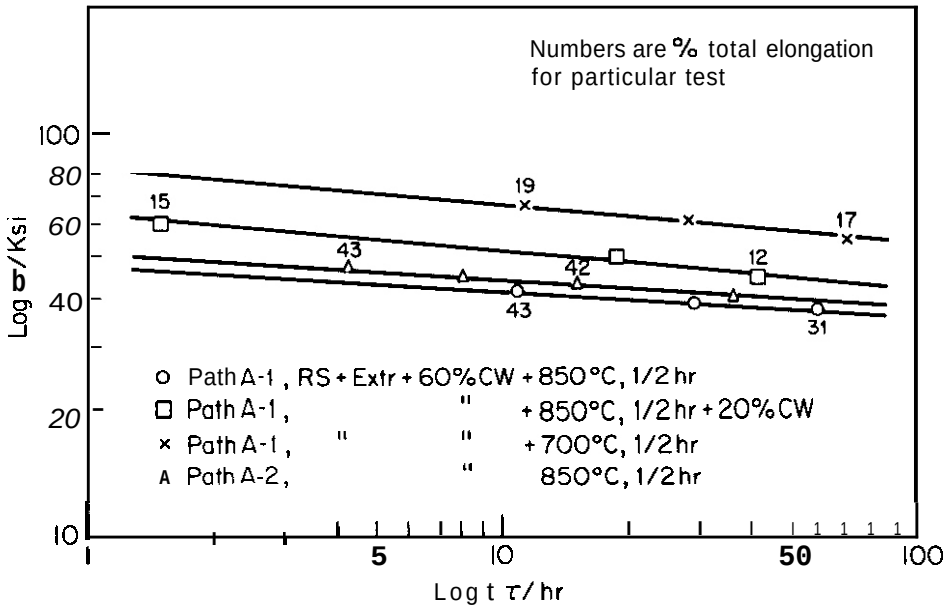

Figure *6.4.1.* Stress rupture data for Path A-1 and Path A-2 alloys. Log stress versus log rupture life at 650°C.

Path A-1 annealed at 850°C after 60% CW shows relatively high elongation at the longest rupture life; this is due to a fine recrys-

tallized grain size. All stress rupture specimens tested at 650°C showed a ductile fracture. Experiments were designed to determine the effect of grain size on the strength and ductility; based on these results and the results of the irradiation testing (currently in progress) an optimum grain size will be developed by choosing an appropriate TMT for this rapidly solidified material.

6.4.4.4 Microstructure of RS and Extruded Path **A-1** and Path A-2 Alloy

The microstructures were examined by TEM using a Siemens Elmiskop *101* and by STEM (Vacuum Generators HB5) equipped with an energy dispersive X-ray detector and an energy loss spectrometer. The size distribution of carbide particles was determined using a computerized image analyzer.

TEM showed that RS, hot extruded Path A-1 and Path **A-2** alloys which were subsequently 60% CW and annealed for 1/2 hr. at *850°C* had a fully recrystallized structure with an average grain size of *10* μm. Titanium carbide precipitates appeared to be distributed randomly in the austenitic matrix and there was no preferential precipitation at the grain boundaries.

The grain boundaries were carefully analyzed **in** situ in the STEM for compositional variations. The results of energy dispersive X-ray analysis of the grain boundary and the areas adjacent to the grain boundary indicated no segregation at the grain boundary.

Precipitate particles have been analyzed in situ in the STEM. Preliminary results showed carbon and titanium. No nitrogen peaks were detected in the energy loss spectra and the X-ray spectra from the precipitates did not show sulphur.

Measurements of the volume fraction of TiC in Path A-1 (annealed) showed that approximately 25% precipitated during hot extrusion as a somewhat coarser TiC and the remaining 75% precipitated during subsequent thermomechanical treatment as a much finer product. The median size of TiC particles was 160 **Å** (Figure 6.4.2) and the particle number density was 900 μm^{-3}. Some particles were aligned on {111} planes. TiC particles in Path **A-2** alloy (fully annealed) were slightly coarser because a billet was held longer at the extrusion temperature due to

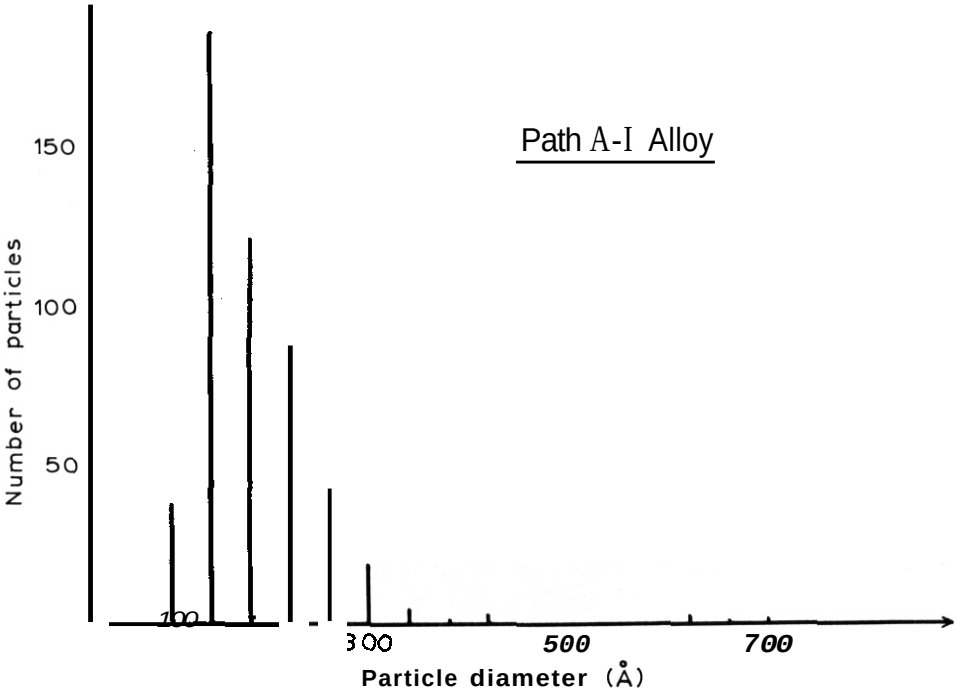

Figure 6.4.2. TiC particle size distribution in Path A-1 alloy (annealed).

problems arising during the extrusion process. If all the carbon is precipitated as TiC the volume fractions are 0.38 and 0.68% for Path A-1 and Path A-2 alloy, respectively.

The recovery annealed structure of Path A-1 alloy showed a small cell structure (Figure 6.4.3); annealing for 1/2 hr. at 700°C promoted recovery of the dislocation network to a cellular structure with a typical cell size of 0.2 μm.

6.4.4.5 Microstructure of RS Foils of Path A-1 and Path A-2 Alloy

The microstructural ctaracterization has been extended to include RS foils of Path A-1 and Path A-2 alloy which were prepared by the roller quenching technique. The purpose of this study was to fully demonstrate the different options which are available in optimizing the structure and properties of the Path A Prime Candidate Alloy by using rapid solidification technology.

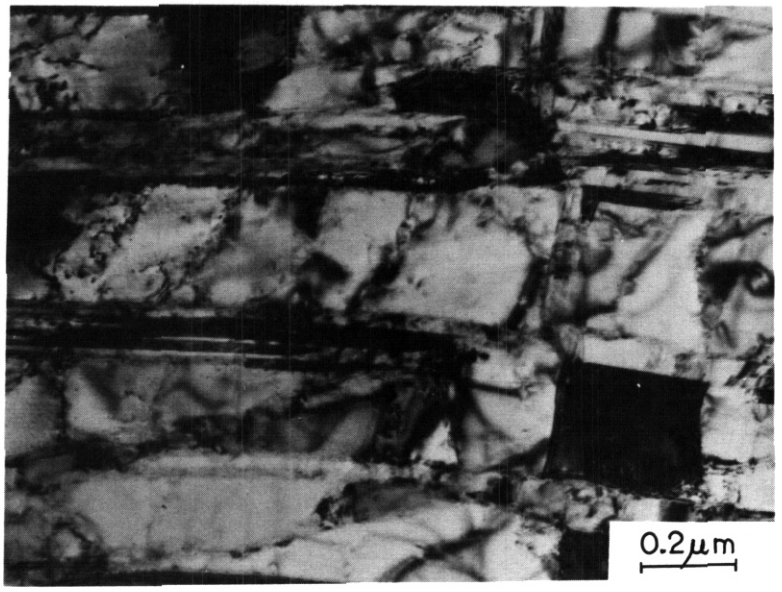

Figure 6.4.3. Bright-field TEM micrograph showing a small cell structure in recovery annealed Path A-1 alloy.

Foils were cold rolled to 40% reduction in thickness and subsequently annealed for 1/2 hr. at 700°C. The carbide size distributions were analyzed by dark field electron microscopy of the unrecrystallized region using $(200)_{TiC}$ reflection. TiC particles (Figure 6.4.4) in Path A-1 alloy precipitated coherently in the austenitic matrix. Their average diameter, as measured, was 22 Å and their distribution was random. Examination of the carbide size distribution in RS foils of Path A-2 alloy showed similarly random distribution of coherent TiC particles with slightly larger diameter (31 Å).

The carbide size distributions in RS foils (Figure 6.4.4) are considerably smaller than the carbide size distributions in RS and extruded material (Figure 6.4.2). If desired, it should be possible to reduce the size of TiC precipitates in RS and extruded Path A-1 and Path A-2 alloys by lowering the extrusion temperature and by choosing appropriate TMTs and to control the carbide particle size within the range of 20 to 100 Å diameter.

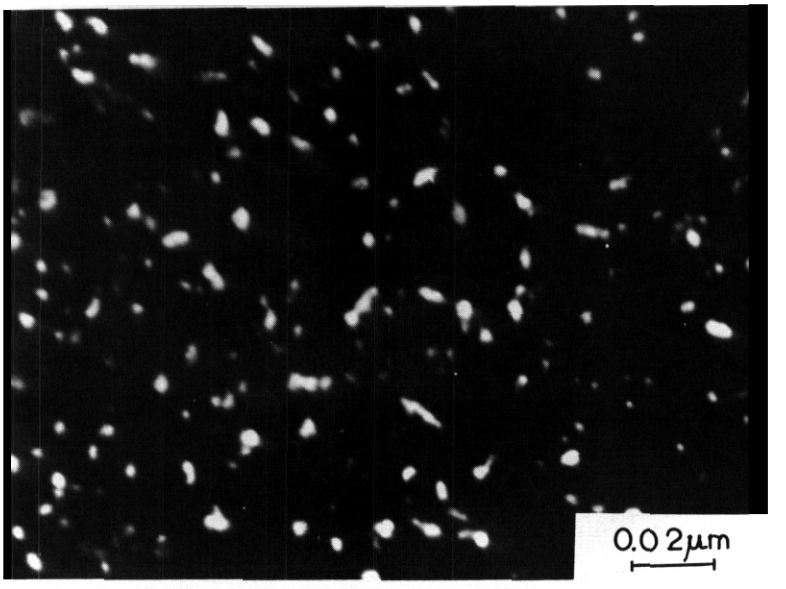

Figure *6.4.4.* Dark-field TEM micrograph showing coherent TiC precipitates in RS foil of Path A-1 alloy which was *40%* cold rolled and annealed 1/2 hr. at 700°C.

6.4.4.6 Stability of TiC Precipitates

It has been shown, based on a modeling approach,[4] that the stability of a dispersion of stable particles under irradiation may be affected by factors including thermal coarsening and resolution due to radiation recoil. At higher irradiation temperatures thermal coarsening becomes a dominant mechanism, based on a modeling approach. Experiments showed a similar result, namely, that coarsening of TiC precipitates limits the use of TiC dispersion strengthened 316 stainless steel at higher temperatures under irradiation conditions.* Consequently, this research has been extended to prepare Al_2O_3 dispersion strengthened *316* type stainless steel and to study the effect of Al_2O_3 particles on the high temperature strength and swelling resistance.

6.4.5 Conclusions and Future Work

The structure and properties of Path A Prime Candidate Alloy have been optimized by rapid solidification and subsequent thermomechanical treatments.

A high density of heterogeneous nucleation sites for helium trapping was provided by reducing the grain size, by increasing TiC content, and by controlling the dislocation structure. These structural modifications are expected to have an effect on swelling and high temperature strength and ductility of Path A alloys under irradiation.

Thermomechanical treatments were developed which resulted in higher strength and elongation than in a 20% cold worked reference state in stress rupture testing at 650°C.

While rapid solidification allowed for a controlled TiC precipitate size, density and distribution, coarsening may effectively limit the application of TiC dispersion strengthened austenitic stainless steel at higher irradiation temperatures. Consequently, this research will be extended to study the effect of Al_2O_3 dispersion on high temperature strength and swelling resistance of rapidly solidified Path A alloy.

6.4.6 References

1. N. J. Grant, "Structure and Property Control through Rapid Quenching of Liquid Metals and Alloys," *Fizika* 2, Suppl. 2: 16.1–16.15 (1970).
2. P. J. Maziasz and E. E. Bloom, "Comparison of Titanium Modified and Standard Type 316 Stainless Steel Irradiated in HFIR–Swelling and Microstructure," *ADIP Quart. Prog. Rep.*: 40–53 (Jan–March 1978).
3. J. P. Durand, R. M. Pelloux and N. J. Grant, "Properties of Splat-Quenched 7075 Aluminum Type Alloys," *Mater. Sci. Eng.* 23: 247–56 (1976).
4. H. Frost and K. C. Russell, "Phase Stability under Irradiation," *DAFS Program Plan, Subtask II.C.1.2* Modeling and Analysis of Effects of Material Parameters on Microstructure, to be published.

7. PATH E ALLOY DEVELOPMENT — FERRITIC STEELS

7.1 PROCUREMENT AND CONVERSION OF THE NATIONAL FUSION-FERRITIC STEEL PROGRAM 12Cr (HT-9) HEAT - R. D. Stevenson, B. E. Thurgood, and S. N. Rosenwasser (General Atomic Company)

7.1.1 ADIP Task

The Department of Energy (DOE)/Office of Fusion Energy (OFE) has stated the need to investigate ferritic alloys under the ADIP program task, Ferritic Steels Development (Path E).

7.1.2 Objective

The primary objective of the General Atomic Fusion-Ferritic Program is to establish the feasibility and develop the procedures for the welding and fabrication of 9-12Cr steels for use in the first wall and blanket structures. An additional objective is to develop the methodology for the management of fracture safe design in the use of ferritic steels in fusion, including the generation and analysis of pertinent, unirradiated property data. In order to carry out these tasks, and others in the national program, it is necessary to procure a large heat of 12Cr-1Mo-0.3V steel.

7.1.3 Summary

A 3,830 kg (8,440 lb.) slab of 12Cr-1Mo-0.3V steel was fabricated into four different plate thicknesses for use by the National Fusion-Ferritics Steel Program. Details of the conversion are discussed in this progress report.

7.1.4 Progress and Status

7.1.4.1 Introduction

A 14,750 kg (32,500 lb.) heat of 12Cr-1Mo-0.3V steel was poured at Electralloy Corporation for the National Fusion-Ferritic Steel Program (Ref. 1). Shown in Table 7.1.1 are the chemistry specifications of the heat, the Electralloy ladle test-pour analysis and the check analysis performed on the ladle test-pour by Combustion Engineering of Chattanooga, Tennessee. Also included are specifications and other chemistries for comparison.

TABLE 7.1.1
SUMMARY OF CHEMICAL COMPOSITIONS PERTINENT TO 12Cr FUSION-FERRITIC STEEL PROGRAM

SPECIFICATIONS:														
· DIN X20CrMoWV 12 1 Material No. 1.4935	0.17/ 0.23	0.10/ 0.50	0.30/ 0.80	0.035 (max)	0.035 (max)	11.0/ 12.5	0.8 1.0	0 0 0 8	0.2 0.3	0 4 0 6				
· Sandvik Nominal HT-9 (1.4935)	0.20	0.4	0.55	0.020 (max)	0.020 (max)	11.5	1.0	0 5	0.3	0.≤				
· AISI 410	0.15	1.0	1.0	0.040	0.030	11.5/ 13.5								
· AISI 422	0.20/ 0.25	0.75	1.0	0.025	0.025	11.0/ 13.0	0.7≤/ 1.2≤	0.50 1.0	0 15/ 0 30	0.75/ 1.25				
· ORNL/FBR Mod. 9Cr-1Mo Heat (Cartech ESR)	0.08/ 0.12	0.10/ 0.25	0.30/ 0.50	0.02 (max)	0.01 (max)	8.0/ 9.0	0.85/ 1.05	0.2 (max)	0 18/ 0 25	0.01 (max)	0.03/ 0.07	0.04 (max)	0.01 (max)	Cu 0.2, Nb (0.06/0.10) Zr 0.01, O_2 0.02, Sb 0.001, B residual
· HEDL/FBR 12Cr Heat (Cartech VIM/ESR)	0.17/ 0.23	0.2/ 0.3	0.4/ 0.7	0.020 (max)	0.010 (max)	11.0/ 12.5	0.8 1.2	0 0 3 0 0 8	0.25 0.05	0.4 0.6	0.010	0.050	0.050	Cu 0.10, As 0.030, Ta 0.020, Co 0.05, B 0.0010
· GA/Fusion-Ferritics 12Cr Heat (Electralloy AOD)	0.18/ 0.22	0.1/ 0.4	0.3/ 0.8	0.02 (max)	0.01 (max)	11.0/ 12.5	0.8 1.2	0 0 4 0 6	0 2≤ 0 0≤	0 4 0 6	0.02 0.06	0.04 (max)	0.01 (max)	Cu 0.10, O_2 0.02, Co 0.05, As 0.01, (B, Bi, Pb, Sb, Sn, Nb, all 0.001)
Target	0.20	0.25	0.55	0.01	0.006	11.5	1.0	0 5	0.3	0.≤	0 0			
EXAMPLES:														
· GA/Fusion-Ferritics Electralloy Heat 9-607 (AOD)	0.20	0.22	0.52	0.020	0.006	11.63	1 0	0 50	0 0	0 5Z	0.047	<0.01	<0.01	Cu 0.04, Co 0.08, As <0.01 B, Sb trace, Pb 0.001, Sn 0.003
Combustion Engineering Check Analysis	0.20	0.26	0.61	0.016	0.007	11.65	1 02	0 4	0 2	0.61	0 01	0.009	<0.01	Cu 0.03, O_2 0.013, Co 0.09, As 0.004, Cb 0.01, Zr 0.002, B 0.001, Sm 0.01
· HEDL/FBR Cartech Heat 91353 (VIM/ESR)	0.20/ 0.21	0.22	0.49/ 0.50	0.006/ 0.007	0.002/ 0.003	11.60/ 11.99	1.00 1.03	0 ≤ 7 0 0 8	0.01 0.02	0 4 9 0 5 0	0.003/ 0.008	0.019/ 0.036	0.002/ 0.003	Cu 0.03-0.0%, Co 0 .0Z, As, Ta <0.010, B < 0.0010
· ORNL/FBR Cartech Heat 30182 (ESR)	0.086	0.16	0.37	0.012	0.003	8.44	0.89	0 1 1	0.2 0	<0.01	0.0≤4	0.014	<0.02	Cu 0.03, Nb 0.0∃, Sn 0.0 0 Zr 0.001, O_2 0.058, Co 0.02

Of all the major elements analyzed by Electralloy in the fusion 12Cr heat ladle test-pour, the phosphorus level (0.020) came closest to the specification (0.020, max). The chemistry check made by Combustion Engineering on the same ladle test-pour indicated a lower value of 0.016. This determination was made by the molybdenum-blue method, which is very accurate for phosphorus determinations. Thus the phosphorus content of the 12Cr-1Mo-0.3V Fusion-Ferritic Steel heat is below its maximum specified level.

7.1.4.2 Conversion of Slab of 12Cr-1Mo-0.3V to Plate

Slab #9-607-2-2-1, measuring 20.3 cm (8") x 96.5 cm (38") x 251.9 cm (99.2"), and weighing 3,830 kg (8,440 lb.) was delivered to Jessop Steel Company in Washington, Pennsylvania, after being given a 10 day cooling period after pouring at Electralloy Corporation in Oil City, Pennsylvania. Figure 7.1.1 shows a flow chart for the conversion that followed.

At Jessop, the slab was heated to 1200°C (2192°F) in a furnace with an oxidizing atmosphere. The slab was held at this homogenization temperature for three hours in order to insure a temperature of 1200°C (2192°F) at the center of the slab for at least one hour. This was done to homogenize any micro-segregation that may have been present after the slab cooled from the molten state. The chemistries of the ends of the slab showed that macro-segregation was not a problem (Ref. 1). The slab was then allowed to cool to 1010°C (1850°F) and was taken to the rolling mill to be reduced (Figure 7.1.2). The reversible four high rolling mill at Jessop has a 280 cm (110") working face on the 76 cm (30") diameter working rolls (Figure 7.1.3(a)). The 20.3 cm (8") slab was reduced down *to* 12.7 cm (5") thick in about six passes. At this point the slab was about 403 cm (160") long.

After the initial reduction, the slab was cut into three billets as follows:

i) one billet to be rolled down to 15.9 mm (5/8") thick
ii) one billet to be rolled down to 28.6 mm (1.25") thick
iii) one billet to be rolled down to 38.1 mm (1.5") thick

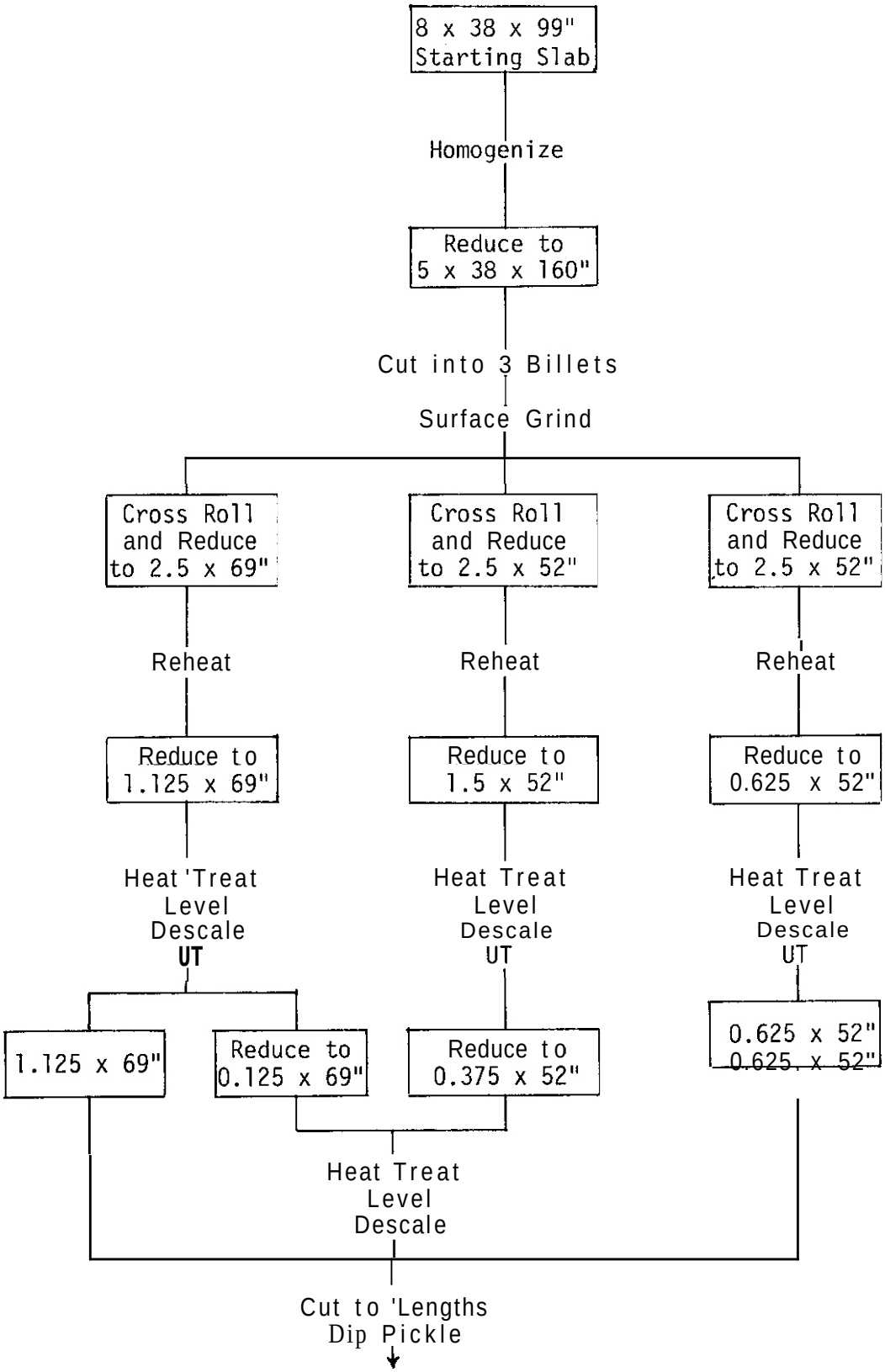

Figure 7.1.1 Flow chart for conversion of 12Cr slab to plate and sheet

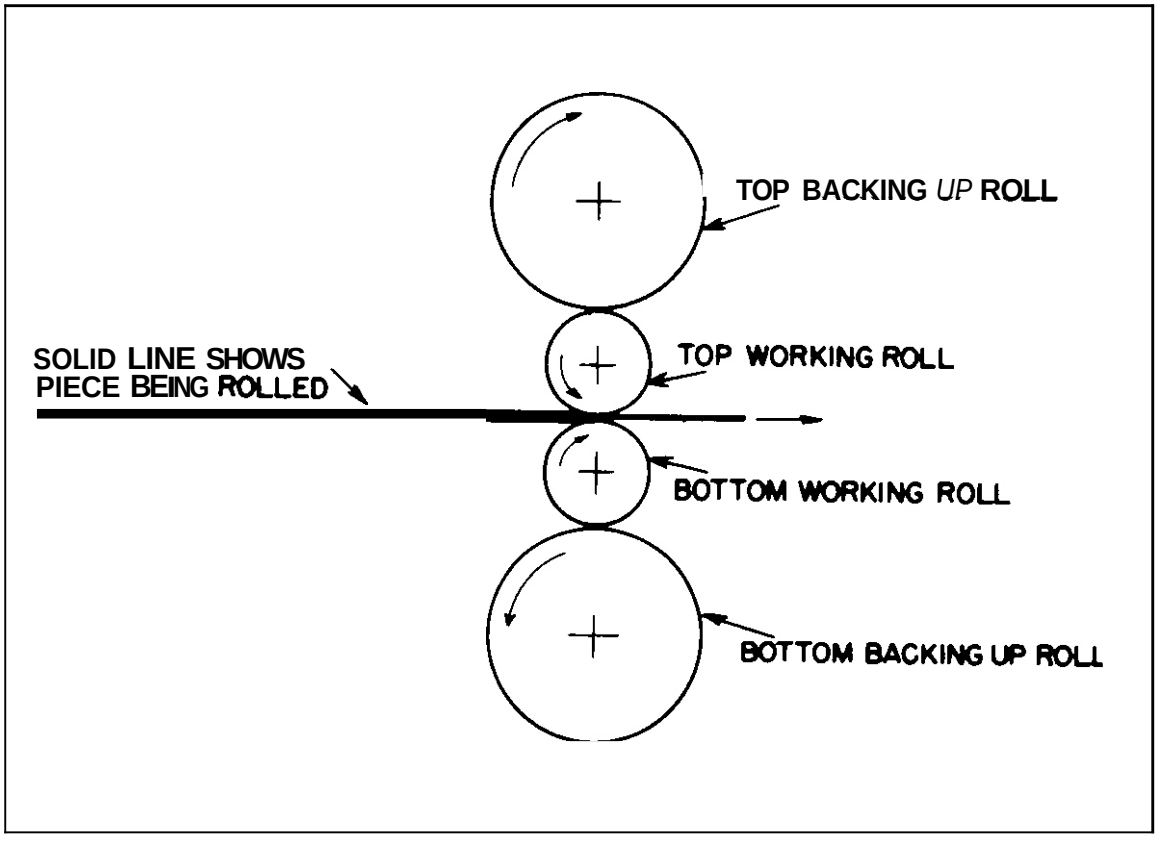

Figure 7.1.2 Schematic of four high rolling mill as used by Jessop Steel Company (Ref. 2)

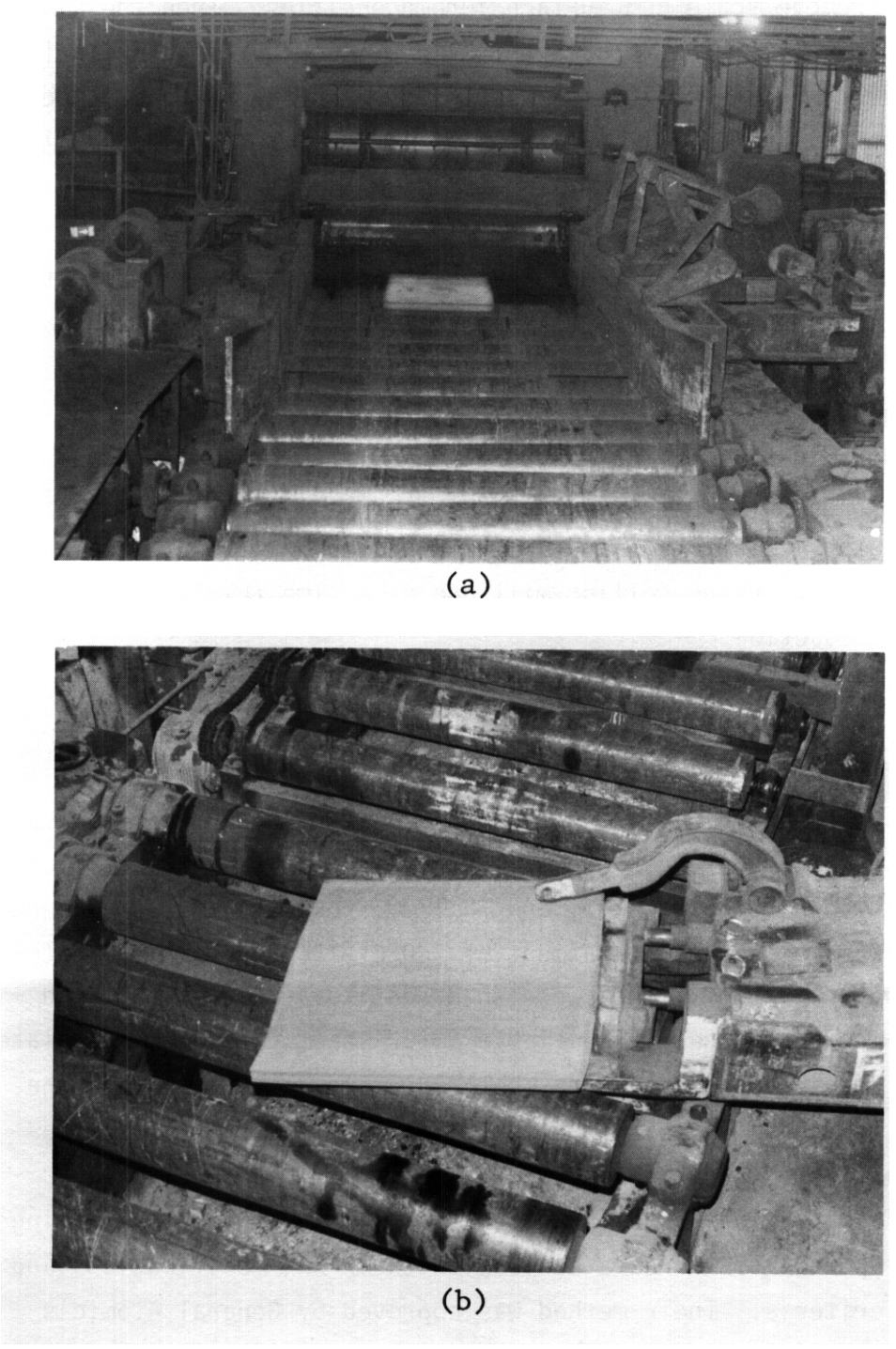

Figure 7.1.3 Photographs of **(a)** Jessop 280 cm (110") four high rolling mill, and (b) a **6.3** cm (2.5") thick plate of 12Cr-1Mo-0.3V steel being placed on a rolling mill bed after being reheated to 1010°C (1850°F)

After cooling the slabs to 150°C, they were surface conditioned (ground) to remove scale and surface inhomogeneities. Then the slabs were placed back into the furnace and held at 1010°C (1850°F) for 1-1/2 hours. This temperature (1010°C) was selected as the rolling temperature because it was thought that the billets could be rolled from 12.7 cm thick down to 1.59 cm thick without intermediate reheating. This would result in a fine grain size.

The next step in the rolling involved cross-rolling the billets to 132 cm (52"). The reason for the cross-rolling was to reduce the amount of texture and inhomogeneities in the plates. The 28.6 mm (1-1/8") plate was accidently cross-rolled to a width of 175.3 cm (69"). After reduction down to about 6.3 cm (2.5"), the billets had cooled to a temperature too low to reduce them further without danger of cracking or overloading the mill. The billets were reheated to 1010°C (1850°F) and were brought back to the rolling mill one at a time (Figure 7.1.3(b)) for further reduction.

The 15.9 mm (0.625") plate was reduced to size without any problems. The 28.6 mm (1.125") and 38.1 mm (1.5") plates both turned upward as they left one side of the working rolls (Figure 7.1.4(a)). This is a common occurrence in rolling some alloys and is corrected by cross-rolling with no reduction (Figure 7.1.4(b)). After the three billets were reduced down to 15.9, 28.6, and 38.1 mm, respectively, they were given a stress relief heat treatment of 740°C (1364°F) for 30 minutes followed by an air cool. They were then sent to a leveler mill and leveled to meet ASTM Spec. A480 (Table 9 for sheet, Table 20 for plate). Next, they were blasted with iron shot to remove scaling. After the descaling, the surface finish was sufficiently clean to allow ultrasonic inspection (UT) to take place.

The UT inspection of the plates was performed by Peabody Testing using ASTM Spec. A-578-78 as a basis with their own modifications and acceptance criteria. Their method was approved by General Atomic's Quality Assurance Department prior to the testing. Since reliable UT inspection of plate under 15.9 mm (0.625") is not feasible, the inspection for the final thicknesses of 3.2 mm (0.125") and 9.5 mm (0.375") were respectively performed on pieces 28.6 mm (1.125") and 38.1 mm

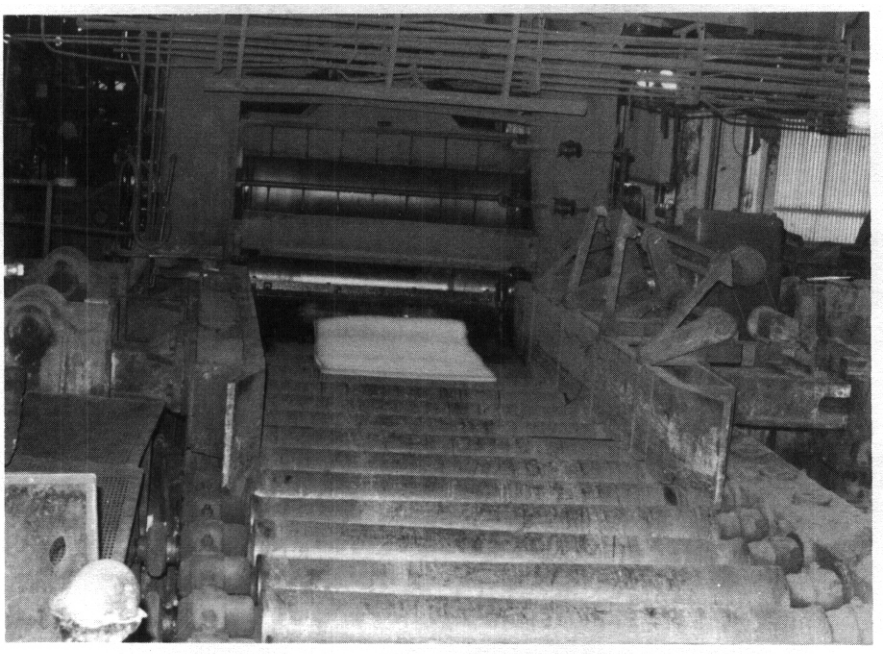

(a)

(b)

Figure 7.1.4 Photographs of turned up plates of 12Cr-1Mo-0.3V steel (a) coming out of working rolls, and (b) turned sideways before being straightened

(1.5") in thickness, prior to further reduction.

The 28.6 mm (1.125") plate was then cut into two pieces, one to be rolled down to 3.2 mm (0.125"), and one to be left at a thickness of 28.6 mm (1.125"). The piece to be rolled down to 3.2 mm (0.125") and the 38.1 mm (1.5") billet [to be rolled down to 9.5 mm (0.375")] were reheated to 1010°C (1850°F) and then rolled without any problems. The plate, 9.5 mm, and the sheet, 3.2 mm, were then annealed, leveled, and blasted as before. All the plates and sheets (3.2-28.6 mm) were then cut into 122 cm (48") lengths and given a dip-pickle finish.

7.1.5 Future Work

The plates and sheets will be characterized by chemistry, mechanical properties (tensile and charpy), and microstructure. Both inter- and intra-plate variations in properties or microstructure will be assessed. Welding test plates will be cut from the large plates and General Atomic's parametric welding study will commence. Materials requested by the other program participants will be distributed.

7.1.6 References

1. Lechtenberg, T. A., R. D. Stevenson, S. N. Rosenwasser, B. E. Thurgood and L. D. Thompson, "Procurement of National 12Cr Heat and Evaluation of Welding Procedures for Irradiation Specimens," from Alloy Development for Irradiation Performance, Quarterly Progress Report for Period Ending March 31, 1980, DOE/ER-0045/2, pp. 109-112.
2. The Making, Shaping, and Treating of Steel, U.S. Steel Co., Pittsburgh, Pennsylvania, 9th Edition, 1971, p. 610.

7.2 THE FRACTURE PROPERTIES OF A TEMPER EMBRITTLED 12Cr-1Mo-0.3V STEEL

T. A. Lechtenberg and S. Helfrich (General Atomic Company)

7.2.1 ADIP Task

The Department of Energy (DOE)/Office of Fusion Energy (OFE) has stated the need to investigate ferritic alloys under the ADIP program task, Ferritic Steels Development (Path E).

7.2.2 Objective

The primary objective of this study is to evaluate the irradiated "worst-case" fracture properties of 12Cr-1Mo-0.3V steel by inducing temper embrittlement. The lower shelf energies of embrittled material would give a lower boundary on energy to cause fracture for this material and would enable the estimation of critical flaw sizes, in advance of the availability of pertinent fracture properties on irradiated material.

7.2.3 Summary

Dynamic fracture toughness, as measured by precracked and instrumented Charpy V-notch specimens, and standard Charpy V-notch tests were performed at temperatures from -192" to 207°C on material in two conditions. Material was austenitized for 1 hour at 1000°C, air cooled, and tempered at 650°C for 1 hour; and austenitized and tempered for 1 hour at 1000°C and 650°C and air cooled, and subsequently aged at 550°C for 100 hours. The aging was done at a temperature known to cause temper-embrittlement in this class of steels (1,2,12). Optical metallography of the microstructure and X-ray analysis of extracted carbides are presented. Fractography to relate the mode of fracture with energy absorbed, and a more complete microstructural evaluation continues and will be presented in the next ADIP quarterly.

7.2.4 Experimental Procedure

Material was obtained from the National Breeder Material Stockpile (Heat #91354) at HEDL in the form of 1-5/16" diameter rod. The chemistry is given in Table 7.2.1. As-received material had been heated to 1150°C for at least an hour, then hot worked with reheats to 1150°C

between each pass, and slow cooled, with a subsequent temper of 750°C for 1 hour with an air cool.

Table 7.2.1. Chemistry of Material* (wt %)

0.21	12.09	1.02	0.33	0.54	0.58	0.50	0.21	0.008	0.003

Specimen blanks were cut from this rod and all material was wrapped in stainless steel foil for protection prior to heat treatment. The heat treatment temperature was carefully monitored by attaching a thermocouple to a blank. When the surface reached temperature (~5 min), the material was held for one hour and then cooled in air. Hardness was determined using a Kentrall Hardness Tester after successive water cooled grindings. Specimens for metallography were cut with a water cooled friction saw, mounted in Bakelite, ground with successively finer grit paper, and polished to a 0.25 μm finish with diamond abrasive. Several etches were used. An etch of composition 65 ml H_2O, 65 ml HCl, 15 ml Acetic Acid, 15 ml HNO_3 was used electrolytically at 0.75 volts for 1 min to determine prior austenite grain size. For general microstructure, 10 ml HF, 5 ml HNO_3, 85 ml H_2O reagent gave the clearest results. Villela's Reagent was used but with less success. Sometimes a sequence of several etches and repolishing revealed features more clearly than a single polish and etch. X-ray analyses were performed using Cu K_α radiation and a Gunier camera on carbides extracted in a 10% HCl-methanol electrolyte. Estimates of relative weight percentages of carbides were also determined.

7.2.5 Determination of Heat Treatment

Figure 7.2.1 shows the effect of austenitizing temperature on the Rockwell hardness of 12Cr-1Mo-0.3V held at temperature for 1 hour and then air cooled. Included on this graph are the ASTM grain size numbers determined by comparison at 100X to a standard template. The as-quenched

*balance iron.

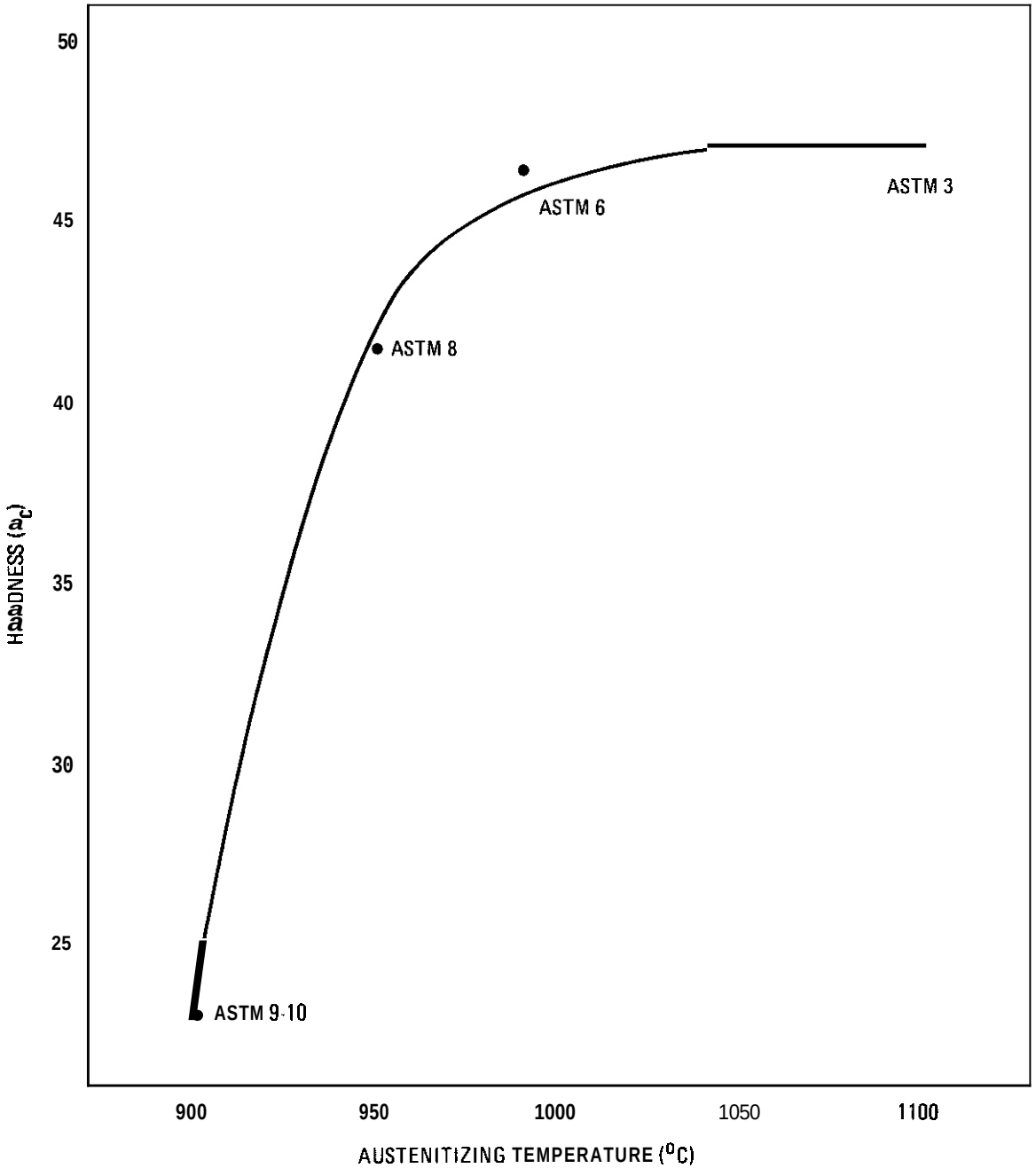

Fig. 7.2.1. Effect of austenitizing temperature on the as-quenched hardness of a 12Cr-1Mo-0.3V steel (austenitizing time was 1 hour)

hardness of a steel is primarily due to the carbon content of the alloy (3,4,5). After 1 hour at 900°C, the as-quenched hardness is R_C 23. It increases to R_C 41 at 950°C. This is due to the dissolution of ferrite and carbides which exist at 900°C. This temperature is very close to the A_3 phase transition line to austenite (6). This was confirmed by optical metallography with the presence of ferrite in the microstructure.

Figure 7.2.2 shows a diffraction interface contrast photomicrograph with areas of ferrite lacking carbides. Most of the increase in hardness was due to the dissolution of ferrite although some larger carbides also dissolved which are shown in Figure 7.2.2. At 1000°C, the hardness increased to R_C 46 and remained nearly constant at 1050" and 1100°C. This indicates that all phases present are stable in this temperature regime after 1 hour.

Figure 7.2.3 shows optical micrographs of the specimens air-cooled from 900°, 950°, 1000°, and 1100°C. The microstructure resembles a collection of needles, typical of acicular martensite. A closer examination showed some small, round features assumed to be carbides. An X-ray analysis is continuing. A one hour 1000°C austenitization treatment was chosen because the hardness did not increase above that temperature. This would ensure the maximum amount of carbon in solution available for precipitation upon tempering to a stable carbide, yet the smallest grain diameter. No areas of ferrite were observed after a careful examination of the microstructure. Specimens were tempered at 650°C for 1 hour to ensure complete precipitation, then half were aged at 550°C for 100 hours. This temperature has been shown to cause temper embrittlement in 12Cr steels. This is the segregation of tramp elements, such as P, As, Sn, to prior austenite grain boundaries which cause decohesion during fracture. At the end of each treatment, the hardnesses were R_C 22.

X-ray analyses were performed on material as-quenched (AQ); AQ and 650°C tempered; and AQ, 650°C tempered, and 550°C aged for 100 hours. The results are given in Table 7.2.2.

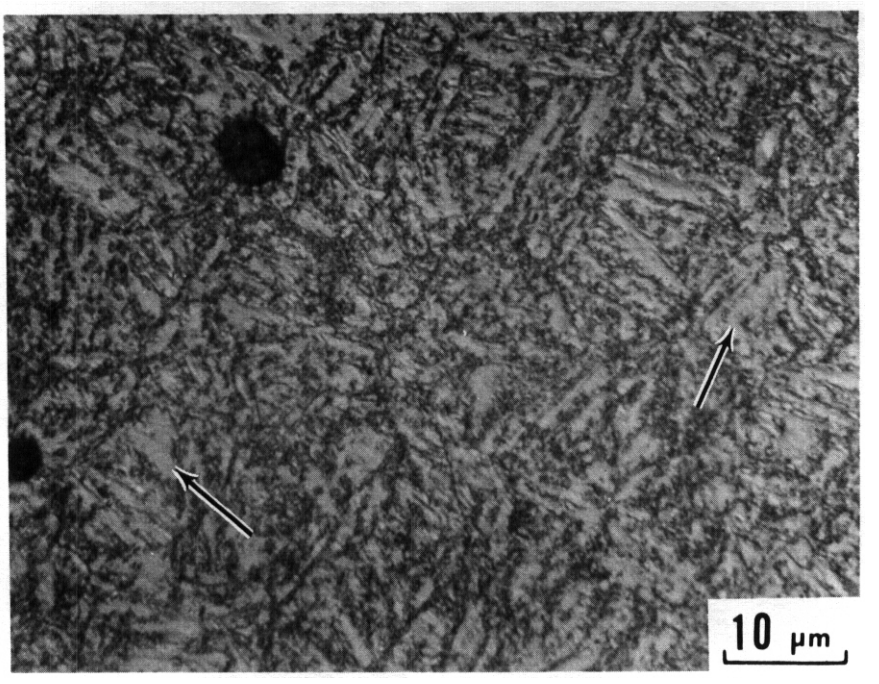

Fig. 7.2.2. 12Cr-1Mo-0.3V steel after 900°C for 1 hour and air-cooling showing undissolved carbides (large black area) and areas of undissolved ferrite (arrows). Etchant was 10% HF, 5% HNO_3, 85% H_2O

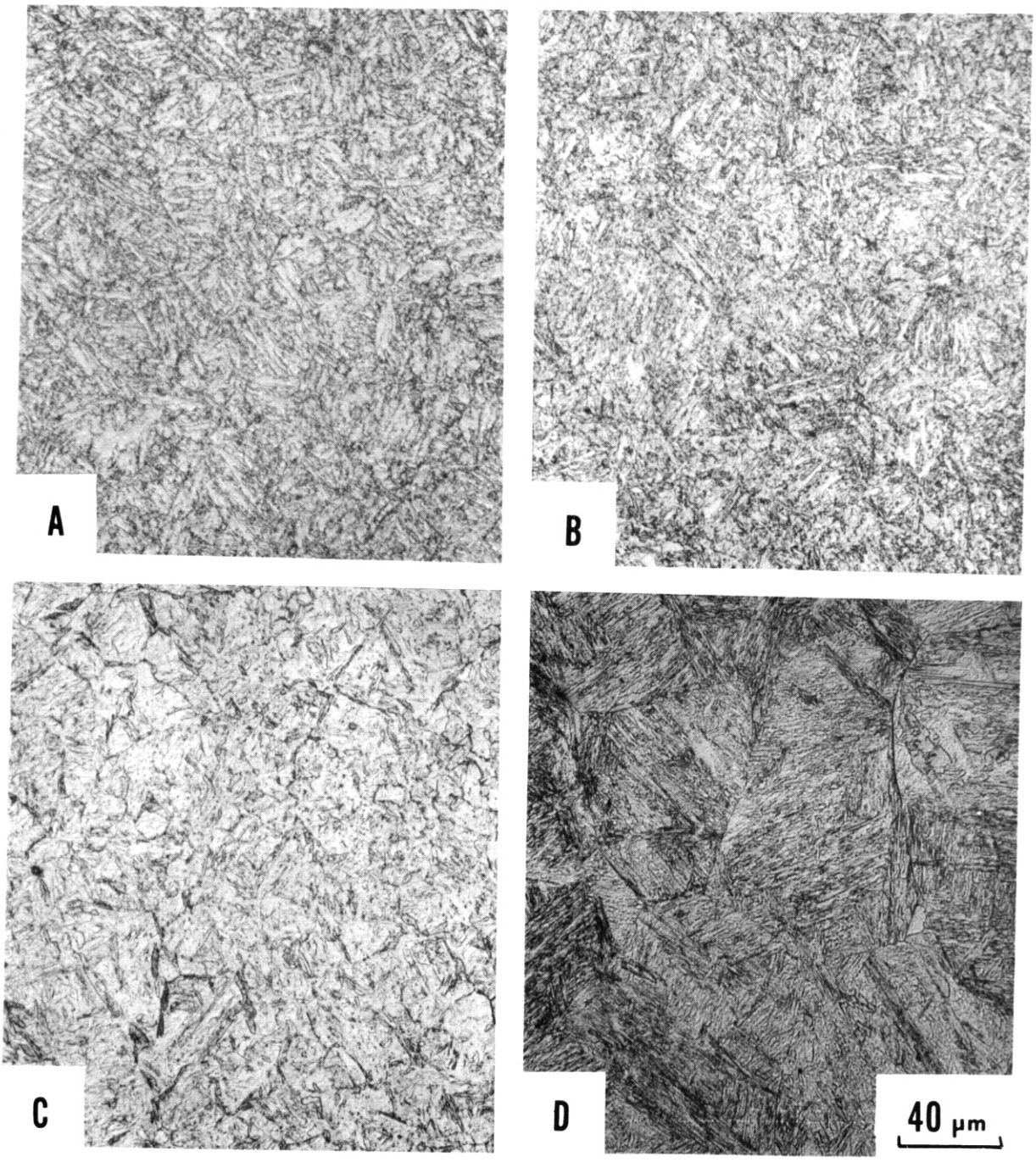

Fig. 7.2.3. Optical photomicrograph of 12Cr-1Mo-0.3V etched in 10% HF, 5% HNO_3, and 85% H_2O shown after austenitizations at (a) 900°, (b) 950°, (c) 1000°, and (d) 1100°C

Condition	Carbide	Amount (wt %)
1000°C, 1 h, air-cool	$M_{23}C_6$	0.86
1000°C, 1 h, air-cool 650°C, 1 h, air-cool	$M_{23}C_6$	2.19
1000°C, 1 h, air-cool 650°C, 1 h, air-cool 550°C, 1 h, air-cool	$M_{23}C_6$	2.65

As seen in the microstructure, the as-quenched martensite did yield some undissolved $M_{23}C_6$, 0.86% by weight of the sample. A high tempering temperature of 650°C yielded the same $M_{23}C_6$ carbide at 2.19 wt %, and after 550°C for 100 hours, 2.65 wt %, a small amount more precipitated, confirming that the 650°C temper condition was nearly stable. This stability was found previously after a 780°C temper and subsequent aging for 80,000 hours at 600°C (8). Figure 7.2.4 shows photomicrographs of the as-quenched, tempered, and temper-embrittled microstructures. Figure 7.2.4(a) shows as-quenched microstructure. Figure 7.2.4(b) shows the 650°C temper, and Figure 7.2.4(c) the 650°C temper with the 100 hour aging at 550°C. There is a difference between the two tempering treatments in the carbide size and distribution. The morphology of the 650°C temper $M_{23}C_6$ carbides is spherical and resolvable with optical techniques. The 100 hour aged microstructure appears to have a fine distribution of carbides as well as the spherical precipitates. Presumably these five carbides are the $M_{23}C_6$ type seen in the X-ray data. Scanning electron microscopy and EDAX is in progress.

7.2.6 Fracture Data

Charpy impact specimens were machined from material in the tempered and tempered-aged conditions. Some from each were precracked such that $0.45 < a/W < 0.55$ where a is the crack length and W is the width of the specimen. The final 10%of crack length was grown at a stress intensity, K_Q, of 33 $MPa\text{-}m^{\frac{1}{2}}$. The specimens were fractured dynamically on a Dynatup instrumented impact pendulum tester with an ETI 300 microprocessor.

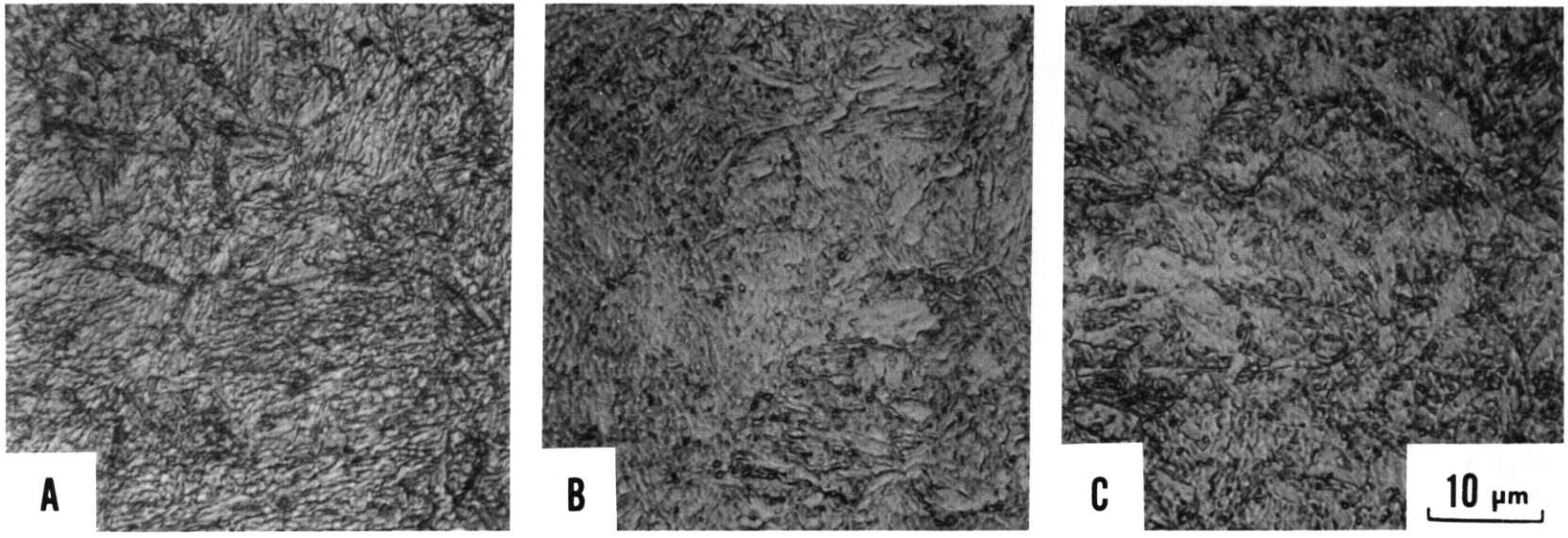

Fig. 7.2.4. Photomicrographs of 1¼Cr-1Mo-0.¼V after (a) 1000°C for 1 hour, air cool, (b) 1000°C for 1 hour, air cool; 650°C for 1 hour, air cool, and (c) 1000°C for 1 hour, air cool; 550°C for 1 hour, air cool, 550°C for 100 hours, air cool

The energy absorbed during fracture is calculated and normalized for crack length. The load at which dynamic yield occurs is used to calculate a stress intensity factor, K_Q, which may be considered plane strain where (1) the load strain trace shows a sharp peak indicating little plastic deformation, and (2) after visual inspection of the specimen indicates little plasticity. If these criteria are fulfilled, the value may be called K_{Id} and used to calculate critical flaw sizes (7). The specimens were fractured at temperatures from -200" to 300°C. The data plotted in Figure 7.2.5 and is given in Table 7.3.3.

Test Temperature (°C)	K_{Id}^* (MPa-$m^{\frac{1}{2}}$)	
	Embrittled	Unembrittled
-200	16.0	27.6
-60	35.2	35.8
-30	38.6	66.2
0	30.9	81.7
20	59.6	96.5
65	85.0"	133.5
100	95.4*	129.1*
185	125.8*	145.7*
310	126.7*	139.6*

The resulting curves have taken the familiar S-shape associated with the transition from a ductile to a brittle fracture mode. The curve associated with temper embrittlement is lower and to the right of the unembrittled material. The ductile-to-brittle transition temperature (DBTT) is shifted upward 80°C. This is defined as the temperature halfway between the upper and lower shelf. Also the fracture energies to cause dynamic fracture are lower on the upper and lower shelves. At -200°C,

*Those values denoted by an * did not fail in plane strain stress state and are apparent dynamic stress intensity values, K_a.

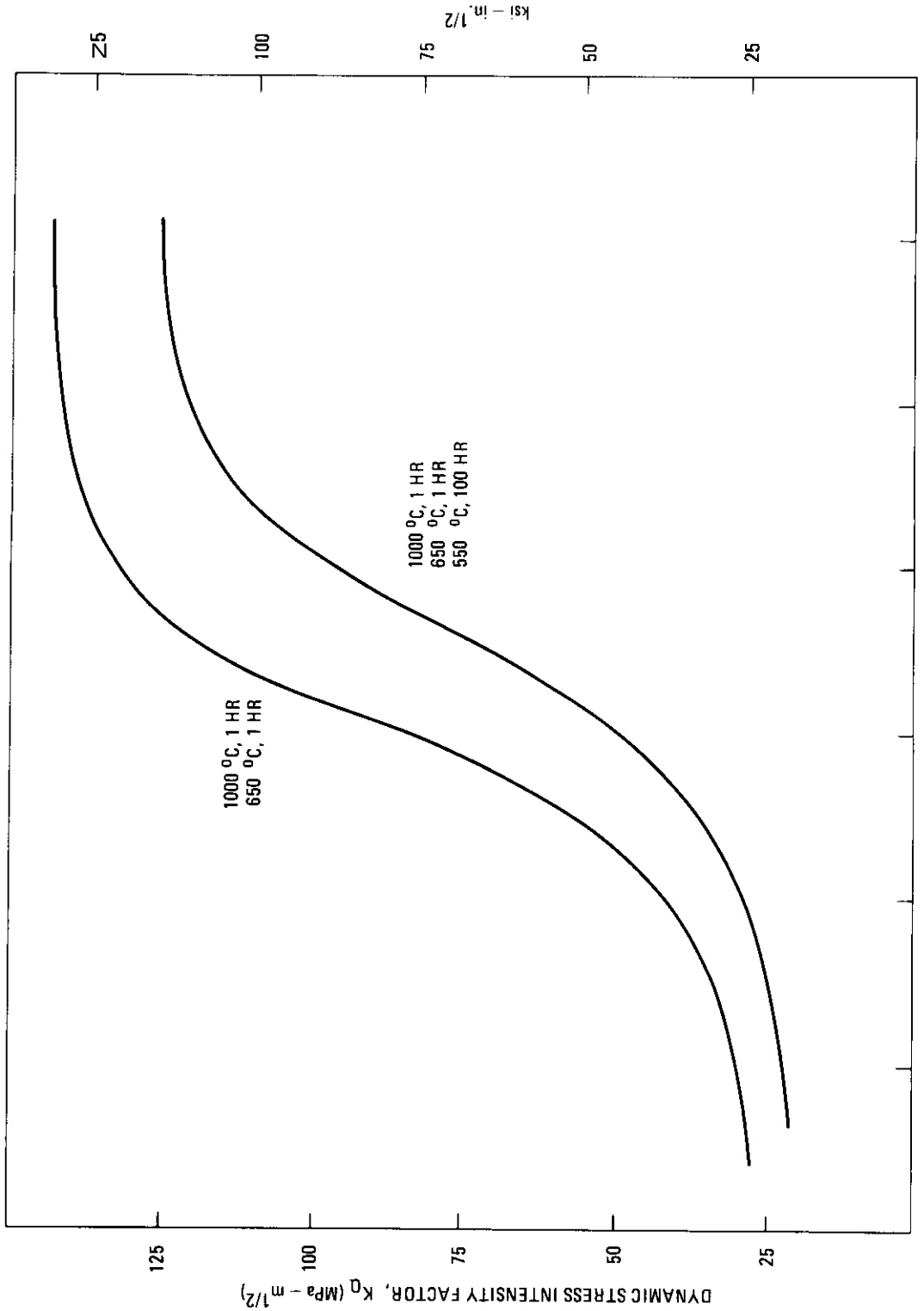

Fig. 7.2.5 Dynamic stress intensity factor as a function of temperature

the K_{Id} of unembrittled material is 28 MPa-$m^{\frac{1}{2}}$, compared to 22 MPa-$m^{\frac{1}{2}}$ for the embrittled case. At the upper shelf, the material was not constrained enough to prevent general yielding so plane strain conditions were not met. However, on the upper shelf the energy absorbed for unembrittled material was 143 MPa-$m^{\frac{1}{2}}$, whereas it was 126 MPa-$m^{\frac{1}{2}}$ for the embrittled. On the lower shelf where plane strain conditions definitely existed, the critical flaw size can be calculated from

$$a_c = \frac{1}{1.21\pi}\left(\frac{K_{Id}}{\sigma_{yd}}\right)^2$$

where the critical flaw size is a constant times the square of the ratio of dynamic stress intensity factor, K_{Id}, and dynamic yield stress σ_{yd}. The dynamic yield stress is found by

$$ayd = P_{GY}\left(\frac{L}{B(W-a)^2(1.21)}\right)$$

where P_{GY} is the load at general yield, B is the specimen thickness, (W-a) is remaining ligament, and L is the load span length. On the lower shelf of the embrittled material, the value of critical flaw size (i.e., the worst case) is 0.226 cm (0.089 in).

By comparison, Dufresne, et al., (10) predicted a critical flaw depth of 0.07 cm on welded 304 stainless steel irradiated to 2.37 dpa (8.18 x 10^{25} n/m^2), although their data was on subsize 3-pt. bend specimens at low He/dpa ratios. Cramer and Davis (11) made estimates of fracture toughness with high helium contents. Using data for 20% cold worked 316 stainless steel irradiated to 50 dpa and 3300 appm helium, they estimated the fracture toughness at 350°C to be 9.5 MPa-$m^{\frac{1}{2}}$. This was 37% of the predicted value for unirradiated material using the same approach. In another estimate they discussed, Wolfer and Conn, using the same data and another approach, estimated the fracture toughness to be 20 MPa-$m^{\frac{1}{2}}$. Recently, data on the same heat of the 12Cr-1Mo-0.3V steel used in this study, irradiated at 419°C to a fluence of 1.1 x 10^{22} n/cm^2 (E>0.1MeV) shows a K_{Jd}, dynamic ductile fracture toughness of 45 MPa-$m^{\frac{1}{2}}$ at 93°C, (12) on the lower shelf. By comparison, in this study at -200°C the K_{Id} was 20 MPa-$m^{\frac{1}{2}}$. This information suggests that

a 12Cr-1Mo-0.3V steel in the irradiated condition may have similar toughness as irradiated 316 stainless steel.

Standard Charpy impact tests were done at various temperatures according to ASTM Standard E23-66. The data is plotted in Figure 7.2.6. The results show the embrittlement time used to be insufficient to increase the DBTT (12), although upper and lower shelf energies decreased. This could be due to the relative cleanliness of this steel which was produced by the Vacuum Induction Melting/Electroslag Remelt (VIM/ESR) processes, or by an aging temperature which was not optimum for this material. This steel is inherently resistant to temper embrittlement which may be due to synergistic effects of Mn and Si (9). This agrees with Smidts' data which shows that aging for 5000 hours at 427°C does not cause an increase in the DBTT or decreases in the upper and lower shelf energies, whereas at 538°C for 5000 hours there is some embrittlement. An analysis of the fracture surface is in progress which may give information about the fracture mode and embrittling process. At this time, scanning electron microscopy data is unavailable to judge whether intergranular fracture occurred or what micromechanism was dominant.

The two types of fracture tests in this study, K_{Id} and CVN, show different tendancies in measuring embrittlement. The transition curves of the precracked specimens showed a definite embrittling effect, whereas there was no change in transition temperature as measured by Charpy impact energy. This suggests that sharp notch testing may be a more sensitive measure of the shift in DBTT caused by embrittlement.

7.2.7 Conclusions

(1) Austenitizing above 950°C for 1 hour results in hardnesses and microstructure associated with martensite and some undissolved $M_{23}C_6$.

(2) At 1000°C for 1 hour, ferrite is dissolved, and a small amount of $M_{23}C_6$ remains undissolved. Hardness data suggest a small amount remains undissolved at 1100°C.

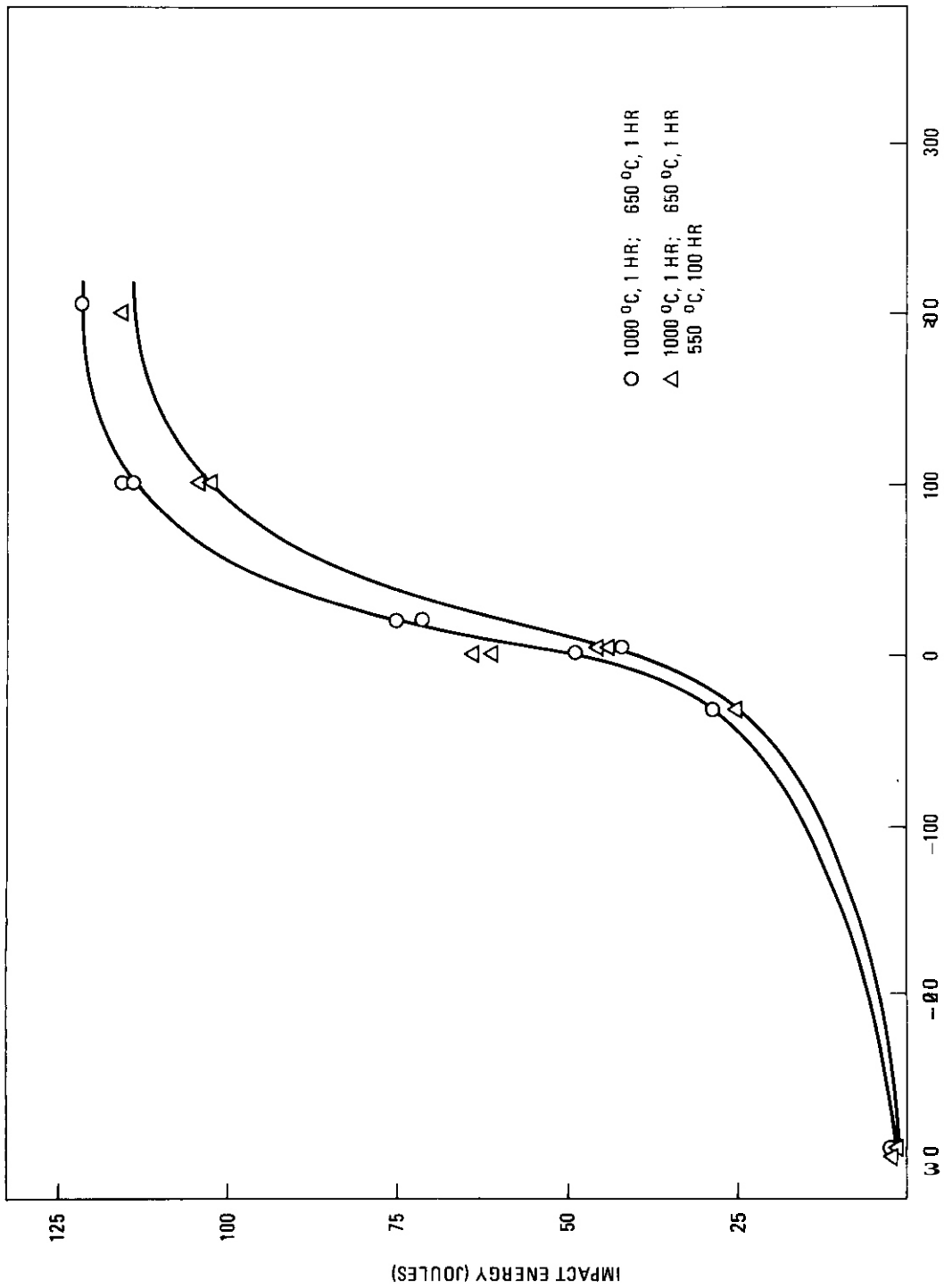

Fig. 7.2 The effect of temperature on Charpy impact energy

(3) Tempering at 650°C for 1 hour produces a nearly stable microstructure. A small amount of carbide will precipitate after 100 hours aging at 550°C.

(4) The OBTT increased 80°C due to aging at 550°C for 100 hours when measured by K_d obtained on precracked Charpy specimens; uppershelf K_d decreased 18 MPa-$m^{1/2}$ to 126 MPa-$m^{1/2}$; lower-shelf K_{Id} decreased 6 MPa-$m^{1/2}$ due to embrittlement.

(5) The lower-shelf, embrittled condition at -200°C has a K_{Id} of 22 MPa-$m^{1/2}$ which corresponds to a critical flaw size of 0.226 cm. This may be a lower boundary on toughness for this material in an overtempered condition and a reasonable estimate of the "worst case" fracture toughness. Dynamic fracture measurements on irradiated specimens with pertinent He/dpa ratios will be required to more completely address the "low" temperature fracture issue.

(6) Precracked and instrumented Charpy impact tests exhibited a shift in DBTT due to embrittlement, whereas standard Charpy V-notch tests did not. This result indicates that precracked instumented dynamic testing is a more sensitive (and perhaps more pertinent) measure of embrittlement then conventional CVN testing.

7.2.8 References

1. Berry, G., and R. Brook, "Influence of Temper Embrittlement on Fracture Toughness," Metal Science, 9 (1976) 286.
2. Lemble, P. H., A. Pineau, J. Castagne, Ph. Oumoulin and M. Guttman, "Temper Embrittlement in 12%Cr Martensitic Steel," Metal Science, 13 (1979) 496.
3. Reed-Hill, R., Physical Metallurgy Principles, 2nd Edition, D. Van Nostrand, New York, New York (1973) 726.
4. Bain, E., and H. Paxton, Alloying Elements in Steel, American Society of Metals, Metals Park, Ohio (1964) 37.
5. Lechtenberg, T., "The Microstructure, Mechanical Properties, and Two-body Abrasive Wear Resistance of Modified Secondary Hardening Steels," University of California, U.C. Press, Berkeley, California (1979).

6. Rickett, R., W. White, C. Walton, and J. Butler, "Isothermal Transformation, Hardening, and Tempering of 12% Chromium Steel," Transactions of the A.S.M., 44 (1952) 141
7. Ireland, D., "Proposed Standard Method of Test for Impact Testing of Precracked Charpy Specimens of Metallic Materials," Effects Technology, Inc., Santa Barbara (1980).
8. Chafey, J., and L. Thompson, "Post-Service Evaluation on the Properties of a 12Cr-1Mo Steel Super Heater Tube," General Atomic Report GA-A15701, 1980.
9. Garrison, W., unpublished data, Materials Science and Mineral Engineering, University of California, Berkeley, California.
10. Dufresne, J., B. Henry, and H. Larsson, "Fracture Toughness of Irradiated AISI 304 and 316L Stainless Steels," Effects on Structural Steels, ASTM STP 683, J. A. Sprague and D. Kramer (eds.), ASTM, 1979, p. 511.
11. Cramer, B., and J. Davis, "Fracture Mechanics Issues for Irradiated Blanket Structures," Nuclear Engineering and Design, 58 (1980) 267.
12. Smidt, F., J. Hawthorne, and V. Provenzano, "Fracture Resistance of HT-9 After Irradiation at Elevated Temperature," Alloy Development for Irradiation Performance, 9th Quarterly, March 31, 1980, DOE/ER-0045/2, p. 163.

7.3 TEMPERING AND TRANSFORMATION BEHAVIOR OF HT9 WELDMENTS

J. C. Lippold (Sandia National Laboratories, Livermore, CA)

7.3.1 ADIP Task

The Department of Energy (DOE)/Office of Fusion Energy (OFE) has cited the need for these data under the ADIP Program Task, Ferritic Alloy Development (Path E).

7.3.2 Objective

The objective of this phase of the investigation was to determine the solid state transformation behavior of HT9 weld and base material using the Gleeble dilatometer, and to evaluate the tempering response of various regions of the fusion zone and heat-affected zone in an autogenous gas tungsten arc weld.

7.3.3 Summary

Dilatometric measurements of HTY weld and base material indicated that the on-heating transformation to austenite occurs at approximately 840°C and that the martensite start temperature (M_s) upon cooling from above the upper critical temperature (Ac_3) occurs at 240°C. Postweld heat treatment of autogenous gas tungsten arc (GTA) welds results in a variety of composite microstructures consisting basically of tempered martensite and secondary carbides. The tempering response is relatively sluggish at tempering temperatures below 600°C. A one-hour heat treatment at 800°C reduced the martensitic hardness in the fusion zone and heat-affected zone (HAZ) to nearly base metal values. Tempering curves for both the fusion zone and HAZ are presented.

7.3.4 Progress and Status

The initial phases of this investigation of HTY martensitic stainless steel has been directed toward characterization of of the microstructure and properties of both the fusion zone and HAZ in the as-welded condition. Formation of untempered martensite in the fusion zone and portions of the HAZ imparts a high residual hardness to the

structure and usually necessitates a postweld heat treatment to produce reasonable toughness in the weldment.

This study investigates the transformation behavior which takes place during the weld thermal cycle and the effect of subsequent tempering on the microstructure and hardness of the as-welded structure. The results will he used to direct future development of alternate preheat and/or tempering treatments compatible with acceptable weld toughness.

7.3.4.1 Experimental Approach

Evaluation of transformation behavior and tempering response of HT9 weldments utilized material originally provided by General Atomic Company in the form of 6.4mm (0.25 in) thick pipe. For reference, the composition of the material is listed in Table 1.

Table 1

C	Si	Mn	Cr	Ni	Mo	W	V	P	S
0.22	0.38	0.52	11.3	0.50	0.85	0.50	0.27	.019	.006

Dilatometry--The transformation temperatures of the material were determined using a dilatometer in conjunction with the Model 1500 Gleeble,* Test samples with a reduced gage section of 5.1 mm (0.2 in) were machined both from the as-received pipe and from a section which contained a circumferential weld. The location of the weld corresponded to the reduced section of the test sample.

Samples were rapidly heated (approximately 250°C/sec) to peak temperatures of 1100, 1200, and 1300°C (2012, 2192, and 2372°F) and allowed to cool to room temperature. Dilation versus temperature data was collected during testing and plotted simultaneously on an X-Y recorder.

*Duffers Associates, Troy, NY

Postweld Heat Treatment. Postweld heat treatments were performed on autogenous bead-on-plate welds which were made using the gas tungsten-arc process with a heat input of 20 kJ/in (0.79 kJ/mm). The material was not preheated prior to welding. Small coupons containing the fusion zone, HAZ, and base metal were sectioned transverse to the welding direction and subsequently heat treated in air at 200, 400, 600, 800, and 900°C (392, 752, 1112, 1472, and 1652°F) for periods of 30 minutes and 1 hour. Heat-treated samples were inspected metallographically and microhardness surveys were performed throughout the weld region.

7.3.4.2 Transformation Behavior

Transformation temperatures upon heating and cooling were determined for both base metal and weld metal microstructures of similar composition. Since a negative volume change is associated with the transformation of BCT (body-centered tetragonal) martensite to FCC (face centered cubic) austenite, a dilation, or change in dimension, can be measured across the diameter of the Gleeble sample gage section. A plot of dilation versus temperature for a base metal sample heated to 1200°C (2192°F) is shown in Figure 1. Within single phase regions dilation increases proportionally with temperature as a consequence of the linear relationship between temperature and the coefficient of thermal expansion in this alloy. A departure from linearity indicates that a phase change has begun and subsequent return to linearity marks the completion of the transformation. Consequently, the Ac_1, Ac_3, M_s and M_f temperatures have been determined from the plot in Figure 1. The actual transformation temperatures have been corrected slightly for thermocouple errors which occur as a result of localized heat-sinking at the thermocouple-specimen junction.

Multiple thermal excursions indicated that the transformation temperatures are relatively insensitive to successive heating and cooling cycles. In addition, dilatometric measurements of weld metal samples indicated that the transformation characteristics of the fusion

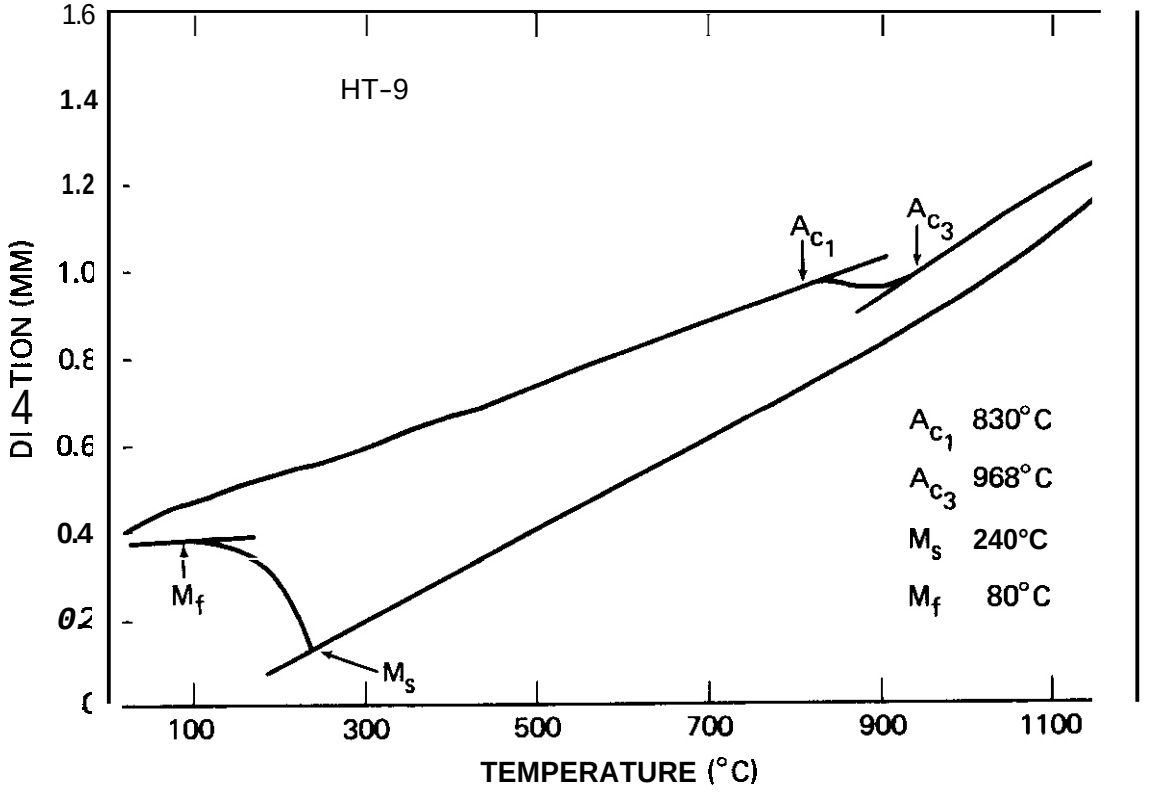

Figure 1. Dilation vs. Temperature Plot of a HT9 Base Metal Sample.

zone are similar to those of the base metal. Results of the dilatometry measurements are summarized in Table 2.

Table 2

Transformation Temperatures for HT9

Ac_3	960-980°C (1760-1800°F)
Ac_1	830-850°C (1525-1565°F)
M_s	240°C (465°F)
M_f	80-90°C (175-195°F)

Attempts to detect the austenite-delta ferrite transformation which occurs at near-solidus temperatures were unsuccessful as a result of the small proportion of delta ferrite which forms in this alloy.

7.3.4.3 Tempering Response

A microhardness traverse across the weld region of an as-welded sample which was not subjected to postweld heat treatment is shown in Figure 2. The relationship between the microhardness results and the microstructural features has been reviewed previously[1]. Note that regions of maximum hardness include the fusion zone and a portion of the HAZ adjacent to the fusion line. The drop in hardness at the fusion line was shown to result from the presence of a two-phase mixture of austenite and ferrite.

The tempering response of samples which were heated to 400, 600, and 800°C (752, 1112, and 1472°F) for one hour is summarized in Figure 3. Tempering of the martensite is extremely sluggish at 200 and 400°C and results in a microstructure with properties similar to the as-welded sample shown in Figure 2. Tempering at 600°C (1112°F) reduces the hardness uniformly in the fusion zone and throughout the HAZ; however, note that a perceptible relative minimum in hardness still exists at the fusion line. After one hour at 800°C the hardness of the entire weld region has dropped to the level of the original base metal microstructure ($\sim$30 R_c). Tempering at 900°C resulted in an increase in hardness in the weld region relative to the 600°C and 800°C heat treatments. Microstructural examination of this sample indicated that partial reaustenization occurred due to heating above the lower critical temperature (A_1) and tends to verify the dilatometric measurements reported previously.

Metallographic examination of the weld sample tempered at 800°C indicated that substantial microstructural transition occurs relative to as-welded microstructures. Micrographs of typical regions in the fusion zone, the coarse-grained and fine-grained regions of the HAZ, and the base metal are shown in Figure 4. Microstructural evolution involves the development of a tempered martensite which manifests itself in a lath-like morphology. Simultaneously, precipitation of secondary carbides serves to maintain adequate mechanical properties during tempering. These carbides were observed both along lath boundaries and within the individual laths. A more detailed evaluation of the effect of tempering on microstructural evolution will be

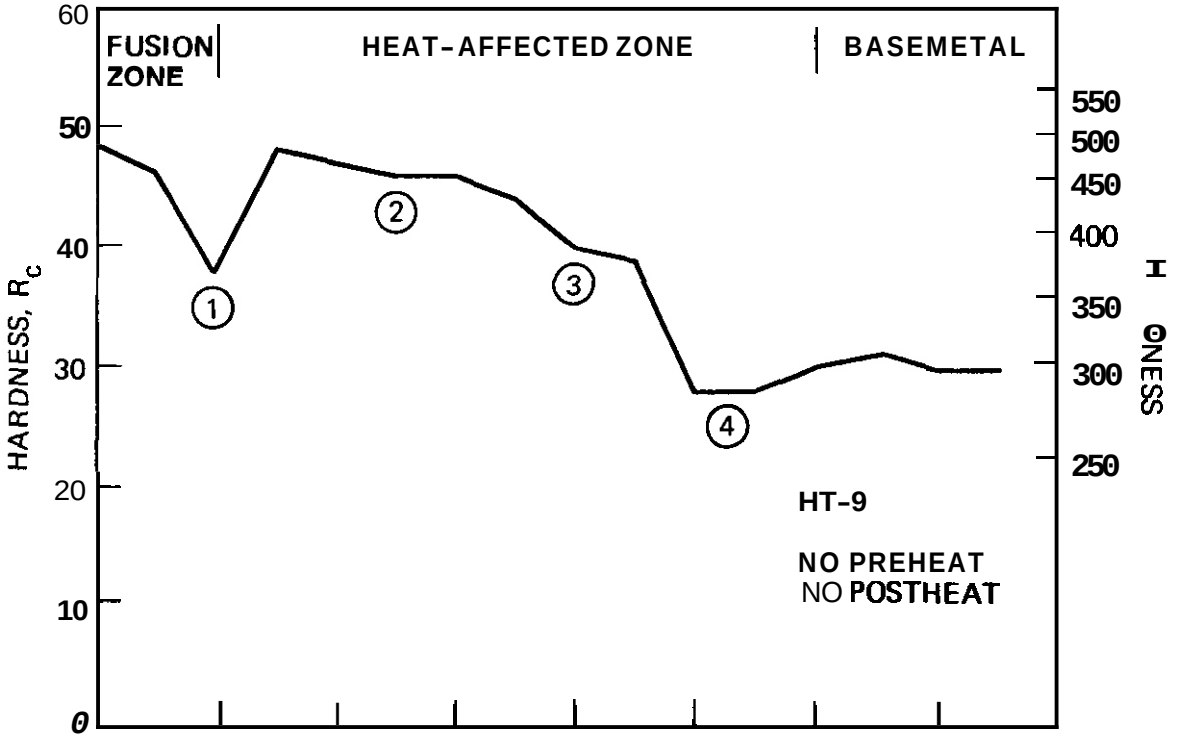

Figure 2. Microhardness Traverse Across the Weld Region of an As-Welded Sample.

included in a future report.

A tempering curve relating the microhardness in both the fusion zone and the coarse-grained region of the HAZ to the time-temperature parameter $T(20 + \log t) \times 10^{-3}$ is presented in Figure 5. The tempering response for both regions is nearly identical and agrees reasonably well with the curve developed by Mervyn et al.[2] for HT9 base metal.

7.3.5 Conclusions

1. Dilatometric measurements indicated that the lower critical temperature (Ac_1) is in the range of 830-850°C (1525-1565°F). The martensite start temperatures (M_s) was 240°C for both base metal and weld metal samples.

2. Tempering response is relatively sluggish below 600°C. After one hour at 800°C the hardness of the weld region is reduced to that

of the base metal.

3. The microstructure in both the fusion zone and HAZ consisted of a mixture of tempered lath-martensite and carbides.

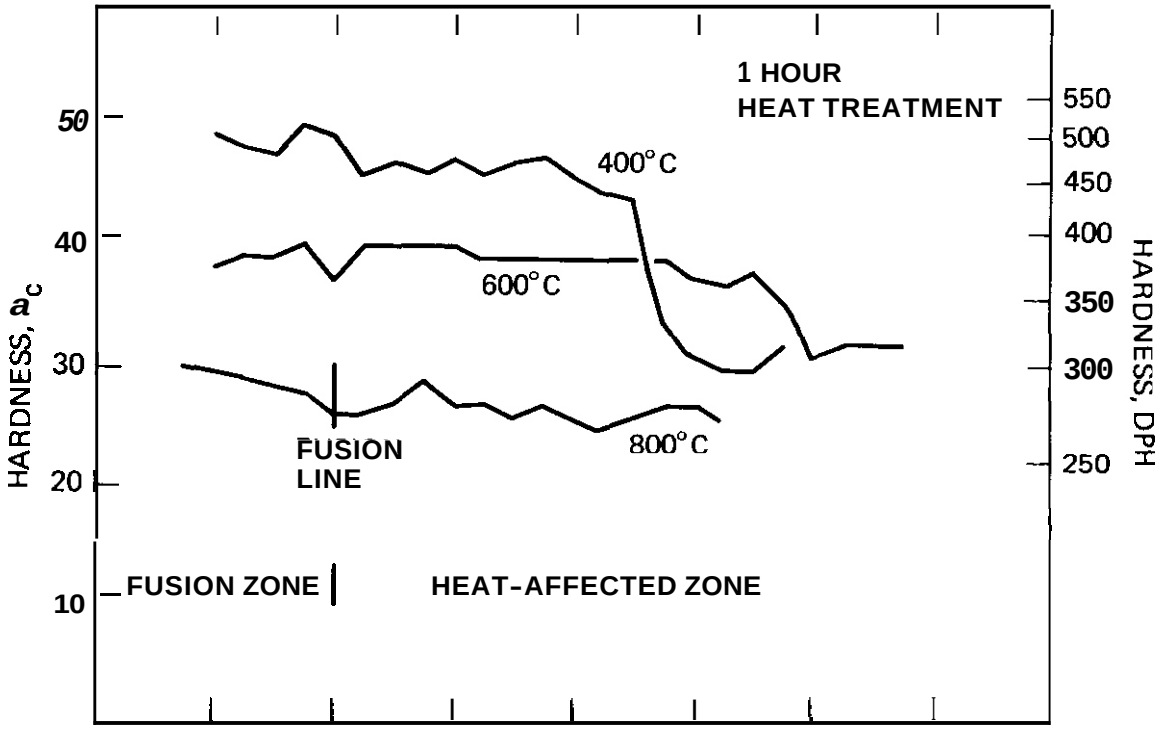

Figure 3. Microhardness Traverses Across the Weld Region of Samples Tempered for One Hour at 400, 600 and 800°C.

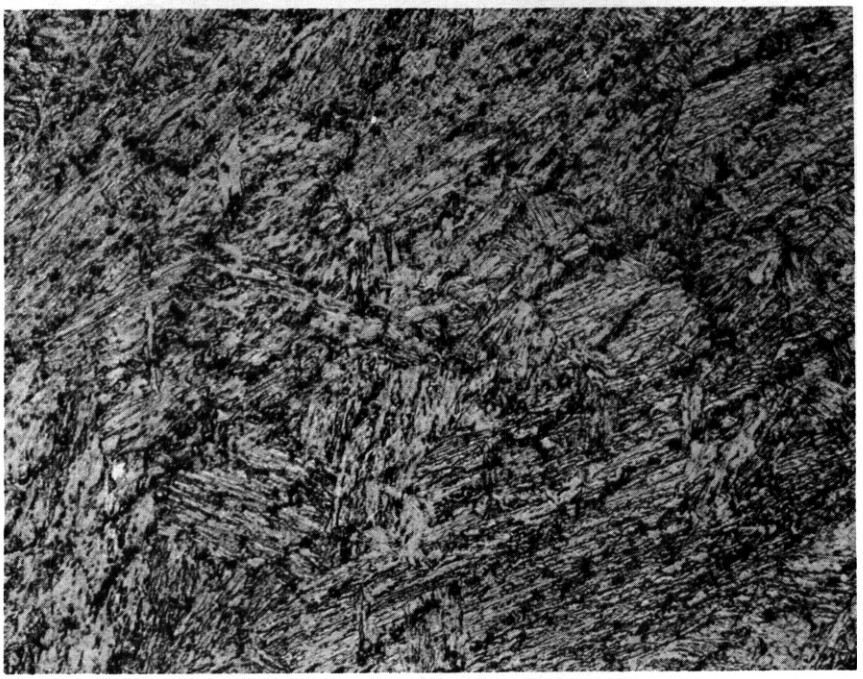

(a)

Fusion Zone

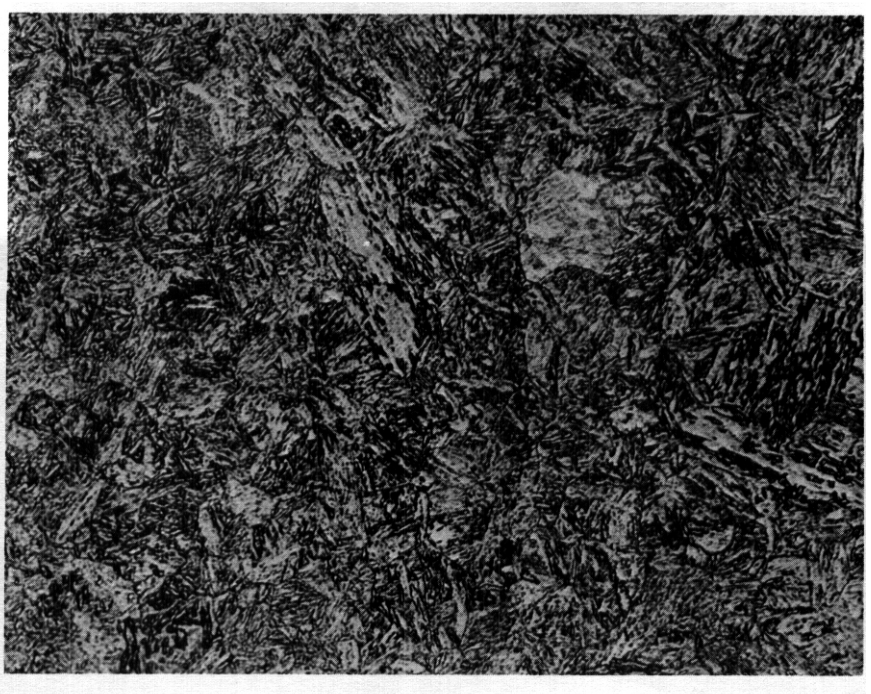

(b)

Coarse-Grained HAZ

Figure *4.* **Microstructure of Sample Tempered at** $800^{o}C$**, 400X.**

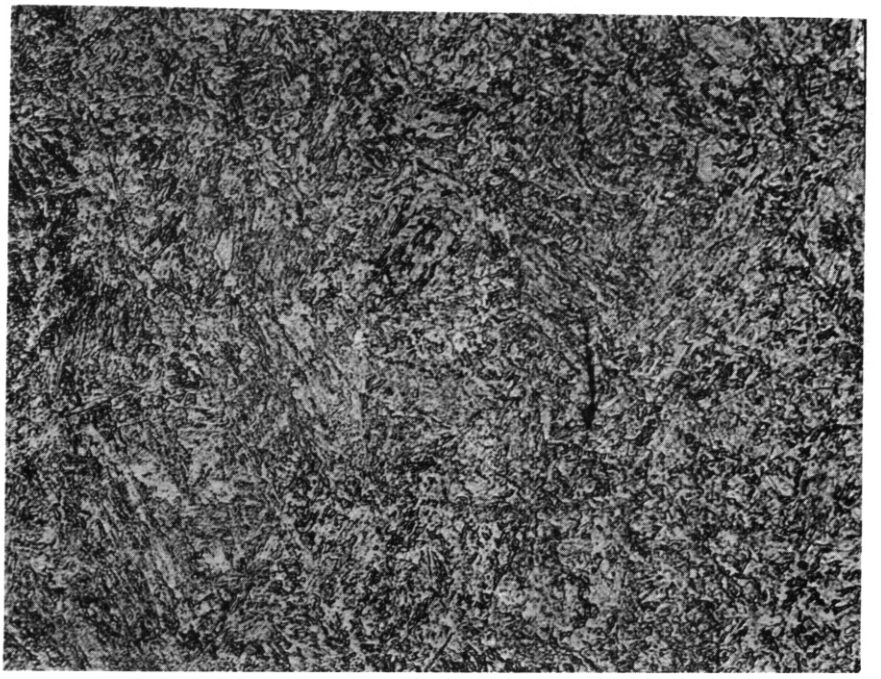

(c)

Fine-Grained HAZ

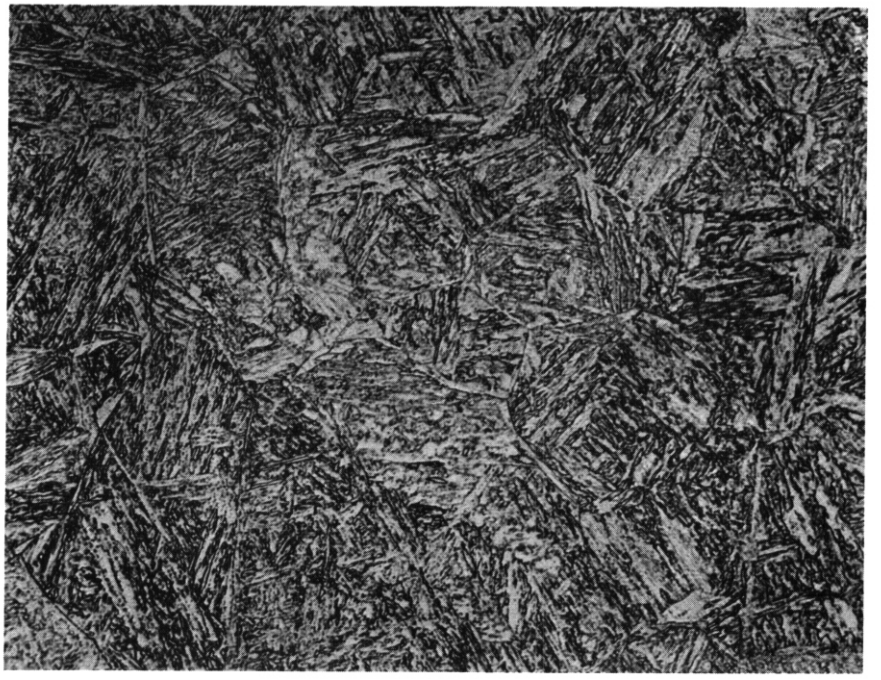

(d)

Base Metal

Figure 4. (continued) Microstructure of Sample Tempered at 800°C, 400X.

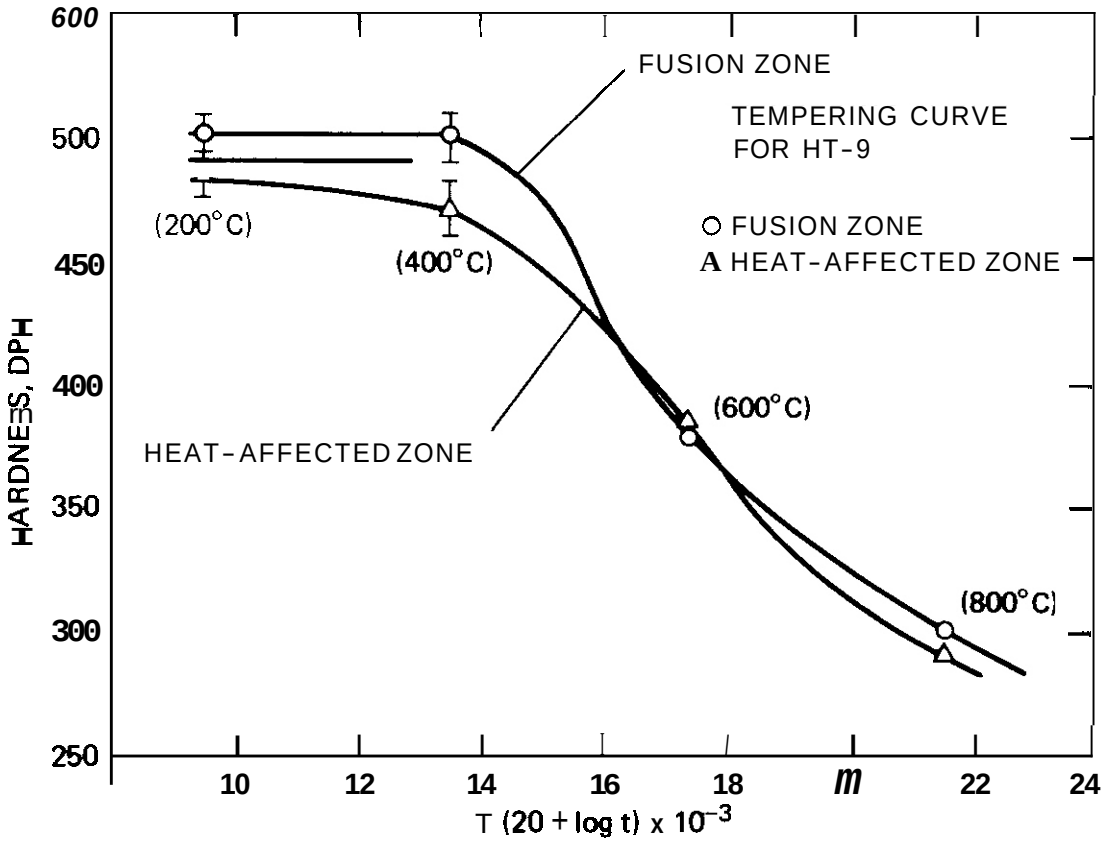

Figure 5. Tempering Curve for the Fusion Zone and HAZ of an Autogenous GTA Weld in HT9.

7.3.6 References

1. Lippold, J.C., "Weldability of HT9: The Autogenous GTA Process", ADIP Quarterly, Progress Report for period ending March 31, 1980, pp. 98–108.

2. Mervyn, D. A., Peterson, D.T., and Huang, F. H., "Microstructural and Fatigue Crack Growth Characterization of HT9", ADIP Quarterly Progress Report for period ending March 31, 1980, pp. 132–155.

7.4 FATIGUE CRACK GROWTH IN PATH E AND PATH B ALLOYS – D. A. Mervyn (Hanford Engineering Development Laboratory).

7.4.1 ADIP Task

Task Number I.B.4 - Fatigue Crack Growth in Special and Innovative Materials (Path E).

Task Number I.B.2 - Fatigue Crack Growth in High Strength/High Temperature Fe-Ni-Cr Alloys (Path B).

7.4.2 Objective

Baseline data on unirradiated Path E (HT-9 and 9Cr-1Mo) and Path B alloys has been generated in order to determine their desirability in reactor first wall applications.

7.4.3 Summary

Fatigue crack growth tests on unirradiated HT-9 in helium at 150, 300, 500 and 600°C and on 9Cr-1Mo at 25°C in air have been conducted. Room temperature air testing of solution treated and aged B1, B2, B3, B4 and B6 alloys has been completed and is compared to the 50% cold-worked B alloys tested under similar conditions. Comparisons of measured fatigue crack growth are made with 20% cold-worked 316 stainless steel.

7.4.4 Progress and Status

7.4.4.1 Introduction

This study was conducted to characterize the fatigue crack propagation behavior of unirradiated HT-9 and 9Cr-1Mo. In addition, the room temperature crack growth behavior of the solution treated and aged Path B alloys was determined.

7.4.4.2 Experimental

Compositions of the alloys tested and their thermomechanical treatments are outlined in Table *7.4.1.* ***The*** austenitized and tempered condition of HT-9 was chosen from a number of themomechanical treatments investigated in a previous study.[1] 9Cr-1Mo was tested in a condition similar to that

TABLE 7.4.1

ALLOY COMPOSITION AND CONDITION
Nominal Wt %

Alloy	Condition	Fe	Ni	Cr	Mo	Nb	Ti	Al	Mn	C
Path B										
B1	50% CW + 1025°C/5 min/AC + 750°C/8 hr/AC	Bal	25.0	10.0	1.0	-	3.0	1.5	1.0	0.08
B2	50% CW + 1025°C/5 min/AC + 800°C/8 hr/AC	Bal	20.0	12.0	3.0	-	1.3	1.5	0.2	0.03
B3	50% CW + 1025°C/5 min/AC + 750°C/8 hr/AC	Bal	30.0	12.0	-	2.0	2.0	0.5	1.0	0.03
B4	50% CW + 1025°C/5 min/AC + 850°C/3 hr/AC + 720°C/8 hr/FC to 620°C/18 hr total furnace time/AC	Bal	20.0	12.0	-	3.0	1.8	0.3	0.2	0.08
B6	50% CW + 1150°C/2 hr/AC + 700°C/20 hr/AC	Bal	75.0	18.0	-	1.0	2.5	1.5	0.2	0.08
Path E						W	V	Si		
HT-9	1038°C/5 min/AC + 780°C/2.5 hr/AC	Bal	0.50	11.3	0.85	0.50	0.27	0.38	0.52	0.2
9Cr-1Mo	1033°C/5 min/AC + 760°C/1 hr/AC	Bal	0.11	8.84	0.93	<0.01	0.21	0.06	0.04	0.01
						S	Nb	Ti	Co	Cu
						0.019	0.06	0.01	0.02	0.09

of HT-9.

Fatigue crack growth tests were conducted using miniature center-cracked specimen technology and the electropotential technique described previously(2) All specimens were cycled sinusoidally using load as the control parameter at a stress ratio R of 0.05. HT-9 was tested in helium at 1 Hz at *150*, 300, 500 and 600°C and at a maximum load of *475* lbs. Room temperature testing of 9Cr-1Mo and the Path B alloys was performed in air at a cyclic frequency of 15 **Hz.**

7.4.4.3 Results and Discussion

HT-9 test results between 150 and 600°C are presented in Figure *7.4.1.*

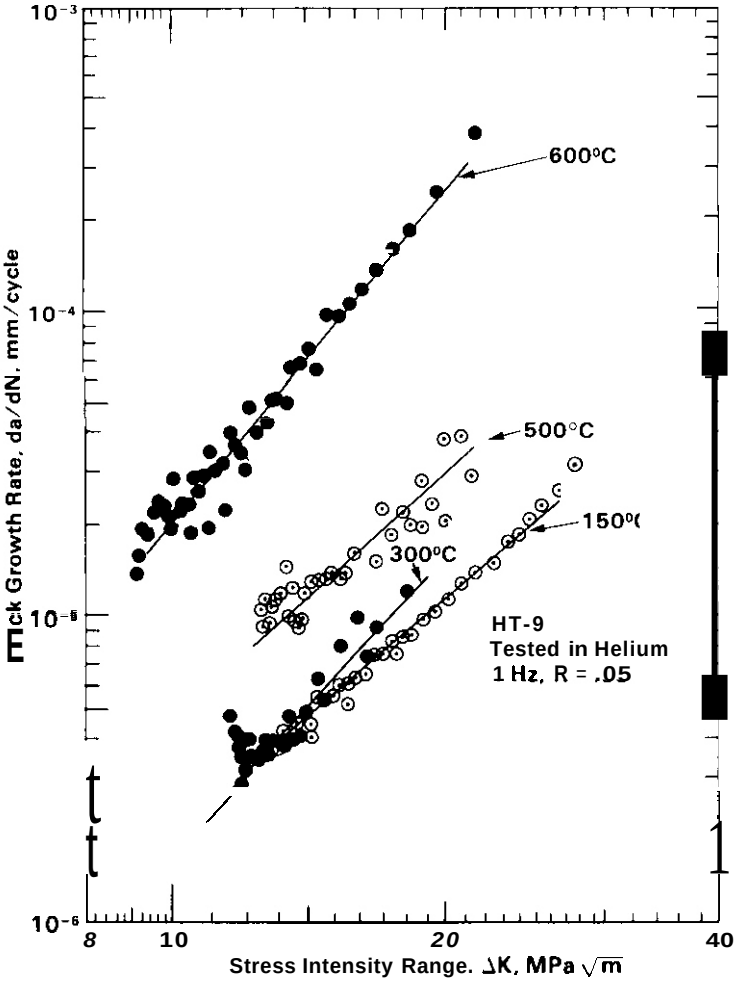

FIGURE *7.4.1* Comparison of Crack Growth Between 150 and 600°C

At a stress intensity factor (ΔK) of 12 MPa $\sqrt{m}$, crack growth at 500°C is a factor of 2.4 higher than at 150°C and at 600°C it is a factor of 12.3 higher. Crack growth at 300°C is essentially equivalent to that at 150°C, considering the data scatter.

A total data scatter of a factor of two, on da/dN, is considered normal for intralaboratory tests conducted on a single heat of material under identical conditions.[3] Therefore, an increase in crack growth by a factor of 2.4 between 150°C and 500°C is relatively insignificant. However, between 500 and 600°C crack growth increases rapidly.

The austenitized and tempered microstructure of HT-9 consist of martensite laths within prior austenite grain boundaries. Precipitate carbides lie within these laths as well as along lath and grain boundaries.[1] The martensite is strengthened by carbon held in solution in its matrix. Between 500 and 600°C the carbon comes out of solution to coarsen the precipitate carbides. Accordingly, the ultimate tensile strength and yield strength decreases between these two temperatures.[4] The HT-9 creep coefficient is also relatively insensitive to temperature below 600°C, but above 600°C it becomes extremely temperature dependent. Some of these microstructural and mechanical property changes may account for the rapid increase in crack growth between 500 and 600°C in HT-9.

The crack growth behavior of 9Cr-1Mo tested in air at room temperature is compared to that of HT-9 in Figure 7.4.2. The behavior of the two ferritics is equivalent under these conditions.

Test results on the solution treated and aged (STA) Path B alloys are presented in Figures 7.4.3, 7.4.4, 7.4.5, 7.4.6 and 7.4.7, where they are compared to results from the 50% cold-worked (CW) alloy tested under the same conditions??' In all cases, the crack growth rate of the 50% CW material was higher than that of the STA material. The crack growth rates differ by as little as a factor of 2 for alloy B4 and as much as a factor of 18 for alloy B6.

If Path B alloy tensile characteristics are similar to its commercial counterpart, the difference between crack growth in the CW and STA conditions can be explained. For instance, B4 has a similar composition and heat treatment as STA Inconel 706.[5] Annealed 706 has a room temperature yield strength of 46,000 psi, while the STA condition has a yield strength of 147,000 psi. A similar trend is observed in Inconel X750, which is like

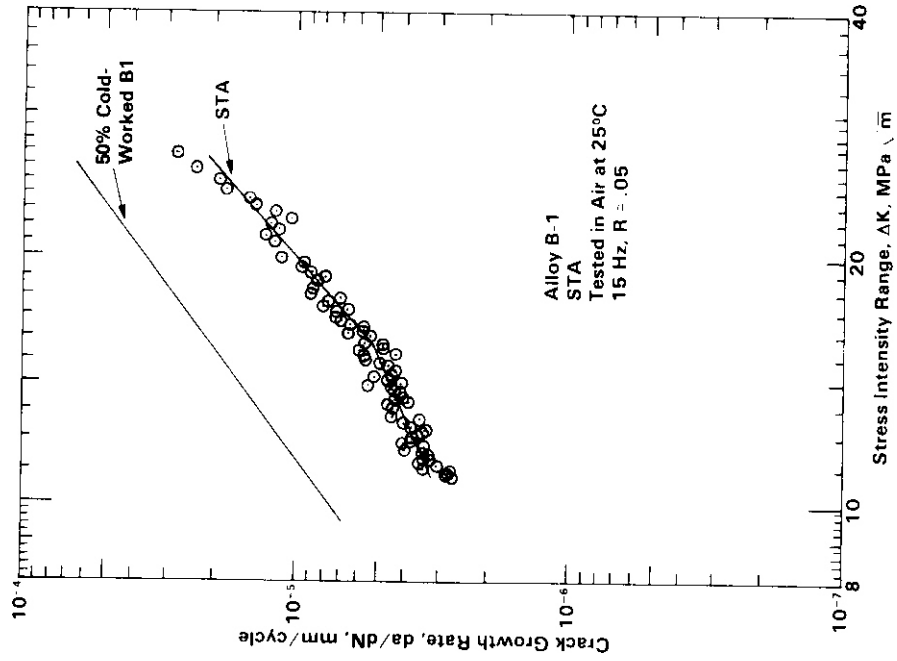

FIGURE 7 4 3 Crack Growth in Alloy B1, STA and CW Conditions.

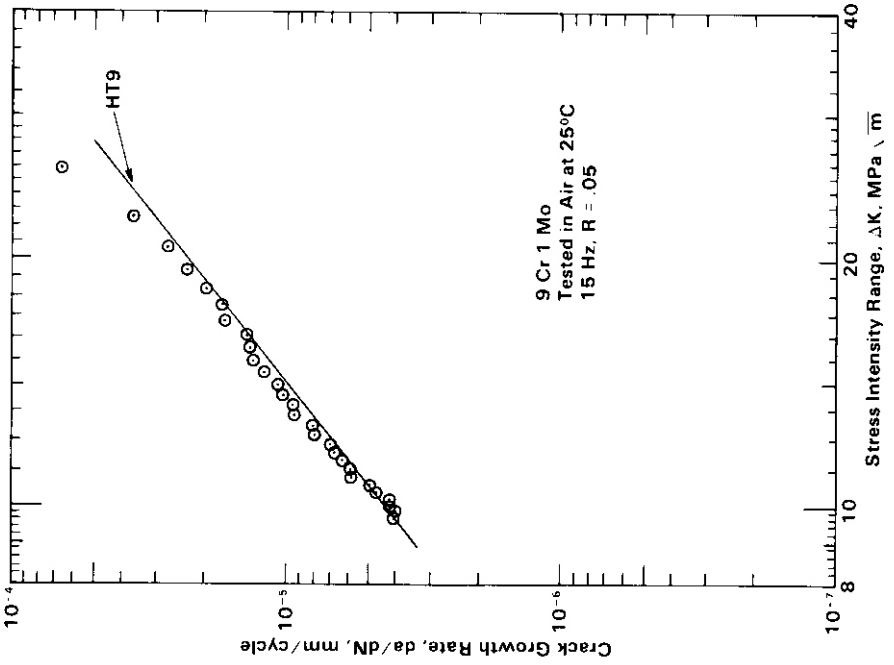

FIGURE 7 4 4 Crack Growth in HT-9 and 9Cr-1Mo.

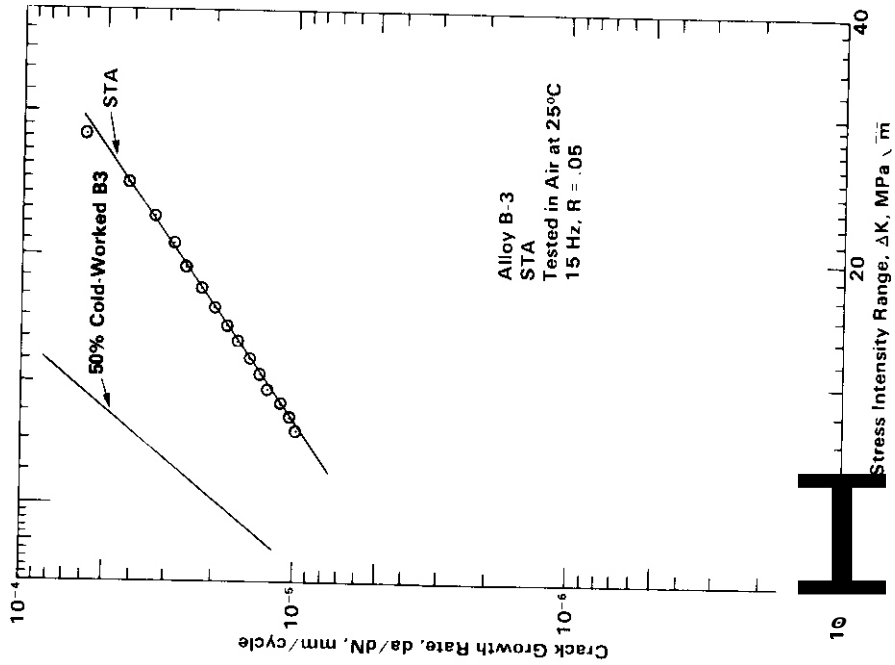

FIGURE 7.4.5 Crack Growth in Alloy B3, STA and CW Conditions.

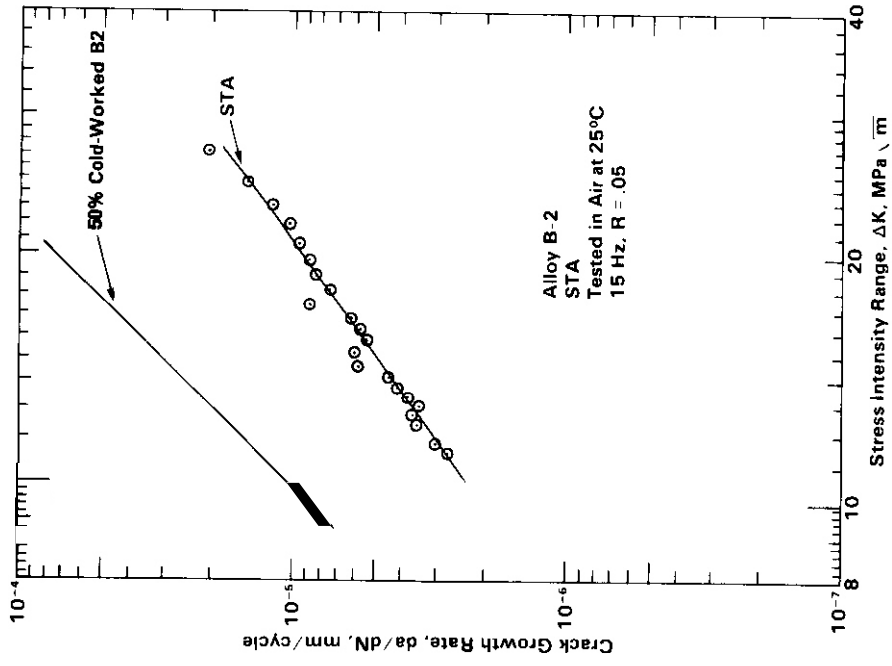

FIGURE 7.4.4 Crack Growth in Alloy B2, STA and CW Conditions.

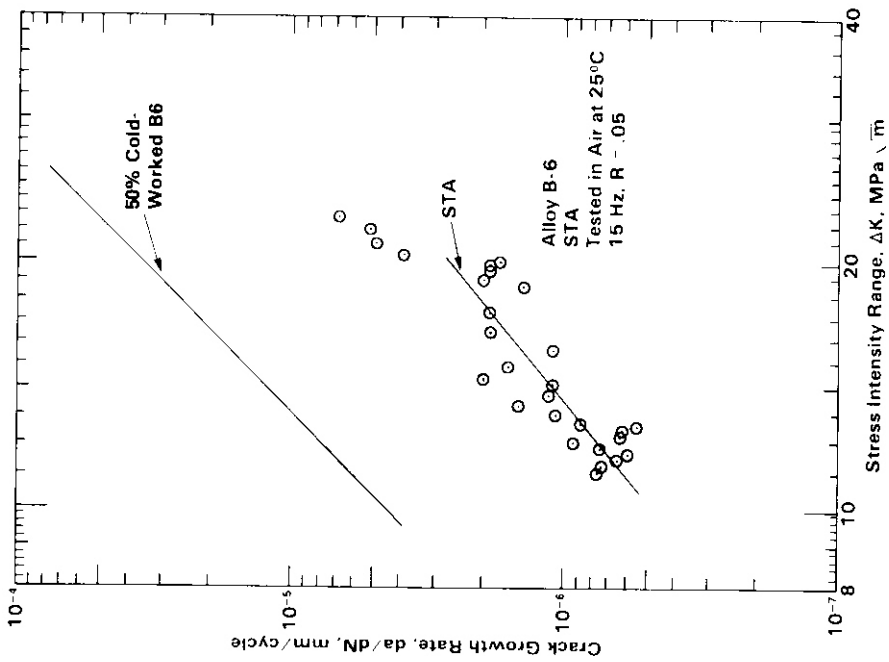

FIGURE 7.4.7 Crack Growth in Alloy B6, STA and CW Conditions.

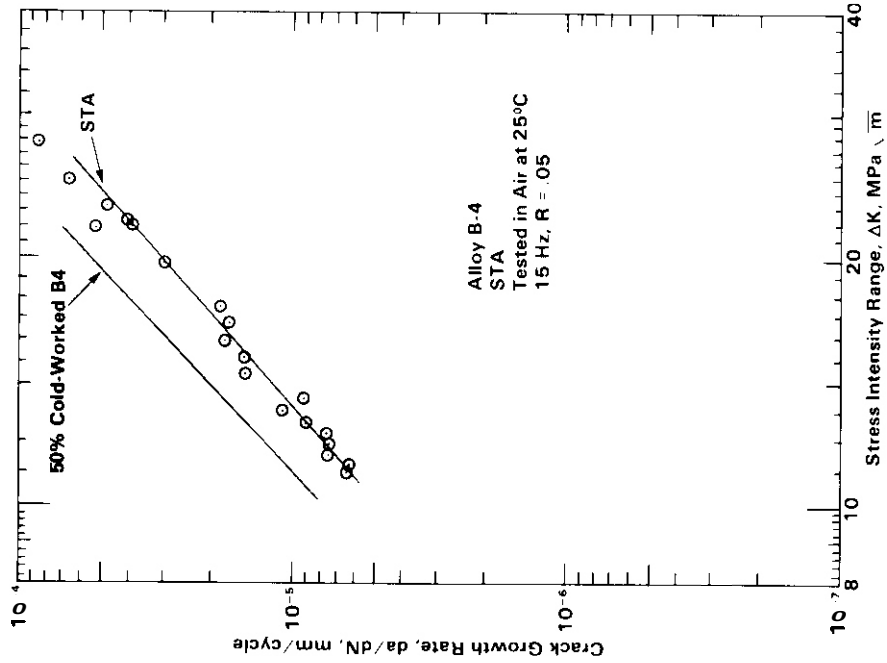

FIGURE 7.4.6 Crack Growth in Alloy B4, STA and CW Conditions.

B6. Since an increase in yield strength increases crack growth resistance, the lower crack growth rates of the STA Path B alloy can be explained if this condition has a higher yield strength than the CW alloy. Other factors influence the fatigue behavior in these alloys, as evidenced by the fact that although STA Inconel 706, or B4, appears to have a higher room temperature yield strength than STA Inconel X750, B6, it has a lower crack growth resistance. Since there is a lack of Path B tensile data, a direct correlation between the alloys, not only in behavior, but also in magnitude, cannot be made at the present time.

A comparison of the STA group is presented in Figure 7.4.8. The crack growth behavior of B1 and B2 are essentially equivalent, as is that of B3 and B4. The crack growth rate at $\Delta K = 11$ MPa $\sqrt{m}$ of B1 and B2 is a factor of 2.7 lower than that of B3 and B4. Crack growth in B6 is a factor of 12 lower than B3 or B4. Crack growth in B1, B2 and B6 is also lower than that in HT-9 or 20% CW 316 SS tested under the same conditions.

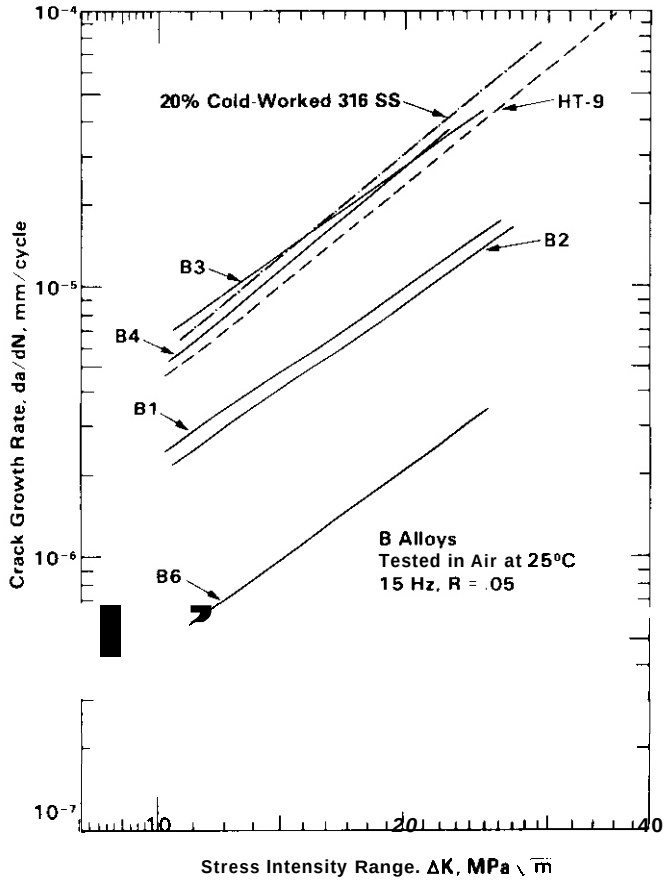

FIGURE 7.4.8 Comparison of Crack Growth in the Path B Alloys, with HT-9[1] and 20% CW 316SS[2].

A correlation between crack growth rate and nickel content of the five alloys, Figure 7.4.9, indicates that Ni content alone does not dictate the crack growth behavior. The Figure does separate the alloys according to their primary strengthening mechanisms. B3 and B4 are both doubly strengthened, B3 by γ' and Laves phase and B4 by γ' and γ''. B1 and B2 are strengthened solely by γ' and B6 by the presence of γ' and a high percentage of nickel. This difference in crack growth behavior as a function of precipitate phases strengthening indicates that the continual addition of strengthening phases may effect other properties in the Path B alloys.

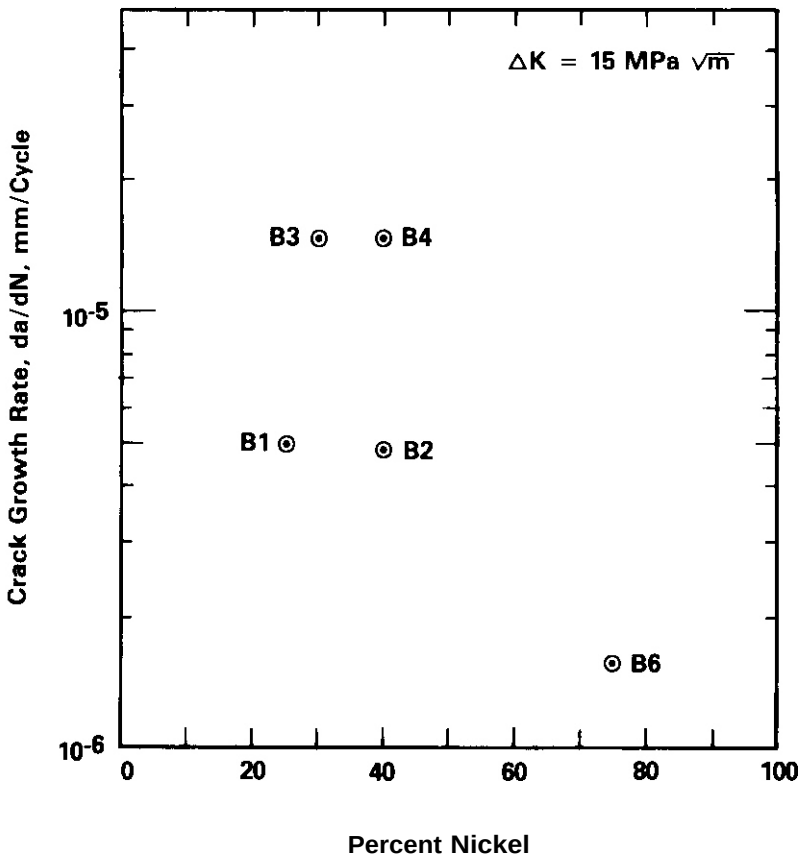

FIGURE 7.4.9 Crack Growth in the Path B Alloys as a Function of Nickel Content.

Embrittling phases such as the Laves phase in B3 or excessive hardening phases such as γ'' in B4 can decrease alloy ductility and therefore adversely effect the crack growth behavior. The high crack growth resistance of

alloy *B6* may not only be attributed to its unembrittled γ' strengthening, but also to the known beneficial influence of its high nickel content.

7.4.5 Conclusions

1. A baseline fatigue crack growth study on unirradiated HT-9 has been completed. Crack growth is relatively insensitive to temperatures between 150 and 500°C. Above this temperature crack growth increases rapidly.

2. The crack growth rates of 9Cr-1Mo and HT-9 are equivalent in room temperature air.

3. Crack growth in room temperature air of Path B alloys B1 and *B2* is a factor of *2.7* lower and alloy *B6* a factor of **12** lower than B3 and *B4.* The low crack growth resistance of B3 and *B4* may be due to the presence of embrittling phases in these alloys, which may lower ductility. The higher nickel content of alloy *B6* tends to enhance its crack growth resistance.

7.4.6 Future Work

A temperature dependent crack growth equation for HT-9 will be developed. Baseline testing of unirradiated 9Cr-1Mo at elevated temperatures will be completed. The STA Path B alloys will also be tested at elevated temperatures.

7.4.7 References

1. D. A. Mervyn, D. T. Peterson and F. F. Huang, "Microstructural and Fatigue Crack Growth Characterization of HT-9," *ADP Quarterly Progress Report, March 31, 1980.*

2. D. A. Mervyn, M. M. Paxton and A. M. Ermi, "Development of the Miniature Fatigue Crack Growth Machine," *ADIP Quarterly Progress Report, September 30, 1979.*

3. L. A. James, "Fatigue Crack Propagation in Austenitic Stainless Steels," ***Atomic*** *Energy Review* *14, 1 (1976).*

4. J. Z. Briggs and T. D. Parker, "The Super 12% Chromium Steels," *Climax Molybdenum Company.*

5. Alloy Digest, November 1970.

7.5 ANALYSIS OF SINGLE SPECIMEN TESTS ON HT-9 FOR J_{1C} DETERMINATIOS

- F. H. Huang and G. L. Wire (Hanford Engineering Development Laboratory)

7.5.1 ADIP Task - ADIP Fusion

7.5.2 Objective

The objective of this work is to evaluate the upper shelf toughness of HT-9 using the electropotential technique. The ultimate goal is to characterize the fracture behavior of fusion first wall materials by single specimen method.

7.5.3 Summary

Fracture toughness tests were performed on unirradiated 2.54 mm thick HT-9 specimens at 25, 149, 232, 315, 427 and 539°C. The electropotential technique was applied to develop single specimen method for J_{1C} determination. Based on experimental data, a semi-emperical expression was obtained for a calibration curve which was used to measure continuous crack extension. With this continuous Δa measurement, it is possible to generate J versus Aa curves from single specimens at various temperatures successfully. Large specimens were also tested at 232°C to study the thickness effect on upper shelf toughness of HT-9. The upper shelf fracture toughness of HT-9 is evaluated at temperatures ranging from room temperature to 539°C.

7.5.4 Progress and Status

7.5.4.1 Introduction

The upper shelf ductile fracture behavior of ferritic steels, which are fusion first wall candidates, is studied using elastic/plastic fracture mechanics. For materials under small-scale yielding conditions when the plastic zone size is small compared to crack length, the stress intensity factor K is used to characterize the material resistance to crack growth. However, under large scale yielding conditions, J-intergral,[1] crack-opening-displacement[2] and near-tip-strain[3] have been successfully used

to characterize the fracture of ductile materials. Because of limitations on irradiation space and the fact that the first wall is expected to be on the order of 3 mm thick, miniaturized circular compact specimens are tested, and single specimen techniques have been developed. The single specimen method requires techniques capable of monitoring continuous crack extension during the test such as electropotential,[4] compliance[5] and acoustic emmission[6] method. The electropotential method is one of the most accurate and sensitive techniques, particularly for small specimens, and has been used for decades to study a wide range of fracture problems. The basis for crack extension measurement by this method is that the potential difference between two points spanning the crack will increase as the crack propagates, because the resistance increases while the current applied to the specimen is maintained constant. A calibration curve relating the potential drop to crack extension is generated from different specimens tested at a variety of elevated temperatures. Through the use of this calibration curve, the continuous crack extension can be measured and the procedure for single specimen fracture toughness measurement established.

The material used in this experimental program is HT-9 which is expected to undergo a ductile-to-brittle transition around room temperature. This transition temperature is known to be elevated by irradiation.[7] All tests in this work were carried out at upper shelf temperatures. The techniques for fracture toughness tests developed in this work will be utilized in the hot cell for tests on irradiated specimens.

7.5.4.2 Experimental Procedure

The 2.54 mm thick test specimens were fabricated from as received HT-9 bar stock in mill annealed condition, hot worked at 1149°C for 1 hour, tempered at 740-760°C for 1 hour and air cooled. Details of the test apparatus and test procedures were described in Reference 8 for room temperature tests and Reference 9 for elevated temperature tests. The schematic diagram of the specimen is shown in Figure 7.5.1(a). The positions of the current input and potential measurement leads were shown in Figure 7.5.1(b). All specimens were fatigue precracked to 1.3 mm below a stress intensity factor of 28 MPa $\sqrt{m}$ using a servo-hydraulic system.

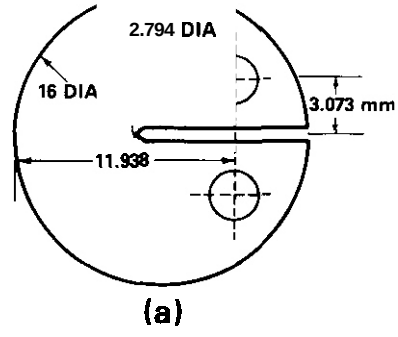

Figure 7.5.1 (a) Circular Compact Test Specimens of HT-9

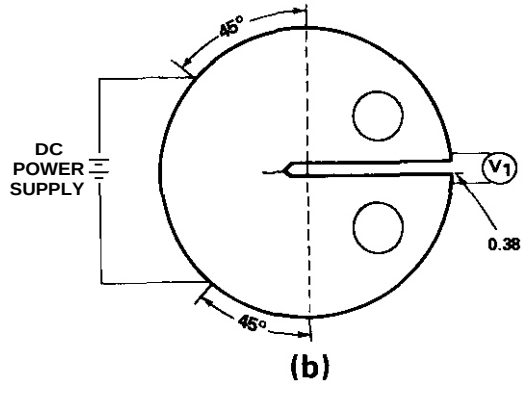

Figure 7.5.1 (b) Schematic Drawing of Electropotential Technique

Fracture toughness tests were performed at 25°C, 149°C, 232°C, 315°C, 427°C and 539°C. A constant DC current of 13.5 amp was applied to the specimen. During each test, the load and electropotential were monitored simultaneously. After the test was completed, each cracked specimen was heat tinted at 529°C for 1 hour to reveal the crack extension (Figure 7.5.2), which provided calibration data points for potential versus crack extension curves.

The values of J were calculated from load versus load-line displacement curves in the form:[10]

$$J = \frac{1 + \alpha}{1 + \alpha^2} \frac{2A}{Bb} \qquad [1]$$

Where: A is the area under load versus load-line displacement curve, B is the specimen thickness, b is unbroken ligament size, a is

$$a = 2\,[(a/b)^2 + (a/b) + 1/21 - (2\,a/b + 1) \qquad [2]$$

The equation is a simplified form of J derived from Merkle-Corten expression [Q] for a/w > 0.5.

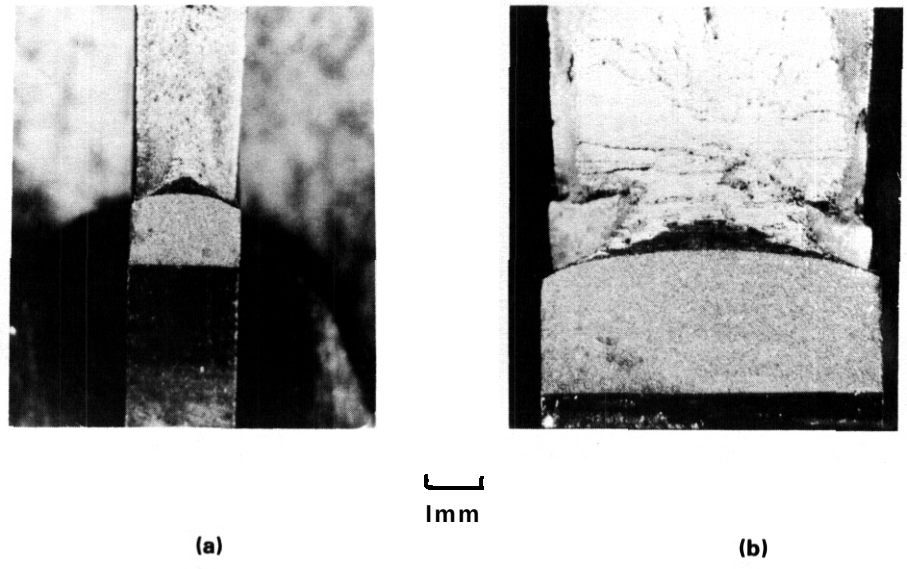

Figure 7.5.2 Crack Extension as Revealed by Heat Tinting for: (a) 2.54 mm Thick: (b) 7.62 mm Thick Specimen of HT-9.

7.5.4.3 Results and Discussions

J versus Δa data for various temperatures were plotted in Figure 7.5.3 through Figure 7.5.8. A J_{1C} value is determined by the intersection of the blunting line having a slope of $2\sigma_f$ and the best fit line drawn through the J versus a data. J_{1C} values for various temperature tests were compiled in Table 7.5.1. The temperature dependence of ductile fracture toughness J_{1C} for HT-9 obtained by multispecimen method is shown in Figure 7.5.9. As can be seen in Figure 7.5.9, J_{1C} decreases with increasing upper shelf temperature from room temperature to 250°C, then increases as temperature is increased up to 550°C.

The temperature dependences of critical J value corresponding to a crack extension of 0.2 mm and to an offset of 0.06 mm were also plotted in Figure 7.5.9. It is interesting to note that the trends do not differ from

that of J_{1C} versus temperature curves where J_{1C} is determined by the conventional multispecimen method. This alternate method may be convenient for designer use to provide for less conservative design criteria.

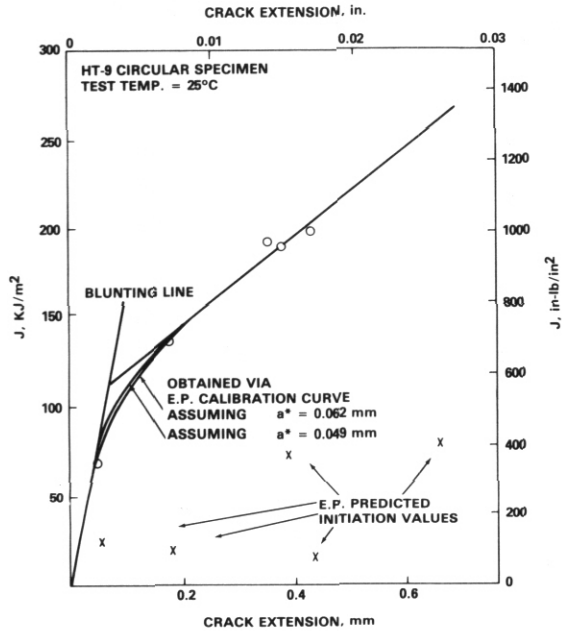

Figure 7.5.3 J Versus a Tested at 25°C for HT-9.

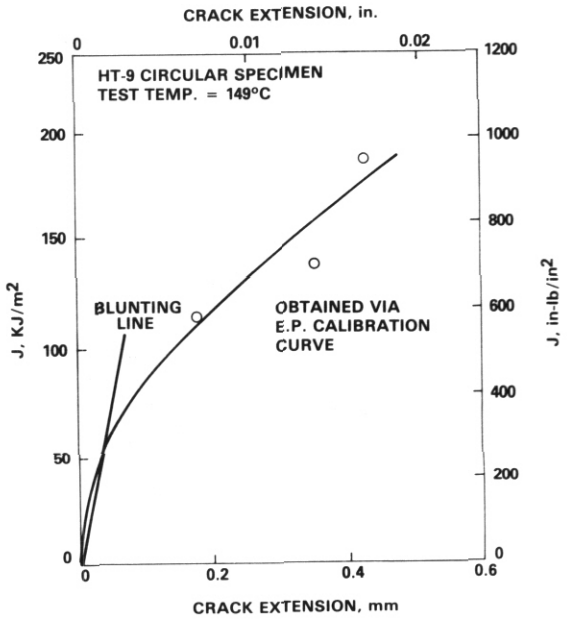

Figure 7.5.4 J Versus a Tested at 149 C°for HT-9.

There are limits on the use of J as a single parameter to characterize the strength of the crack tip singular field. One of the limits is specimen size. The thickness criterion is expressed by

$$B \geq \frac{25\ J_{1C}}{\sigma_f} \qquad [3]$$

For HT-9, σ_f = 717.2 MPa, J_{1C} = 112.3 KJ/m^2 at room temperature. The thickness criterion is 3.5 mm which is close to the test specimen thickness of 2.54 mm. Fracture toughness tests were also performed on larger specimens to study size effects on fracture toughness. Figure 7.5.10 shows the J values obtained from 2.54 mm thick specimens and larger specimens at 232°C. The larger specimen is 7.6 mm thick with other dimensions doubled those of 2.54 mm thick specimens. It can be seen from Figure 7.5.10 that the fracture resistance of the large specimen is smaller than that of

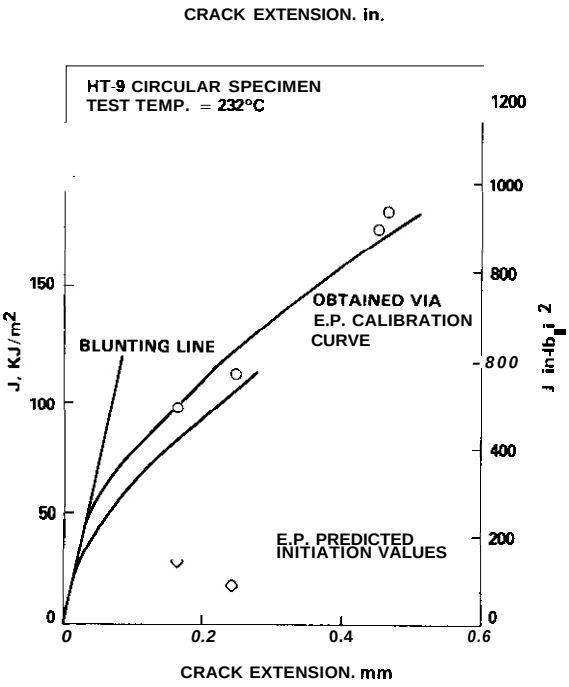

Figure 7.5.5 J Versus a Tested at 232°C for HT-9.

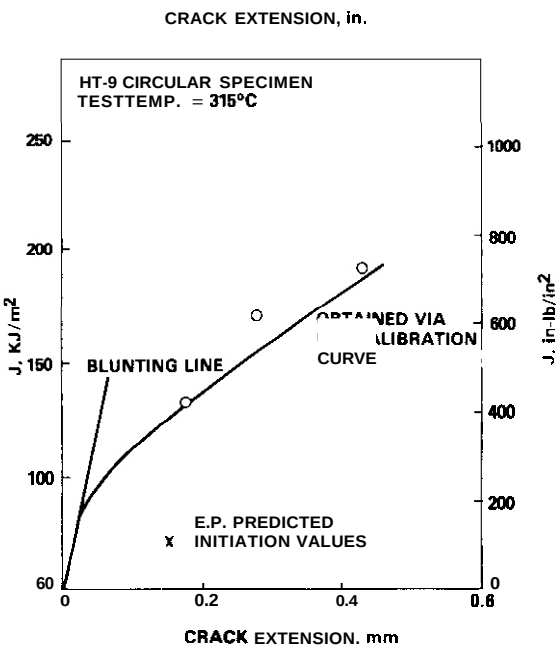

Figure 7.5.6 J Versus *a* Tested at 315°C for HT-9.

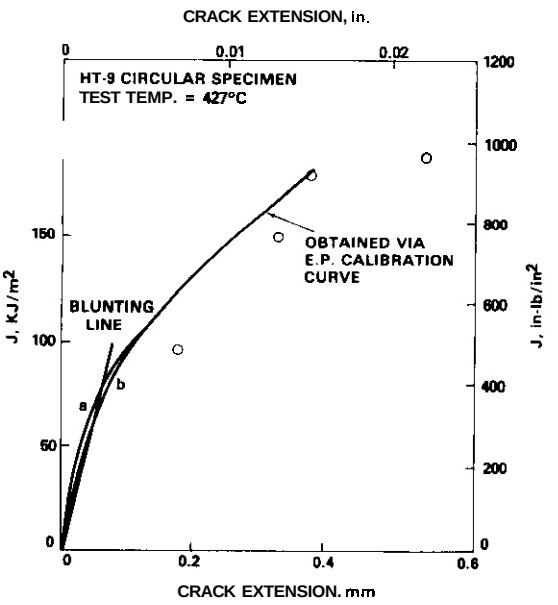

Figure 7.5.7 J Versus a Tested at 427°C for HT-9.

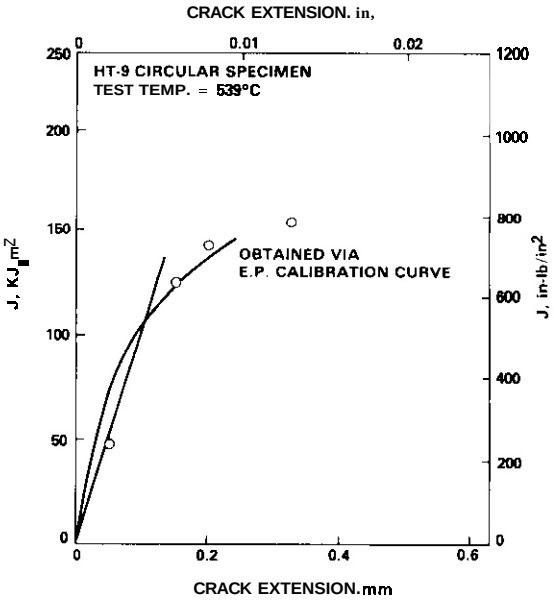

Figure 7.5.8 J Versus *a* Tested at 539°C for HT-9.

Table 7.5.1

FRACTURE TOUGHNESS TEST RESULTS AND MECHANICAL PROPERTIES OF HT-9

Test Temperature	Nominal σ_{ys} (KSi	MPa)	Nominal σ_{uts} (KSi	MPa)	J_{1c} (in-1b/in^2)	KJ/m^2)	T
25	90	620.6	118	813.7	573.4	112.4	121
149	87	600.0	111	765.5	385.4	75.5	131
232	84	579.3	106	731.0	287.3	56.3	146
316	80	551.7	100	689.6	302.5	59.3	118
427	73	503.4	89	613.7	411.6	80.7	147
539	59	406.9	70	482.7	638.6	125.2	130

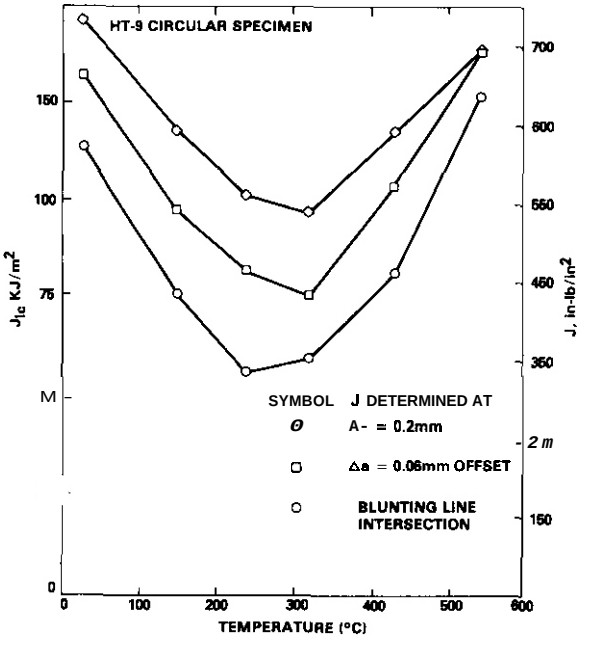

Figure 7.5.9 Temperature Dependence of Fracture Toughness for HT-9.

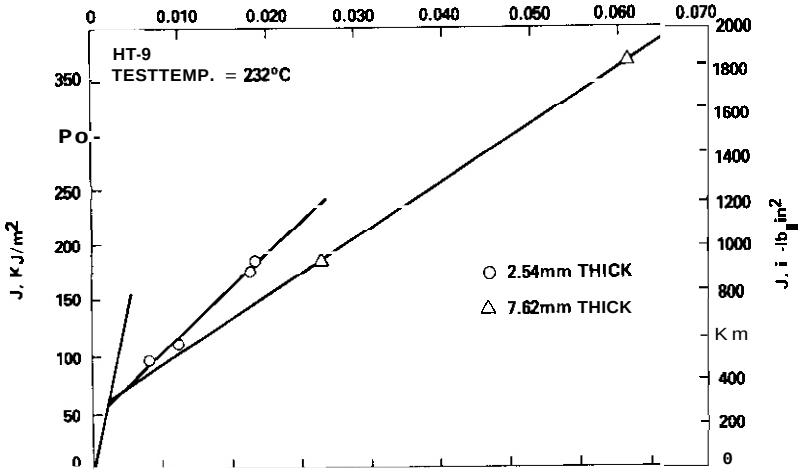

7.5.4.3.1 Calibration Curve for Crack Extension. The number of specimens needed for fracture toughness tests using the above multispecimen method can be reduced significantly if crack extension is measured continuously. The whole curve of J versus Aa can be determined from a single specimen. In this work the electropotential techniques were used to measure continuous crack extension through a calibration curve which is essential for a successful single specimen test method. Theoretical calibration curves relating crack extension to electropotential measurement can be obtained by using conformal mapping[12,13] and finite element techniques[14] to solve Laplace's equation

$$\nabla^2 (\phi) = o \qquad [4]$$

These calculations showed that the potential distribution is sensitive to the notch geometry of the specimen and the location of the current leads.

A convenient and widely used method to obtain the calibration curve and to determine optimum locations for the current leads and potential probes is simulation using an electrically conductive paper for a

particular specimen geometry. The results of such simulation performed on compact tension specimen are shown in Figure 7.5.11. The potential drop is found to be more sensitive to crack extension for the current leads located at A than at B. Similarly, an experimental calibration curve can be obtained by fatigue cracking the specimen, recording the potential change and measuring the crack length optically. However, certain restrictions must be imposed on the application of the calibration curves obtained by the methods mentioned above. Crack extensions calculated from these calibration curves are assumed to have straight crack fronts. In an actual specimen, the crack front is always curved. These calibration curves are applicable only when the curved region is small in comparison with the total crack extension. Therefore, they can only be considered as an approximation for our case where the curved fracture front advance is counted as the crack extension. In this study, interrupted tests of a series of specimens were made to obtain calibration curves correlating potential drop to crack extensions which were measured by heat tinting. The test results of electropotential and crack extension for various temperatures were presented in Figure 7.5.12 through Figure 7.5.15. Calibration curves are given in the form of V/Vo versus a/ao where V is the potential drop across the crack length a and Vo is the initial potential drop across the initial crack length ao. Calibration curves plotted in this way are independent of specimen thickness and material properties. Because the test specimens are small, shear lips which form as the crack estension becomes large are expected to have a significant effect as the side ligaments begin tearing. The tearing caused the rapid increase of the potential and was evident by heat tinting. Only those specimens having no shear lip formation at the final crack extension were used for calibration purpose. The shear lip formation can be suppressed by side grooving the specimen to 12-1/2% of gross thickness.(15) Side-grooving is not considered practical for this thickness (2.54 mm) as the effective thickness would be reduced substantially.

All potential ratios and crack extension ratios from various temperature tests were plotted in Figure 7.5.16. It would appear that straight lines with the same slope of 1 satisfactorily describe the V/V_o versus a/a_o data outside the blunting region. This indicates that the

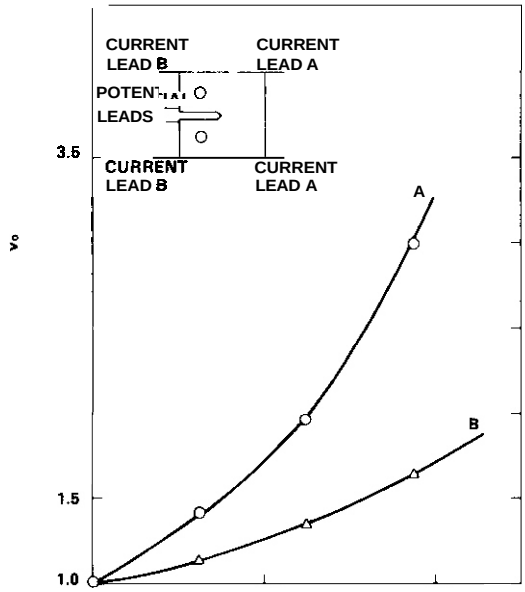

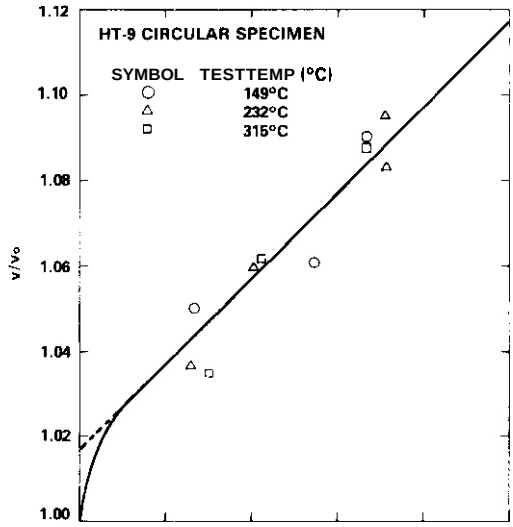

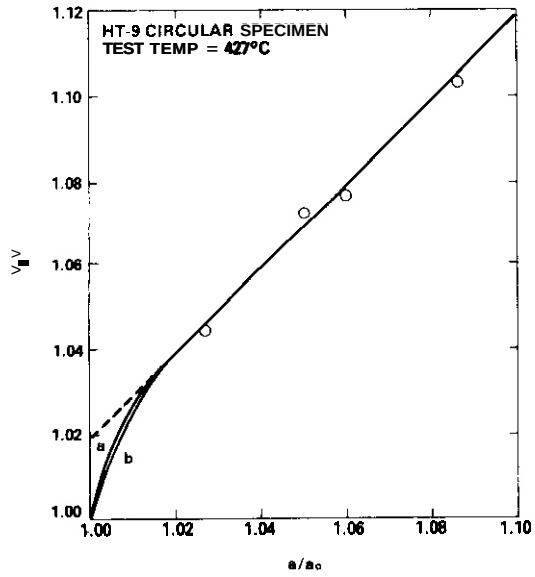

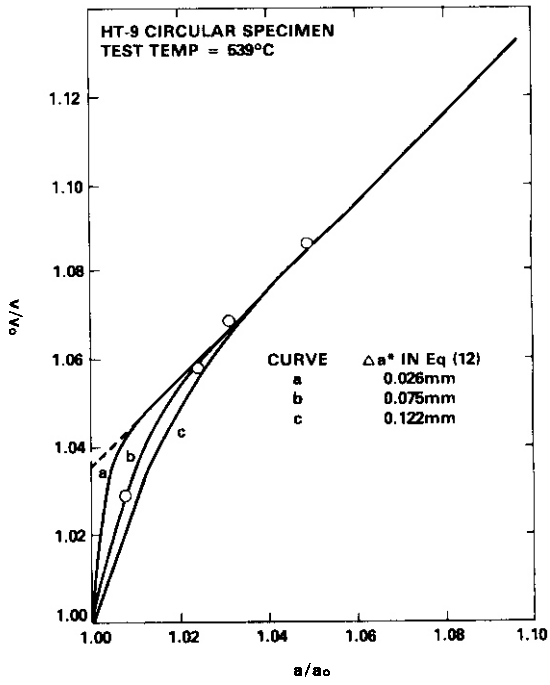

Figure 7.5.13 Electropotential Calibration Curve for BT-9 Tested at 427°C.

Figure 7.5.14 Electropotential Calibration Curve for HT-9 Tested at 539°C.

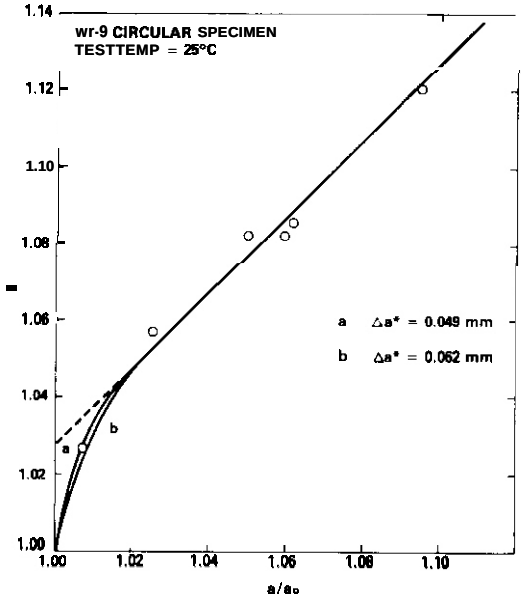

Figure 7.5.15 Electropotential Calibration Curve for **HT-9** Tested at 25°C..

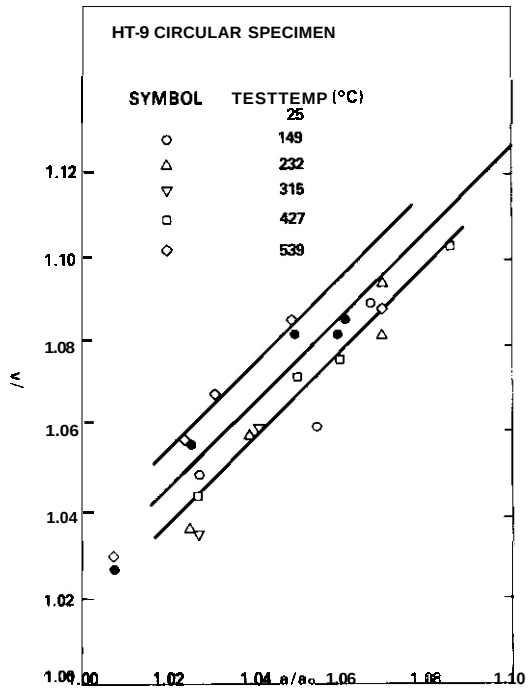

Figure 7.5.16 Electropotential Calibration Curve for **HT-9** at Various Temperatures.

potential change is sensitive primarily to crack growth. The data trend of V/Vo versus a/ao agrees with the simple intuitive notion that resistance is inversely proportial to the area of unbroken ligament. The linearity of V/Vo versus a/ao curve is a good approximation for a small range of crack extension.

7.5.4.3.2 Experical Potential Change–Crack Extension Expression. The V/Vo versus a/ao outside the blunting region appear to be linear, and can be expressed by

$$V/V_o = X_i - 1 + \beta\, a/a_o \qquad [5]$$

Here X_i is the voltage ratio at initial crack length, β is the slope of the straight line equal to 1 for **HT-9** specimens tested in this work. X_i is related to the extent of blunting which is dependent on the fracture toughness and tensile strength of the material, as shown in Figure 7.5.17.

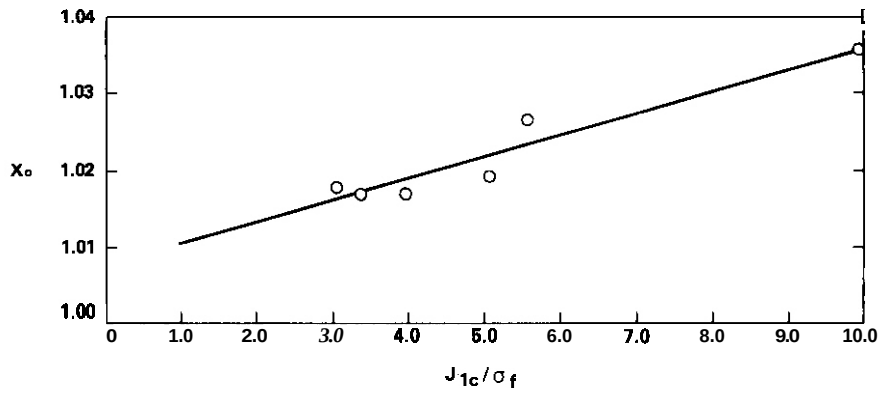

Figure 7.5.17 Potential Ratio X_o Versus J_{1c}/σ_f.

As discussed in Reference 8, the experimental calibration curve does not extrapolate to a $V/V_o = 1.0$ from crack extensions. It was difficult to obtain low crack extension data, few data points of crack extension less than 0.1 mm and the error for these is of order ± 0.02 mm in Figure 7.5.14 and Figure 7.5.15. However, it seems reasonable to assume that the potential change immediately after loading can be attributed to the extent of blunting due to plastic deformation. The potential change rates before and after the crack initiation are different, although a continuity between these two regions is expected. As the load is applied to the specimen, the potential increases rapidly due to separation of the fatigue-crack surfaces,[4] then increases linearly with elastic load. A departure from linearity starts as soon as plastic deformation and/or crack extension occurs. As a result of dislocation density increase caused by plastic deformation, the electrical resistance is increased but the contribution is negligible because of the high grown-in dislocation density due to the martensitic transformation.

In the blunting process, the potential change is approximated to be proportional to the degree of blunting (Figure 7.5.17) and can be expressed by

$$V/V_o = 1 + S\ (a/a_o - 1) \qquad [6]$$

where S is the slope of calibration curve in the blunting region. Let the blunting be equal to Δa^* when the additional crack advance occurs from the blunted crack, from Equation [5] we obtain

$$\left(V/V_o\right)_{\Delta a^*} = X_o + \frac{\Delta a^*}{a_o} \qquad [7]$$

S is solved from Equation [6] and [7],

$$S = 1 + \frac{a_o}{\Delta a^*}\,(X_o - 1) \qquad [8]$$

Substituting Equation [8] into Equation [6] it follows

$$V/V_o = (X_o - 1)\,\frac{a_o}{\Delta a^*}\left(\frac{a}{a_o} - 1\right) + \frac{a}{a_o} \qquad \text{for } 0 \le \Delta a \le \Delta a^* \qquad [9]$$

Equation [9] becomes Equation [5] when $a = a_o + \Delta a^*$ at crack initiation, and must be abandoned beyond initiation, (Figure 7.5.18).

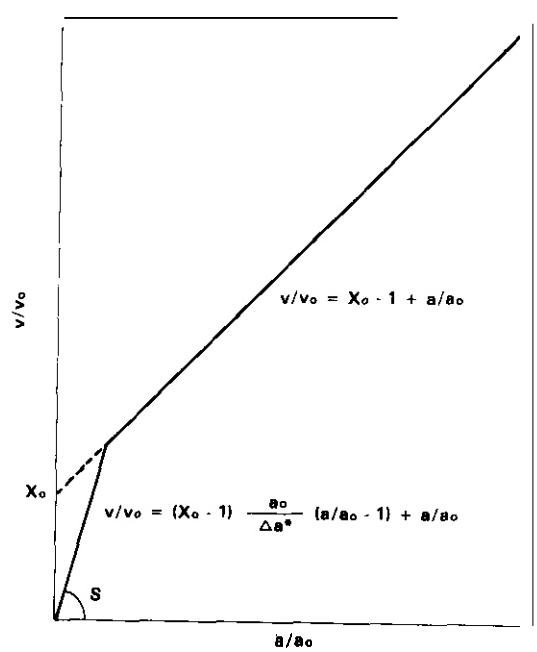

Figure 7.5.18 Semi-Emperical Calibration Curve

Experimentally, Aa* can be estimated from a widely accepted blunting curve which is in the form

$$\Delta a = \frac{J}{2\sigma_f} \qquad [10]$$

Where $\sigma_f = (\sigma_{ys} + \sigma_{uts})/2$

To combine Equation [5] and Equation [9] into a unified equation, the hyperbolic tangent function is used because of the following properties:

$$\tanh X = \begin{matrix} 0 \\ 0.75 \\ 0.91 \\ 1.00 \end{matrix} \text{ as } X \rightarrow \begin{cases} 0 \\ 1.0 \\ 1.5 \\ \infty \end{cases} \qquad [11]$$

The analytical form of the calibration curve, therefore, is chosen based on the experimental data as

$$V/V_o = (X_o - 1) \quad \text{Tanh} \quad \left\{\frac{a_o}{\Delta a^*}\left(a/a_o - 1\right)\right\} + \frac{a}{a_o} \qquad [12]$$

Equation [12] offers a smooth slope change near the crack initiation area which is more realistic in light of plastic deformation and crack initiation occurring simultaneously. It will now be shown how J_{1C} can be derived using this relationship to obtain a continuous plot of J versus Δa.

7.5.4.3.3 Locating Crack Initiation. The crack tip blunting increases with an increase in loading. J_{1C} is defined as the J value at the point where the first crack advance occurs beyond blunting. The crack initiation cannot be universally detected precisely since cracking may begin as oids in front of the blunted crack tip coalesce. With the electropotential technique, the crack initiation is usually determined at the first deviation from linearity of the potential-load displacement curve,[4] as illustrated in Figure 7.5.19. The J_{1C} value, so obtained, tended to under-estimate the initiation value predicted by multispecimen R-curve method[16] (Figure 7.5.3). However, the calibration curves of Equation [12] were not sensitive to the variation of Δa^* value as shown in Figure 7.5.15 for room temperature tests. In Figure 7.5.14, three 539°C calibration curves with Δa^* values of 0.026, 0.075 and 0.122 mm were plotted. The one with $\Delta a^* = 0.075$ mm provides the best fit to the experimental data. This value is calculated from Equation [10] using J value corresponding to $V/V_o = X_o$. As shown in the figures, the

calibration curves described by Equation [12) with these Δa* values fit experimental data quite well.

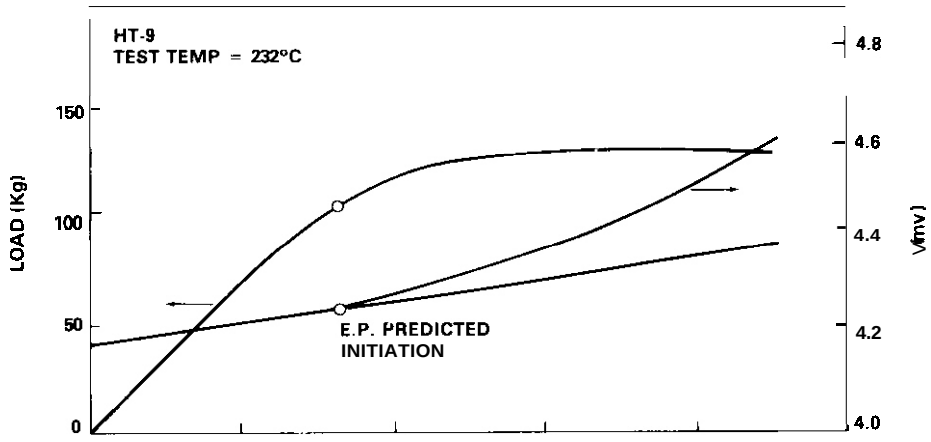

Figure 7.5.19 Crack Initiation Predicted by Electropotential.

7.5.4.3.4 Recipe for Single Specimen J-Integral Measurement. To summarize, the recipe for producing J versus Aa curves is as follows:

1. Determine X, from the optically measured crack extension. Experimentally, load and voltage are monitored simultaneously during the test at any temperature. The test is terminated after the maximum load is reached. The specimen is then heat-tinted and broken to reveal crack extension. One data point of V/V_o and a/a_o is obtained from the single specimen. X_o can be determined from Equation [5]: $X_o = V/V_o - a/a_o + 1$. A straight line with a slope of 1, is drawn through the data point. The intercept of $a/a_o = 1$ vertical line gives the X_o value. As an example for simple specimen tests, HT-9 specimen HR24 was tested, the test results were: $J = 180.4$ KJ/m^2, $V/V_o = 1.077$ and $a/a_o = 1.060$. The data points $(V/V_o, a/a_o)$ and $(J, \Delta a)$ were plotted in Figure 7.5.13 and Figure 7.5.7, respectively. A straight line with a slope of 1 was drawn through the data point in Figure 7.5.13. X_o was found to be 1.017 through extrapolation of the straight line to the line $a/a_o = 1$.

2. Estimate Aa* from $a = J/2\sigma_f$ using J correspondingly to X_o. The corresponding J value of X_o is 55.5 KJ/m^2 which gives $\Delta a^* = 0.04$ mm.

3. Use Equation [12] = $V/V_0 = (X_0 - 1)\tanh\left\{a_0 / Aa^* (a/a_0 - 1)\right\} + a/a_0$ to construct calibration curve.

The values of X_0 and Aa* were input into this equation for the calibration curve plotted in Figure 7.5.13, curve. The calibration curves for various temperature tests were obtained following the same procedure and presented in Figure 7.5.12 through Figure 7.5.15.

4. Construct J versus Aa curves using data and calibration curves. Using this curve, we were able to calculate the continuous crack extensions from potential-change data, and obtain the J versus Aa curve which was plotted in Figure 7.5.7, curve a. For other temperature tests, the continuous J versus Aa curves via the calibration curves are presented in Figure 7.5.3 to Figure 7.5.8.

5. Now construct blunting line to on J versus Aa curve and find new Δa^*. If this is significantly different than calculated in step 2, repeat step 3 and 4 using the new Δa^*. In our example, curve a in Figure 7.5.5 intersects the blunting line at J = 78.4 KJ/m^2 or Δa^* = 0.063 mm which was used to obtain the new calibration curve b in Figure 7.5.13, and J versus Δa curve in Figure 7.5.7, curve b. The difference between these curves was sufficiently small so that no far iteration was needed.

7.5.4.3.5 Crack Growth Stability. The J-integral R-curve approach has been used to characterize the toughness properties of ductile metals in terms of crack initiation. Attempts have also been made, based on the same approach, to understand crack growth instability. In general, crack instability occurs either in cleavage mode or tearing mode. A material's stable tearing properties can be characterized by the tearing modulus which is defined[17] as

$$T = \frac{dJ}{da} \times \frac{E}{\sigma_{ys}^2} \qquad [13]$$

Here $\frac{dJ}{da}$ is the slope of the straight line portion of J versus Δa curve. Table 7.5.1 contains a compilation of T values for various temperature tests. All T values are much greater than 1, indicating that the crack growth of HT-9 on upper shelf is under J-controlled growth condition.[18] Under this condition, plastic loading is predominantly proportional, and the singularity field, which is measured uniquely by J, is dominant at the crack tip.

7.5.5 Conclusion

1. A semi-emperical expression is formulated to account for crack blunting in converting electropotential to crack extension data.
2. The single specimen J-integral measurement using electropotential techniques was demonstrated in detail.
3. The 2.54 mm thick HT-9 specimens satisfies the thickness requirement for a valid J_{1C} test. The thickness effect on the fracture toughness of HT-9 does not appear to be great.
4. The upper-shelf toughness of HT-9 decreases with increasing temperature from room temperature to 250°C, but increases as temperature is increased from 250°C to 550°C.
5. The single specimen test techniques developed on unirradiated HT-9 specimens should be applicable for irradiated specimens since irradiation is expected to reduce the upper shelf toughness of HT-9.

7.5.6 Future Work

Single specimen method will be applied to a variety of ferritic composition and thermomechanical treatments.

7.5.7 References

1. J. A. Begley and J. D. Landes, "The Integral as a Fracture Criterion," *ASTM STP 514,* p.1.
2. British Standard D.D. 19, "Methods for Crack Opening Displacement (COD) Testing," 1972
3. J. S. Ke and H. W. Liu, "Near Tip Strain As A Ductile Fracture Criterion, ***International*** *Journal* of ***Fracture, Vol. 7,*** p. 487, 1971.
4. E. A. Steigerwald and G. T. Hanna, "Initiation of Slow Crack Propagation in High Strength Materials," ***Proceedings,*** *Vol.* 62, ASTM, p. 885, 1962.
5. G. A. Clarke, W. R. Andrews, P. C. Paris and D. W. Smith in, "Mechanics of Crack Growth," *ASTM, STP* 590, p. 27, 1976.
6. M. H. Jones and W. F. Brown, Jr., "Acoustic Detection of Crack Initiation in Charpy Notched Specimens," ***Materials Research & Standards, Vol. 4, No.*** 3, p. 120, 1964; "Acoustic Emission," ASTM, STP 505, 1972.

7. F. A. Smidt, Jr., and J. R. Hawthorne, "Evaluation of Fracture Toughness and Tensile Properties of Irradiated HT-9," *ADIP Quarterly Progress Report,* April-June, 1979.

8. F. H. Huang and G. L. "lire, "Initial Test Results on Miniature Compact Tension Fracture Toughness Specimen," *ADIP Quarterly Progress Report,* September-December, 1979.

9. F. H. Huang and G. L. Wire, "Fracture Toughness Tests on HT-9 at Elevated Temperatures," *ADIP Quarterly Progress Report,* January-March, 1980.

10. G. A. Clarke and J. D. Landes, "Evaluation of The J-Integral for the Compact Specimen," *Journal of Testing and Evaluation, Vol. 7,* p. 264, 1979.

11. J. G. Merkle and H. T. Corten, *TRANS. ASME, Journal of Pressure Vessel Technology,* p. 286, 1974.

12. H. H. Johnson, "Calibrating the Electric Potential Method for Studying Slow Crack Growth," *Materials Research and Standards, Vol. 5,* p. 422, 1965.

13. G. Clark and 3. F. Knott, "Measurement of Fatigue Cracks in Notched Specimens by Means of Theoretical Electrical Potential Calibrations," *Journal of The Mechanics and Physics of Solids, 23,* p. 265, 1975.

14. G. H. Aronson and R. O. Ritchie, "Optimization of The Electrical Potential Technique for Crack Growth Monitoring in Compact Test Pieces Using Finite Element Analysis," *ASTM, Journal of Testing and Evaluation, Vol. 7, No. 4,* p. 208, 1979.

15. W. R. Andrews and C. F. Shih, "Thickness and Side-Groove Effects J- and S-Resistance Curves for A533-B Steel at 93°C," *ASTM STP* 688, p. 426, 1979.

16. T. Ingham and E. Morland, "The Measurement of Ductile Crack Initiation: A Comparison of Data from Multiple and Single Specimen Methods and Some Considerations of Size Effects," NUREQ/CP-0010, CSNI Report NO. 39, p. 330, 1979.

17. P. C. Paris, H. Tada, A Fahoor and H. Ernst, "The Theory of Instability of The Tearing Mode of Elastic-Plastic Crack Growth," ASTM, STP 688, p. 5, 1979.

18. J. W. Hutchinson and P. C. Paris, "Stability Analysis of J-Controlled Crack Growth," ASTM, STP 688, p. 37, 1979.

7.6 ENVIRONMENTAL EFFECTS ON PROPERTIES OF FERRITIC STEELS - O. K. Chopra and D. L. Smith (Argonne National Laboratory)

7.6.1 ADIP Task

ADIP tasks are not defined for ferritic steels in the 1978 program plan.

7.6.2 Objective

The objective of this work is to develop a data base on the corrosion, compatibility, and the influence of chemical environment on the mechanical properties of ferritic steels under environmental conditions proposed in fusion reactor applications. Emphasis will be placed on the combined effect of stress and chemical environment on corrosion and mechanical properties of ferritic steels. Test environments to be investigated include lithium, water, and helium as well as candidate solid breeding materials and neutron multipliers. Initial tests will focus on the Sandvik Alloy HT-9 and a developmental Fe-9Cr-1Mo alloy.

7.6.3 Summary

Calibration fatigue tests were conducted with HT-9 ferritic steel specimens at 755 K in a flowing lithium environment. The procedure for strain control and strain measurement has been established. Several continuous cycle fatigue tests have been performed with gauge specimens of HT-9 alloy. The results are being analyzed to determine the strain-life relationship. Exposure of corrosion specimens of HT-9 steel with solid Li_2O, $LiAlO_2$, and Li_2SiO_3 breeding materials at 873 K has been completed. Metallographic evaluation of the corrosion specimens is in progress.

7.6.4 Progress and Status

7.6.4.1 Introduction

Ferritic steels, such as Sandvik HT-9 and developmental Fe-9Cr-1Mo, have been proposed as candidate materials for the first wall/blanket of magnetically confined fusion reactors. Although these alloys are

ferromagnetic, initial analyses indicate that the magnetic effects of ferritic steels are relatively small and can be accommodated by the reactor design. The primary incentive for consideration of ferritic steels was the preliminary indication that HT-9 alloy potentially offered lower void swelling and higher in-reactor creep resistance than austenitic stainless steels. Also, the better physical properties provide a reduced thermal stress factor. However, relatively little information is available on the influence of the chemical environment on mechanical properties of ferritic steels. There is also concern regarding the combined effects of stress and coolant environment on the compatibility.

The first wall undergoes the most severe thermal cycling because of its exposure to the plasma. Consequently, the fatigue behavior of the material is the most important consideration relative to the design of the blanket region. The initial phase of the present program is designed to provide data on (1) the effects of liquid lithium environment on the fatigue and creep-fatigue properties of HT-9 and Fe-9Cr-1Mo alloys and (2) the compatibility of candidate ferritic steels with liquid lithium and solid tritium-breeding materials.

7.6.4.2 Fatigue Tests

The facility for conducting fatigue tests in a flowing lithium environment has been described in an earlier report.' The lithium loop has operated continuously for *2.3500* h; the initial 200 h at a maximum temperature of *1.630* K and the remainder at *2.750* K. The cold trap temperature was maintained at 500 K. Filtered lithium dip samples were taken after fixed intervals for analysis of nitrogen and carbon in lithium. The initial concentration of nitrogen in lithium obtained after *2.150* h of operation at 630 K was ~445 ppm. Recent analyses show nitrogen concentration between 80 and 130 ppm. Specimens of zirconium, vanadium, and yttrium were exposed to lithium to determine the concentrations of oxygen and hydrogen in lithium.

Several fatigue tests have been conducted with 2.5-mm-diameter specimens of HT-9 alloy at *755* K in a flowing lithium environment. Detailed dimensions of the gauge-length and hourglass calibration specimens were described earlier.[2] The fatigue tests were performed in a stroke-control

mode by means of a standard resistance-type extensometer located on the upper portion of the fixture in an ambient-temperature region. An enlarged view of the test specimen and fixture is shown in Fig. 1. The flexible pins at the top of the specimen are used to maintain proper alignment during the test.

The extensometer measures the sum of the strains in the fixture and the gauge and shoulder region of the specimen. To determine the amount of strain in the gauge section of a test specimen, hourglass specimens with identical geometry, except for the gauge section, were used as reference. Calibration tests were performed with the hourglass specimen to determine elongation in the fixture and shoulder region of the specimen as a function of load. During calibration tests, hysteresis loops were recorded when the plastic strain and load attained steady-state values. The strain was increased incrementally and the procedure repeated at various strain ranges to obtain the complete calibration curve. Tests were also conducted to determine the load required to bend the alignment pins as a function of axial displacement. For a given strain-cycling condition, the load due to pin bending was subtracted from the measured load to obtain the load in the test specimen. The displacement obtained with an hourglass specimen was subtracted from the measured displacement of a test specimen under identical loading conditions to determine the total strain in the gauge section of the test specimen. The calibration curve for the HT-9 specimen tested in lithium at 755 K is shown in Fig. 2. The continuous cycle fatigue data are being analyzed to determine the strain-life relationship for the material in a lithium environment.

7.6.4.3 Compatibility

The combined effects of stress and liquid lithium environment on the corrosion behavior of ferritic steels will be evaluated by exposing stressed specimens of HT-9 and Fe-9Cr-1Mo steels in the specimen-exposure vessel of the lithium loop. For this investigation, tapered specimens will be used and stress applied by deadweights. Fabrication of the corrosion specimens and the specimen holder is in progress.

Initial tests to study the compatibility of ferritic steels with candidate solid breeding materials have been completed. Corrosion specimens of HT-9 ferritic steel were exposed with solid Li_2O, $LiAlO_2$, and Li_2SiO_3 at 873 K for ∿2000 h. The specimens are being examined metallographically to evaluate the corrosion behavior.

7.6.5 Conclusions

Several continuous cycle fatigue tests have been conducted with HT-9 ferritic steel specimens at 755 K in a flowing lithium environment. The results are being analyzed to establish the strain-life behavior.

7.6.6 References

1. O. K. Chopra and D. L. Smith, "Environmental Effects on Properties of Ferritic Steels," ADIP Quarterly Progress Report, March 31, 1980.

2. D. L. Smith, O. K. Chopra, and R. R. Schlueter, "Environmental Effects on Properties of Ferritic Steels," ADIP Quarterly Progress Report, December 31, 1979, DOE/ER-0045/1, pp. 115-118.

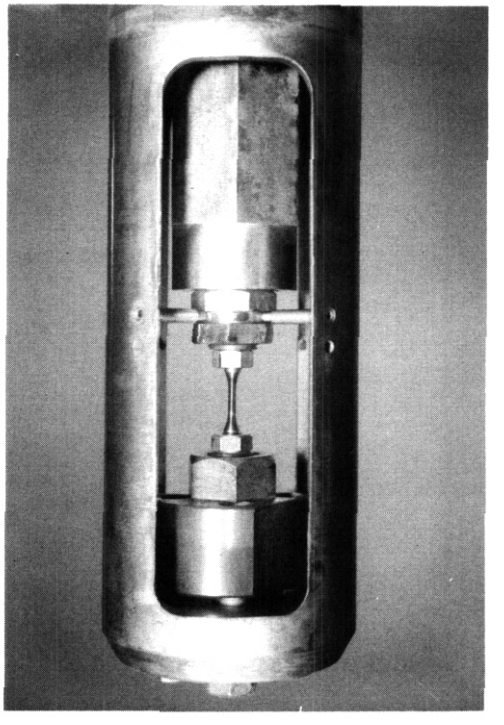

Fig. 1. Test Specimen in the Fixture Prior to Testing.

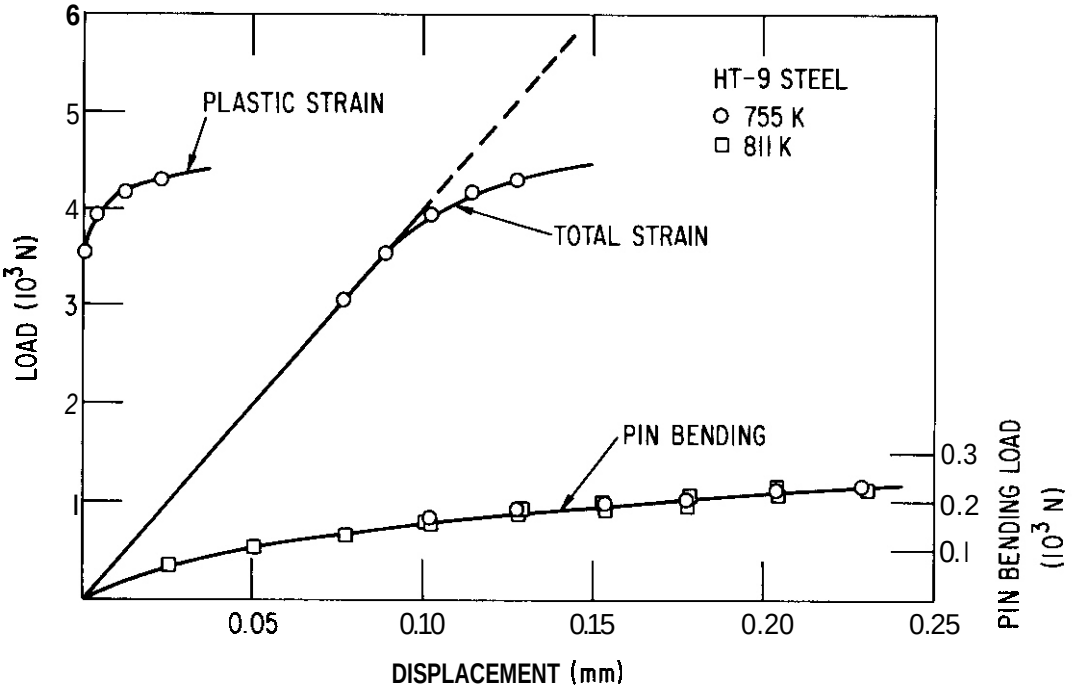

Fig. 2. Calibration Curves for HT-9 Steel Tested in Lithium at 755 K.

7.7 SPECIMEN PREPARATION AND LOADING FOR THE AD-2 FERRITICS EXPERIMENT - R. J. Puigh and N. F. Panayotou (Hanford Engineering Development Laboratory).

7.7.1 ADIP Task

The Department of Energy (DOE), Office of Fusion Energy (OFE) has cited the need for these data under the ADIP Program Task, Ferritic Material Development (Path E).

7.7.2 Objective

The objective of the AD-2 experiment is to provide baseline, high fluence data at several temperatures for the ferritic alloys HT-9 and 9Cr-1Mo. Developmental 2-1/4Cr-1Mo will also he scoped in this experiment. The AD-2 experiment is designed to yield data concerning the radiation effects on the mechanical properties of these alloys with particular emphasis on their fatigue, fracture toughness and weld properties. Characterization of the radiation effects on the microstructure of these alloys will also he performed.

7.7.3 Summary

Experimental hardware has been built and specimens have been fabricated for the AD-2 experiment. The loading of the specimens into the six uninstrumented B-7C capsules has been completed and these capsules have been shipped to Idaho Falls for insertion into EBR-II, Cycle 109.

7.7.4 Progress and Status

7.7.4.1 Introduction

The ferritic alloys, HT-9 and developmental 9Cr-1Mo, exhibit desirable mechanical properties when considered in applications as materials for the first wall or blanket of a fusion power reactor!') Except for irradiation creep,[2] relatively little information has been gathered about the radiation effects at high fluences upon the mechanical properties of these ferritic alloys. Of particular concern are the fracture and weld properties of these materials. The AD-2 experiment has been designed to provide data on

these properties. Alloy selection and irradiation temperatures have been specified by the Alloy Development for Near Term Applications Working Group and approval in principle for this experiment has been granted by DOE(3) This report will describe the fabrication procedure for the specimens and will give the specimen matrix which was loaded into the six B-7c capsules comprising the AD-2 experiment.

7.7.4.2 Specimen Material Processing

The vendor certified compositions for the alloy stocks used for the AD-2 experiment are listed in Table 7.7.1. Overchecks of the chemical compositions of each alloy were also performed. The HT-9 material stock was manufactured by Carpenter Technology Corporation. Material used in the fabrication of the welded plate and the fatigue initiation specimens came from heat number 91353. Material used for all other specimens fabricated from HT-9 came from heat number 91354. These two heats of HT-9 are from the same melt and both have comparable chemical compositions, as seen in Table 7.7.1. The modified 9Cr-1Mo material stock was also manufactured by Carpenter Technology Corporation and came from ESR ingot 30182. The developmental 2-1/4Cr-1Mo material was taken from a section of pipe fabricated from Mannesman heat number 38649 material.

General Atomic Corporation was responsible for the welding of the 6.35 mm thick HT-9 and 9Cr-1Mo plates. Thyssen Specialty Steels, Inc. supplied the 1.2 mm diameter weld wire for the HT-9 plates and San Diego Welders Supply, Inc. supplied the 4.8 mm diameter weld wire for the 9Cr-1Mo plates. The chemical compositions of these weld wires are given in Table 7.7.2. The chemical compositions of HT-9 and its associated weld wire are similar. From a comparison of the chemical compositions of the developmental 9Cr-1Mo and its associated weld wire one finds that the weld wire has more sulphur and silicon alloying elements than are found in the plate metal. The chemical compositions of modified 9Cr-1Mo and its associated weld wire are similar for the other alloying elements. The 9Cr-1Mo weld wire meets ASME SFA 5.9 specifications.

TABLE 7.7.1

CHEMICAL COMPOSITIONS OF SPECIMEN MATERIALS

ELEMENT	HT-9 (91353) VENDOR[1]	HT-9 (91353) OVERCHECK[2]	HT-9 (91364) VENDOR[3]	HT-9 (91364) OVERCHECK[4]	9Cr-1Mo (30182) VENDOR[5]	9Cr-1Mo (30182) OVERCHECK[6]	2¼Cr-1Mo (38649) VENDOR[7]	2¼Cr-1Mo (38649) OVERCHECK[6]
C	0.21	0.23	0.21	0.20	0.086	0.008	0.093	0.083
Mn	0.50	0.39	0.60	0.39	0.37	0.37	0.52	0.49
P	0.007		0.008		0.012	0.011	0.011	0.011
S	0.003		0.003		0.003	0.004	0.011	0.016
Si	0.22	0.21	0.21	0.14	0.16	0.19	0.17	0.19
Ni	0.58	0.46	0.58	3.49	0.11	0.90	0.40	
Cr	11.80	12.34	12.11	12.39	8.41	8.47	2.15	2.17
Mo	1.02	0.99	1.03	0.99	0.89	0.88	0.95	0.99
V	0.32	0.45	0.33	0.45	0.24	0.21		
Nb					0.08	0.07		
Ti	0.003		0.002		<0.02	0.001		
Co			0.01		0.02	0.017		
Cu	0.04	0.07	0.00	0.07	0.03	0.03	0.16	
Al	0.028		0.034		0.014	0.009	0.001	
B	<0.0010		0.0007		<0.001	<0.001		
As	<0.01		<0.005			<0.001		0.017
Sn						0.002		0.0088
Zr						<0.001		
N	0.006		0.004			0.054		0.010
O					0.0058	0.008		
Pb						<0.001		
Sb						<0.001		0.0024
Ta	<0.01		<0.01					
W	0.50		0.53			<0.01		
Fe	BAL.	BAL.	BAL.	BAL.	BAL.	BAL.	BAL.	BAL.

All numbers ~ r weight percents.

[1]Carpenter Technology Certificate of Composition, dated July 22, 1975.

[2]Koon-Hall Test Report, dated August 21, 1979.

[3]Carpenter Technology Certificate of Composition, dated December 19, 1975.

[4]Carpenter Technology (ORNL report "Modified 9Cr-1Mo Steel Development Progress Report for Period Ending September 30, 1979").

[5]Combution Engineering (ORNL report, "Modified 9Cr-1Mo Steel Development Progress Report for Period Ending September 30, 1979").

[6]Mannesmann Company.

[7]Climax Molybdinum Company of Michigan.

TABLE 7.1.2
CHEMICAL COMPOSITIONS OF WELD WIRES

ELEMENT	HT-9[1]	9Cr-1Mo[2]
C	0.26	
Mn	0.50	
P	0.011	0.011
S	0.005	0.015
Si	0.26	0.32
Ni	0.62	0.046
Cr	11.6	8.93
Mo	0.95	0.98
V	0.29	
Nb	<0.01	
Ti	<0.01	
co	0.03	0.020
cu	0.04	
Al	0.011	
N	0.024	
Ta	<0.01	
W	0.49	
Fe	Bal.	Bal.

All numbers are weight percents.

[1]Thyssen Specialty Steels, Inc.
[2]San Diego Welders Supply, Inc.

The HT-9 fracture toughness and miniature Charpy base metal specimens were machined directly from the 33.3 mm diameter, heat number 91354, bar stock. This bar stock was hot worked after soaking at 1149°C for a minimum of one hour, tempered at 750°C for one hour, and followed by an air cool. This thermomechanical treatment is referred to as the "mill annealed" condition for HT-9 in this report.

Figure 7.7.1 outlines the processing steps HEDL used to obtain the HT-9

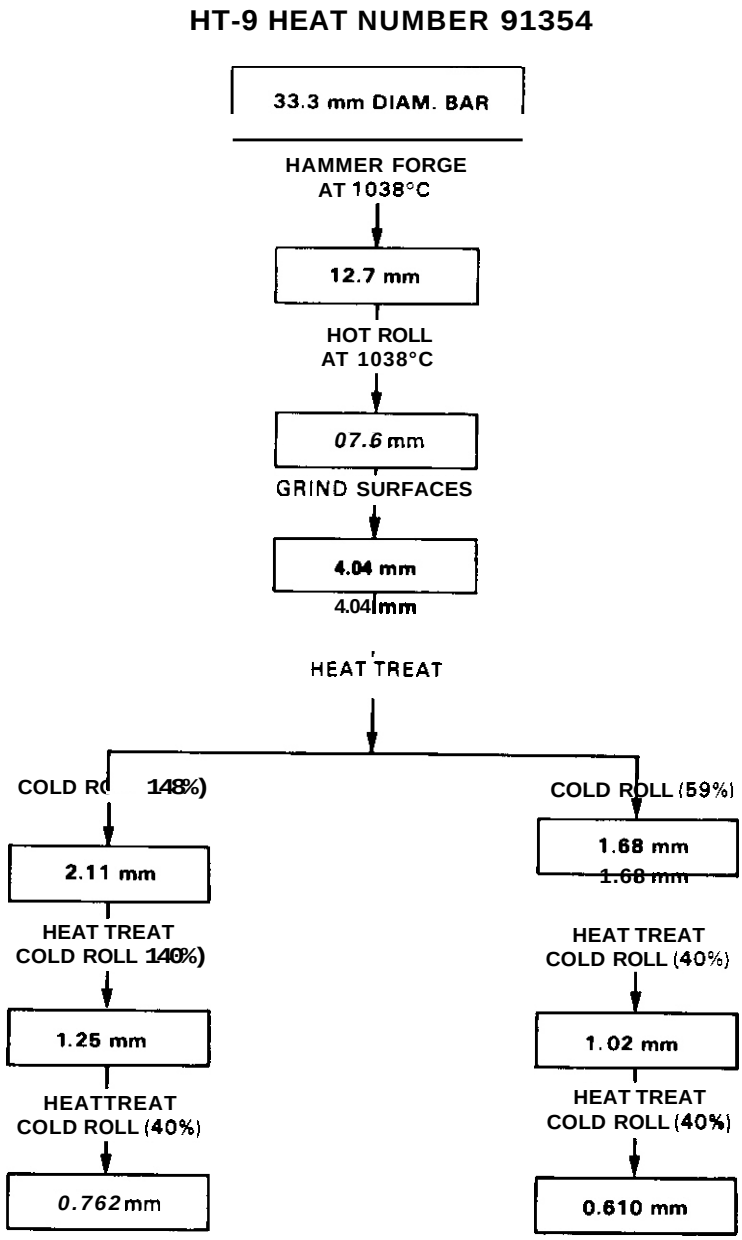

FIGURE 7.7.1 Mechanical Processing of HT-9 Sheet Alloy Stock.

stock, from which the Grodzinski fatigue, fatigue crack growth and tensile specimens were fabricated. The 33.3 mm diameter bar, heat number 91354, was hammer forged at 1038°C to a thickness of 12.7 mm and then hot rolled at 1038°C to a thickness of 7.6 mm. The surfaces of the bar were then

ground and grit-blasted to remove any decarburized layer formed during this process. Micrographs were taken of cross sections from the material stock to ensure no decarburized layer remained on the bar. The material was then cut and cold rolled to a thickness of 4.04 mm (47% cold-work (CW)). The material was then encapsulated in quartz with 1/4 atmosphere of argon and given the following heat treatment: 1038°C/30 min/AC + 760°C/2.5 hr/AC. At this point the material stock was cut and divided into two approximately equal quantities. Half the material would be processed to a thickness of 0.762 mm and the other half would be processed to a thickness of 0.610 mm. This was done to ensure that the last two reductions in thickness for both lots resulted in cold work levels of 40%. The material stock then went through a series of thickness reductions in the following sequence: 1) cold roll; 2) cut into shorter lengths; 3) encapsulate in quartz with 1/4 atmosphere argon; and 4) heat treatment. Since two conditions of HT-9 are to be investigated in the AD-2 experiment, two different intermediate heat treatments were given to the material stock for the rest of the processing. Approximately 40% of the material stock received intermediate heat treatments of 1038°C/30 min/AC + 760°C/2.5 hr/AC. The remaining 60% of the material stock received intermediate heat treatments of 1038°C/8 min/AC + 760°C/30 min/AC.

Microhardness measurements were performed upon the 40% CW material. The sheet stock receiving the intermediate heat treatments, 1038°C/8 min/AC + 760°C/30 min/AC, was found to have a hardness of 326 DPH (500 gm). This corresponds to a R_C hardness value of 33. Similarly, the sheet stock receiving the intermediate heat treatments, 1038°C/30 min/AC + 760°C/2.5 hr/AC was found to have a hardness of 303 DPH (500 gm). This corresponds to a R_C hardness value of 30.5. To improve the machinability of this material, the sheet stock was given its final heat treatments prior to specimen fabrication.

A recent study of the effects of different thermomechanical treatments (TMTs) on HT-9[4] has indicated that for a given TMT involving relatively short austenitizing times, the grain size is dependent upon the thickness of the material. Since we wished to investigate grain size effects on the properties of HT-9, the final heat treatments chosen for the 0.610 and 0.762 mm HT-9 sheet stock were: a) 1038°C/30 min/AC + 760°C/2.5 hr/AC, and b) 1038°C/4 min/AC + 760°C/30 min/AC. These TMTs resulted in prior

austenitic grain sizes of ASTM 5 and ASTM 7, respectively, for this HT-9 sheet stock.

Figure 7.7.2 outlines the processing steps ORNL used to obtain the 6.35 mm thick HT-9 plate, which was welded by General Atomic Corporation. The 79.4 mm diameter bar, heat number 91353, after machining was extruded at 1100°C through a 22.3 x 50.8 mm^2 sheet die bar. Extrusion loads varied from 2.67 to 3.11 x 10^6 Nt. and resulted in a reduction of 12.25 to 1. The pieces were then wrapped in stainless steel foil and heat treated: 950°C for one hour, furnace cooled to 700°C, held at 700°C for sixteen hours, then air cooled. The hardness of the material at this point varied from R_C 42 to R_C 48. The material was then hot rolled at 1000°C with heavy passes of up to 3.18 mm per pass being taken. The material was first cross rolled with respect to the extrusion direction until the desired width of 10.16 cm was obtained, and then the material was straight rolled until the plate had a thickness of 6.60 to 6.86 mm. Observable edge, lead and tail cracking occurred during the fabrication process. Also, hardness and thickness variations were measured in the same piece.

General Atomic Corporation used this material in the fabrication of welded plate material for specimens. They gave the 6.60 to 6.86 mm thick plates the following heat treatment: 1050°C/30 min/AC + 760°C/2.5 hr/AC. From an investigation of a number of welding procedures for HT-9,[5] the process using a gas-tungsten arc was chosen for fabrication of the welded plate material stock. The HT-9 plate is preheated to 93°C and interpass temperatures between 93°C and 143°C were used during welding. The post-weld tempering treatment for the weld material was 780°C for one hour. Each plate, which measured 12.7 x 30.5 cm, was then inspected using dye penetrant and radiography to ensure the quality of the weld.

Figure 7.7.3 outlines the processing steps ORNL used to obtain the modified 9Cr-1Mo material stock from which specimens were fabricated. The 59.9 cm diameter bar was first machined into extrusion billets and then side forged at 1200°C to a slab thickness of 31.8 mm. These slabs were given a

HT-9 HEAT NUMBER 91353

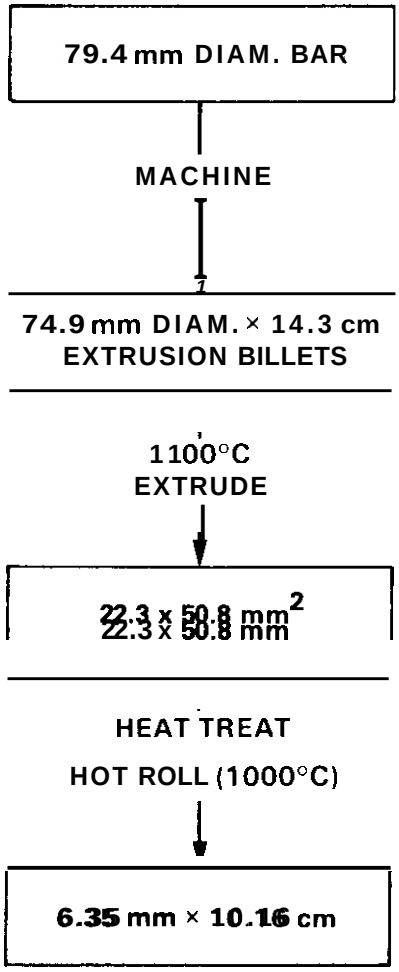

FIGURE 7.7.2 Mechanical Processing of HT-9 Plate for Weld Material

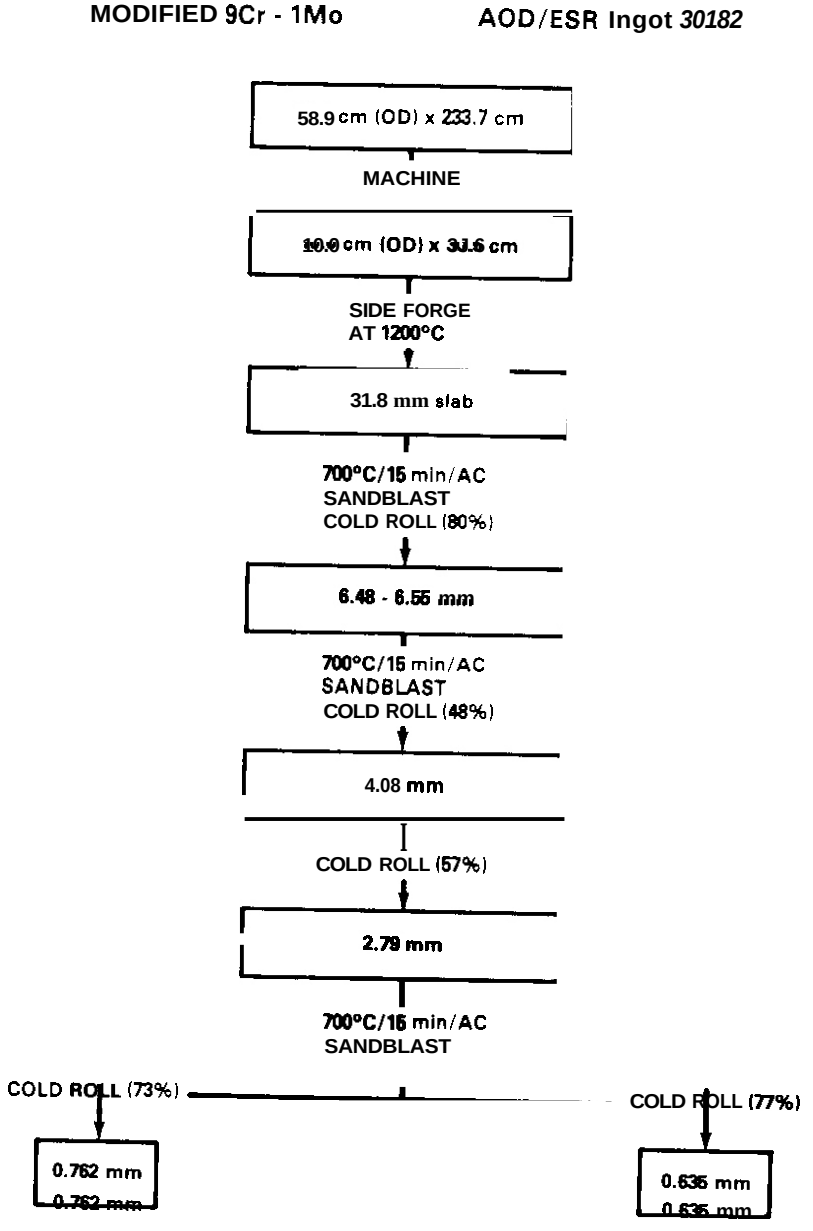

FIGURE 7.7.3 Mechanical Processing of Modified 9Cr-1Mo Alloy Stock

softening treatment of 700°C for fifteen minutes followed by an air cool and sandblasted to remove the sealing. The material was cold rolled to a thickness of approximately 6.5 nun. A portion of this material was then used in the fabrication of weld plate material and the fabrication of miniature Charpy specimens. The rest of the material was then given a softening treatment of 700°C for fifteen minutes and sandblasted. The material stock was cold rolled to a thickness of 4.06 mm. Some of this material stock was used to fabricate the fracture toughness specimens and the remainder of the stock was cold rolled to a thickness of 2.79 mm. The material stock was again given a softening treatment of 700°C for fifteen minutes followed by an air cool, sandblasted and then cold rolled down to thicknesses of 0.762 and 0.635 nun. All the material stock was given a heat treatment of 1038°C/1 hr/AC + 760°C/1 hr/AC before the fabrication of 9Cr-1Mo specimens and of the welded plate material stock.

General Atomic Corporation welded some of the modified 9Cr-1Mo 6.35 nun thick plate to provide weld material for AD-2 specimens. The same welding procedure used for HT-9 was also used for 9Cr-1Mo. The same post-weld tempering treatment of 780°C for one hour was also used. Each plate was inspected using dye penetrant and radiography to ensure the quality of the weld.

Figure 7.7.4 outlines the processing steps HEDL used to obtain the 2-1/4Cr-1Mo sheet stock from which the fatigue crack growth, Crodzinski fatigue and tensile strength specimens were fabricated. Material came from a section of pipe and was cut and divided into two approximately equal lots. Half of the material was processed to a thickness of 0.711 to 0.762 nun and the other half was processed to a thickness of 0.559 to 0.610 mm. All heat treatments were given with the material encapsulated in quartz at 1/4 atmosphere argon. Initially, both lots were given an anneal: 1250°C/5 hr/FC. The material stock then went through a series of thickness reductions using the following sequence: 1) cold roll; 2) cut into shorter lengths; 3) encapsulate; and 4) heat treatment. The specimens were fabricated from the cold work material and the final heat treatment for 2-1/4Cr-1Mo material was chosen to be 900°C/30 min/AC + 700°C/1 hr/AC.

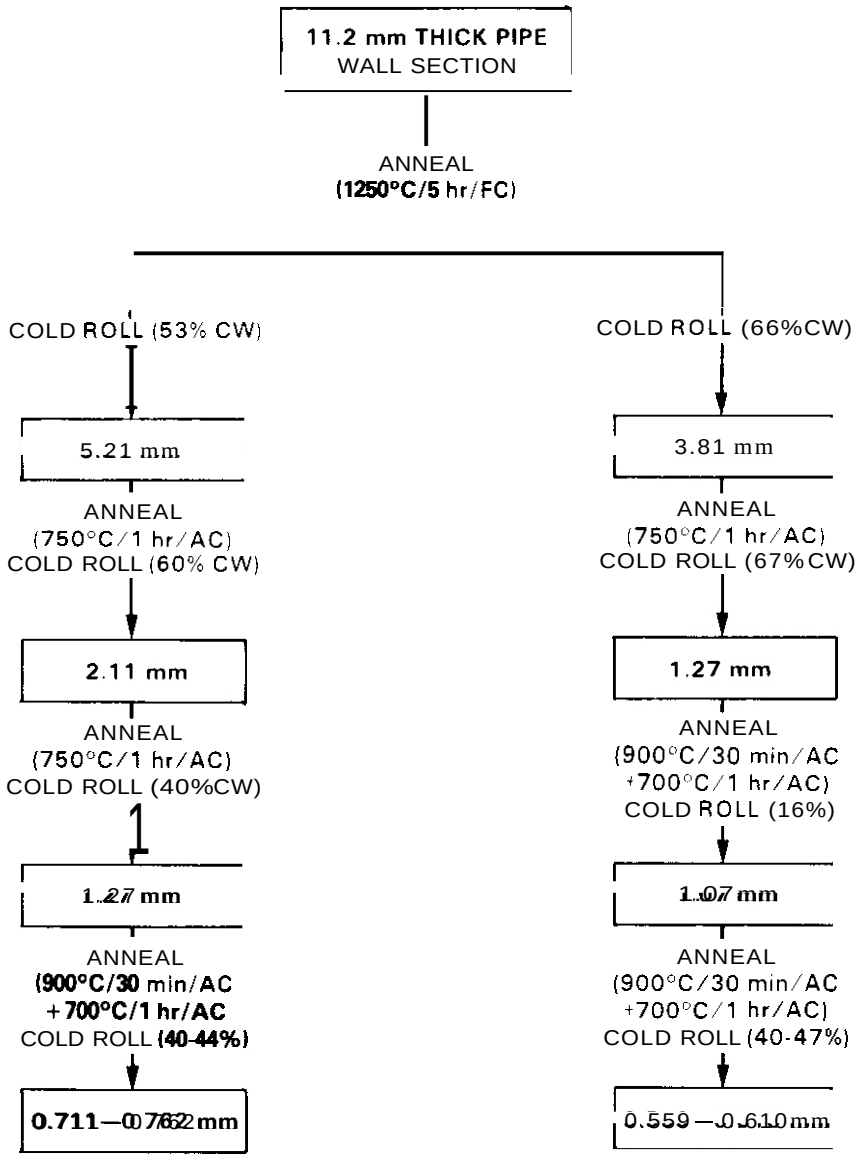

FIGURE *7.7.4* Mechanical Processing of 2-1/4Cr-1Mo Alloy Stock

7.7.4.3 Metallographic Characterization of Specimen Materials

A micrographof the mill annealed *33.3* mm diameter HT-9 bar from which fracture toughness and miniature Charpy specimens were fabricated is shown in Figure *7.7.5.* This transverse view at 400x shows the martensitic

FIGURE 7.7.5 Micrograph at 400x of Transverse Section from 33.3 mm Diameter HT-9 Bar Stock

structure in HT-9. An estimate of the prior austenitic grain size for this material is between ASTM 8 and ASTM 9. The microhardness of this material was found to be 270 DPH (500 gm).

Micrographs of the transverse sections of the 0.610 mm HT-9 sheet stock are shown in Figure 7.7.6. There was no evidence of any decarburized layer on this material. For the material receiving the final heat treatment, 1038°C/30 min/AC + 760°C/2.5 hr/AC, the prior austenitic grain size was estimated to be between ASTM 4 and ASTM 6. Microhardness measurements for this material yielded values of 266 ± 4 DPH (500 gm) for the 0.610 mm thick material and 271 ± 7 DPH (500 gm) for the 0.672 mm thick material. For the material receiving the final heat treatment, 1038°C/4 min/AC + 760°C/30 min/AC,

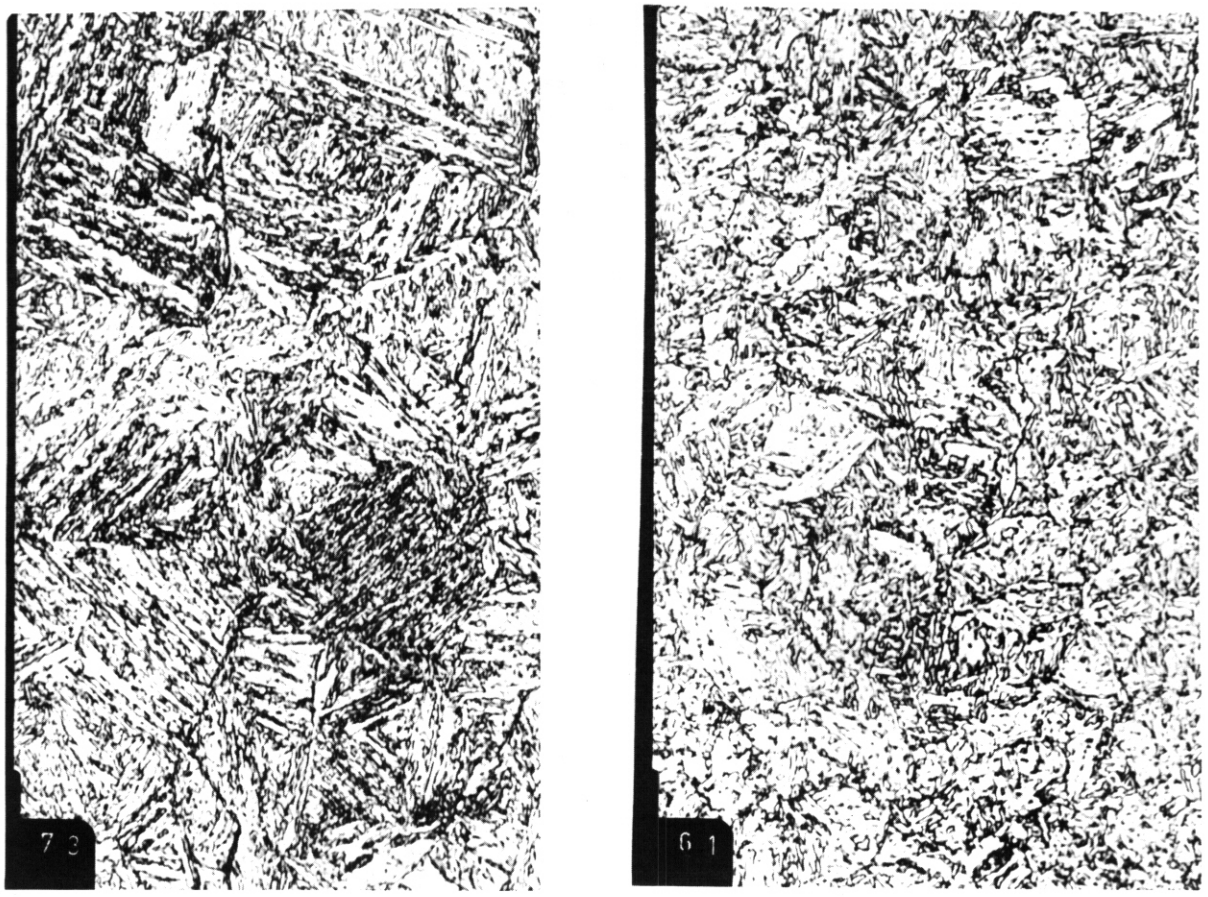

(a) (b)

FIGURE 7.7.6 Micrographs at 400x of Transverse Section of HT-9 Sheet Stock:
a) 0.61 mm (1038°C/30 min/AC + 760°C/2.5 hr/AC), and
b) 0.61 mm (1038°C/4 min/AC + 760°C/30 min/AC).

the prior austenitic grain size was estimated to be between ASTM 6 and ASTM 8. Microhardness measurements for this material yielded a value of 272 ± 6 DPH (500 gm) for both thicknesses, 0.610 and 0.762 mm.

The fracture toughness and Charpy specimens, machined from mill annealed HT-9 bar stock, have TMTs which differ from the tensile and fatigue type specimens, which were machined from heat treated, 40% CW sheet stock. The relevance of any comparison or correlation between the tensile and fracture toughness data depends upon whether or not the properties which result from these different TMTs are comparable. Table 7.7.3 lists the prior history, microhardness and grain size of the four conditions of HT-9.

TABLE 7.7.3

TMT NUMBER	PRIOR HISTORY	MICROHARDNESS 500 gm DPH	GRAIN SIZE ASTM
#1	40% CW + 1038°C/4 min/AC + 760°C/30 min/AC	270	6-8
#2	40% CW + 1038°C/0.5 hr/AC + 760°C/2.5 hr/AC	268	4-6
#3	Mill Annealed[1]	270	8-9
#4	Mill Annealed[1] + 1050°C/0.5 hr/AC + 780°C/2.5 hr/AC	244	3-4

[1] See page 4 of this report.

The aim of TMT #1 and #3 was to obtain a structure with a grain size of ASTM 7 or smaller. The aim of TMT #2 and #4 was to increase the prior austenitic grain size to ASTM 5. TMTs #1 and #3 resulted in comparable microhardness and grain size, while TMT #2 and #4 have comparable grain size, but differ in microhardness. It is known that microhardness values are indicative of tensile properties and that both microhardness and grain size will affect fracture toughness. Therefore, it appears that while valid correlations can be obtained for data generated from specimens with TMT #1 and #3, data correlations between specimens with TMTs #2 and #4 may not be valid. Actual fracture toughness tests will be performed on control specimens in each of the four TMTs to verify these assumptions. The results will be reported in the next quarterly report.

Micrographs of the modified 9Cr-1Mo 6.35 and 0.635 mm thick sheet stock are shown in Figure 7.7.7. Although there was significant scaling of the material from the final heat treatment, no evidence of any decarburized layer was found in any of the material stock. An estimate of the prior austenitic grain size for this material is between ASTM 8 and ASTM 10. Microhardness measurements on this material indicate that the material has a hardness of 226 DPH (500 gm).

A micrograph at 400x of the transverse section of the 2-1/4Cr-1Mo material is shown in Figure 7.7.8. An estimate of the prior austenitic grain size is between ASTM 8 and ASTM 9. Microhardness measurements indicate the hardness of the material to be 207 DPH (500 gm).

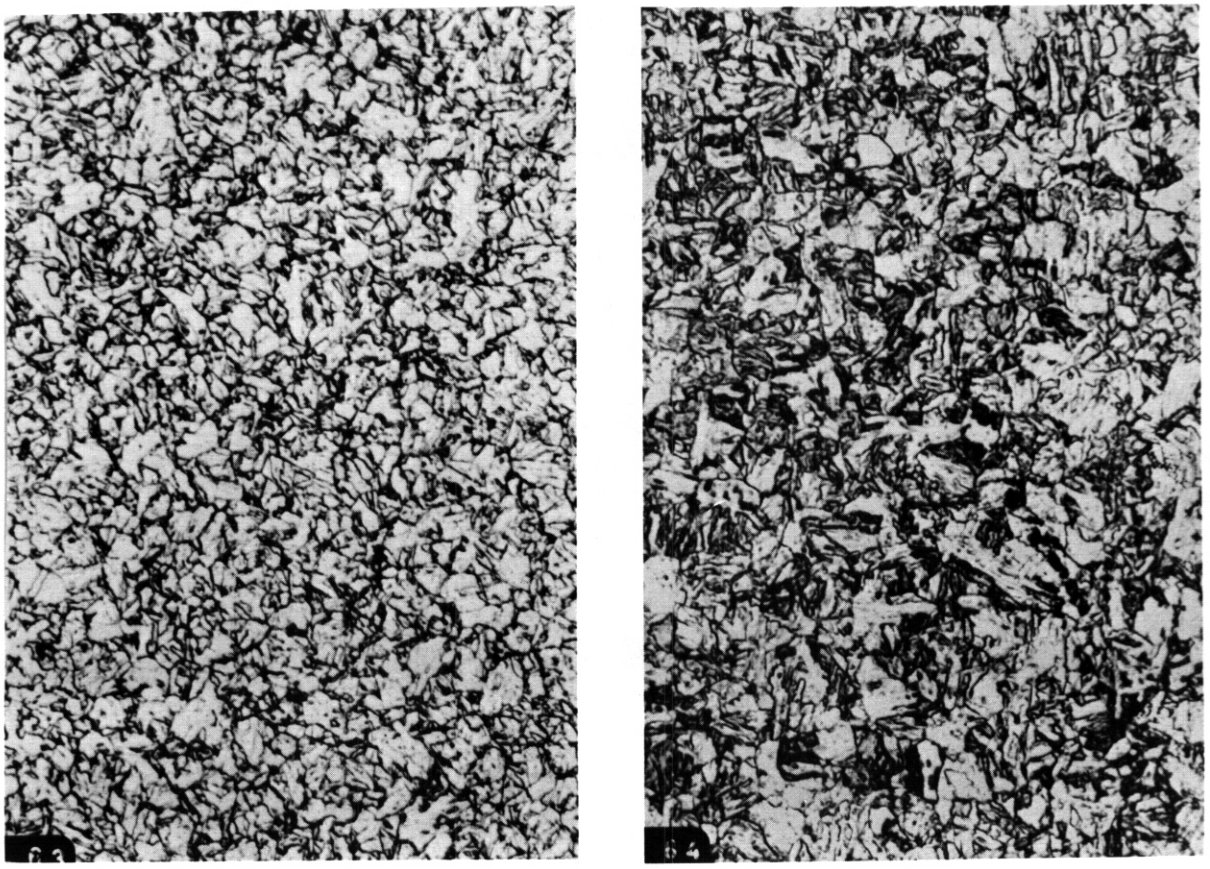

(a) (b)

FIGURE 7.7.7 Micrograph at 400x *of* Transverse Section of Modified 9Cr-1Mo Alloy Stock Thickness: (a) 0.635 mm; (b) 6.35 mm.

FIGURE 7.7.8 Micrograph at 400x of Transverse Section of 2-1/4Cr-1Mo Alloy Stock

Metallography and hardness measurements were performed on the HT-9 and modified 9Cr-1Mo butt welded plate materials. Representative samples were cut from the centers of various plates. Figure 7.7.9 shows a 5x macrograph of a transverse section for HT-9 welded plate. The surfaces on the left hand side from the weld appear to have a different structure from the middle of the plate. Also, this structure is not apparent on the surfaces of the righthand side from the weld. An estimate of the prior austenitic grain size in the center of the plates is between ASTM 4 and ASTM 5. Microhardness measurements across the width of the left hand side from the weld gave a variance in hardness for the plate from 247 ± 6 DPH (500 gm) in the center of the plate to 160 ± 8 DPH (500 gm) at the surfaces of the plate.

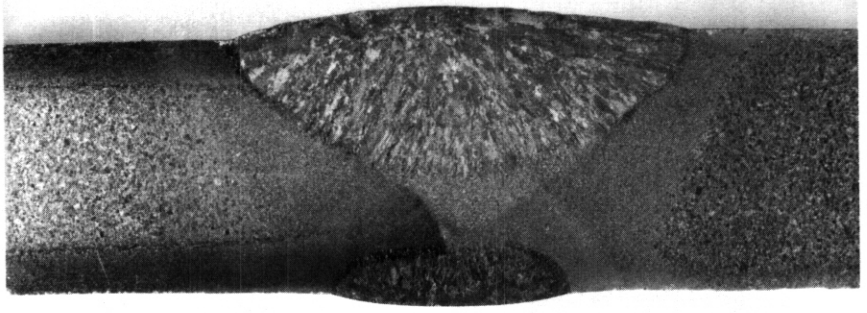

FIGURE 7.7.9 Macrograph at 5x of Transverse Section of HT-9 Weld Material

This is indicative of a decarburized layer, which probably occurred during fabrication. To determine what fraction of the welded plate material exhibited evidence of a decarburized layer, Rockwell B type hardness measurements were also performed on all plates. The hardness was found to vary between R_B 84 and R_B 103. Approximately 60% of the HT-9 welded plate stock had hardness values of less than R_B 95. The material stock with lower hardness values was used in the fabrication of the fatigue crack growth specimens since these specimens could be cut from the center of the weld plate to ensure that no decarburized material was included in the final specimen. The material stock with little or no decarburized layer was used in the fabrication of the fracture toughness and Charpy specimens.

Microhardness measurements were also performed across the weld region. The post-weld temper produced hardness values of *263 ± 7* DPH *(500* gm) in the weld metal, *250* ± 9 DPH (500 gm) in the heat affected zone (HAZ), and *247 ± 6* DPH *(500 gm)* in the base metal. The welds themselves in the HT-9 material appear to be very good.

A macrograph of the modified 9Cr-1Mo welded plate is shown in Figure 7.7.10. There was no evidence for a decarburized layer on any of the modified 9Cr-1Mo plates. Microhardness measurements across the weld varied from *209 ± 7* DPH *(500* gm) in the base material to *226* ± 16 DPH *(500* gm) in the HAZ to *266* ± 11 DPH (500 gm) in the weld metal.

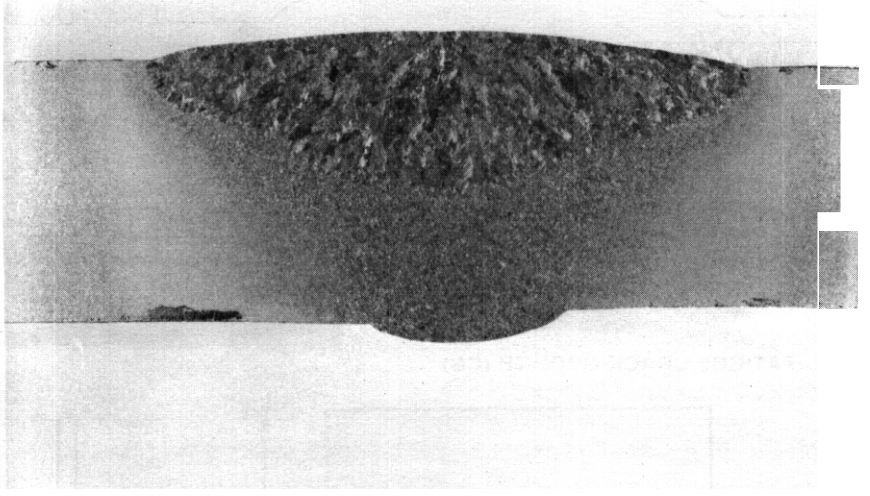

FIGURE 7.7.10 Macrograph at 5x of Transverse Section of Modified 9Cr-1Mo Weld Material

7.7.4.4 Specimen Preparation

The nominal dimensions for the specimens in the AD-2 experiment are shown in Figures 7.7.11 and 7.7.12. Further specifications on the dimensions of the specimens may be obtained from the drawings listed in Table 7.7.4. The fatigue initiation and Grodzinski fatigue specimens were fabricated by Oak Ridge National Laboratory, and HEDL had responsibility for fabrication of all the other specimens for the AD-2 experiment.

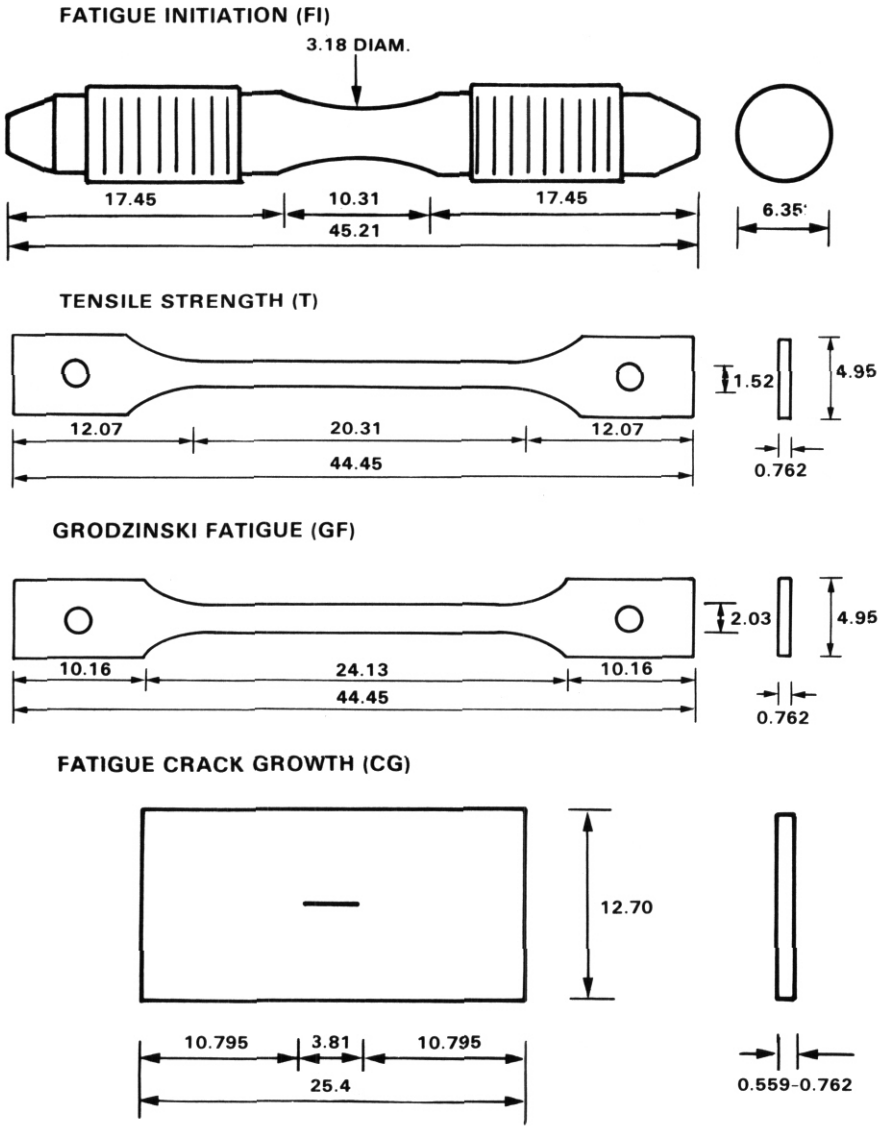

FIGURE 7.7.11 Nominal Dimensions of Specimens in AD-2 Experiment (All dimensions in mm.)

FRACTURE TOUGHNESS (FT)

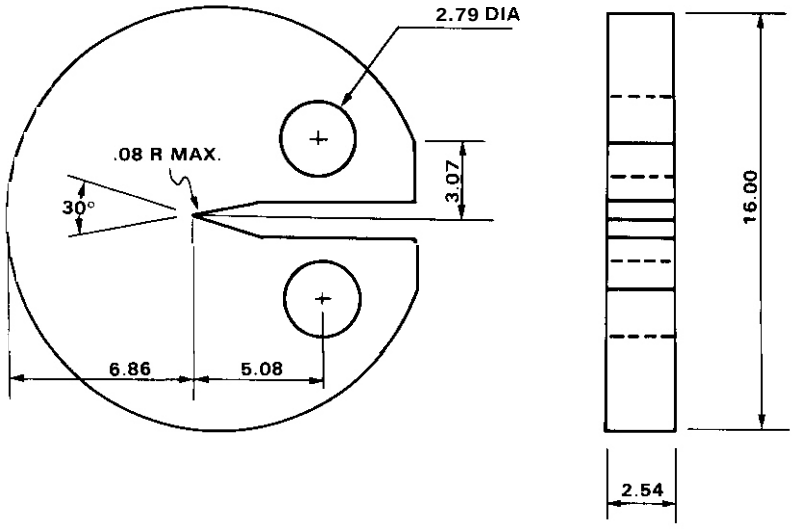

MINIATURE CHARPY (C)

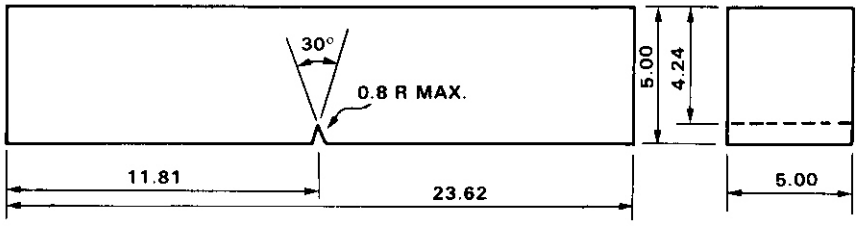

ALL DIMENSIONS IN mm

FIGURE 7.7.12 Nominal Dimensions of Specimens in AD-2 Experiment

TABLE 7.7.4

SPECIMEN TYPE	DRAWING NUMBER
Charpy Specimen - C	H-3-46299 (HEDL)
Fracture Toughness Specimen - FT	H-3-46752 (HEDL)
Tensile Specimen - T	H-3-37395 (HEDL)
Fatigue Initiation Specimen - FI	M-11950-EM-003C (Union Carbide)
Fatigue Specimen - GF	00E057069 (McDonnell-Douglas)
Crack Growth Blank - CG	H-3-46018 (Part A) (HEDL)
TEM Disc - D	H-3-39231 (P/N 5) (HEDL)

The Grodzinski fatigue specimens were fabricated from 0.762 mm thick material stock and specimens were oriented both parallel and perpendicular to the rolling direction. The HT-9 fatigue initiation specimens were fabricated from 6.35 mm diameter mill annealed rod stock and the modified 9Cr-1Mo fatigue initiation specimens were fabricated from the 6.35 mm thick plate and oriented so that the specimen axis was parallel to the rolling direction. All HT-9 and modified 9Cr-1Mo tensile strength specimens were oriented with their gage length sections perpendicular to the rolling direction. Because of the final dimensions of the 2-1/4Cr-1Mo 0.762 mm thick material stock, the tensile or specimens for this alloy were all oriented parallel to the rolling direction. All the fatigue crack growth specimens, expect weld specimens, were fabricated from sheet stock 0.559 to 0.610 mm thick and were oriented with the notch length parallel to the rolling direction.

The dimensions of the fracture toughness and miniature Charpy specimens are shown in Figure 7.7.12. The details of the fracture toughness specimen have been reported elsewhere!') The miniature Charpy specimen has the same cross sectional dimensions as a half-size standard Charpy specimen but differs in length and notch dimensions. The overall specimen length was limited by the irradiation capsule hardware restrictions. However, the length is sufficient to permit the use of the standard span dimension 4W (W = 5.00 mm) for both precracking and Charpy type testing.

The orientation in which the circular fracture toughness and Charpy specimens were machined from the HT-9 and 9Cr-1Mo alloy stock is shown in Figure 7.7.13. HT-9 fracture toughness and Charpy specimens were machined from 33.3 mm diameter mill annealed bar stock, heat number 91354. The fracture toughness of this mill annealed bar stock has been studied and the results have been reported elsewhere.[6] The 9Cr-1Mo fracture toughness and miniature Charpy specimens were machined from 4.1 mm and 6.4 mm thick plates, respectively.

Charpy specimens were precracked in accordance with ASIM specification E-399.[7] Precracking was accomplished using an 89kN Materials Test System (MTS) load frame and a model 436-406 controller. The crack extension was measured using a traveling microscope which was accurate to 2.54 μm. The precracking was done in three point bending using a fixture designed to the specifications of ASIM E-399. Precracking was performed using a

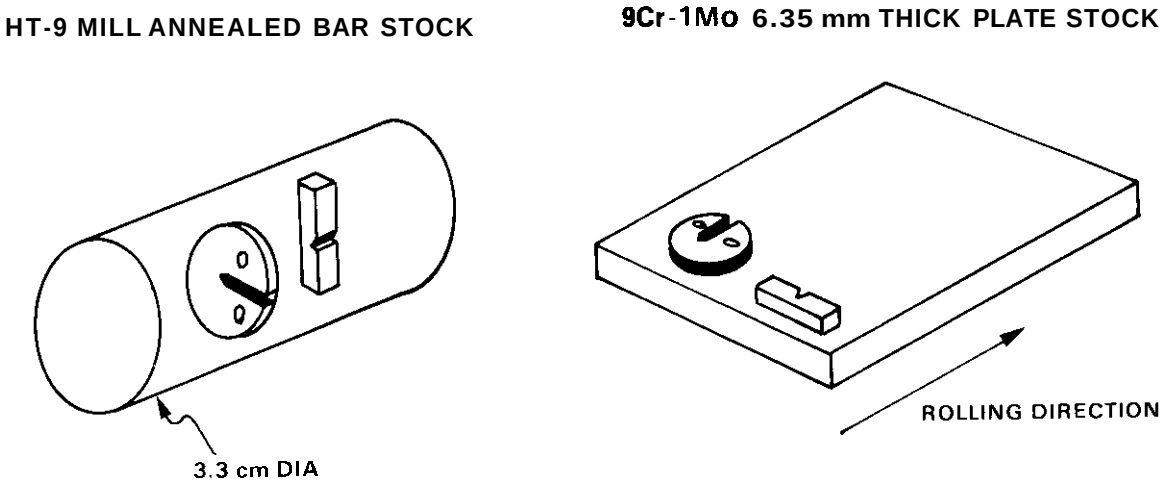

FIGURE 7.7.13 Orientation of Fracture Toughness and Charpy Specimens with Respect to Material Stock

sinosodial 30 Hz loading waveform. The loading was adjusted to obtain a value of about 0.1 for the ratio of minimum to maximum load.

Using standard procedures, the precracking load, P, was calculated as follows,

$$P = \frac{KBw^{3/2}}{Sf(a/w)} \qquad [1]$$

were K is a stress intensity factor, B and w are the cross sectional dimensions of the miniature Charpy specimen, S is the distance between the two specimen support points and f(a/w) is calculated from the standard formulation for bend specimens:

$$f(a/w) = \frac{3(a/w)^{1/2}\,[1.99 - (a/w)(2.15 - 3.93\ a/w + 2.7\ a^2/w^2)]}{2(1 + 2\ a/w)(1 - a/w)^{3/2}} \qquad [2]$$

where a is the length of the machined notch plus the fatigue precrack. In this experiment, B = w = 5.00 mm, S = 20.00 mm and specimens were precracked until a = *2.41* ± 0.3 mm, that is until the length of the fatigue crack was 1.7 ± 3 mm. This resulted in an a/w ratio of *0.48*.

In order to produce a true fatigue precrack, a maximum stress intensity factor, K, of 16 MPa • $m^{1/2}$ was specified for the final 0.25 mm of crack extension. According to Equation [1], if a maximum value is specified for K,

the maximum value of the precracking load, P, as a function of crack extension, is also specified. The calculated precracking required to obtain a maximum K of 16 MPa • $m^{1/2}$ for the miniature Charpy specimens is plotted as a function of crack length in Figure *7.7.14*.

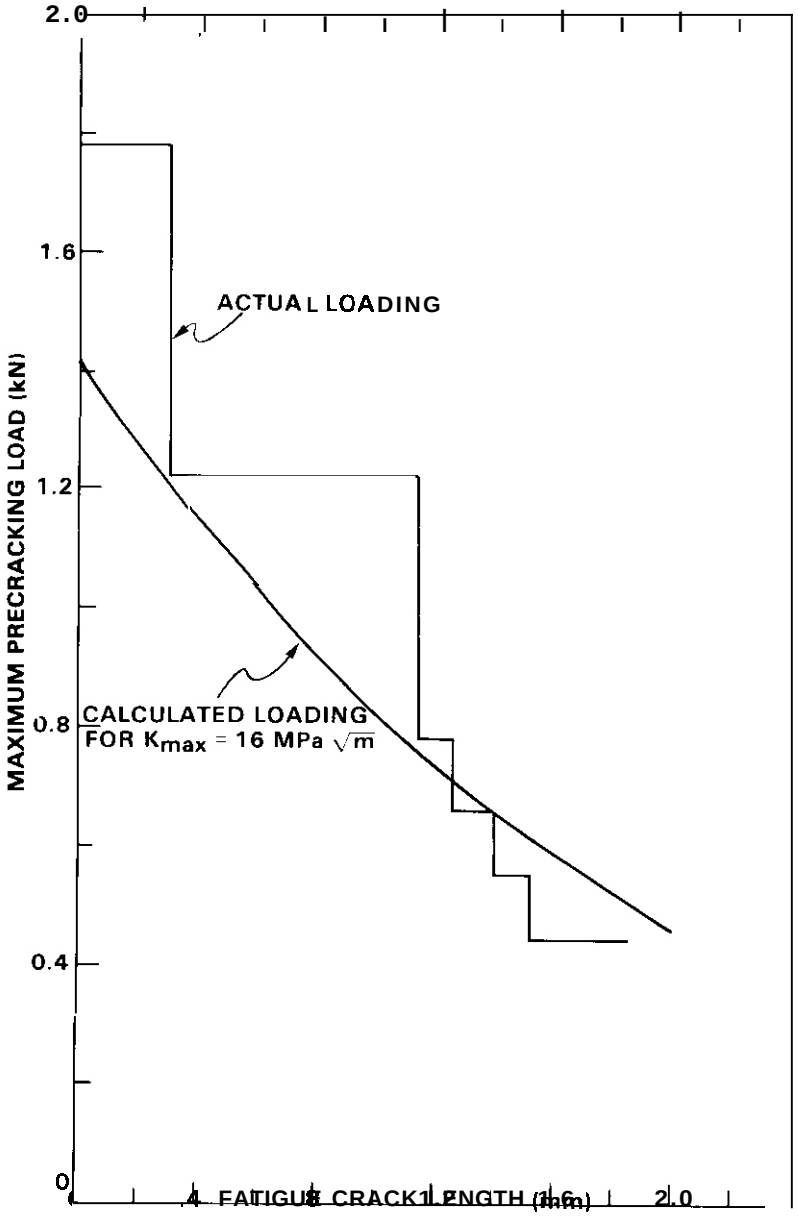

FIGURE *7.7.14* Calculated and Actual Maximum Load Fatigue Precracking Loading Schedules.

A typical maximum load history is also plotted. Loads in excess of the calculated value were employed in the early stages of crack growth in order to ensure prompt crack initiation and propagation. After about 1.275 mm of crack extension the magnitude of the loading was controlled so that the specified maximum stress intensity value would not be exceeded. The rate of crack growth during the final 0.25 mm of crack extension was also maintained below 2.54×10^{-5} mm/cycle. Although the value of 16 MPa • $m^{1/2}$ was specified for the precracking of HT-9 specifically, it was judged to be a sufficiently conservative value for 9Cr-1Mo as well, based on a comparison of the relative yield strengths of these alloys. A fatigue cracking record was maintained for each precracked specimen. The length of one surface crack was monitored continuously while the length of the second surface crack was checked periodically. The longer of the two surface cracks determined the termination of the precracking procedure. The precracking of all 9Cr-1Mo and HT-9 Charpy specimens was accomplished without any deviation from loading, crack length or growth rate specifications.

The general orientation of the Charpy, fracture toughness and fatigue crack growth specimens, with respect to the welded plate stock, is shown in Figure 7.7.15. The Charpy specimens were machined so that properties of the fusion metal and the heat affected zone (HAZ) would be sampled for the HT-9 weld material. The location of the notch within the weld region was verified for each specimen loaded into AD-2 by visual examination following an oxalic acid electrolytic etch. Typical examples of the Charpy notch locations are shown in Figure 7.7.16. Although the notch in both weld and weld/HAZ Charpy specimens is located within the weld, fatigue cracks were produced in each miniature Charpy specimen, which, in the case of the weld/HAZ specimen, extendedinto the HAZ.

The fracture toughness specimens were machined so that properties of the fusion metal and the HAZ would be investigated for the HT-9 welded material. The notch was oriented so that the crack would propagate along the middle of the fusion metal and parallel to the fusion line for those specimens machined to investigate the fracture properties of the fusion metal. For those specimens machined to investigate the fracture properties of the HAZ, the notch was oriented in the centerofthe HAZ so that the crack would propogate parallel to the fusion line and in the HAZ. The

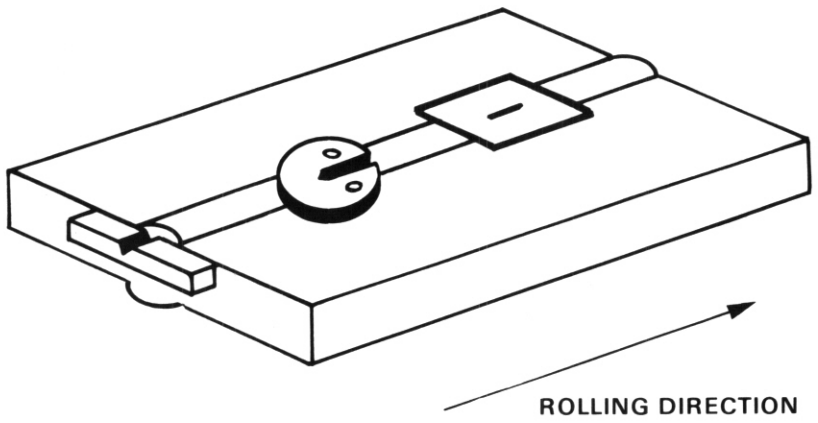

FIGURE 7.7.15 Orientation of Charpy, Fracture Toughness and Fatigue Crack Growth Specimens with Respect to Weld Material

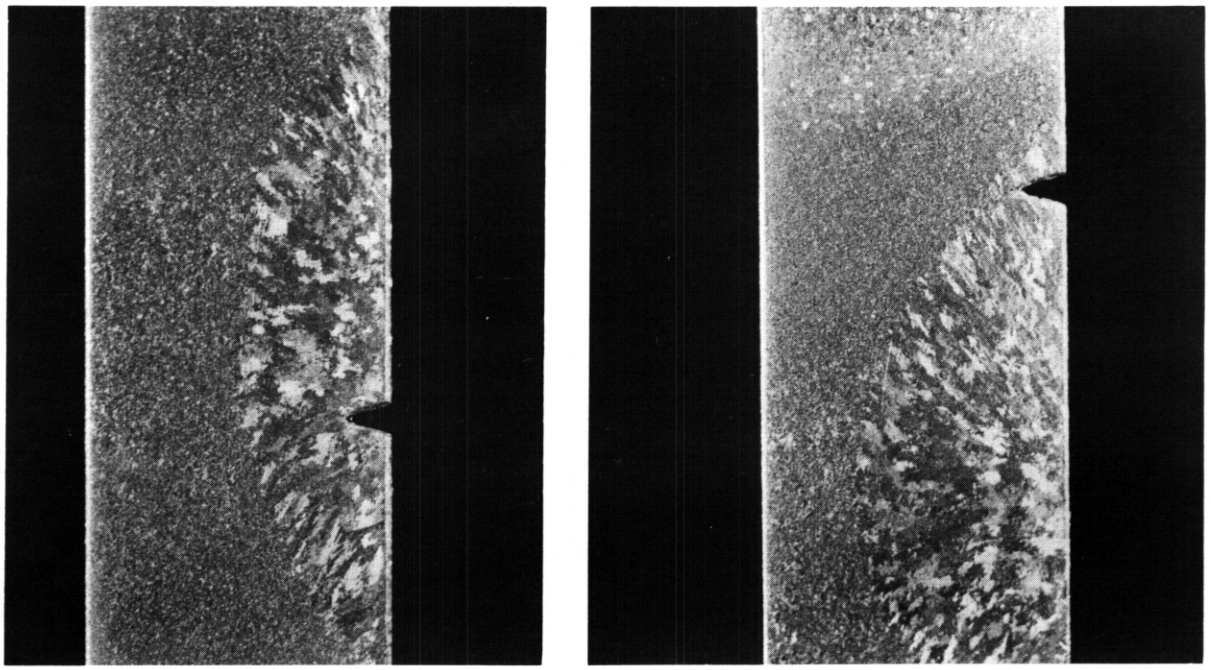

(a) (b)

FIGURE 7.7.16 Charpy Specimen Notch Location: (a) weld metal; (b) weld/HAZ region.

location of the notch with respect to the weld material was visually verified after each specimen was electrolytically etched in oxalic acid.

For the fatigue crack growth specimens fabricated from the HT-9 welded plate the orientation of the specimen within the material stock was chosen so that the fatigue properties of the weld metal, the heat affected zone, and the fusion line between the weld material and HAZ could be explored. A specific example of a fatigue crack growth specimen with its notch located along the fusion line is shown in Figure 7.7.17. The figure shows both sides of a specimen which has been etched to bring out the pertinent weld microstructures within the specimen. On the front side the notch appears to be in the weld metal and on the other side the specimen's notch appears to be completely within the HAZ. Because of the geometry of the weld and the fact that we wished to stay away from the decarburized layers on these plates, it was difficult to place the notch precisely on the fusion line. Therefore, each specimen of this type is unique. Eachspecimenwas etchedinanoxalicacid

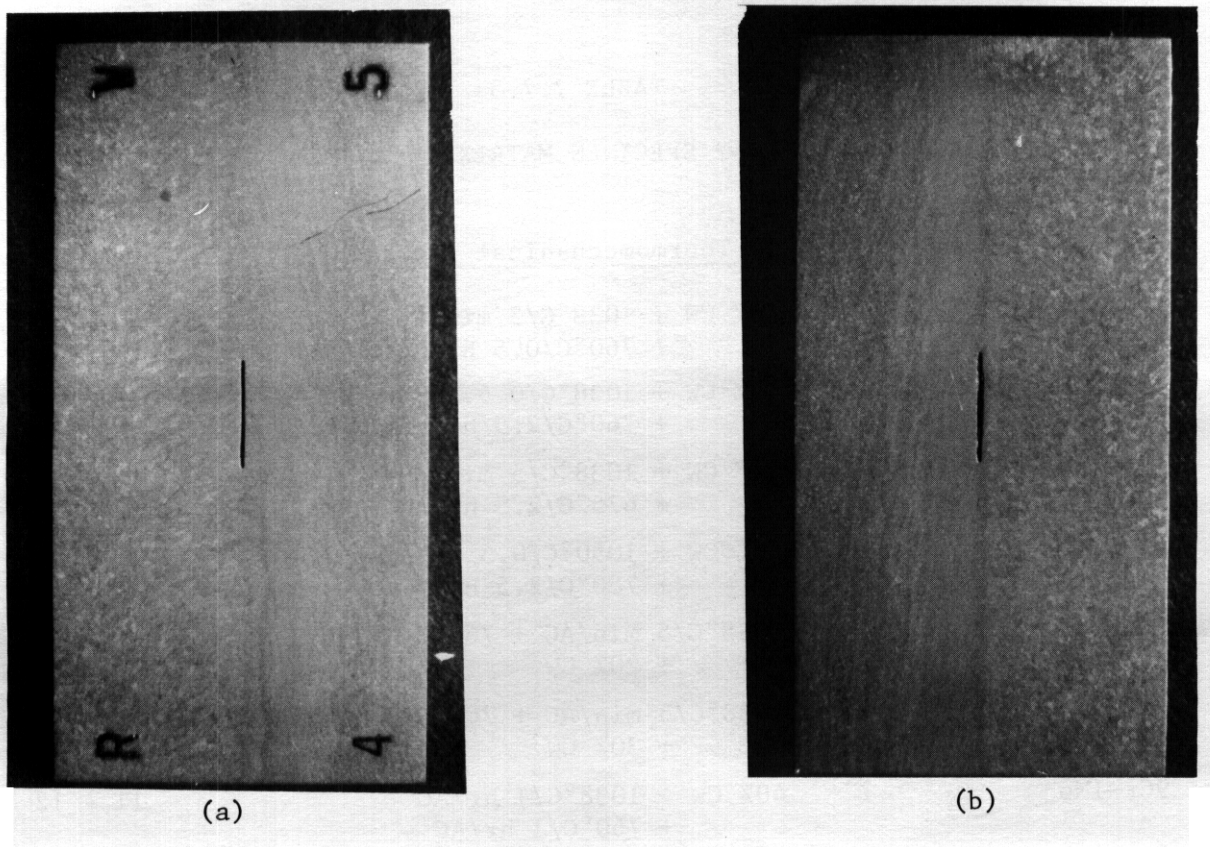

FIGURE 7.7.17 Fatigue Crack Growth Specimen with Notch Along Fusion Line: (a) Front Side; (b) Back Side.

and photographs of both sides of each specimen were taken to characterize them individually. The placement of the notch in each specimen was checked visually after each specimen had been etched. All the fatigue crack growth specimens fabricated from the 9Cr-1Mo welded plate were oriented with the notch in the center of the fusion metal.

Upon receipt of the specimens for the AD-2 specimen at HEDL, each specimen was checked by HEDL Quality Assurance to determine compliance of the as-machined specimens with the drawing specifications. Specimens were then engraved using a laser engraving technique.

Table 7.7.5 lists the TEM specimen matrix for the AD-2 experiment and the multiplicty for each thermomechanical treatment that is being investigated. In addition to the primary alloys being investigated in this experiment, the TEM matrix also contains alloys which are part of the DAFS program and specimens provided by MIT. The TEM discs are loaded into disc packets which hold approximately 60 TEM discs each.

TABLE 7.7.5

AD-2 SPECIMEN MATRIX

Alloy	Thermomechanical Treatment	Multiplicity
HT-9	40% CW + 1038°C/5 min/AC + 760°C/0.5 hr/AC	11 - 12
HT-9	40% CW + 1038°C/0.5 hr/AC + 760°C/2.5 hr/AC	11 - 12
HT-9	40% CW + 1038°C/5 min/AC + 675°C/2.5 hr/AC	4
HT-9	40% CW + 1050°C/0.5 hr/AC + 780°C/2.5 hr/AC	4
HT-9	1038°C/5 min/AC + 760°C/0.5 hr/AC + 20% CW	4
HT-9	1038°C/5 min/AC + 760°C/0.5 hr/AC + 30% CW	4
9Cr-1Mo	40% CW + 1038°C/1 hr/AC + 760°C/1 hr/AC	11 - 12
9Cr-1Mo	40% CW + 1038°C/5 min/AC + 760°C/1 hr/AC	4
9Cr-1Mo	40% CW + 1038°C/5 min/AC + 675°C/2.5 hr/AC	4

TABLE 7.7.5
(cont'd)

Alloy	Thermomechanical Treatment	Multiplicity
9Cr-1Mo	1038°C/1 hr/AC + 760°C/1 hr/AC + 20% CW	4
9Cr-1Mo	1038°C/1 hr/AC + 760°C/1 hr/AC + 30% CW	4
2-1/4Cr-1Mo	900°C/0.5 hr/AC + 700°C/1 hr/AC	11 - 12
2-1/4Cr-1Mo	900°C/0.5 hr/AC + 650°C/1 hr/AC	4
2-1/4Cr-1Mo	920°C/10 min/WQ + 720°C/1 hr/AC	4
2-1/4Cr-1Mo	40% CW + 750°C/1 hr/AC	4
Amorphous Ni-Nb		4
Fe-BeO	Annealed	4
Fe-BeO	CW	4
316-Al_2O_3	Annealed	4
316 Al_2O_3	CW	4
AISI 316 + 1000 appm ^{10}B + Zr	850°C/1 hr/WQ	7 - 8
AISI 316 + 5000 appm B + Zr	980°C/0.5 hr/AC	7 - 8
AISI 316 (N-Lot)	1050°C/2 min/AC + 20% CW	7 - 8
AISI 316 (MFE Heat)	1050°C/2 min/AC + 20% CW	7 - 8
A508 (Class 3)	As received[1]	7 - 8
A533-B (Class 1)	As received[2]	7 - 8
B2	1025°C/5 min/AC + 800°C/8 hr/AC	7 - 8
B3	1025°C/5 min/AC + 750°C/8 hr/AC	7 - 8
B4	1025°C/5 min/AC + 850°C/3 hr/AC + 720°C/8 hr/FC to 620°C/18 total/AC	7 - 8
D57-B	1025°C/5 min/AC + 25% CW	7 - 8
10Cr-2Mo-V-Nb	1050°C/0.5 hr/AC + 800°C/1 hr/AC	7 - 8
AISI 316 (N-Lot)	1050°C/2 min/AC + 20% CW	7 - 8
AISI 316 (MFE Heat)	1050°C/2 min/AC + 20% CW	7 - 8

[1]Belgian forging steel
[2]See Reference 8

7.7.4.5 Specimen Loading

The specimens were loaded into two B-7c weeper capsules, which were designed to maintain the specimen temperature at 390°C, and into four B-7c subcapsules designed to maintain the specimen temperatures at 450°C, 500°C (two subcapsules), and 550°C during irradiation. The specific level loading for each capsule is given in Tables 7.7.6 through 7.7.9. Each level measured approximately 50 mm in length. The fracture toughness specimens were stacked vertically within a level with wire spacers separating each specimen.

7.7.5 Conclusions and Future Work

The fabrication of specimens and experimental hardware for the AD-2 experiment has been completed. The experiment has been assembled and shipped to EBR-II. Irradiation of specimens will begin in EBR-II, Cycle 109, August 11, 1980. The schedule of future work expected in this experiment is:

Ship to EBR-II	June 25, 1980
Begin Irradiation	August 11, 1980
Remove for Interim Examination	June 7, 1981
Continue Irradiation	October 6, 1981
End Irradiation	August 1982

Work is now in progress on baseline tests on the alloys being investigated in the AD-2 experiment.

7.7.6 References

1. L. D. Thompson and S. N. Rosenwasser, "Ferritic Stainless Steels for Fusion Applications," ADIP *Quarterly Progress Report, June 30,* 1979. S. N. Rosenwasser, P. Miller, J. A. Dalessandro, J. M. Rawls, W. F. Toffolo, and W. Chen, "The Application of Martensitic Stainless Steels in Long Lifetime Fusion Wall/Blankets," *J. Nucl. Mat, 85 & 86, (1979),* pp. 177-182.

TABLE 7.7.6

SPECIMEN MATRIX FOR INSERTION INTO EBR-II SUBASSEMBLY X-344a

Temperatures - 390°C (743°F) and 500°C (932°F)

	Level No.	Distance From Center of Level to Core Midplane (mm)	Specific Alloy Loading+
3 FI 8 T 1 TED	1	158	3 FI HT-9 (84) 5 T HT-9 (112) 3 T 2-1/4Cr-1Mo
6 FT 6 FT(W)	2	108	6 FT HT-9 (#4) 6 FT(W) HT-9
23 CG(W) 2 D	3	56	7 CG(W/HAZ) HT-9 10 CG(W) HT-9 6 CG(W) 9cr-1Mo 2 D Discs Packets
26 CG 1 TED	4	0.0	11 CG HT-9 (#1) 5 CG HT-9 (#2) 5 CG 9Cr-1MO 5 CG 2-1/4Cr-1Mo
8C 5T 2D	5	-54	4 C(W/HAZ) HT-9 4 C HT-9 (#3) 5 T HT-9 (#1) 2 D Disk Packets
4 c 4 C(W) 7 GF 3 T	6	-102	1 C(W/HAZ) HT-9 4 C 9Cr-1Mo 3 C(W) HT-9 5 GF HT-9 (#1) 2 GF 9Cr-1Mo 3 T 9Cr-1Mo
3 FI 8 T 1 TED	7	-152	3 FI 9Cr-1Mo 5 T HT-9 (#1) 3 T 9Cr-1Mo

+See Table 7.7.3 for specific thermomechanical heat treatments used for HT-9 specimens. See Table 7.7.4 for specimen name abbreviations used in this table.

TABLE 7.7.7

SPECIMEN MATRIX FOR INSERTION INTO EBR-II SUBASSEMBLY X-344a

Temperature - 550°C (1022°F)

	Level No.	Distance From Center of Level to Core Midplane (mm)	Specific Alloy Loading +
3 FI 8 T 1 TED	1	158	3 FI HT-9 (#4) 5 T HT-9 (#2) 3 T 2-1/4Cr-1Mo
6 FT 6 FT(W) 6 FT(W)	2	108	6 FT HT-9 (#3) 3 FT(W/HAZ) HT-9 3 FT(W) HT-9
23 CG(W) 2 D	3	56	7 CG(W/HAZ) HT-9 10 CG(W) HT-9 6 CG(W) 9Cr-1Mo 2 D Discs Packets
26 CG 1 TED	4	0.0	11 CG HT-9 (#1) 5 CG HT-9 (#2) 5 CG 9Cr-1Mo 5 CG 2-1/4Cr-1Mo
8 C 5 T 2 D	5	-54	8 C HT-9 (#3) 5 T HT-9 (#1) 2 D Disc Packers
4 C 4 C(W) 7 GF 3 T	6	-102	4 C 9Cr-1Mo 4 C(W) HT-9 5 GF HT-9 (#1) 2 GF 9Cr-1Mo 3 T 9Cr-1Mo
3 FI 8 T 1 TED	7	-152	3 FI 9Cr-1Mo 5 T HT-9 (#1) 3 T 9Cr-1Mo

+ See Table 7.7.3 for specific thermomechanical heat treatments used for HT-9 specimens. See Table 7.7.4 for specimen name abbreviations used in this table.

TABLE 7.7.8

SPECIMEN MATRIX FOR INSERTION INTO EBR-II SUBASSEMBLY X-359

Temperatures - 390°C (743°F) and 500°C (932°F)

	Level No.	Distance From Center of Level to Core Midplane (mm)	Specific Alloy Loading+
3 FI 8 T 1 TED	1	158	3 FI HT-9 (#4) 5 T HT-9 (#2) 3 T 2-1/4Cr-1Mo
4 FT 8 FT(W)	2	108	4 FT 9Cr-1Mo 7 FT(W) HT-9 1 FT(W/HAZ) HT-9
12 FT	3	56	10 FT HT-9 (#3) 2 FT 9Cr-1Mo
26 CG 1 TED	4	0.0	11 CG HT-9 (#1) 5 CG HT-9 (#2) 5 CG 9Cr-1Mo 5 CG 2-1/4Cr-1Mo
8 C 5 T 2 D	5	-54	2 C(W/HAZ) HT-9 6 C HT-9 (#3) 5 T HT-9 (#1) 2 D Disc Packets
4 C 4 C(W) 5 GF 2 D	6	-102	4 C 9Cr-1Mo 4 C(W) HT-9 5 GF HT-9 (#1) 2 D Disc Packets
3 FI 8 T 1 TED	7	-152	3 FI 9Cr-1Mo 5 T HT-9 (#1) 3 T 9Cr-1Mo

+See Table 7.7.3 for specific thermomechanical heat treatments used for HT-9 specimens. See Table 7.7.4 for specimen name abbreviations used in this table.

TABLE 7.7.9

SPECIMEN MATRIX FOR INSERTION INTO EBR-II SUBASSEMBLY X-359

Temperature - 450°C (842°F)

	Level No.	Distance from Center of Level to Core Midplane (mm)	Specific Alloy Loading+
	1	158	3 FI HT-9 (#4) 5 T HT-9 (#2) 3 T 2-1/4Cr-1Mo
12 FT(W)	2	108	6 FT(W) HT-9 6 FT(W/HAZ) HT-9
	3	56	6 FT HT-9 (#3) 6 FT 9Cr-1Mo
26 CG	4	0.0	11 CG HT-9 (#1) 5 CG HT-9 (#2) 5 CG 9Cr-1Mo 5 CG 2-1/4Cr-1Mo
	5	-54	8 C HT-9 (113) 5 T HT-9 (#1) 2 D Disc Packets
4 C(W)	6	-102	4 C 9Cr-1Mo 4 C(W) HT-9 5 GF HT-9 (#1) 2 GF 9Cr-1Mo 2 D Disc Packets
3 FI 1 TED	7	-152	3 FI 9Cr-1Mo 5 T HT-9 (#1) 3 T 9Cr-1Mo

+See Table 7.7.3 for specific thermomechanical heat treatments used for HT-9 specimens. See Table 7.7.4 for specimen name abbreviations used in this table.

2. B. A. Chin, E. R. Gilbert, M. M. Paxton and J. L. Straalsund, "A Comparison of the In-Reactor Creep Behavior of Selected Commercial Alloys at a Temperature of 593°C," presented at the 9th ASIM International Symposium on the Effects of Irradiation on Structural Materials, Richland, WA (July 1978).

3. Letter, D. K. Magnus (RRT) to C. S. Carlisle (HEDL), dated January 14, 1980.

4. D. A. Mervyn, D. T. Peterson and F. F. Huang, "Microstructural and Fatigue Crack Growth Characterization of HT-9," *ADIP Quarterly Progress Report, March 31, 1980.*

5. T. A. Lechtenberg, R. D. Stevenson, S. N. Rosenwasser, B. E. Thurgood and L. D. Thompson, "Procurement of National 12Cr Heat and Evaluation of Welding Procedures for Irradiation Specimens," *ADP Quarterly Progress Report, June 30, 1980.*

6. F. F. Huang and G. L. Wire, "Initial Test Results on Miniature Compact Tension Fracture Toughness Specimen," *ADIP Quarterly Progress Report, December 31, 1979.*

7. Annual Book of ASIM Standards, Part 10, "Standard Test Method for Plane-Strain Fracture Toughness of Metallic Materials," pp. 512-533.

8. J. M. Steichen and J. A. Williams, "Effects of Strain Rate and Temperature on Tensile Properties of Irradiated ASIM A533-B Steel," *J. Nucl. Mat., 57 (1975),* pp. 303.

7.8 CHARACTERIZATION OF FERRITIC STEELS FOR HFIR IRRADIATION — R. L. Klueh and J. M. Vitek (ORNL)

7.8.1 ADIP Task

ADIP Tasks are not defined for Path E ferritic steels in the 1978 program plan.

7.8.2 Objective

The goal of this project is to prepare ferritic steels for irradiation experiments that will produce both displacement damage and transmutation helium at levels relevant to fusion reactor service.

7.8.3 Summary

Small heats of ferritic (martensitic) steels based on 12% Cr–1% Mo and 9% Cr–1% Mo were prepared containing about 0, 1, and 2% Ni. Additional heats were made with 2% Ni, in which the content of the ferrite-forming elements was adjusted to restore the net chromium equivalent to a value near that of the unmodified alloy. During irradiation in the High Flux Isotope Reactor (HFIK), transmutation of the ^{58}Ni will give helium concentrations approximating those produced in such steels in fusion reactor service. Because the addition of nickel can affect the response to heat treatment, the microstructures of the alloys are being characterized.

After normalizing, the alloys without nickel and those containing 1 and 2% Ni (but with no chromium equivalent adjustments) had microstructures that were entirely martensite. The 2% Ni addition lowered the Ac_1 temperature, making it necessary to temper these alloys at temperatures no greater than 700°C. The normalized microstructure of the 2% Ni alloys with adjusted chromium equivalent contained large amounts of a phase in addition to the predominant martensite. Work is in progress to determine if this phase is δ-ferrite or retained austenite.

7.8.4 Progress and Status

7.8.4.1 Introduction

The irradiation-resistant properties of ferritic (martensitic) steels, such as those based on 12% Cr-1% Mo and 9% Cr-1% Mo, have led to these alloys being considered for use as fusion reactor blanket structural components. Since an adequate source of deuterium-tritium fusion neutrons is not available, an alternative method for simulating 14-MeV (2.2-pJ) neutron irradiation must be used. For austenitic stainless steels, sufficient nickel is present in the alloy that irradiation in some mixed spectrum fission reactors produces the required helium by thermal neutron captures. However, the commercial steels based on 12 Cr-1 Mo and 9 Cr-1 Mo generally contain less than 0.5% Ni, which is not adequate for this helium simulation. If these alloys contained approximately 2% Ni, they could be irradiated in the HFIR to obtain approximately the same helium production rate as the original alloys would develop during fusion reactor service for a neutronic wall loading near 3 MW/m^2. The rate of displacement damage production under these conditions is also appropriate for this wall loading.

Seven electroslag-remelted heats of ferritic steel with varying nickel contents were prepared by Combustion Engineering (CE):[1] four heats were based on 12 Cr-1 Mo and three on 9 Cr-1 Mo (the base alloys also contain strong carbide formers). Because nickel can affect the microstructure and strength of a martensitic steel, we began a series of heat treatment studies to determine the proper heat treating procedures to use for these materials.

7.8.4.2 Results

The compositions of the 12 Cr-1 Mo alloys prepared for the present studies were based on the commercial Sandvik alloy designated HT9. This alloy with about 0.2% C also contains the carbide-forming elements vanadium (~0.3%) and tungsten (~0.5%). It contains nominally 0.5% Ni. In addition to preparing this basic HT9 alloy, alloys were prepared with the basic HT9 composition but with 1 and 2% Ni additions. Finally, an

HT9-type alloy with 2% Ni was prepared in which the ferrite-forming element concentrations were increased to increase the net chromium equivalent to a value similar to that of the unmodified HT9 alloy.[1] The net chromium equivalent was calculated by the following equation:[2]

$$\text{Net Cr Equiv} = \%\,\text{Cr} + 6(\%\,\text{Si}) + 4(\%\,\text{Mo}) + 1.5(\%\,\text{W}) + 11(\%\,\text{V}) + 5(\%\,\text{Nb}) - 40(\%\,\text{C}) - 2(\%\,\text{Mn}) - 4(\%\,\text{Ni}) - 2(\%\,\text{Co}) - 30(\%\,\text{N}) \quad (1)$$

This is essentially the difference between the chromium equivalent (positive terms) and nickel equivalent (negative terms) for the alloy. To adjust the net chromium equivalent to account for the nickel additions, the ferrite-forming elements Cr, Mo, and W were added in amounts to keep within the HT9 composition range specified for these elements. For ease of discussion, these alloys will hereafter be referred to as 12 Cr-1 Mo, 12 Cr-1 Mo-1 Ni, 12 Cr-1 Mo–2 Ni, and 12 Cr-1 Mo-2 Ni (adjusted). The actual chemical compositions were presented previously. Table 7.8.1 gives the chemical compositions for elements important to this discussion.

Table 7.8.1. Chemical Composition of Major Elements in 12 Cr-1 Mo and 9 Cr-1 Mo Steels

Alloy	Heat	Content, wt %							
		Cr	Mo	Ni	V	Nb	W	C	N
12 Cr-1 Mo	XAA–3587	11.99	0.93	0.43	0.27	0.018	0.54	0.21	0.020
12 Cr-1 Mo-1 Ni	XAA–3588	11.97	1.04	1.14	0.31	0.015	0.53	0.20	0.016
12 Cr-1 Mo–2 Ni	XAA–3589	11.71	1.02	2.27	0.31	0.015	0.54	0.20	0.017
12 Cr-1 Mo–2 Ni (Adjusted)	XAA–3592	13.60	1.59	2.30	0.30	0.016	0.64	0.15	0.014
9 Cr-1 Mo	XAA–3590	8.62	0.98	0.11	0.21	0.063	0.01	0.09	0.050
9 Cr-1 Mo–2 Ni	XAA–3591	8.57	0.98	2.17	0.22	0.066	0.01	0.064	0.053
9 Cr-1 Ma–2 Ni (Adjusted)	XAA–3593	12.30	1.70	2.24	0.29	0.074	0.01	0.067	0.059

The commercial 9 Cr-1 Mo steel with about 0.1% C (without carbide formers) has been modified by CE and ORNL[3] by the addition of the carbide-forming elements V (~0.2%), Nb (~0.1%), and N (~0.06%; HT9 contains ~0.02% N). This alloy contains nominally 0.2% Ni. A basic modified 9 Cr-1 Mo alloy was prepared along with an alloy that contained 2% Ni. Another alloy with 2% Ni was adjusted by Cr and Mo additions to get a net chromium equivalent similar to that for the modified 9 Cr-1 Mo steel without a Ni addition. The result was a steel with about 12.3% Cr and 1.7% Mo; all remaining elements were present in amounts similar to those in the basic modified 9 Cr-1 Mo alloy. For the present discussion we will refer to these three alloys as 9 Cr-1 Mo, 9 Cr-1 Mo-2 Ni, and 9 Cr-1 Mo-2 Ni (adjusted). The chemical compositions of the elements that are important for the present discussion are also given in Table 7.8.1.

These steels are to be used in the normalized-and-tempered condition. In normal steelmaking practice, normalizing consists of heating the steel above the Ac_3 temperature to transform the steel to austenite (austenization) and then air cooling. For the present study, where 0.254- and 0.762-mm sheet are being used, we austenitized in a tube furnace containing dynamic helium, after which the specimens were pulled into the cold zone and cooled in the flowing helium. The four 12 Cr-1 Mo alloys and the 9 Cr-1 Mo alloys were austenitized for 0.5 h at 1050 and 1040°C, respectively. The tempering treatments were carried out in the same helium-atmosphere furnace by using the same cooling procedure.

After normalizing, the microstructures of the 12 Cr-1 Mo (Fig. 7.8.1) and the 9 Cr-1 Mo (Fig. 7.8.2) were entirely martensite. Similarly, all-martensitic structures were observed for the normalized 12 Cr-1 Mo-1 Ni, 12 Cr-1 Mo-2 Ni, and 9 Cr-1 Mo-2 Ni alloys. When the 12 Cr-1 Mo-2 Ni (adjusted) and the 9 Cr-1 Mo-2 Ni (adjusted) alloys were normalized, the microstructures contained two constituents. The major constituent was again martensite. The 12 Cr-1 Mo-2 Ni (adjusted) alloy (Fig. 7.8.3) contained more of the second constituent than the 9 Cr-1 Mo-2 Ni (adjusted) alloy (Fig. 7.8.4).

A series of specimens from each of the alloys was normalized and then tempered for 1 h at 650, 700, 730, 760, and 780°C; specimens were also tempered 2.5 h at 650 and 780°C.

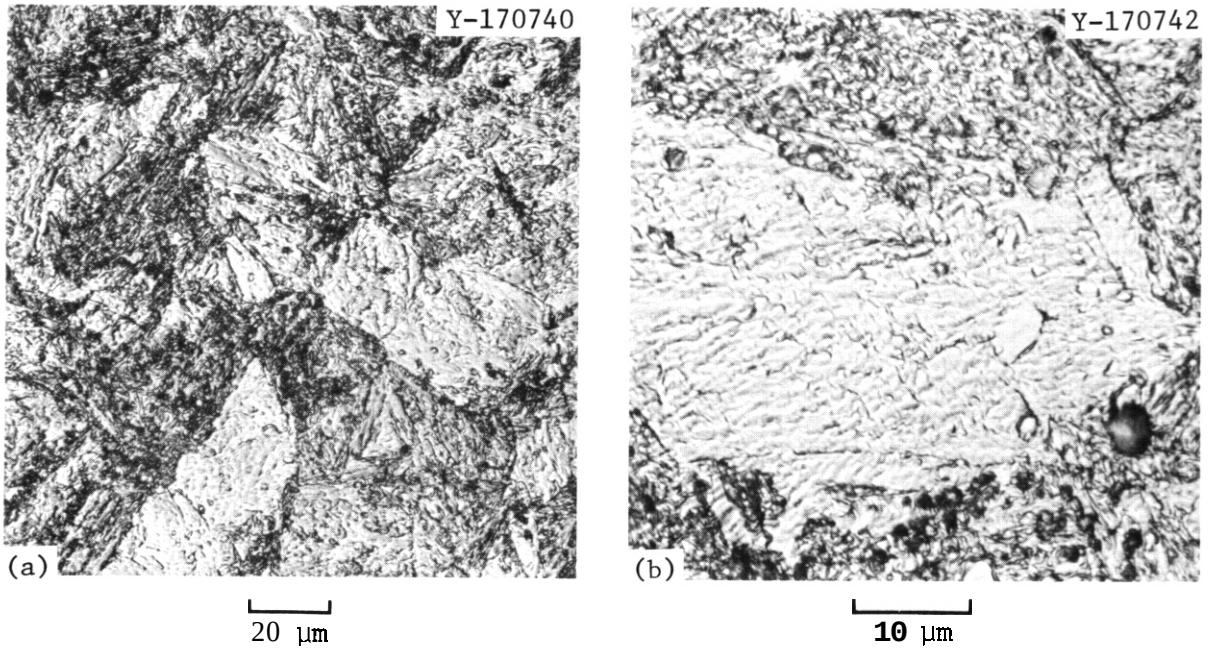

Fig. 7.8.1. Microstructure of Normalized 12 Cr-1 Mo Steel.

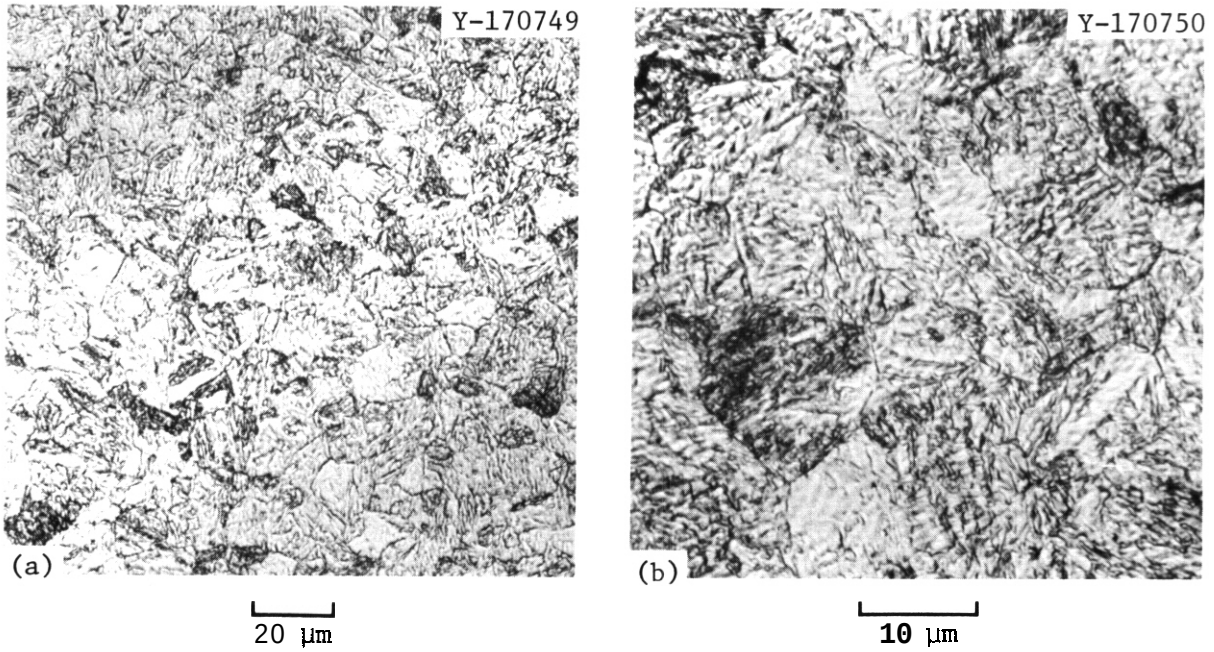

Fig. 7.8.2. Microstructure of Normalized 9 Cr-1 Mo Steel.

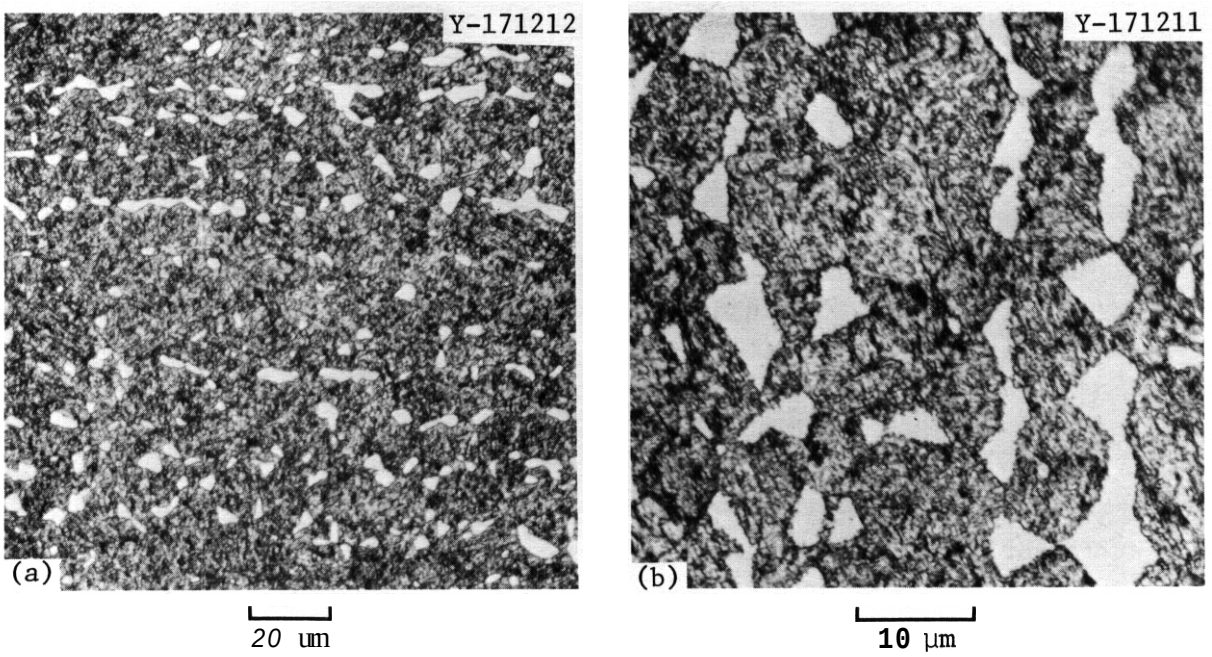

Fig. 7.8.3. Microstructure of Normalized 12 Cr-1 Mo-2 Ni (Adjusted) Steel.

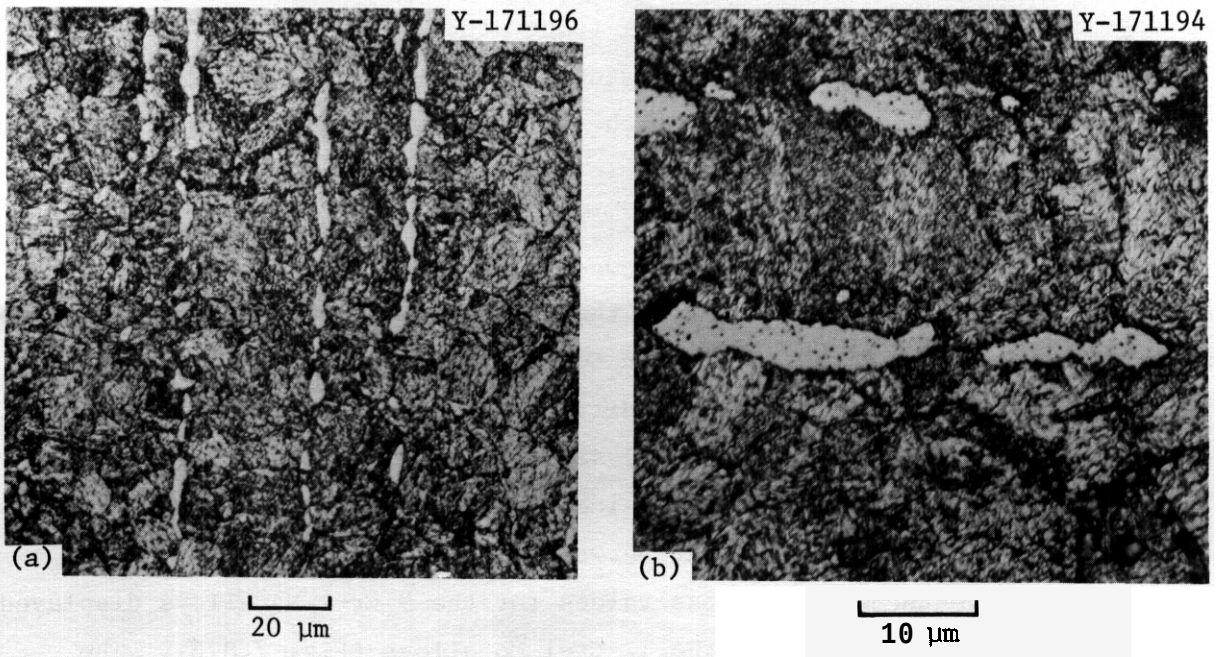

Fig. 7.8.4. Microstructure of Normalized 9 Cr-1 Mo-2 Ni (Adjusted) Steel.

Metallographic examination showed no major changes resulting from the tempering treatments. At high magnification, there were indications of fine precipitate particles in the martensite that did not appear to be present in the untempered condition. However, these alloys have proved difficult to etch, and a detailed description of precipitate particle changes will require electron microscopy studies. The second constituent in the 12 Cr-1 Mo-2 Ni (adjusted) and 9 Cr-1 Mo-2 Ni (adjusted) alloys also showed little change as a result of tempering.

Hardness and microhardness measurements were made on the normalized and tempered alloys (Tables 7.8.2 and 7.8.3). Rockwell F hardness measurements (1.6-mm ball indenter under a 60-kg load) were made on the surface of the 0.76-mm sheet, and diamond pyramid microhardness (1000-g load, 20× objective) values (DPH) were determined on the polished cross section of the 0.76-mm-sheet specimens mounted for metallographic study. In general, the hardness trends determined by the two methods agreed qualitatively (Figs. 7.8.5 and 7.8.6).

The hardnesses of the 12 Cr-1 Mo and 12 Cr-1 Mo-1 Ni showed a general decrease with increasing tempering temperature (Fig. 7.8.5). Although the hardness values of these two steels differ at temperatures between 650 and 780°C, the hardnesses of the two alloys differ little after 1 h at 780°C. A slight further decrease in hardness occurred when these alloys were tempered for 2.5 h at 780°C (Table 7.8.2).

The 12 Cr-1 Mo-2 Ni alloy showed a decrease in hardness when tempered 1 h at 650 and 700°C, after which the hardness went through a minimum and began to increase with increase in tempering temperature. The hardness of the alloy essentially did not differ when tempered 1 or 2.5 h at 780°C. For the 12 Cr-1 Mo-2 Ni (adjusted) alloy, the hardnesis decreased between 650 and 700°C, after which it remained fairly constant (the microhardness values remained fairly constant between 650 and 780°C).

Hardness and microhardness values for the 9 Cr-1 Mo alloys displayed trends similar to those for the 12 Cr-1 Mo alloys (Fig. 7.8.6). The hardness of the 9 Cr-1 Mo decreased continuously between 650 and 780°C. The rate of decrease was larger than for 12 Cr-1 Mo, thus giving a final hardness for the 9 Cr-1 Mo after 1 h at 780°C considerably less than that

Table 7.8.2. Hardnesses of 12 Cr-1 Mo Steels After Normalizing-and-Tempering Treatments

Normalizing[a]-and-Tempering Treatment	Hardness, Rockwell F (DPH)			
	12 Cr-1 Mo	12 Cr-1 Mo-1 Ni	12 Cr-2 Mo-2 Ni	12 Cr-1 Mo-2 Ni (Adjusted)
N	25.5 (545)	25.4 (511)	25.3 (568)	24.1 (494)
N + 1 h 650°C	19.1 (309)	18.0 (313)	18.6 (313)	18.3 (295)
N + 2.5 h 650°C	17.9 (307)	18.5 (300)	17.4 (303)	18.6 (293)
N + 1 h 700°C	15.9 (304)	15.6 (301)	16.0 (300)	16.0 (300)
N + 1 h 730°C	16.2 (276)	13.7 (268)	16.4 (293)	15.7 (300)
N + 1 h 760°C	14.8 (263)	12.8 (266)	17.0 (317)	14.9 (302)
N + 1 h 780°C	10.7 (249)	11.8 (254)	18.2 (330)	15.5 (302)
N + 2.5 h 780°C	10.3 (225)	11.3 (254)	17.7 (333)	15.3 (302)

[a]Normalizing (N) treatment was 0.5 h at 1050°C followed by rapid cooling.

Table 7.8.3. Hardnesses of 9 Cr-1 Mo Steels After Normalizingand-Tempering Treatments

Normalizing[a]-and-Tempering Treatment	Hardness, Rockwell F (DPH)		
	9 Cr-1 Mo	9 Cr-1 Mo-2 Ni	9 Cr-1 Mo-2 Ni (Adjusted)
N	22.4 (388)	22.7 (384)	23.5 (412)
N + 1 h 650°C	18.6 (313)	19.1 (315)	19.6 (326)
N + 2.5 h 650°C	18.1 (295)	18.8 (305)	19.0 (313)
N + 1 h 700°C	14.2 (286)	14.9 (300)	16.9 (315)
N + 1 h 730°C	12.0 (257)	15.0 (290)	16.0 (308)
N + 1 h 760°C	8.8 (222)	16.2 (317)	16.3 (305)
N + 1 h 780°C	6.6 (197)	18.4 (351)	16.0 (308)
N + 2.5 h 780°C	5.4 (196)	18.7 (358)	16.2 (310)

[a]Normalizing (N) treatment was 0.5 h at 1040°C followed by rapid cooling.

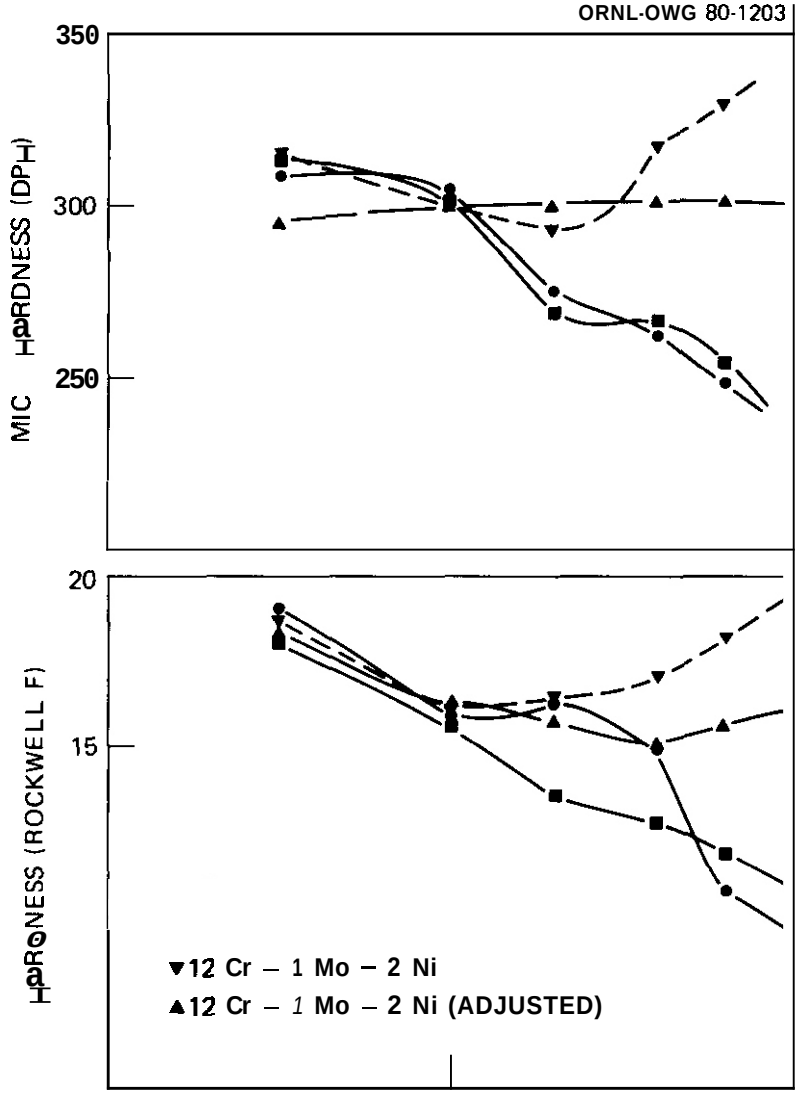

Fig. 7.8.5. **Microhardness (DPH) and Hardness (Rockwell F) of 12 Cr–1 Mo Steels (0.76–mm Sheet) Normalized and Then Tempered 1 h at Temperatures in the Range 650 to 780°C.**

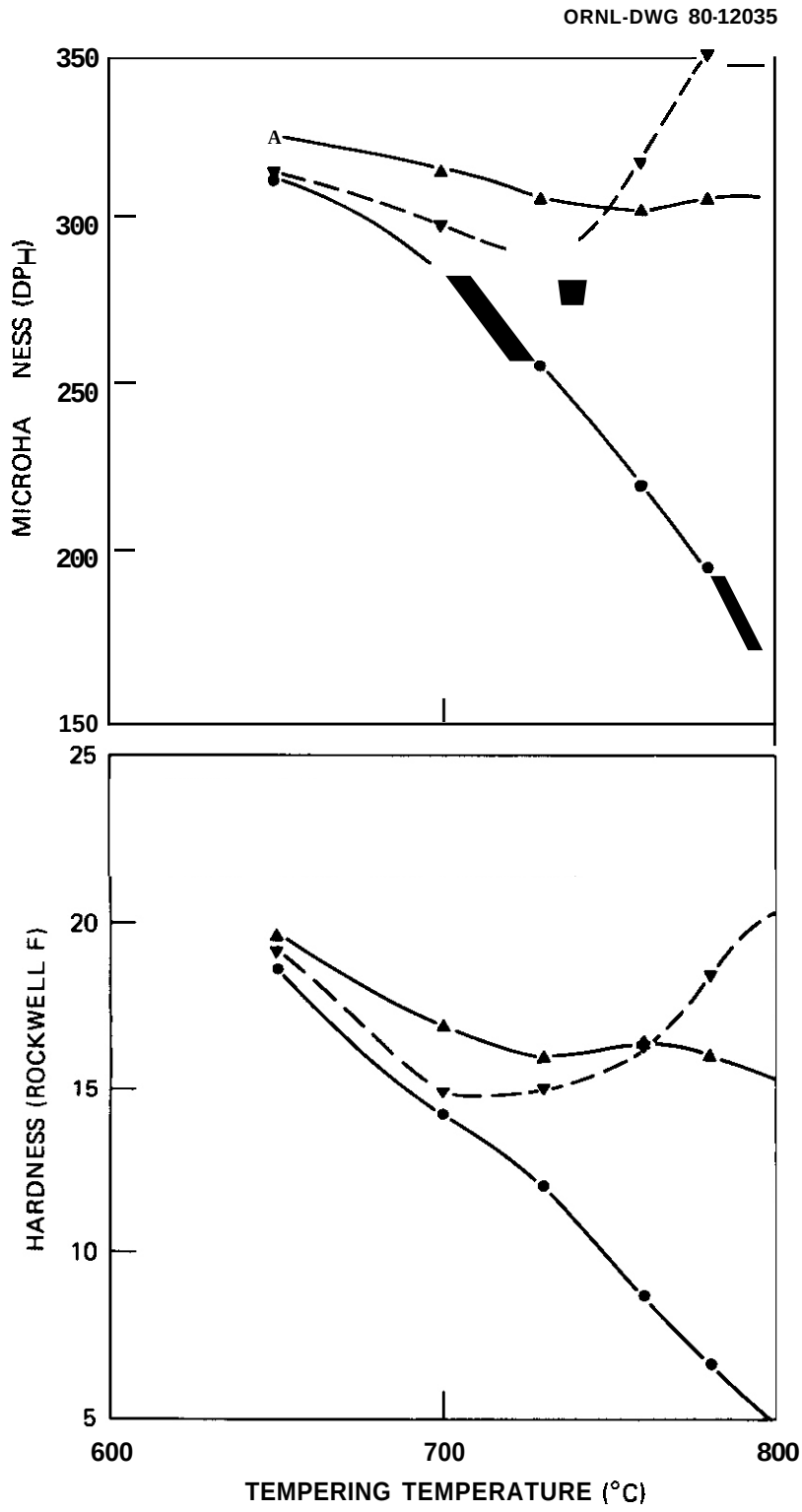

Fig. 7.8.6. Microhardness (DPH) and Hardness (Rockwell F) of 9 Cr-1 Mo Steels (0.76-mm Sheet) Normalized and Then Tempered 1 h at Temperatures in the Range 650 to 780°C.

for the 12 Cr-1 Mo. The 9 Cr-1 Mo-2 Ni and 9 Cr-1 Mo-2 Ni (adjusted) alloys displayed hardness trends similar to those of the 12 Cr-1 Mo-2 Ni and 12 Cr-1 Mo-2 Ni (adjusted) alloys, respectively. In fact, when the hardness curves for the respective alloys are superimposed, the absolute hardness values differ very little.

The changes in hardness for the 12 Cr-1 Mo, 12 Cr-1 Mo-1 Ni, and 9 Cr-1 Mo steels are easily understood. In the normalized condition, the microstructures are entirely martensite. When tempered, carbide particles precipitate from the supersaturated solution of carbon that gives untempered martensite its high hardness. The higher the tempering temperature, the more rapidly this precipitation process occurs. For alloy steels, the precipitation sequence is often quite complicated and will not be discussed for any of these alloys until after the electron microscopy studies are complete. For the present discussion suffice it to say that the continuous decrease in hardness for the three alloys in question results from the carbide precipitation.

Nickel can affect a ferritic steel containing 9 to 12% Cr in two ways.[4] First, it can lead to a lowering of the Ac_1 temperature. If the steel is subsequently tempered above the Ac_1 temperature, part of the steel is reaustenitized. On cooling, martensite forms, and the resulting microstructure will contain tempered and untempered martensite. The second effect of a Ni addition, as well as additions of Cr, Mo, and W, is the lowering of the martensite start (M_s) and finish (M_f) temperatures. If the M_f is below room temperature, the normalized microstructure will contain retained austenite. When a steel with retained austenite is tempered, carbon precipitates, which in turn increases the M_s and M_f. The austenite can subsequently transform to martensite when the steel is cooled from the tempering temperature.

The effect of tempering temperature on the hardness of the 12 Cr-1 Mo-2 Ni and 9 Cr-1 Mo-2 Ni can be explained by the lowering of the Ac_1 temperature. Judging from Figs. 7.8.5 and 7.8.6, we would estimate that the Ac_1 for these alloys is somewhere above 700°C. When these alloys are tempered above this temperature, austenite forms, which then transforms to martensite on cooling. Although it is not possible to

discern the untempered martensite metallographically, the microstructures of these alloys must contain both tempered and untempered martensite. As the tempering temperature is raised, the amount of untempered martensite increases. The increase in hardness with increased tempering temperature indicates that the hardness increase results from the formation of untempered martensite. This increase must exceed the hardness decrease accompanying the tempering of the martensite that does not transform to austenite during tempering.

If the Ac_1 temperature is above about 700°C, then we should be able to temper at 700°C. This happened when the 12 Cr-1 Mo-2 Ni and 9 Cr-1 Mo-2 Ni steels were tempered for up to 10 h at 700°C (Fig. 7.8.7). The decrease in hardness of the 9 Cr-1 Mo-2 Ni steel was slightly greater than that for 12 Cr-1 Mo-2 Ni steel. This relative difference is comparable with the tempering behavior of 12 Cr-1 Mo and 9 Cr-1 Mo (Figs. 7.8.5 and 7.8.6). The decrease in hardness with tempering at 700°C agrees with our conclusion that Ac_1 is at least 700°C.

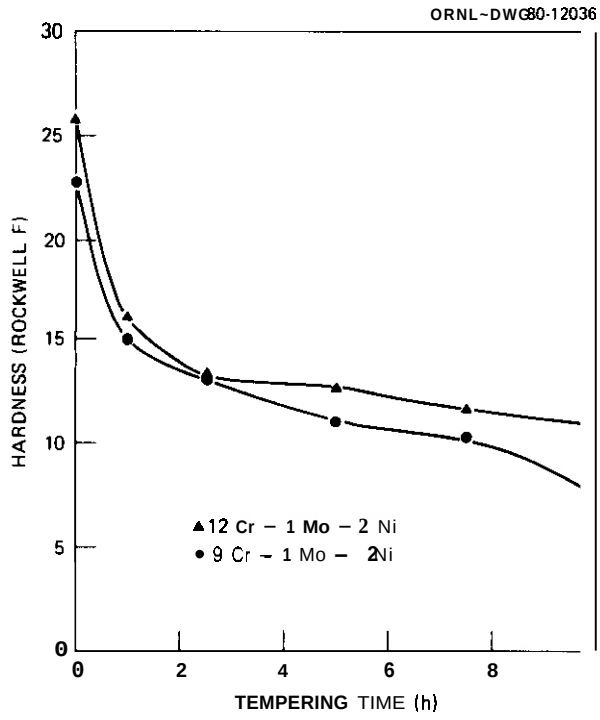

Fig. 7.8.7. Change in Rockwell F Hardness for 12 Cr-1 Mo-2 Ni and 9 Cr-1 Mo-2 Ni Alloys with Tempering Time at 700°C.

Without further study we are not presently able to adequately explain the observations on the 12 Cr-1 Mo-2 Ni (adjusted) and 9 Cr-1 Mo-2 Ni (adjusted) steels. When these alloys were tempered for up to 10 h at 700°C, the hardness decreased with most of the decrease occurring in the first 2.5 h (Fig. 7.8.8). Essentially, neither the hardness nor hardness changes of the 12 Cr-1 Mo-2 Ni (adjusted) and the 9 Cr-1 Mo-2 Ni (adjusted) steels differed. This is not unexpected, since the chemical compositions of the two alloys differ little (Table 7.8.1); most of the chromium equivalent adjustment for the 9 Cr-1 Mo-2 Ni (adjusted) alloy was made by adding chromium.

We can attempt to understand these alloys by examining the effect of ferrite-forming elements (Cr, Mo, Si, V, Al, Nb, Ti, and W) and austenite-forming elements (Ni, Co, Mn, Cu, N, and C) on microstructure. Figure 7.8.9 shows the Schaeffler diagram as modified by Schneider[4] where the chromium equivalent is plotted against the nickel equivalent. This diagram gives the microstructure expected when the alloy is quite rapidly cooled from the austenitizing temperature. The equations used to calculate the chromium and nickel equivalents are:

$$\text{Chromium Equivalent} = (\%\ \text{Cr}) + 2(\%\ \text{Si}) + 1.5(\%\ \text{Mo}) + 5(\%\ \text{V}) + 5.5(\%\ \text{Al}) + 1.75(\%\ \text{Nb}) + 1.5(\%\ \text{Ti}) + 0.75(\%\ \text{W}) \quad (2)$$

$$\text{Nickel Equivalent} = (\%\ \text{Ni}) + (\%\ \text{Co}) + 0.5(\%\ \text{Mn}) + 0.3(\%\ \text{Cu}) + 25(\%\ \text{N}) + 30(\%\ \text{C}) \quad (3)$$

By using Eqs. (2) and (3) we calculated the 12 Cr-1 Mo-2 Ni (adjusted) alloy chromium and nickel equivalents to be approximately 18.2 and 7.3, respectively. For the 9 Cr-1 Ma-2 Ni (adjusted) alloy, the values are approximately 16.7 and 5.9, respectively. According to Fig. 7.8.9 this would place both alloys in the austenite plus martensite plus δ-ferrite

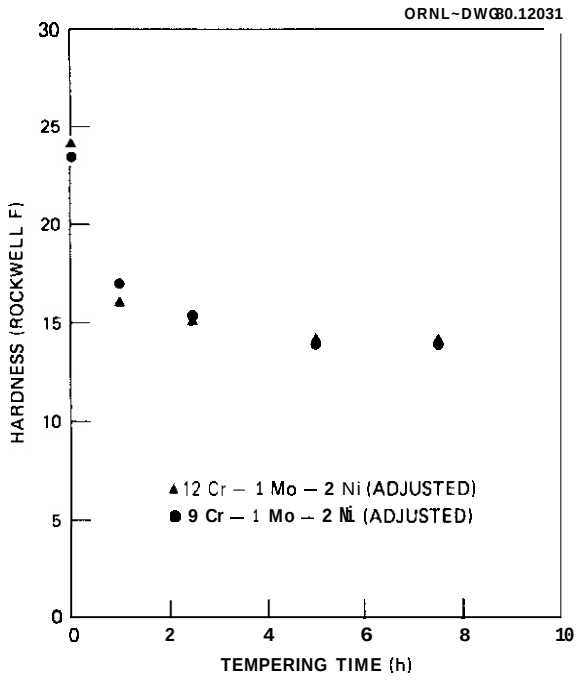

Fig. 7.8.8. Change in Rockwell F Hardness for 12 Cr–1 Mo-2 Ni (Adjusted) and 9 Cr–1 Mo–2 Ni (Adjusted) Alloys **with Tempering Time at 700°C.**

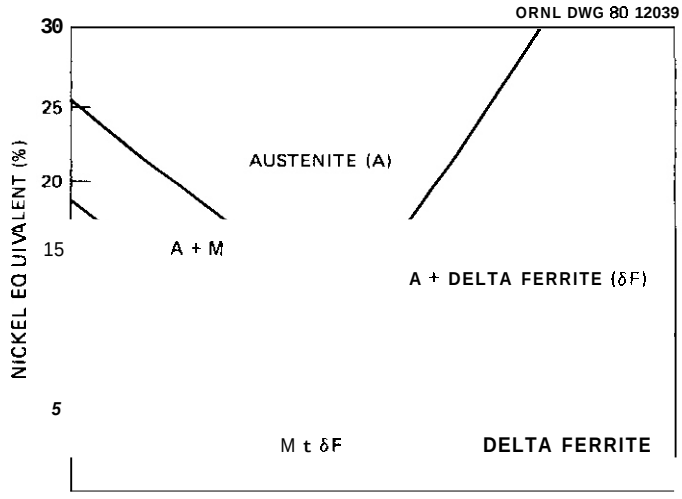

Fig. 7.8.9. Schaeffler Diagram as Modified by Schneider, Showing Expected Phases for Chromium-Equivalent and Nickel-Equivalent Compositions. Source: H. Schneider, "Investment Casting of High-Hot-Strength 12-Percent Chrome Steel," *Foundry* ***Trade J.*** **108: 562–63 (1960).**

region. The δ-ferrite would be present because the steel was heated into the two-phase $\delta + \gamma$ region during austenization treatment. The retained austenite would be caused by an M_f below room temperature.

It should be noted that a diagram such as Fig. 7.8.9 is qualitative at best. Several different equations for chromium and nickel equivalents have been derived. Indeed, the net chromium equivalent given by Eq. (1) differs from Eqs. (2) and (3). In our microstructural studies on the two nickel (adjusted) alloys, we were only able to distinguish two constituents, one of which was martensite. Thus, if both δ-ferrite and retained austenite are present, one must be present in very small amounts. We are presently conducting further heat treatment experiments along with electron microscopy studies to determine the nature of the second phase in these alloys.

7.8.5 References

1. M. L. Grossbeck et al., "Preparation of Nickel-Doped Ferritic Alloys for HFIK Irradiation to Produce Helium," *ADIP Quart. Prog. Rep. Dec. 31*, 2979, DOE/ER-0045/1, pp. 100–04.
2. C. J. Boyle and D. L. Newhouse, "A New Stainless Steel for Turbine Rotors," *Met. Prog.* 87(3): 61-62 (March 1965).
3. G. C. Bodine et al., "The Development of a 9 Cr Steel With Improved Strength and Toughness," pp. 151–54 in *Ferritic Steels for Fast Reactor Service, Proc. Int. Conf.*, Vol. 1, British Nuclear Energy Society, London, 1978.
4. H. Schneider, "Investment Casting of High-Hot-Strength 12-Percent Chrome Steel," *Foundry Trade J.* 108: 562–63 (1960).

8. STATUS OF IRRADIATION EXPERIMENTS AND MATERIALS INVENTORY

8.1 IRRADIATION EXPERIMENT STATUS AND SCHEUULE

The following bar charts show the schedule for all **ADIP** reactor irradiation experiments. Experiments are presently under way in the Oak Ridge Research Reactor (ORR) and the High Flux Isotope Reactor (HFIR), which are mixed spectrum reactors, and in the Experimental Breeder Reactor (EBR-II), which is a fast reactor.

During the reporting period irradiation was begun for two irradiation experiments: ORR-MFE-4A in the ORR and HFIK-CTK-33 in the HFIK.

The ORR spectral tailoring experiment, ORR-MFE-4A, operates at 300 and 400°C and will achieve the fusion reactor He/dpa ratio in austenitic stainless steels. It will serve as a major irradiation vehicle for the ADIP program over the next five years. It provides for specimen discharge and reencapsulation. The second capsule, ORR-MFE-4B, will operate at 500 and 600°C. It will begin irradiation in early FY 1981.

The HFIK-CTK-33 experiment includes specimens for the evaluation of tensile, swelling, and microstructural properties in ferritic alloys irradiated at 50°C, a temperature relevant to Engineering Test Facility (ETF) operation.

An EBR-II experiment, *AD-2*, was constructed for insertion in August 1980. It was designed to supplement the EBR-II irradiation data generated by the Fast Breeder Reactor (FBR) program with fracture toughness, fatigue, and crack growth data on ferritic alloys.

Experiment Designation	Major Objective
A. Oak Ridge Research Reactor	
ORR-MFE-1 / ORR-MFE-2	Experiments to scope the effects of composition and microstructure on the tensile, fatigue, and irradiation creep of representative path A, B, and C alloys.
ORR-MFE-3	Effects of irradiation on postirradiation fatigue crack growth in representative path A, B, and C alloys.
ORR-MFE-4 [2]	Effect of irradiation on tensile, fatigue, and irradiation creep of path A PCA (Prime Candidate Alloy) and path B base research alloys. Spectral tailoring to maintain correct He/dpa ratio. Irradiation on continuing basis.

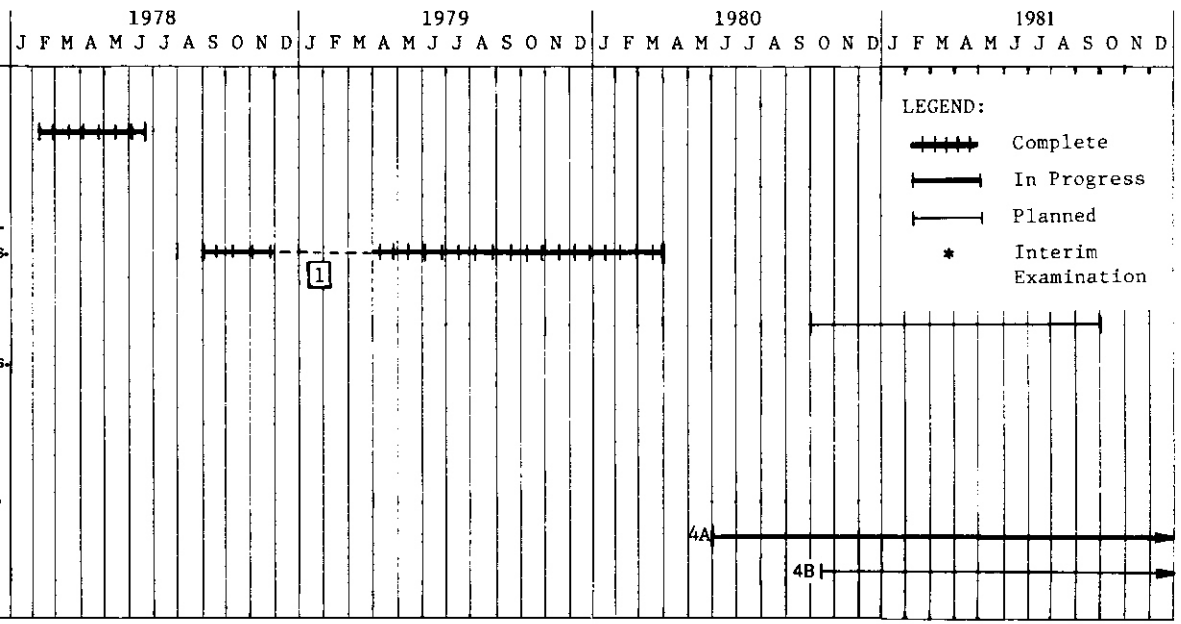

[1] MFE-2 out of reactor for repair of a small leak.

[2] MFE-4A will operate at 300 and 400 C; MFE 4B will operate at 500 and 600 C.

Experiment Designation	Major Objective	1980 J F M A M J J A S O N D	1981 J F M A M J J A S O N D	1982 J F M A M J J A S O N D	1983 J F M A M J J A S O N D
ORR-MFE-5	In-reactor fatigue c ≡ ⊳ growth experiment	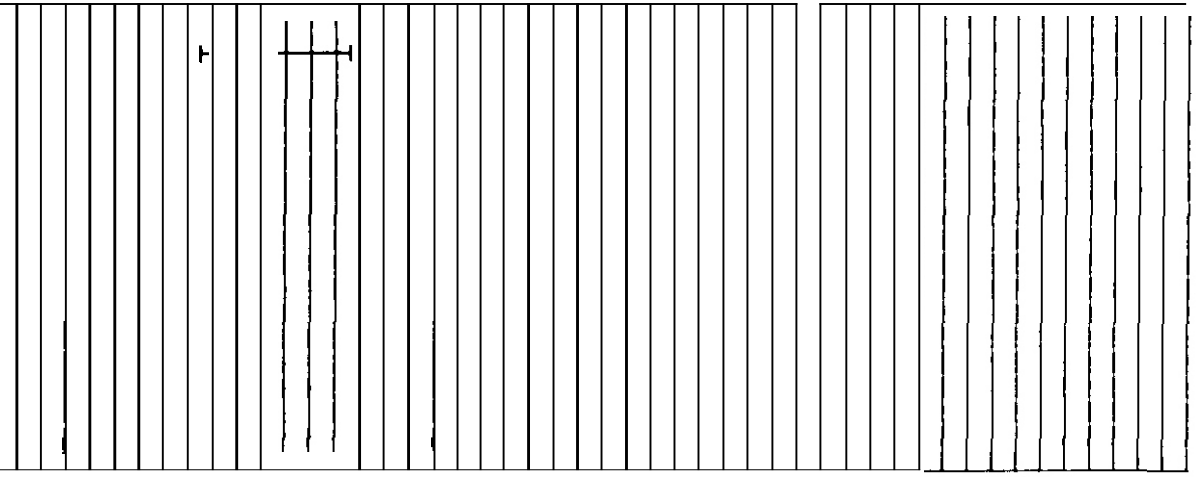			

Experiment Designation	Major Objective	1977 J F M A M J J A S O N D	1978 J F M A M J J A S O N D	1979 J F M A M J J A S O N D	1980 J F M A M J J A S O N D
B. Experimental Breeder Reactor II					
Subassembly X 264	Effect of preinjected helium (2–200 at. ppm) on microstructure and tensile properties of 316 SS, PE-16, V and Nb alloys. Fluence $\leq 2.3 \times 10^{26}$ n/m^2, 500–825°C.				
Subassembly X 287	Effect of preinjected helium (2–200 at. ppm He) on microstructure and tensile properties of 316 SS, PE-16, V and Nb alloys. Fluence $\leq 4 \times 10^{26}$ n/m^2, 400–700°C.				
Subassembly X 217D	Stress relaxation, Ti Alloys				
See footnotes [1] [2] and [3]	Effect of irradiation on swelling, tensile, fatigue, and crack growth properties of Ti scoping alloys. 370, 450, and 550°C, fluence 4.5–5.5 × 10^{26} n/m^2.		[1] [2]		

[1] EBR-II, row 2, pins B285 and B286.

[2] Subassembly removed for EBR-II run 99.

[3] Pin B284, row 2 for runs 96–98; row 4 for runs 100–102.

Experiment Designation	Major Objective
Experiment plan depends on alloy availability. EBR-II space not yet identified.	Effect of irradiation on swelling, tensile, fatigue, and crack growth properties of V and Nb scoping alloys. 370, 450, 550, and 650°C. Position in reactor not finalized, therefore no fluence estimate. [1]
AD-2 (6 pins in separate subassemblies of row 4)	To supplement present EBR-II data on ferritic alloys with data on crack growth, fatigue, and fatigue toughness. Temperature 390, 450, 500, and 550°C. 19 and 38 dpa.

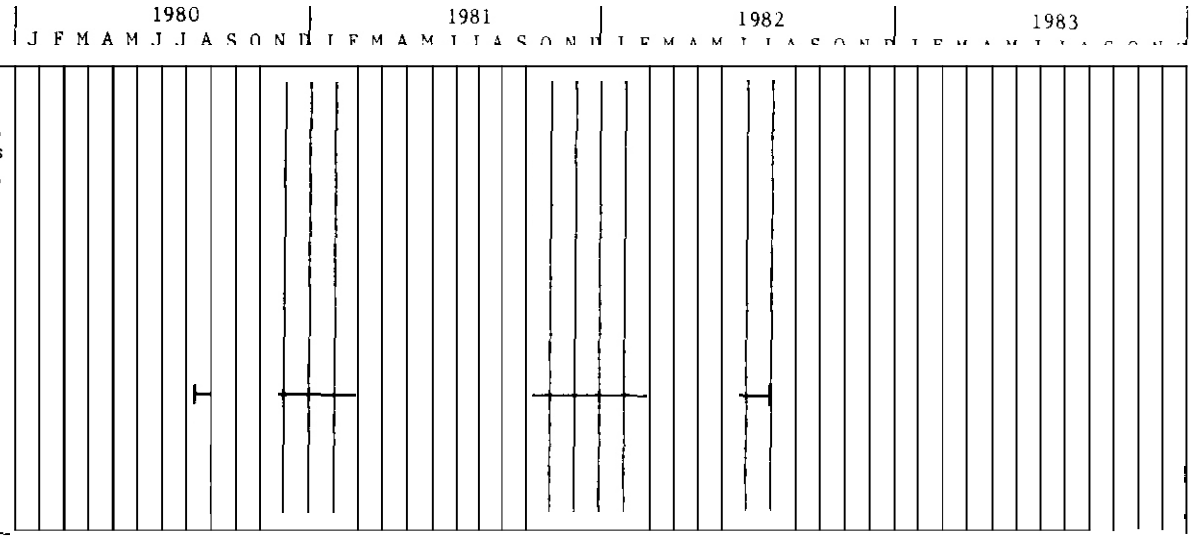

[1] Delayed for undetermined period.

Experiment Designation	Major Objective	1977 J F M A M J J A S O N D	1978 J F M A M J J A S O N D	1979 J F M A M J J A S O N D	1980 J F M A M J J A S O N D
C. High Flux Isotope Reactor (HFIR)					
HFIR-CTR-4	PE-16 for swelling and tensile properties, 300–700°C 2.2–4.5 dpa, 100–350 at. ppm He				
HFIR-CTR-7	PE-16 for swelling and tensile properties, 300–700°C 9–18 dpa, 1250–3000 at. ppm He				
HFIR-CTR-8	duplicate of –7				
HFIR-CTR-9	316 and 316 + Ti for swelling and tensile properties, 280–680°C, 9–18 dpa, 400–1000 at. ppm He				

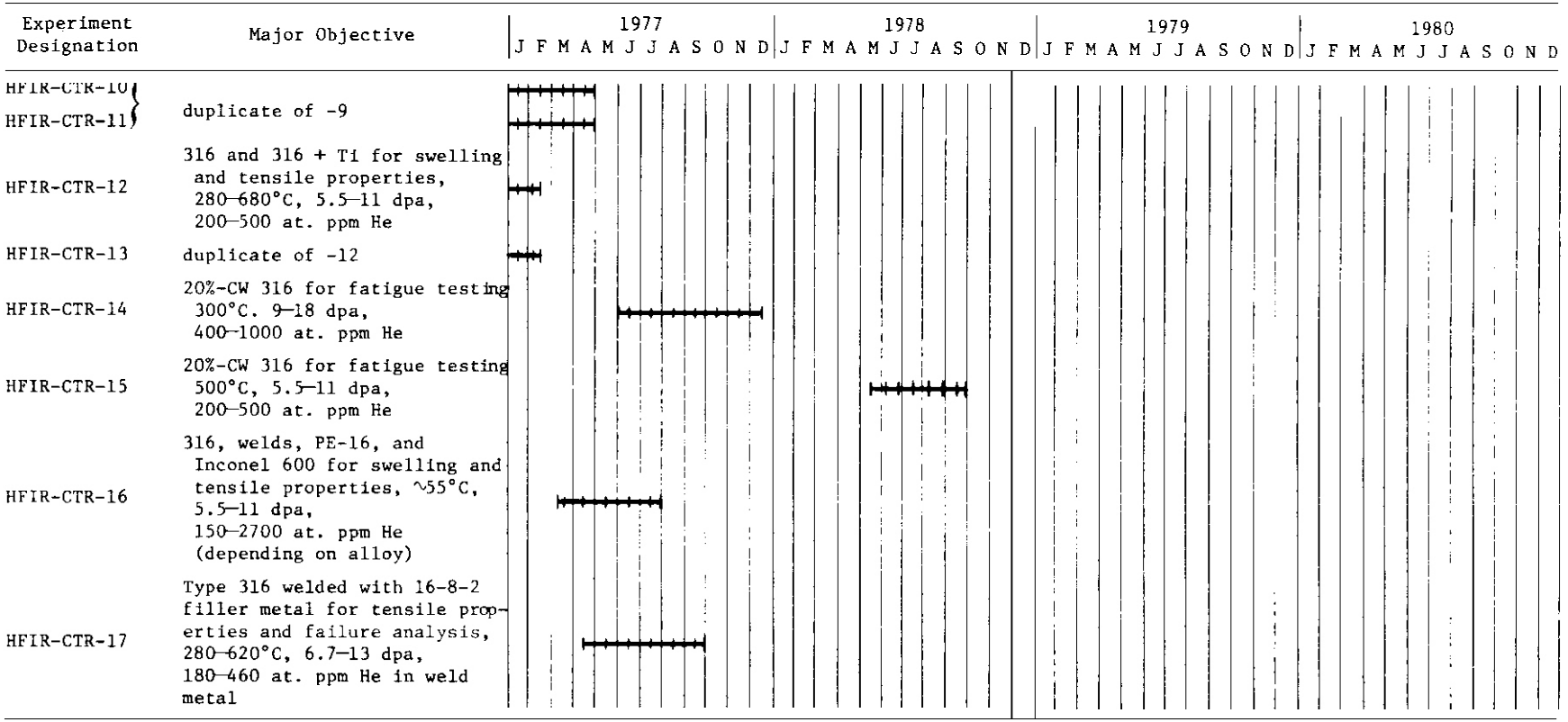
Experiment Designation
Major Objective
1977
1978
1979
1980
J F M A M J J A S O N D
HFIR-CTR-10
HFIR-CTR-11
duplicate of -9
HFIR-CTR-12
316 and 316 + Ti for swelling and tensile properties, 280–680°C, 5.5–11 dpa, 200–500 at. ppm He
HFIR-CTR-13
duplicate of -12
HFIR-CTR-14
20%-CW 316 for fatigue testing 300°C. 9–18 dpa, 400–1000 at. ppm He
HFIR-CTR-15
20%-CW 316 for fatigue testing 500°C, 5.5–11 dpa, 200–500 at. ppm He
HFIR-CTR-16
316, welds, PE-16, and Inconel 600 for swelling and tensile properties, ~55°C, 5.5–11 dpa, 150–2700 at. ppm He (depending on alloy)
HFIR-CTR-17
Type 316 welded with 16-8-2 filler metal for tensile properties and failure analysis, 280–620°C, 6.7–13 dpa, 180–460 at. ppm He in weld metal

Experiment Designation	Major Objective
HFIR-CTR-18	PE-16 and 20%-CW type 316 for swelling and tensile properties, 280–700°C, PE-16: 17–27 dpa, 3400–5600 at. ppm He 316: 27–34 dpa, 1600–2100 at. ppm He
HFIR-CTR-19	316 welded with 316 filler metal for tensile properties, 280–620°C, 5.5–11 dpa, 200–500 at. ppm He
HFIR-CTR-20	20%-CW 316 for fatigue testing, 300°C, 5.5–11 dpa, 200–500 at. ppm He
HFIR-CTR-21	20%-CW 316 for fatigue testing, 500°C, 9–18 dpa, 400–1000 at. ppm He
HFIR-CTR-22	duplicate of -20
HFIR-CTR-23	PE-16 for fatigue testing, 300°C, 4.4–9 dpa, 370–1000 at. ppm He

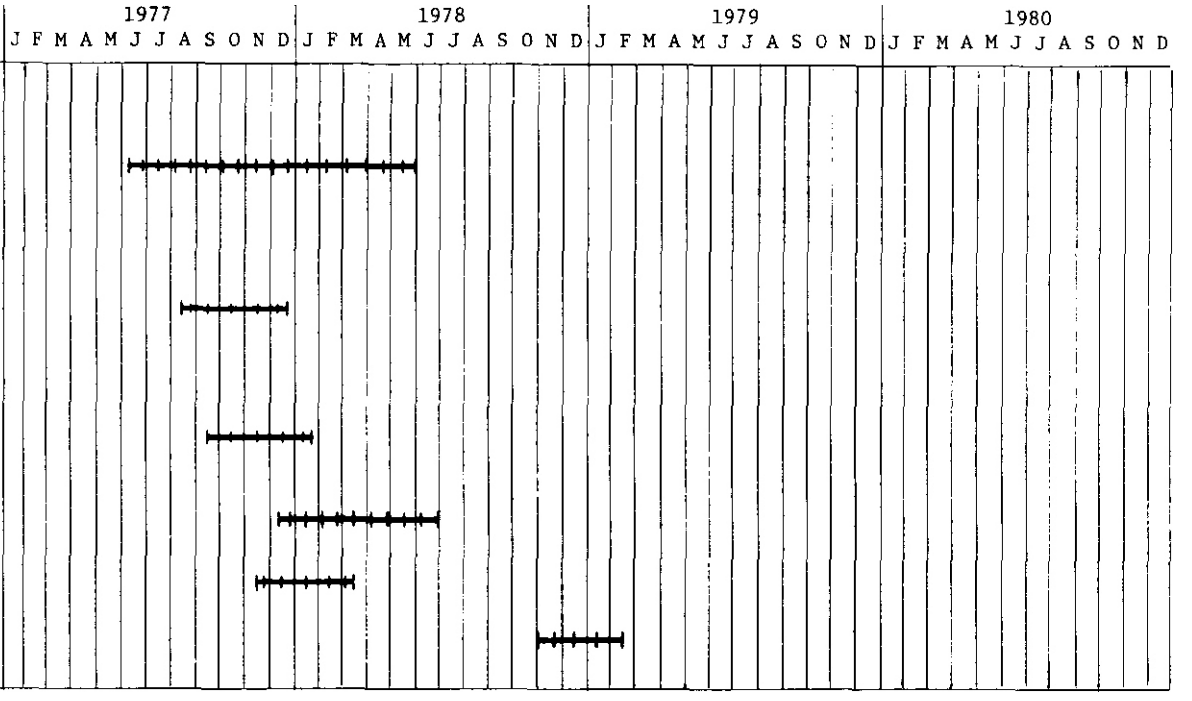

Major Objective
Temperature calibration, tensile properties of MFE ref. 316, 2.25 dpa, 30 at. ppm He
Temperature calibration, tensile properties of MFE ref. 316, 2.25 dpa, 30 at. ppm He [1]
Swelling and tensile properties of MFE ref. 316, 32 dpa, 1900 at. ppm He
Swelling and tensile properties of MFE ref. 316, 56 dpa, 3450 at. ppm He
Swelling and tensile properties of MFE ref. 316, 32 dpa, 1900 at. ppm He
Swelling and tensile properties of MFE ref. 316, 56 dpa, 3450 at. ppm He
Swelling and tensile properties, Paths A, B, and D microstructural variations, 40 dpa, 2500 at. ppm He (Path A)
Swelling and tensile properties, Paths A, B and D microstructural variations, 20 dpa, 1200 ppm He (Path A)
Swelling and tensile properties, Paths A, B and D microstructural variations, 10 dpa, 500 ppm He (Path A)
Swelling and tensile properties, Path E alloys, 10 dpa, 50°C

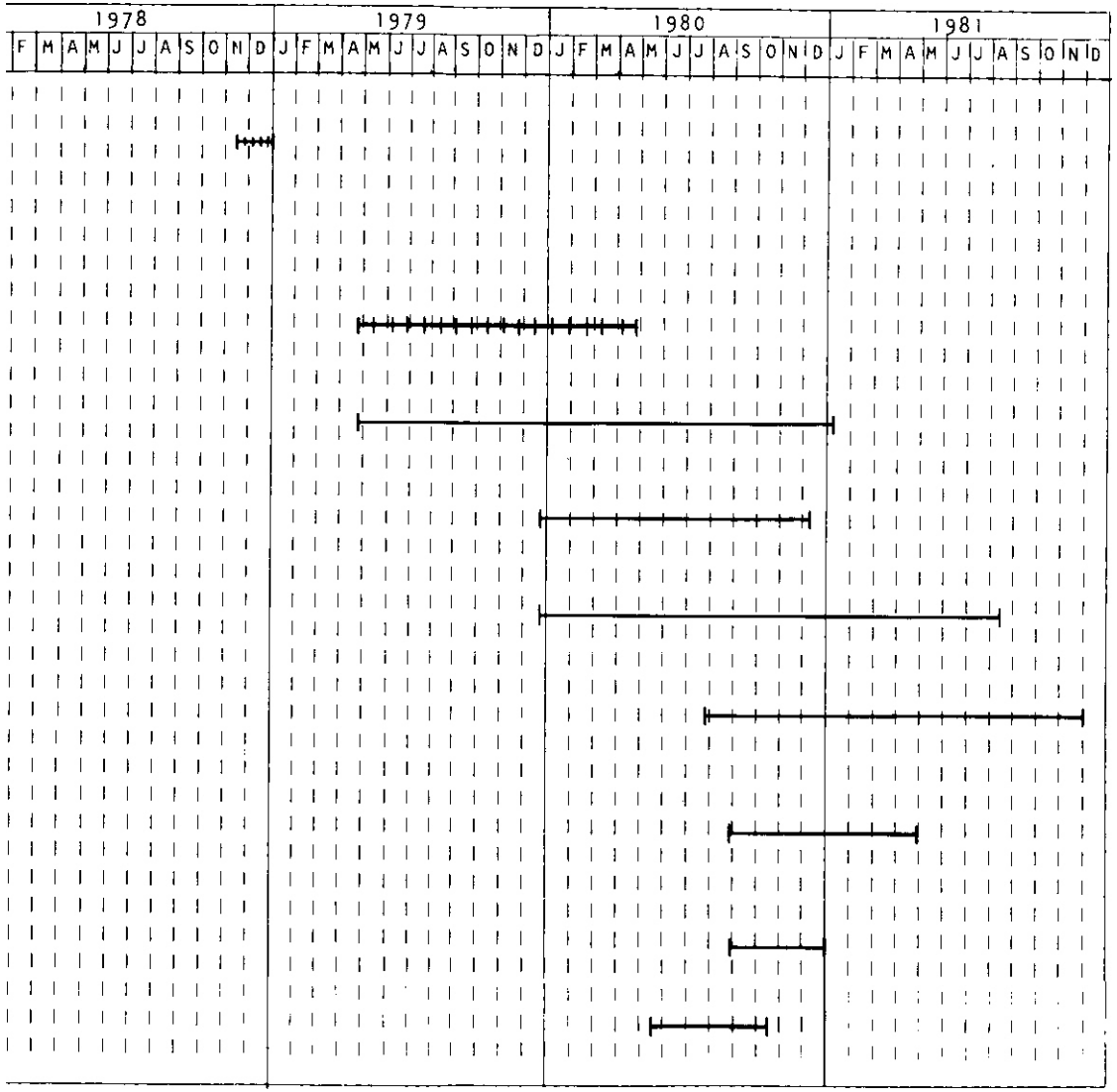

for undetermined period.

8.2 ETM RESEARCH MATERIALS INVENTORY — F. W. Wiffen, T. K. Roche (ORNL) and J. W. Davis (McDonnell Douglas)

8.2.1 ADIP Task

ADIP Task I.D.1, Materials Stockpile for MFE Programs.

8.2.2 Objective

The Office of Fusion Energy has assigned program responsibility to ORNL for the establishment and operation of a central inventory of research materials to be used in the Fusion Reactor Materials research and development programs. The objective is to provide a common supply of materials for the Fusion Reactor Materials Program. This will minimize unintended materials variables and provide for economy in procurement and for centralized recordkeeping. Initially this inventory is to focus on materials related to first-wall and structural applications and related research, but various special purpose materials may be added in the future.

The use of materials from this inventory for research that is coordinated with or otherwise related technically to the Fusion Reactor Materials Program of DOE, but which is not an integral or directly funded part of it, is encouraged.

8.2.3 Materials Requests and Release

Materials requests shall be directed to ETM Research Materials Inventory at ORNL (Attention: F. W. Wiffen). Materials will be released directly if:

(a) The material is to be used for programs funded by the Office of Fusion Energy, with goals consistent with the approved Materials Program Plans of the Materials and Radiation Effects Branch.

(b) The requested amount of material is available, without compromising other intended uses.

Materials requests that do not satisfy both (a) and (b) will be discussed with the staff of the Materials and Radiation Effects Branch, Office of Fusion Energy, for agreement on action.

8.2.4 Records

Chemistry and materials preparation records are maintained for all inventory material. All materials supplied to program uses will be accompanied by summary characterization information.

8.2.5 Summary of Current Inventory and Material Movement in Period Apr. 1 to June 30, 1980

A condensed, qualitative description of the content of materials in the ETM Research Materials Inventory is given in Table 8.2.1. This table indicates the nominal diameter of rod or thickness of sheet for product forms of each alloy and also indicates by weight the amount of each alloy in larger sizes available for fabrication to produce other product forms as needed by the program. Table 8.2.2 lists materials received into the inventory in the quarter covered. Materials distributed from the inventory are listed in Table 8.2.3.

Alloy compositions and more detail on the alloys and on alloy procurement and/or fabrication are given in earlier ADIP quarterly progress reports.

Table 8.2.1. Summary Status of Material Availability in the ETM Kesearch Materials Inventory

Alloy	Product Form			
	Ingot or Bar,[a] Weight (kg)	Rod,[b] Diameter (mm)	Sheet,[c] Thickness (mm)	Thin-Wall Tubing, Wall Thickness (mm)
		Path A Alloys		
316 SS	900	16 and 7.2	13 and 7.9	0.25
PCA	490	12	13	0.25
USSR — Cr-Mn Steel[d]	0	10.5	2.6	0
		Path B Alloys		
PE-16	140	16 and 7.1	13 and 1.6	0.25
B-1	180	0	0	0
B-2	180	0	0	0
B-3	180	0	0	0
B-4	180	0	0	0
B-6	180	0	0	0
		Path C Alloys		
Ti-64	0	0	0.76	0
Ti-62425	0	0	0.76	0
Ti-5621s	0	0	6.3. 2.5. and 0.76	0
Ti-38644	0	0	0.76	0
Nb—1% Zr	0	6.3	2.5, 1.5, and 0.76	0
Nb—5% Mo—1% Zr	0	6.3	2.5. 1.5. and 0.76	0
V—20% Ti	0	6.3	2.5. 1.5. and 0.76	0
v—15% Cr—5% Ti	0	6.3	2.5, 1.5, and 0.76	0
Vanstar-7	0	6.3	2.5, 1.5. and 0.76	0
		Path D Alloys — No Material in Inventory		
		Path E Alloys		
HT9	0	0	4.5 and 18	0
HT9 + 1%Ni	0	0	4.5 and 18	0
HT9 + 2% Ni	0	0	4.5 and 18	0
HT9 + 2% Ni + Cr adjusted	0	0	4.5 and 18	0
T-9 modified	0	0	4.5 and 18	0
T-9 modified + 2% Ni	0	0	4.5 and 18	0
T-9 modified + 2% Ni + Cr adjusted	0	0	4.5 and 18	0
2 1/4 Cr-1 Mo	0	0	e	0

[a] Greater than 25 mm, minimum dimension.

[b] Less than 25 mm in diameter. Some Path A and Path B alloys are available in two different diameters.

[c] Less than 15 mm thick. Some Path A, Path B, and Path C alloys are available in two or three different thicknesses.

[d] Rod and sheet of a USSR stainless steel supplied under the U.S.-USSR Fusion Reactor Materials Exchange Program.

[e] Material is thick-wall Pipe, rerolled as necessary to produce sheet or rad.

Table 8 2 2 ≤TM Res≡arch Materials Inventory, Fusion Reactor Program, Receipts ⊂-1-80 to 6-30-80

Alloy	Heat	Product Form	Dimensions		Quantity							Source
			(mm)	(in.)	(kg)	(lb)	(m)	(in.)	(m^2)	($in.^2$)	(pieces)	
				Path A Alloys – Austenitic Stainless Steels								
Low Ni-High Mn SS	Type EP 838	Sheet	2.64 thick	0.104 thick					0.99	1530	10	USSR
		Rod	10.5 diam	0.415 diam			28.1	1106			28	USSR
				Path E Alloys – Ferritic Steels								
HT9	ESR-XAA-3587-4	Plate	533 × 102 × 18	21 × 4 × 0.7							1	Combustion Engineering
HT9 + 1% Ni	ESR-XAA-3588-9	Plate	508 × 102 × 18	20 × 4 × 0.7							1	Combustion Engineering
HT9 + 2% Ni	ESR-XAA-3589-9	Plate	610 × 102 × 18	24 × 4 × 0.7							1	Combustion Engineering
HT9 + 2% Ni[a]	ESR-XAA-3592-9	Plate	508 × 102 × 18	20 × 4 × 0.7							1	Combustion Engineering
T-9 modified	ESR-XA-3590-9	Plate	584 × 102 × 18	23 × 4 × 0.7							1	Combustion Engineering
T-9 modified + 2% Ni	ESR-XA-3591-9	Plate	584 × 102 × 18	23 × 4 × 0.7							1	Combustion Engineering
T-9 modified + 2% Ni[a]	ESR-XA-3593-9	Plate	533 × 102 × 18	21 × 4 × 0.7							1	Combustion Engineering
2 1/4 Cr-1 Mo	38649	Pipe	114 × 71 × 13	4.5 × 2.8 × 0.5							1	Combustion Engineering

[a]With chromium equivalent adjusted.

Table 8.2.3 ETM Research Materials Fusion Reactor Disbursements 4- to 6-30-80

Alloy	Heat	Product Form	Dimensions		Quantity							Sent to[a]
			(mm)	(in.)	(kg)	(lb)	(m)	(in.)	(m^2)	($in.^2$)	(pieces)	
Path A Alloys — Austenitic Stainless Steels												
PCA	K-280	Tubing	4.57 OD × 0.25 wall	0.180 OD × 0.010 wall			1.5	60				HEDL
PCA	K-280	Sheet	0.25 thick	0.010 thick					0.244	348		Radiation Effects Group, ORNL
Path E Alloys — Ferritic Steels												
HT9	ESR-XAA-3587-4	Plate	533 × 102 × 18	21 × 4 × 0.7							1	Metals Processing Group, ORNL
		Rod	6.91 diam	0.272 diam			2.4	95				Radiation Effects Group, ORNL
		Rod	4 57 diam	0.180 diam			1.8	72				Radiation Effects Group, ORNL
HT9 + 1% Ni	ESR-XAA-3588-9	Plate	508 × 102 × 18	20 × 4 × 0.7							1	Metals Processing Group, ORNL
		Rod	6.91 diam	0.272 diam			≥ 3	91				Radiation Effects Group, ORNL
		Rod	4 57 diam	0.180 diam			1 7	67				Radiation Effects Group, ORNL
HT9 + 2% Ni	ESR-XAA-3589-9	Plate	610 × 102 × 18	24 × 4 × 0.7							1	Metals Processing Group, ORNL
		Rod	6.91 diam	0.272 diam			≥ 2	87				Radiation Effects Group, ORNL
		Rod	4.57 diam	0.180 diam			1.6	62				Radiation Effects

Table 3.2.3 (Continued)

Alloy	Heat	Product Form	Dimensions		Quantity							Sent to[a]
			(mm)	(in.)	(kg)	(lb)	(m)	(in.)	(m^2)	($in.^2$)	(pieces)	
9Cr-1Mo-V-Nb + 2% Ni[b]	ESR-XAA-3592-9	Plate	508 × 102 × 18	20 × 4 × 0.7							1	Metals Processing Group ORNL
		Rod	6.91 diam	0.272 diam			2.4	93				Radiation Effects Group, ORNL
		Rod	4.57 diam	0.180 diam			1.7	68				Radiation Effects Group, ORNL
T-9 modified	ESR-XA 3590-9	Plate	584 × 102 × 18	23 × 4 × 0.7							1	Metals Processing Group, ORNL
		Rod	6.91 diam	0.272 diam			2.2	88				Radiation Effects Group, ORNL
		Rod	4.57 diam	0.180 diam			1.7	68				Radiation Effects Group, ORNL
T-9 modified + 2% Ni	ESR-XA-3591-9	Plate	584 × 102 × 18	23 × 4 × 0.7							1	Metals Processing Group, ORNL
		Rod	6.91 diam	0.272 diam			2.1	82				Radiation Effects Group, ORNL
		Rod	4.57 diam	0.180 diam			1.6	64				Radiation Effects Group, ORNL
T-9 modified + 2% Ni[b]	ESR-XA-3593-9	Plate	533 × 102 × 18	21 × 4 × 0.7							1	Metals Processing Group, ORNL
		Rod	6.91 diam	0.272 diam			2.3	91				Radiation Effects Group, ORNL
		Rod	4.57 diam	0.180 diam			2.5	98				Radiation Effects Group, ORNL
2 1/4 Cr-1 Mo	38649		114 × 71 × 13	4.5 × 2.8 × 0.5							1	Metals Processing Group, ORNL
		Rod	4.57	0.180			0.7	29				Radiation Effects Group, ORNL

[a]HEDL = Hanford Engineering Development Laboratory; ORNL = Oak Ridge National Laboratory.

[b]With chromium equivalent adjusted.

9. CORROSION TESTING AND HYDROGEN PERMEATION STUDIES

9.1 HYDROGEN DISSOLUTION AND PERMEATION STUDIES OF ADIP PROGRAM ALLOYS – E.H. Van Deventer and V. A. Maroni (Argonne National Laboratory).

9.1.1 ADIP Task

I.A.4 Hydrogen Dissolution and Permeation Effects. The results presented in this section contribute to Subtask 1.A.4., Milestones I.A.a through I.A.d.

9.1.2 Objectives

The objective of the work reported in this section is to provide base-line hydrogen dissolution and permeation data for alloys currently under study in the ADIP Program. The hydrogen dissolution, outgassing and permeation characteristics of these materials are vital to an understanding of their performance as first-wall and blanket structural materials for fusion devices. A further objective of this work is to examine methods for overcoming any serious hydrogen isotope uptake and migration problems associated with the rather strong hydride-forming nature of some classes of alloys.

9.1.3 Summm

No report for this period. The next reporting of progress on this task will be at the end of the fourth quarter of FY-1980.

9.2 VANADIUM ALLOY/LITHIUM PUMPED-LOOP STUDIES - D. L. Smith, R. H. Lee, and R. M. Yonco (Argonne National Laboratory)

9.2.1 ADIP Task

I.A.3. Chemical and Metallurgical Compatibility Analysis. The results presented in this section contribute to Subtask I.A.3.4, Milestones I.A.3.c and I.A.3.d.

9.2.2 Objective

The objective of this work is to develop preliminary data on the compatibility of candidate Path C alloys exposed to a flowing lithium environment. The major effort involves investigations of nonmetallic element interactions in reactive/refractory metal-lithium systems and the effects of lithium exposure on the mechanical properties of refractory metal alloys. Information relating to atmospheric contamination of reactive/refractory metal alloys will also be generated. Specific near-term experiments include measurements of the distribution of nonmetallic elements between selected refractory metals and lithium. The results of this work will contribute to the data base that relates compatibility and corrosion phenomena to other alloy development activities and will provide a basis for selecting candidate Path C alloys for further development.

9.2.3 Summary

No report for this period. The next reporting of progress on this task will be at the end of the fourth quarter of FY-1980.

9.3 COMPATIBILITY OF STATIC LITHIUM WITH A LONG-RANGE-ORDERED Fe-Ni-V ALLOY AND 2 1/4 Cr-1 Mo STEEL — P. F. Tortorelli, J. H. DeVan, and C. T. Liu (ORNL)

9.3.1 ADIP Task

ADIP Task **I.A.3,** Perform Chemical and Metallurgical Compatibility Analyses.

9.3.2 Objective

The purpose of this program is to determine the chemical compatibility of fusion reactor candidate materials with metallic lithium. Specimens are exposed to static lithium containing selected solute additions to identify the kinetics and mechanisms that govern corrosion by lithium. Specific program objectives are: (1) to determine the effects of N, C, H, and O on apparent solubilities of metals in Li; (2) to determine the C and N partitioning coefficients between alloys and Li; *(3)* to determine the effects of soluble (Ca, Al) and solid (Y, Zr, Ti) active metal additions on corrosion by Li; and *(4)* to determine the tendencies for dissimilar-metal mass transfer.

9.3.3 Summary

Tests of 2 1/4 Cr-1 Mo steel in static lithium at 400, 500, and 600°C for exposures up to 3000 h have been completed. Analysis of the post-test lithium from the 500- and 1000-h experiments at 500°C indicated a decarburization of the 2 1/4 Cr-1 Mo steel, which probably caused the observed decreases in yield and ultimate tensile strengths of the steel when exposed to lithium at 600°C for 3000 h. A long-range-ordered (LRO) Fe—31.8 Ni—22.5 W .4 Ti (wt %) alloy with a critical ordering temperature (T_c) of 680°C was compatible with static lithium after 2000 h at 650 and 710°C.

9.3.4 Progress and Status

Tests of 2 1/4 Cr-1 Mo steel in static molten lithium were initiated at the first stage in a study of the compatibility of ferritic steels with this element. These preliminary experiments will be used to establish

baseline data on carbon transfer and its effects on mechanical properties as an aid in determining the optimum alloy composition and microstructure for lithium compatibility.

Specimens of 2 1/4 Cr-1 Mo steel were given two different heat treatments before testing in lithium. The first heat treatment, HT1, involved austenitizing for 1 h at 930°C in flowing argon followed by furnace cooling to room temperature at about 60°C/h. The resulting microstructure is shown in Fig. 9.3.1(a). The second heat treatment, HT2, consisted of a similar austenitizing procedure followed by rapid cooling to room temperature in argon and tempering at 700°C for 1 h. This produced the microstructure shown in Fig. 9.3.1(b).

Purified lithium and tensile specimens of 2 1/4 Cr-1 Mo steels with gage lengths of 12.7 mm and 3.2- by 0.6-mm gage sections were sealed inside 22.1-mm-ID by 1.6-mm-wall capsules. The capsules were of the same composition and heat treatment as the internal test specimens. One control sample from each heat treatment was placed in an argon-filled capsule for each test temperature. The capsules were then placed in tube furnaces at 400, 500, and 600°C for various exposure times.

In the preceding quarterly[1] we reported some results from static tests of 2 1/4 Cr-1 Mo steel exposed for 500 and 1000 h to 500°C lithium and argon. Weight changes were negligible, although the yield and ultimate tensile strengths decreased 4 to 10% for the lithium-exposed specimens. Exposures of 3000 h have now been completed, and the results from these experiments are summarized in Table 9.3.1. While the weight losses were not large and did not vary greatly between the two heat treatments, they did increase with increasing temperature. Relative to the tests in argon, yield and ultimate tensile strengths of 2 1/4 Cr-1 Mo steel exposed to lithium decreased at 600°C (Table 9.3.2).

The partitioning of the carbon between the 2 1/4 Cr-1 Mo steel and the lithium is of concern since the mechanical properties of the steel are sensitive to its carbon concentration. The analytical results for both the 500- and 1000-h tests are given in Table 9.3.3. We previously reported[1] that carbon transfer from the steel to the lithium was less

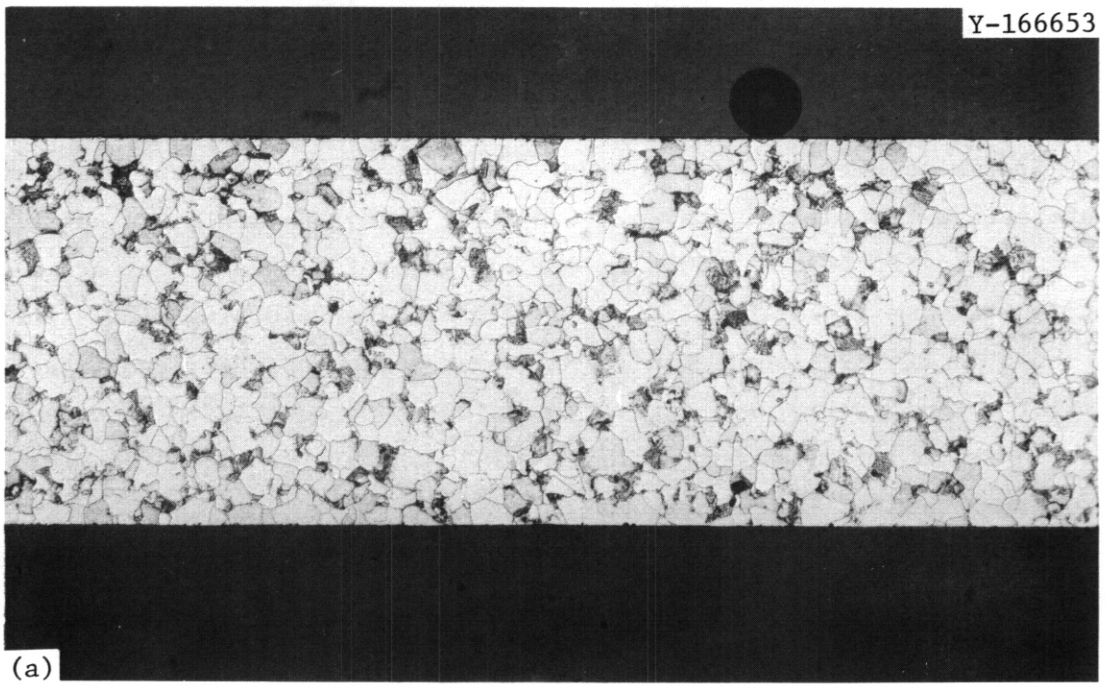

100 μm

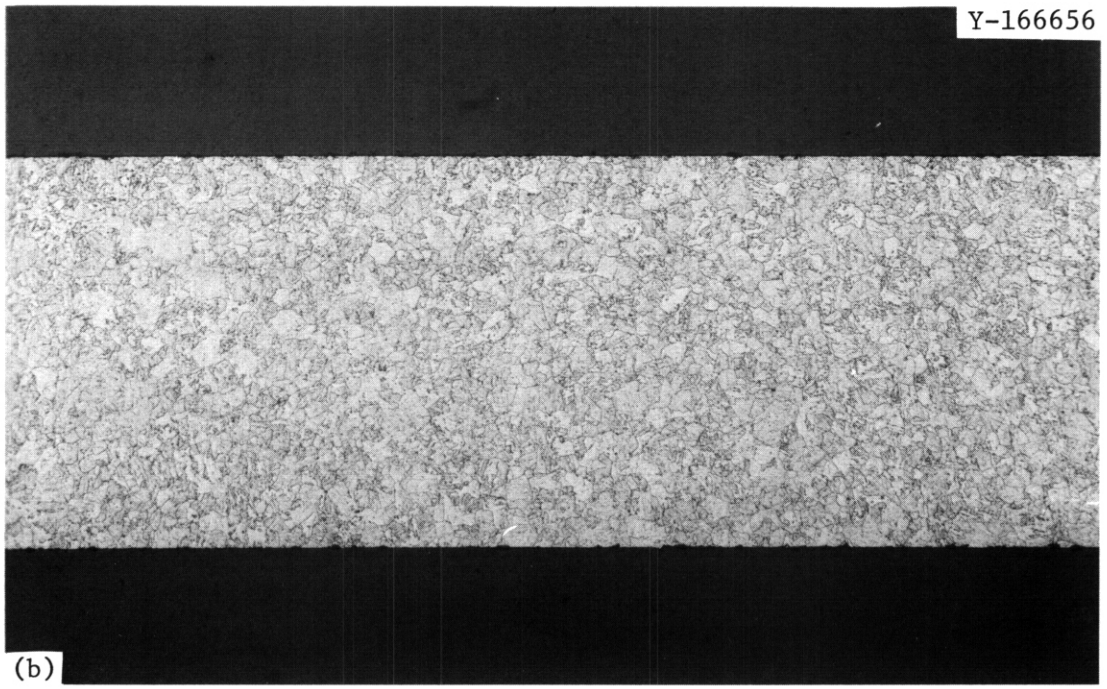

Fig. 9.3.1. The 2 1/4 Cr-1 Mo Before Exposure to Lithium.
(a) Annealed at 930°C for 1 h and cooled at 60°C/h to room temperature.
(b) Normalized at 930°C for 1 h and tempered at 700°C for 1 h.

Table 9.3.1. Weight Change and Tensile Properties[a] of 2 1/4 Cr-1 Mo Steel Exposed to Static Argon and Lithium for 3000 h

Heat Treatment	Environment	Temperature (°C)	Weight Change (g/m^2)	Strength, MPa		Elongation (%)
				Yield	Ultimate Tensile	
HT1	Ar	400	+0.5	251	480	14.9
HT1[b]	Li	400	−0.5	232	494	17.2
HT2	Ar	400	+0.5	452	607	11.2
HT2[b]	Li	400	−0.6	459	602	9.3
HT1	Ar	500	−0.9	265	521	16.4
HT1[b]	Li	500	−1.4	219	478	15.1
HT2	Ar	500	−0.5	485	620	8.6
HT2[b]	Li	500	−1.0	484	616	8.7
HT1	Ar	600	−0.5	212	452	19.2
HT1[b]	Li	600	−2.5	161	356	23.2
HT2	AK	600	−0.2	323	499	17.1
HT2[b]	Li	600	−2.6	153	338	21.7

[a]Room temperature tensile tests with a strain rate of 3.33×10^{-3}/s.

[b]Average of two specimens.

Table 9.3.2. Relative Changes in Yield Strength, Ultimate Tensile Strength, and Elongation of 2 1/4 Cr-1 Mo Exposed to Static Lithium for 3000 h

Temperature (°C)	Heat Treatment	Relative Change,[a] %		
		Yield Strength	Ultimate Tensile Strength	Elongation
400	HT1	-a	+3	+15
	HT2	+2	0	−17
500	HT1	−17	-8	-8
	HT2	0	0	0
600	HT1	−24	−21	+21
	HT2	−53	−32	+27

[a]Relative to 2 1/4 Cr-1 Mo specimens exposed to argon under the same conditions.

Table 9.3.3. Carbon Concentrations of Post-Test Lithium Used in 2 1/4 Cr-1 Mo Experiments[a]

Test Time (h)	Carbon Concentrations,[b] ut ppm	
	From 500°C HT1 Capsules	From 500°C HT2 Capsules
500	243	103
1000	238	136

[a]Analyses were performed by R. M. Yonco of Argonne National Laboratory using the acetylene-evolution method. This method is described in E. M. Hobart and R. G. Bjork, "Validity of Determining Carbon in Lithium by Measurement of Acetylene Evolved on Hydrolysis," *Anal. Chem.* 39: 202 (1967). A control lithium sample was found to have a concentration of 3 wt ppm.

[b]Filtered lithium samples were taken at 500°C.

after 500 h for the specimens that were normalized and tempered (HT2) than for those that were simply annealed (HT1). The 1000-h experiments showed the same trend (Table 9.3.3): the carbon loss from the HT1 steel was greater than that from the HT2 steel. Note that the amounts of carbon gained by the lithium in the HT1 experiments were the same at 500 and 1000 h, while the carbon transfer between the HT2 steel and lithium was slightly greater after 1000 than after 500 h. The decarburization of 2 1/4 Cr-1 Mo steel when exposed to molten lithium may explain the reduction in the yield and ultimate tensile strengths and the increase in elongation noted above. We will be able to make a more definite correlation between the redistribution of carbon and the changes in tensile properties when the carbon analyses of the lithium from the 3000-h tests are completed.

The above results are consistent with decarburization studies of 2 1/4 Cr-1 Mo steel in molten sodium.[2,3] Decarburization was found to

depend on the prior metallurgical structure such that carbon loss in sodium was less rapid for normalized and tempered specimens than for specimens that were just normalized. This difference in the amount of carbon transferred has been attributed to the relatively slow decomposition of carbides in the normalized and tempered steel.[2]

Ductile LRO alloys have been developed at ORNL for high-temperature applications.[4] In previous corrosion tests[5] an LRO alloy composed of Fe—31.8 Ni—22.5 V—0.4 Ti (wt %) was found to be compatible with static lithium at 500 and 600°C. This was in contrast to alloy 800 [46 Fe—32 Ni—21 Cr (wt %)], which, like other higher nickel alloys,[6,7] suffered significant attack by static lithium.[5] To determine if the corrosion resistance of the LRO alloy could be attributed to its ordered structure (for example, as a result of reduced nickel activity and mobility in the LRO lattice), similar experiments were conducted at temperatures slightly above and below the critical ordering temperature of 680°C. The weight change results of Fe—31.8 Ni—22.5 V—0.4 Ti (wt %) LRO exposed to static lithium for 2000 h are shown below.

Test Temperature (°C)	Weight Change (g/m^2)
500	-0.2, —0.5, -0.5
600	—0.2, —0.5, -0.5
650	0.0, 0.0, —0.2
710	+0.2, 0.0, —0.2

These results include data from previous tests at 500 and 600°C. Three weight change values are indicated for each temperature since three specimens were tested in a single capsule at that temperature. Note that the specimens in the disordered state (those held at 710°C in static lithium) did not suffer greater weight losses than the specimens at 650°C. On the other hand, the specimens exposed at 710°C did show marked increases in yield strength and decreases in elongation when compared with the control specimens, while the same properties of those exposed below T_c did not change substantially (Table 9.3.4). Metallographic

Table 9.3.4. Tensile Properties of Long-Range-Ordered [Fe—31.8 Ni—22.5 V—0.4 Ti (wt %)] Specimens Exposed to Static Lithium for 2000 h

Temperature, °C		Strength, MPa		Elongation (%)
Lithium Exposure	Tensile Test	Yield	Ultimate Tensile	
Unexposed	25	270	1124	42.1
650	25	270	1034	44.5
710	25	701	1122	5.1
Unexposed	650	391	027	33.6
650	650	367	726	30.2
710	650	507	791	15.3

examination of the specimens revealed distinctly different post-test microstructures (Fig. 9.3.2). The micrograph in Fig. 9.3.2(b) and the characteristics of the stress-strain curves suggest that sigma phase formed during the 710°C exposure. Subsequent x-ray diffraction confirmed the presence of this phase which would then account for the reduced ductility of the specimens held above T_c. It therefore appears that the increases in yield strength and decreases in elongation can be ascribed strictly to thermal effects and probably not to any influence of the lithium.

9.3.5 Conclusions

1. Relative to tests in argon, the room temperature yield and ultimate tensile strengths of 2 1/4 Cr-1 Mo steel exposed to 600°C lithium for 3000 h decreased significantly. This can probably be ascribed to decarburization. Carbon was transferred from 2 1/4 Cr-1 Mo steel to lithium at 500°C after 1000-h exposures with the amount of carbon loss being greater for the annealed steel than for the alloy in a normalized and tempered condition.

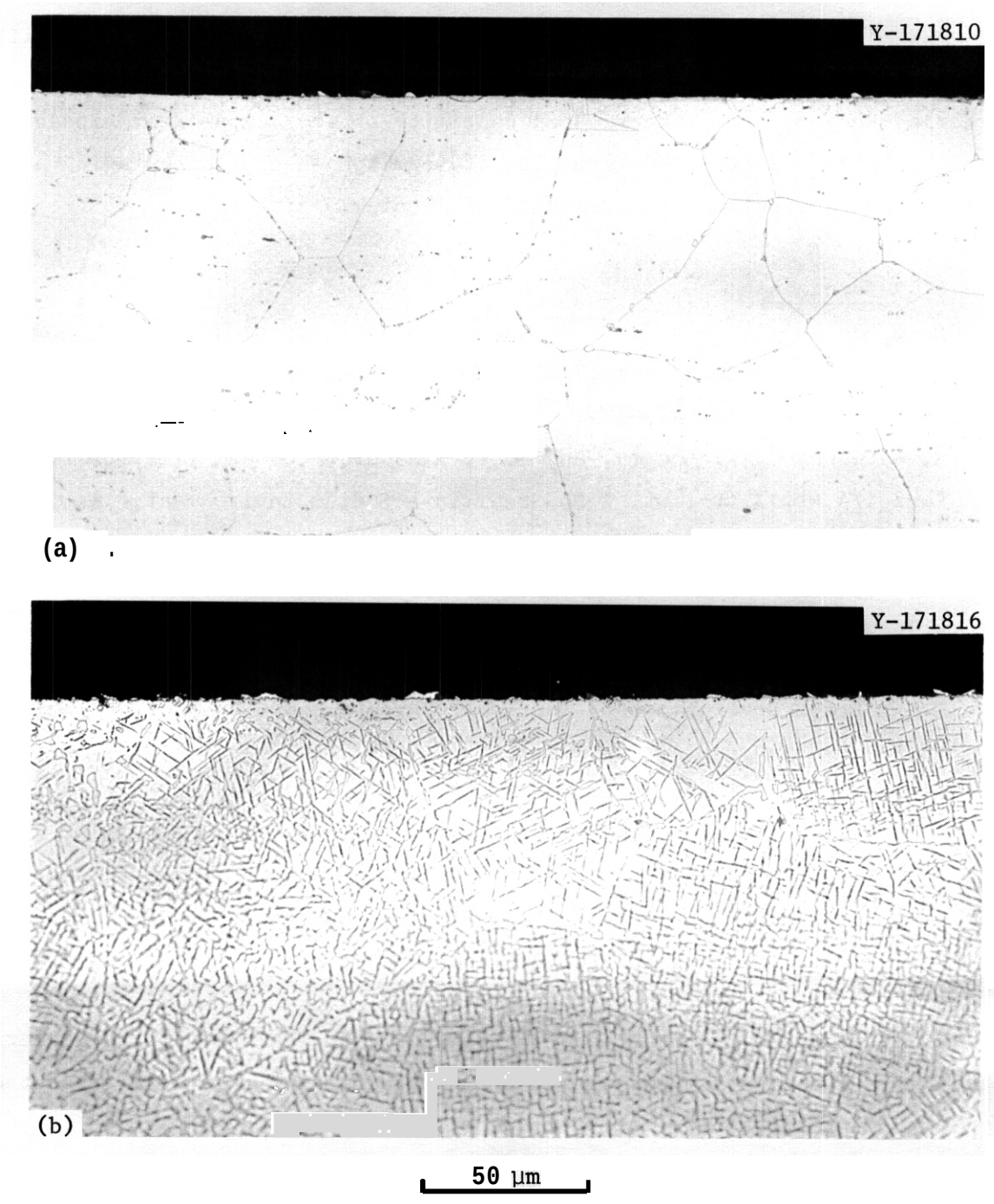

Fig. 9.3.2. Long-Range-Ordered [Fe—31.8 Ni—22.5 *W*. *4* Ti (wt %)] Alloy Exposed to Static Lithium for 2000 h. (a) 650°C. (b) 710°C.

2. The LRO Fe—31.8 Ni—22.5 W .4 Ti (wt %) alloy is compatible with static lithium up to 710°C (2000 h), which is 30°C above the critical ordering temperature. The reduced ductility of the alloy after exposure at 710°C resulted from the formation of sigma phase by thermal aging and thus is not a result of the presence of lithium.

9.3.6 References

1. P. F. Tortorelli and J. H. DeVan, "Compatibility of 2 1/4 Cr-1 Mo Steel with Static Lithium," *ADIP Quart. Prog. Rep. Mar. 31, 1980,* DOE/ER-0045/2, pp. 213—18.
2. K. Natesan, O. K. Chopra, and T. F. Kassner, "Compatibility of Fe-2 1/4 wt. % Cr-1 wt. % Mo Steel in a Sodium Environment," *Nucl. Technol.* 28: 441—51 (1976).
3. K. Matsumoto et al., "Carbon Transfer Behavior of Materials for Liquid-Metal Fast Breeder Reactor Steam Generators," *Nuct. Technol.* 28: 452—70 (1976).
4. C. T. Liu, "Development of Ductile Long-Range Ordered Alloys for Fusion Systems," *J. Nucl. Mater.* 85 & 86(II,B): 907—11 (1979).
5. P. F. Tortorelli and J. H. DeVan, "Corrosion of Fe-Ni-Cr and Fe-Ni-V Alloys in Static Lithium," *ADIP Quart. Prog. Rep. Dec.* 31, *1979,* DOE/ER-0045/1, pp. 152—57.
6. P. F. Tortorelli and J. H. DeVan, "The Corrosion of Ni-Fe-Cr and Co-V-Fe (LRO) Alloys in Static Lithium," *ADIP Quart. Prog. Rep. Mar.* 31, *1979,* DOE/ET-0058/5, pp. 141—47.
7. G. R. Edwards, D. Bates, and D. L. Olson, "An Evaluation of Engineering Alloys for High Temperature Lithium Containment," paper 118 presented at NACE Corrosion/79, Atlanta, Georgia, March 12—16, 1979.

9.4 MASS TRANSFER OF TYPE *316* STAINLESS STEEL IN LITHIUM THERMAL-CONVECTION LOOPS — P. F. Tortorelli and J. H. DeVan (ORNL)

9.4.1 ADIP Task

ADIP Task I.A.3, Perform Chemical and Metallurgical Compatibility Analyses.

9.4.2 Objective

The purpose of this task is to evaluate the corrosion resistance of candidate first-wall materials to flowing lithium in the presence of a temperature gradient. Corrosion rates (in both dissolution and deposition) are measured as functions of time, temperature, additions to the lithium, and flow conditions. These measurements are combined with chemical and metallographic examinations of specimen surfaces to establish the mechanisms and rate-controlling processes for dissolution and deposition reactions.

9.4.3 Summary

The possible effects of nitrogen in lithium-type 316 stainless steel thermal-convection systems are discussed. Variations in the normally low nitrogen concentrations of the lithium did not significantly alter the short-time dissolution rate. However, the presence of nitrogen in lithium may influence the distribution of the dissolved elements around the loops through nitrogen interactions with other elements (especially chromium) in the lithium.

9.4.4 Progress and Status

We have continued our study of the mass transfer of type *316* stainless steel in flowing lithium using previously described[1] thermal-convection loops (TCLs) with accessible specimens. These loops are designed *so* that lithium samples can be taken and corrosion coupons can be withdrawn and inserted without altering the loop operating conditions. Each of three such loops have been operating for several thousand hours

and have yielded data on dissolution and deposition processes as a function of time.[2,3] Plugging from mass transfer deposits has necessitated eventual replacement of the cold legs in all three loops.

While enhanced levels of nitrogen in static lithium (>1000 wt ppm) have been shown[4] to promote the corrosion of stainless steel, the effect has been much less pronounced in our thermal-convection systems, which have operated at a maximum temperature of 600°C. McKee[5] found a significant increase in mass transfer in loops operated at 800°C when the nitrogen content of the lithium was increased from 125 to 370 wt ppm. On the other hand, other experiments[6,7] have shown that nitrogen additions to flowing lithium have a negligible effect on the overall mass transfer rate. Recent results from our long-term TCLs operating at a maximum temperature of 600°C with a *AT* of 150°C have shown that variations of no more than 100 wt ppm in the baseline nitrogen and oxygen concentrations of lithium have no effect on dissolution. This can be seen from the data in Table 9.4.1, which lists the average weight losses after initial 500-h

Table 9.4.1. The 500-h Average Weight Losses[a] for Type 316 Stainless Steel Exposed to Flowing Lithium in Thermal-Convection Loops

Concentrations in Lithium, wt ppm		Average Weight Loss (g/m^2)
Nitrogen[b]	Oxygen[c]	
30	90	11.5
44	12	7.3[d]
124	86	10.0
128	134	9.1

[a]An average of five coupons situated between 520 and 600°C.

[b]Nitrogen concentration determined by micro-Kjedahl method.

[c]Oxygen concentration determined by neutron activation analysis.

[d]Results from a fresh type 316 stainless steel loop with fresh coupons; in the other three cases, fresh coupons were in loops that had already circulated lithium for several thousand hours.

exposures of the specimens in the dissolution regions (H3 through H6, Fig. 9.4.1) of the three TCLs described above and the corresponding starting nitrogen and oxygen concentrations. No correlation between the impurity levels of the lithium and the average weight losses is apparent. This may result from these concentrations heing less than threshold Levels €or observing an effect. However, it does appear that, at least for flow velocities typical of this study (–30 mm/s), nitrogen concentrations in lithium may he allowed to vary over an order of 1 to 130 wt ppm or greater without significantly affecting compatibility. By analogy with oxygen effects in sodium,[8] it is possible that at higher lithium velocities even these relatively low nitrogen levels may have a detrimental effect on the corrosion resistance of stainless steels.

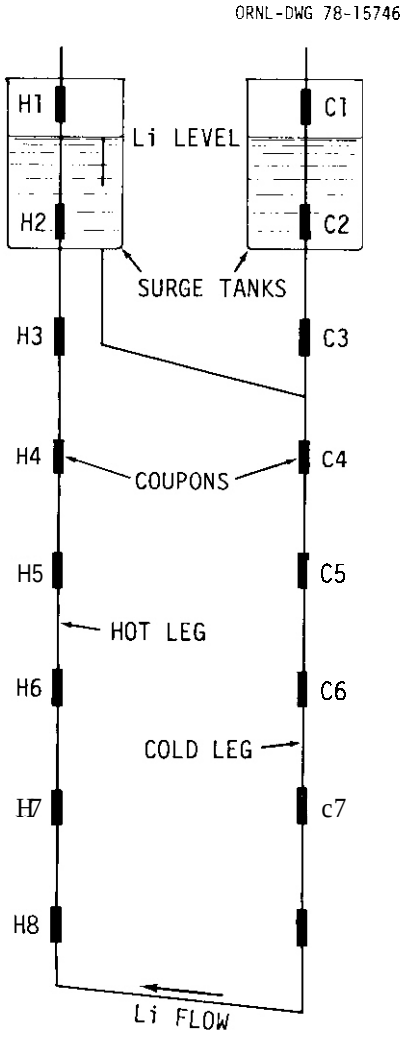

Fig. 9.4.1. Schematic of Coupons in Their Positions in a Thermal–Convection Loop.

The presence of nitrogen in lithium may influence mass transfer of stainless steel in ways other than those possibly affecting the dissolution rate. For example, there are indications' that the presence of nitrogen at levels of 500 and 1700 wt ppm in lithium may change the dissolution and deposition pattern around the loop without causing a drastic change in the rate of material loss. Furthermore, recent data on Cr-Li_3N interactions in lithium[9] may help explain the deposition of pure chromium in the cold legs of type 316 stainless steel-lithium TCLs during the initial period of operation.[3] Specifically, Calaway[9] has reported that chromium reacts with nitrogen in solution in lithium above 500°C and has proposed the existence of a Li-Cr-N ternary compound. It is possible that this type compound formed in the hotter regions of our TCLs (500–600°C) hut decomposed in the cooler areas (450–500°C), where elemental chromium was then deposited. Since nitrogen would react eventually with the other elements in the lithium and with those of the loop wall, this process would he a transient one. This proposed mechanism would explain the observed initial deposition characteristics; however, the reported reaction of chromium with Li_3N in lithium occurred at nitrogen levels in lithium down to concentrations of about 1000 wt ppm, which were still much greater than the normal concentrations in our loops. Further work on the effect of nitrogen in lithium on mass transfer is thus required. We are planning to more definitively study this effect by modifying one of our type 316 stainless steel TCLs to allow direct additions of nitrogen into the flowing lithium.

9.4.5 Conclusions

1. Variations in the residual nitrogen and oxygen concentrations of naturally convective flowing lithium from 30 to 135 wt ppm did not significantly alter the short-time dissolution rate of type 316 stainless steel.

2. The presence of nitrogen in lithium may influence the distribution of the dissolved elements around the loop circuits through nitrogen interactions with other elements in the lithium.

9.4.6 References

1. J. H. DeVan and J. R. DiStefano, "Thermal-Convection Loop Tests of Type 316 Stainless Steel in Lithium," *ADIP Quart. Prog. Rep. Mar. 31, 1978,* DOE/ET-0058/1, pp. 200–08.

2. P. F. Tortorelli and J. H. DeVan, "Thermal-Gradient Mass Transfer in Lithium-Stainless Steel Systems," *J. Nucl. Mater.* 85 & 86(II,A): 289—93 (1979).
3. P. F. Torturelli and J. H DeVan, "Mass Transfer Deposits io Lithium-Type 316 Stainless Steel Thermal-Convection Loops," paper presented at Second International Conference on Liquid Metal Technology in Energy Production, Richland, Wash., April 21—24, 1980.
4. P. F. Tortorelli and J. H. DeVan, "The Compatibility of Type 316 Stainless Steel with Nitrogen-Contaminated Static Lithium," *ADIP Quart. Prog. Rep. Sept. 30, 1979,* DOE/ET-0058/7, pp. 162—69.
5. J. M. McKee, *Effect of Nitrogen on Corrosion by Lithium,* NDA-40 (June 1957).
6. E. E. Hoffman, *Corrosion of Materials by Lithium at Elevated Temperatures,* ORNL-2674 (March 1959).
7. P. F. Torturelli, J. H. DeVan, and J. E. Selle, "Corrosion in Lithium-Stainless Steel Thermal-Convection Systems," paper presented at Secund International Conference on Liquid Metal Technology in Energy Production, Richland, Wash., April 21—24, 1980.
8. B. H. Kolster, "The Influence of Sodium Conditions on the Rate for Dissolution and Metal/Oxygen Reaction of AISI 31h in Liquid Sodium," paper presented at Second International Conference on Liquid Metal Technology in Energy Production, Richland, Wash., April 21—24, 1980.
9. W. F. Calaway, "The Reaction of Chromium with Lithium Nitride in Liquid Lithium," paper presented at Second International Conference on Liquid Metal Technology in Energy Production, Richland, Wash., April 21—24, 1980.

DOE/ER-0045/3
Distribution
Category
uc-20, 20c

DISTRIBUTION

1–4. Argonne National Laboratory, 9700 South Cass Avenue, Argonne, IL 60439

L. Greenwood
V. Maroni
D. L. Smith
H. Wiedersich

5–6. Battelle-Pacific Northwest Laboratory, P.O. Box 999, Richland, WA 99352

J. L. Brimhall
D. Dingee

7. Carnegie-Mellon University, Schenley Park, Pittsburgh, PA 15213

J. C. Williams

8–203. Department of Energy, Technical Information Center, Office of Information Services, P.O. Box 62, Oak Ridge, TN 37830

For distribution as shown in TID-4500 Distribution Category, UC-20 (Magnetic Fusion Energy), and UC-20c (Reactor Materials)

204–209. Department of Energy, Office of Fusion Energy, Washington, DC 20545

M. M. Cohen
T. C. Reuther, Jr. (5 copies)

210. Department of Energy, Oak Ridge Operations Office, P.O. Box E, Oak Kidge, TN 37830

Office of Assistant Manager for Energy Research and Development

211. General Atomic Company, P.O. Box 81608, San Diego, CA 92138

S. N. Rosenwasser

212–218. Hanford Engineering Development Laboratory, P.O. Box 1970, Kichland, WA 99352

D. G. Doran
D. S. Gelles
J. J. Holmes
R. E. Nygren
E. C. Opperman
K. W. Powell
J. L. Straalsund

219–221. Lawrence Livermore Laboratory, P.O. Box 808, Livermore, CA 94550

E.N.C. Dalder
M. Guinan
C. M. Logan

222–225. Massachusetts Institute of Technology, Cambridge, MA 02139

O. K. Harling
N. J. Grant
D. J. Rose
V. B. Vander Sande

226–227. McDonnell Douglas Astronautics Company, East, P.O. Box 516, St. Louis, MO 63166

J. W. Davis
D. L. Kummer

228–230. Naval Research Laboratory, Washington, DC 20375

Superintendent, Materials Science and Technology Division
J. A. Sprague
H. Watson

231–263. Oak Ridge National Laboratory, P.O. Box X, Oak Ridge, TN 37830

Central Research Library (2 copies)
Document Reference Section
Laboratory Records Department (2 copies)
Laboratory Records Department, RC
ORNL Patent Section
B. G. Ashdown
E. E. Bloom (10 copies)
D. N. Braski
J. H. DeVan
T. A. Gabriel

11. L. Grossbeck
M. R. Hill (3 copies)
K. C. Liu
P. J. Maziasz
C. J. McHargue
T. K. Roche
J. L. Scott
K. R. Thoms
P. F. Tortorelli
F. W. Wiffen

264–265. Sandia National Laboratories, Livermore Division 8316, Livermore, CA 94550

J. Swearengen
W. Baller

266. University of California, Department of Chemical, Nuclear, and Thermal Engineering, Los Angeles, CA 90024

R. W. Conn

267. University of California, Santa Barbara, CA 93106

G. R. Odette

268. University of Virginia, Department of Materials Science, Charlottesville, VA 22901

W. A. Jesser

269. University of Wisconsin, 1500 Johnson Drive, Madison, WI 53706

W. G. Wolfer

270. Westinghouse Electric Company, Fusion Power Systems Department, P.O. Box 10864, Pittsburgh, PA 15236

R. E. Gold

☆ U S GOVERNMENT PRINTING OFFICE 1980-640 245/301